

**DESIGN AND TESTING OF A COMPOSITE MATERIAL
FOR MODELLING WIND TURBINE BLADE
STRUCTURES IN TROPICAL REGION**



**UNIVERSITY OF[™]
KWAZULU - NATAL**

**INYUVESI
YAKWAZULU-NATALI**

By

Getahun Aklilu Tefera

214584680

*A thesis submitted to the College of Agriculture, Engineering and Science, School of
Engineering, University of KwaZulu-Natal, South Africa in fulfilment of the degree
Of*

Doctor of Philosophy in Mechanical Engineering

MARCH 2018

As the candidate's Supervisor I agree/~~do not agree~~ to the submission of this thesis.

.....
Prof Sarp Adali

.....
Date

.....
Prof Glen Bright

.....
Date

.....
Prof Innocent Davidson

.....
Date

Declaration 1 - Plagiarism

I, Getahun Aklilu Tefera declare that

1. The research reported in this thesis, except where otherwise indicated, is my original research.
2. This thesis has not been submitted for any degree or examination at any other university.
3. This thesis does not contain other persons' data, pictures, graphs or other information, unless specifically acknowledged as being sourced from other persons.
4. This thesis does not contain other persons' writing, unless specifically acknowledged as being sourced from other researchers. Where other written sources have been quoted, then:
 - a. Their words have been re-written but the general information attributed to them has been referenced
 - b. Where their exact words have been used, then their writing has been placed in italics and inside quotation marks, and referenced.
5. This thesis does not contain text, graphics or tables copied and pasted from the Internet, unless specifically acknowledged, and the source being detailed in the thesis and in the References sections.

Signed:  08/March/2018
Getahun Aklilu Tefera Date

Declaration 2 – Publications

Details of contribution to publications that form part and/or include research presented in this thesis (include publications in preparation, submitted, in press and published and give details of the contributions of each author to the experimental work and writing of each publication)

Publication 1

Tefera, G.A, Adali, S., Bright, G., 2017. Experimental Characterization of Hybrid and Non-Hybrid Polymer Composites at Elevated Temperatures (Submitted to International Journal of Engineering Research in Africa – Accepted).

Contribution: Getahun A. Tefera - experimental work and writing; Prof. Adali, S., and Prof. Bright, G., - supervision.

Publication 2

Tefera, G.A, Adali, S., Bright, G., 2017. Failure Analysis of Rotating Hybrid Laminated Composite Beams (submitted to Journal of Engineering Failure Analysis - under review).

Contribution: Getahun A. Tefera- experimental work and writing; Prof. Adali, S., and Prof. Bright, G., - supervision.

Publication 3

Tefera, G.A, Adali, S., Bright, G., Davidson, I. 2016. Characterization of Fiber Reinforced Polymer (FRP) Composite Materials Applicable on Wind Turbine Blade Structures at Elevated and High Environmental Conditions, Part I (conference: College of Agriculture, Engineering and Science research day, 29 November 2016)

Publication 4

Tefera, G.A, Adali, S., Bright, G., Davidson, I. 2017. Characterization of Fiber Reinforced Polymer (FRP) Composite Materials Applicable on Wind Turbine Blade Structures at High Temperatures, Part II (accepted, conference paper on Composite and Advanced Material Expo- CAMX-2017, Orlando Florida, September 11-14, 2017)

Publication 5

Tefera, G.A, Adali, S., Bright, G., Davidson, I. 2017. Effects of elevated Temperatures on the mechanical properties of carbon, glass and glass-carbon fiber epoxy composite specimen (submitted to Journal of Construction and Building Materials - under review)
Contribution: Getahun A. Tefera- experimental work and writing; Prof. Adali, S., Prof. Bright, G., and Prof. Davidson, I., - supervision.

Publication 6

Tefera, G.A, Bright, G., Adali, S., 2017. Effect of Temperature on Failure of Rotating Beam of Hybrid Composite (submitted to Journal of Sandwich Structures and Materials - under review)
Contribution: Getahun A. Tefera- experimental work and writing; Prof. Adali, S., and Prof. Bright, G., - supervision.

Publication 7

Tefera, G.A, Adali, S., Bright, G., Davidson, I. 2018. The effects of Temperature on Mechanical Behavior of Composite Wind Turbine Blade Structures (accepted, conference paper on Advanced Energy Materials, Stockholm, Sweden 25-28, March 2018)

Signed 08/March/2018
Getahun Aklilu Tefera Date

Acknowledgements

First, I would like to give all the glory to God for giving me the wisdom, knowledge and strength to do this research.

To my supervisor Professor Sarp Adali I owe so much of my personal development to your relentless quest to push me further and explore the unknown confidently. I am grateful for your support both in the technical and personal circles of my life. I thank you for your patience and guidance during the course of this research.

Another thank you to my co-supervisor Professor Glen Bright. I am grateful for your valuable guidance and encouragement.

I express thanks to my co-supervisor Professor Innocent Davidson providing simulation software and his financial support. I would like earnestly thank you for all composite laboratory technicians in DUT.

Finally, thanks to my friends and family for their encouragement and support.

Getahun Aklilu Tefera

Abstract

Currently large wind turbine blades have been installed in several offshore and onshore wind farms around the world, particularly in the desert areas of North East Africa where wind turbine blades and nacelles are affected by elevated temperatures. The aim of this study is to investigate the effect of temperature variation on the mechanical behaviour of composite wind turbine blades installed in tropical wind farms. The blades are constructed from unidirectional carbon fibre/epoxy, glass fibre/epoxy and hybrids of these two composite materials. ASTM standards were taken into account when the composite specimens were manufactured for testing purposes. Short Beam Shear (SBS), Dynamic Mechanical Analysis (DMA) and tensile tests were conducted under increasing temperatures to investigate the mechanical behaviour of composite materials when used for structural modelling of wind turbine blades. Experimental findings revealed that the strength and stiffness properties of composite specimens were reduced when temperatures increased. Betz's element momentum theory and Glauert's modelling methods were used to investigate the characteristics of composite wind turbine blades measuring 54m and generating 2MW power. Flap-wise loading was taken into account along the length of the wind turbine blades when they were analysed using the Blade Element Momentum (BEM) theory. The wind turbine blades were developed using carbon fibre/epoxy, glass fibre/epoxy, glass-carbon fibre/epoxy and carbon-glass fibre/epoxy composite materials. The tip deflection of the blades was analysed allowing for different flap-wise and thermal loadings. Simulation results indicated that a glass/epoxy blade has the highest and a carbon/epoxy blade the lowest tip deflection. The values for the tip deflections of the blades show minimal change under thermal loading. To study the mechanical behaviour of the blades under thermal loading, an element-wise approach was developed and the failure index for different composite materials was computed. Tsai-Wu failure criterion was employed to determine the failure index of each composite material under thermal and mechanical loadings. Blades failed when the thermal loading was above 40°C irrespective of the flap-wise loading. This finding was similar to the experimental results mentioned above. Carbon/epoxy showed non-linear behaviour when the test temperature approached 40°C.

Generally, experimental and numerical results are comparable and can be considered valid. To conclude carbon-glass fibre/epoxy composite wind turbine blades are observed to be a better option for tropical wind farms based on experimental and simulation results.

Table of Contents

Contents.....	viii
List of Figures.....	xi
List of Tables.....	xvii
Introduction.....	1
1.1 Wind Energy and Blade Materials.....	1
1.2 Problem Definition.....	2
1.3 Motivation.....	2
1.4 Aims and Objectives.....	3
1.5 Methods and Materials.....	3
1.6 Technical and Scientific Contributions.....	4
1.7 Structure of the Thesis.....	5
Chapter 2.....	6
Literature Review.....	6
2.1 Wind Power Development and Effect of Temperature on FRP Materials.....	6
2.2 Composite Materials for Construction of Wind Turbine Blades.....	9
2.2.1 Behavior of FRP Composite Material under High Temperatures.....	11
2.2.1.1 Strength Properties of FRP Materials under High Temperatures.....	11
2.2.1.2 Stiffness Properties of FRP Material under High Temperatures.....	13
2.2.1.3 Effect of Temperature on Impact Damages of FRP Material.....	17
2.2.1.4 Effect of Temperature on Fatigue Strength of FRP Material.....	19
2.3 Summary of Review.....	25
Chapter 3.....	27
Materials and Testing Methods.....	27
3.1 Materials and Manufacturing Process.....	27
3.2 Manufacturing Process of FRP Composite Specimens.....	27
3.3 Testing Equipment and Experimental Methods.....	38
3.3.1 Short Beam Shear (SBS) Testing Method.....	38
3.3.2 Dynamics Mechanical Analysis (DMA) Testing Method.....	39
3.3.3 Tensile Strength Tests.....	40
3.3.4 Matrix Digestion Testing Methods.....	41
3.4 Numerical Analysis.....	42
3.4.1 Chi-square Test Methods.....	42

3.4.1.1	Normal Distribution	42
3.4.1.2	Log-Normal Distribution	43
3.4.1.3	Weibull Distribution	43
3.4.1.4	Chi-Square Goodness of Fit Test Method	44
3.4.2	Finite Element Methods	44
3.5	Experimental Summary	45
Chapter 4	46
Testing and Characterization of FRP Composite Materials at Elevated Temperatures	.	46
4.1	Testing Principles of FRP Composite Specimens	46
4.2	Short Beam Shear (SBS) Test Results	47
4.2.1	Statistical Analysis of Experimental Results.....	49
4.3	Dynamic Mechanical Analysis (DMA) Test Results.....	55
4.4	Principles of Tensile Strength Testing and Results.....	61
4.4.1	Finite Element Modeling Methods and Results	69
4.4.2	Comparison of Experimental and FEA on Tensile Testing.....	73
4.4.3	Statistical Analysis of Test Results for Tensile Strength	75
4.5	Test Summary	81
Chapter 5	82
Development of Airfoil Profiles to Model Optimized Shapes of HAWT Blades	82
5.1	Principles of a Wind Turbine Energy Conversion System	82
5.2	Betz's Elementary Momentum Theory.....	82
5.3	Flow through Horizontal-Axis Wind Turbine with Wake Rotation	86
5.4	Airfoil Characterization and Non-Dimensional Parameters	89
5.5	Lift, Drag and Moment Coefficients Analysis of a Turbine Blade.....	90
5.5.1	Parameters Considered on Modelling Wind Turbine Airfoils	91
5.5.1.1	Modelling and Selection of Airfoils using QBlade/XFoil Techniques..	95
5.5.1.2	Modelling and Selection of Airfoil using CFD Technique.....	102
5.6	Momentum Theory and Blade Element Theory for Modelling Blades.....	120
5.6.1	Momentum Theory.....	120
5.6.2	Blade Element Theory	121
5.6.3	Combined Blade Element Momentum Theory for Modelling Blades	124
5.7	Summary of Chapter	129
Chapter 6	131

Development of Composite Wind Turbine Blade Structures	131
6.1 Elements of Modern Wind Turbine Blades.....	131
6.2 Micromechanical Modelling of Material for Wind Turbine Blade	131
6.3 Numerical Modelling of Turbine Blade under Variable Temperature	141
6.3.1 Geometrical Modeling.....	141
6.3.2 Boundary and Loading Conditions under Variable Temperatures.....	145
6.4 Finite Element Analysis and Results.....	146
6.5 FEM Blade Structural Failure Analysis.....	151
6.6 Summary of Chapter	160
Chapter 7.....	161
Discussion of Results.....	161
7.1 Introduction.....	161
7.2 Static Mechanical Behaviour.....	161
7.3 Dynamic Mechanical Behaviour.....	163
7.4 Airfoil Profile and Structural Development of HAWT	165
7.5 Summary of Discussion	170
Chapter 8.....	171
Conclusions and Recommendations	171
8.1. Conclusions	171
8.2. Recommendations for Future Research	173
References.....	174

List of Figures

Figure 2. 1 Wind power capacity of the top five countries in 2016	8
Figure 2. 2 Wind power capacity of African and Middle Eastern countries	9
Figure 2.3 Definition of different material states and transitions under increasing temperatures.....	15
Figure 3. 1 Unidirectional carbon, glass fibre types and Ampreg 21 epoxy resin.....	28
Figure 3. 2 Hand lay-up tools and lamination process of composite laminates	29
Figure 3. 3 Unidirectional FRP composite specimens prepared for SBS testing	30
Figure 3. 4 Unidirectional FRP composite specimens prepared for DMA testing.....	30
Figure 3. 5 Unidirectional fibre lay-up process before resin infusions	33
Figure 3. 6 Vacuum resin infusion and curing process of glass fibre/epoxy specimens.	34
Figure 3. 7 Resin infusion and curing process of carbon fibre/epoxy specimens.	35
Figure 3. 8 Vacuum resin infusion and curing process for hybrid glass-carbon fibre/epoxy specimens.....	36
Figure 3. 9 Tab manufacturing process	37
Figure 3. 10 Composite specimens prepared for tensile tests.....	37
Figure 3. 11 Tools and machine applicable for short beam shear testing.....	39
Figure 3. 12 Dynamic Mechanical Analyser (DMA)	39
Figure 3. 13 Lloyd LR 30KN longitudinal tensile testing machine and assembled oven	40
Figure 3. 14 Matrix digestion process and tools.....	41
Figure 3. 15 Geometries for tensile tests	45
Figure 4.1 ILSS of unidirectional glass, carbon and hybrid composite laminates	47
Figure 4. 2 SEM image of unidirectional delamination failure modes on FRP composite specimens.....	49
Figure 4.3 Comparison of experimental and theoretical results for inter-laminar shear strength of glass/epoxy specimens.....	52
Figure 4.4 Comparison of experimental and theoretical results for inter-laminar shear strength for carbon/epoxy specimens	53
Figure 4.5 Comparison of experimental and theoretical results for inter-laminar shear strength for hybrid glass-carbon/epoxy specimens.....	54
Figure 4.6 Comparison of experimental and theoretical results for inter-laminar shear strength for hybrid carbon-glass/epoxy specimens.....	55

Figure 4.7 Storage modulus vs. temperature for glass/epoxy, carbon/epoxy and hybrid specimens.....	57
Figure 4.8 Loss modulus vs. temperature for glass/epoxy, carbon/epoxy and hybrid specimens.....	58
Figure 4.9 Loss factor vs. temperature for glass/epoxy, carbon/epoxy and hybrid specimens.....	59
Figure 4.10 Cole-Cole graphs of GFRP, CFRP and hybrid composite specimens	60
Figure 4.11 Stress vs strain curves of glass/epoxy specimens at various temperatures.	62
Figure 4.12 Stress vs. strain curves of carbon/epoxy specimens at various temperatures	64
Figure 4.13. Stress vs. strain curves of hybrid glass/carbon specimens at various temperatures.....	65
Figure 4.14 Average experimental tensile strength vs. temperature.....	66
Figure 4.15 Failure specimens collected after testing of the three composite specimens	67
Figure 4.16 SEM image of composite specimens after failure (a) carbon/epoxy (b) glass/epoxy (c) carbon fibre in hybrid/epoxy (d) glass fibre in hybrid/epoxy.....	68
Figure 4.17 Tensile tests using ANSYS software (a) input parameters (b) fixing the specimen and applying force (c) thermal loading (d) force and thermal loading.....	69
Figure 4.18 Stress distribution in the top ply of carbon/epoxy specimens at temperatures 25°C, 40°C and 55°C.....	70
Figure 4. 19 Stress distribution at the top ply of glass/epoxy specimens at temperatures 25°C, 40°C and 55°C.....	70
Figure 4. 20 Stress distribution at the top ply of hybrid glass-carbon specimens at temperatures 25°C, 40°C and 55°C.	71
Figure 4.21 Simulation on tensile stress vs. variable testing temperature	71
Figure 4.22 Glass/epoxy failure index values at temperatures (a) 25°C, (b) 40°C, (c) 55°C (d) location of failure	72
Figure 4.23 Carbon/epoxy failure index values at temperatures (a) 25°C, (b) 40°C, (c) 55°C, d) location of failure.....	73
Figure 4.24 Hybrid glass-carbon/epoxy failure index values at temperatures (a) 25 ⁰ C, (b) 40 ⁰ C, (c) 55 ⁰ C d) location of failure	73
Figure 4.25 Average experimental and simulation failure stresses vs. temperature.....	74

Figure 4.26 Comparisons of experimental and theoretical results for tensile strengths for glass/epoxy at temperature 25°C, 40°C and 55°C.	78
Figure 4.27 Comparisons of experimental and theoretical results for tensile strength for carbon/epoxy at temperatures 25°C, 40°C and 55°C.....	79
Figure 4.28 Comparisons of experimental and theoretical results for tensile strength for hybrid glass-carbon/epoxy at temperatures 25°C, 40°C and 55°C.....	80
Figure 5. 1 An actuator disc model of a wind turbine; U is air velocity; 1, 2, 3, and 4 indicate locations (McGowan, 2009).....	82
Figure 5. 2 Operating parameters for a Betz wind turbine model	86
Figure 5.3 Airfoil nomenclature (McGowan, 2009).....	89
Figure 5. 4 Forces and moments on an airfoil section (McGowan, 2009)	90
Figure 5.5 Different NACA airfoils.....	92
Figure 5.6 Non-dimensional parameters vs. angle of attack for NACA 4415 airfoil at different Reynolds numbers.....	93
Figure 5.7 Non-dimensional parameters vs. angle of attack for NACA 23012 airfoil at different Reynolds numbers.....	94
Figure 5.8 Non-dimensional parameters vs. angle of attack for NACA 23012 airfoil at different Reynolds numbers.....	95
Figure 5.9 Lift coefficient vs (AOA) at Reynolds number ($6e^6$)	96
Figure 5.10 Drag coefficient model vs. (AOA) at Reynolds number ($6e^6$)	97
Figure 5.11 Ratio of lift to drag coefficient vs. (AOA) at Reynolds number ($6e^6$)	97
Figure 5.12 Non-dimensional parameter (L/D) ratio vs. (AOA) at Reynolds number ($6e^6$)	98
Figure 5.13 Lift coefficient vs. drag coefficient at Reynolds number ($6e^6$)	99
Figure 5.14 Pressure coefficient vs angle of attack at Reynolds number ($6e^6$) for NACA 4415 airfoil.....	100
Figure 5.15 Pressure coefficient vs angle of attack at Reynolds number ($6e^6$) for NACA 23012 airfoil.....	100
Figure 5.16 Pressure coefficient vs. angle of attack at Reynolds number ($6e^6$) for NACA 23015 airfoil.....	101
Figure 5.17 Boundary of the airfoils.....	103
Figure 5.18 Mesh around NACA 4415 airfoil and the data.....	104

Figure 5.19 Mesh around NACA 23012 airfoils geometry and data.....	104
Figure 5.20 Mesh around NACA 23015 airfoils geometry and data.....	105
Figure 5.21 Lift coefficient vs the number iterations for NACA 4415 airfoil.....	106
Figure 5.22 Lift coefficient vs the number of iterations for NACA 23012 airfoil	106
Figure 5.23 Lift coefficient values vs the number of iterations for NACA 23015 airfoils	107
Figure 5.24 Drag coefficient vs the number of iterations for NACA 4415 airfoil	108
Figure 5.25 Drag coefficient vs the number of iterations for NACA 23012 airfoil	108
Figure 5.26 Drag coefficient vs the number of iterations for NACA 23015 airfoils....	109
Figure 5.27 Contours of the velocity of the airflow around NACA 4415 airfoil	110
Figure 5.28 Contours of the velocity of the airflow around NACA 23012 airfoil	110
Figure 5.29 Contours of the velocity of the airflow around NACA 23015 airfoil	111
Figure 5.30 Contours of the velocity of the airflow around NACA 4415 airfoil	112
Figure 5.31 Contours of the velocity of the airflow around NACA 23012 airfoil	112
Figure 5.32 Contours of the velocity of the airflow around NACA 23015 airfoil	112
Figure 5.33 Contours of static pressure (Pascal) on NACA 4415 airfoil	113
Figure 5.34 Contours of static pressure (Pascal) on NACA 23012 airfoil	114
Figure 5.35 Contours of static pressure (Pascal) on NACA 23015 airfoil	114
Figure 5.36 Contours of static pressure (Pascal) on NACA 4415 airfoil	115
Figure 5.37 Contours of static pressure (Pascal) on NACA 23012 airfoil	115
Figure 5. 38 Contours of static pressure (Pascal) on NACA 23015 airfoil	116
Figure 5.39 Contours of turbulence kinetic energy on NACA 4415 airfoil at a wind velocity of 9.56m/s.	116
Figure 5.40 Contours of turbulence kinetic energy on NACA 23012 airfoil at a wind velocity of 9.56m/s	117
Figure 5.41 Contours of turbulent kinetic energy on NACA 23015 at wind velocity 9.56m/s.....	117
Figure 5.42 Contours of turbulence kinetic energy on NACA 4415 airfoil at a wind velocity of 25m/s.	118
Figure 5.43 Contours of turbulence kinetic energy on NACA 23012 airfoil at a wind velocity of 25m/s	119
Figure 5.44 Contours of turbulence kinetic energy on NACA 23015 airfoil at a wind velocity of 25m/s	119
Figure 5.45 Geometry of rotor (McGowan, 2009)	121

Figure 5.46 Schematic of blade element model; C airfoil chord length; dr radial lengths of elements; r radius of elements; R rotor radius (Grant Ingram, 2011)	122
Figure 5.47 Blade geometry for analysis of forces on wind turbine blade (McGowan, 2009)	123
Figure 5.48 Airfoils used for baseline blade model	127
Figure 5.49 Chord length distribution along the length of wind turbine blade	128
Figure 5.50 Flap-wise shear force distribution at various wind speeds	128
Figure 5.51 Flap-wise moment distribution at various wind speeds	129
Figure 6.1 Structural components of horizontal axis wind turbine blade	134
Figure 6.2 Thickness distribution on shell and spar-caps along the length of the blades	138
Figure 6.3 Ratio of weight to thickness on shell and spar-caps along the length of the blades	139
Figure 6.4 Ratio of weight to thickness of shell, spar-caps and shear web along the length of the blades	139
Figure 6.5 Mass distribution vs ratio of total length	140
Figure 6.6 Total mass of the blade vs. blade types	140
Figure 6.7 NACA aerofoil twisting angles	141
Figure 6.8 Wind turbine blade model using SolidWork software	142
Figure 6.9 Sectional elements of the blades	142
Figure 6.10 Wind turbine blade meshed surface using ANSYS software	143
Figure 6.11 FEM blade thickness distributions	144
Figure 6.12 Composite blade profile in ANSYS ACP (pre)	144
Figure 6.13 FE model of the blades after placing the composite material on each element	145
Figure 6.14 FEM model simulation on ANSYS static structure	146
Figure 6. 15 Total deformation of blades under various flap-wise loadings and thermal conditions	147
Figure 6.16 Total deformations of blades	148
Figure 6.17 Tip deflection of blades under various flap-wise wind loads and thermal conditions	149
Figure 6.18 Tip deflections of blades	150
Figure 6. 19 Failure index vs. flap-wise and thermal loading for carbon fibre blade ..	152
Figure 6. 20 Failure index vs. flap-wise and thermal loading for glass fibre blade	152

Figure 6. 21 Failure index vs. flap-wise and thermal loading on carbon-glass fibre blade	153
Figure 6. 22 Failure index vs. flap-wise and thermal loading on a glass-carbon fibre blade	153
Figure 6.23 Failure index vs. flap-wise and thermal loading for carbon/epoxy blade .	154
Figure 6.24 Failure index vs. flap-wise and thermal loading on glass fibre blade	154
Figure 6.25 Failure index vs. flap-wise and thermal loading for carbon-glass blade...	155
Figure 6.26 Failure index vs. flap-wise and thermal loading on glass-carbon blade ...	155
Figure 6. 27 Failure index vs. flap-wise and thermal loading for carbon/epoxy blade	156
Figure 6.28 Failure index vs. flap-wise and thermal loading on glass/epoxy blade.....	157
Figure 6.29 Failure index vs. flap-wise and thermal loading for carbon-glass blade...	157
Figure 6.30 Failure index vs. flap-wise and thermal loading on glass- carbon fibre blade	157
Figure 6. 31 Failure on FEM structural models of composite blades under variable loading	159
Figure 7.1 Airfoil distribution of three NACA airfoils along the length of the blade ..	166
Figure 7.2 Flow chart to model the optimized shape of wind turbine blades.....	169

List of Tables

Table 2. 1 Global installed wind power capacity (MW)-Regional distribution data.....	7
Table 3.1 Physical and mechanical properties of unidirectional glass fibre, carbon fibre and epoxy resin [70].	27
Table 3.2 Sample code, layer configuration and thickness of laminates	28
Table 3.3 Sample code, layer configuration and thickness of composite laminates	31
Table 4.1 The ILSS of unidirectional glass/epoxy, carbon/epoxy and hybrid/epoxy at temperatures 25°C, 40°C and 55°C measured by Short Seam Shear (SBS) tests	48
Table 4. 2 Distribution parameters for ILSS [MPa] at temperatures 25°C, 40°C and 55°C.	50
Table 4.3 Chi-square test results	51
Table 4.4 R-square values (Experimental data vs fitted responses)	51
Table 4.5 Storage modulus, loss modulus and T_g of GFRP, CFRP, hybrid GFRP-CFRP and CFRP-GFRP specimens	59
Table 4. 6 Average values of the experimental and simulation results at temperatures 25°C, 40°C and 55°C.....	74
Table 4.7 Distribution parameters for tensile strength (MPa) values at temperatures 25°C, 40°C and 55°C.....	75
Table 4.8 Chi-square test results	76
Table 4.9 R-square values (Exp. Data vs fitted responses)	76
Table 5.1 Aerodynamic behaviour of NACA airfoils used as wind turbine blades	101
Table 6.1 Mechanical properties of GFRP and CFRP composites.....	132
Table 6. 2 Properties of PVC foam.....	133
Table 6.3 Rectangular shear web distribution on the airfoil and circular cross sections	134
Table 6.4 Elements of the blade and its mass using carbon/epoxy.....	135
Table 6.5 Elements of the blade and its mass using glass/epoxy	136
Table 6.6 Elements of the blade and its mass using hybrid glass-carbon/epoxy.....	137
Table 6.7 Total deformation of blades under different wind speeds and thermal conditions	148
Table 6.8 Tip defections of blades under different wind loads and thermal conditions	151

Chapter 1

Introduction

1.1 Wind Energy and Blade Materials

Energy produced by using different sources such as wood and coal results in increased pollution of the environment (generation of waste). This phenomenon turned the focus towards sustainable energy sources. Wind power is a source of non-polluting renewable energy which delivers power with significantly less effect on the environment. These sources are normally more green/clean compared to other energy sources. The advantage of wind energy is that the wind is free, takes less space and wind farms can be installed in remote locations such as offshore, mountains and deserts [1]. Today, wind turbines have generated megawatts of power using large and increasing rotor diameters in onshore and offshore wind farms [2]. Historically, wind turbine blades were made of wood, but due to high moisture absorption and production costs, they were replaced by steel and aluminium. Steel is stronger and stiffer but more difficult to achieve optimized twist blade shape. Aluminium is better for modelling wind turbine blade structures but it has low fatigue strength and stiffness.

The prevailing materials for the construction of modern wind turbine blades are Fibre Reinforced Polymer (FRP), a composite material. The important characteristics of composites are that they have high stiffness, are light in weight, have good corrosion resistance, high fatigue strength and intricate shapes can be manufactured with ease. Unidirectional glass fibre reinforced polymer, carbon fibre reinforced polymer and the hybrid of these two materials have been the choice of most blade manufacturing industries [3, 4, 5].

Composite wind turbine blades were installed in several tropical wind farms in the last few years. The aim of this study is to choose the most suitable material for the manufacture of tropical wind turbine blades and to find out the influence of temperature variation on the static and dynamic mechanical behaviour of composite materials. In the current experimental and numerical study, characterizations and comparisons are used to determine the most suitable materials for modelling wind turbine blades which can carry flap-wise and thermal loadings.

1.2 Problem Definition

Modern wind blade manufacturing industries use glass fibre with polymeric resin as a binder to build different sections of horizontal axis wind turbine blades. Currently, carbon fibre with polymeric resin as a binder has been the choice of large wind turbine blade manufacturing industries due to their high strength and stiffness as well as low weight. Structures designed using FRP composite materials experience various failure modes such as matrix cracking, delamination, fibre breakage and interfacial de-bonding.

Sand dust adversely affects the rotating blades by influencing their power curve causing a loss of power. Sand particles on the surface of wind turbine blades increase surface roughness and changes the boundary layers which have a high impact on decreasing the lift forces and increasing drag forces. Boundary layers may be removed during wind turbine blade rotation eroding the blades, resulting in a shorter life expectancy. Birds crashing into the blades erode the blade surface, lowering the power output. Tropical wind farms have major environmental problems like high elevated temperature conditions especially in Northern and Eastern African countries where the daily temperatures can be fairly high. The glass Transition Temperature (T_g) of a polymeric matrix is low and the stiffness of the composite wind turbine blade decreases as the working temperature rises. The recommended temperature by IEC 61400-1 [6] for modelling the blades is between -20°C to 50°C . The properties of the current composite materials available for construction of blade structures have to be tested in order to identify the static and dynamic mechanical properties of materials under elevated temperatures. The idea is to select suitable materials for turbine blades to be used in tropical wind farms.

1.3 Motivation

Using wind turbines is one of the main methods of extracting energy from wind. The selection of proper airfoil, shape, distribution of non-dimensional parameters and light materials is important to maximize the power output. Currently, different airfoil shapes have been developed which have high lift and low drag coefficients and also better distribution of the chord length. Failure of wind turbine blades can occur before completing the design life due to adverse loading conditions, particularly due to rising temperatures which are problematic for blades in the tropical wind farms. The structural components of wind turbine blades are manufactured from FRP composite materials.

Particularly as the daily temperature in Africa is rising, further investigation is needed to ascertain the mechanical behaviour of current materials in order to design the blade structure. The medium and large wind turbine blades are imported to Africa from different countries without taking into account the environmental conditions of the wind farm areas. It will be a large concern and objective of this study to maximize the power coefficient and identify the composite materials which can last longer under flap-wise and thermal loadings in the tropical wind farms.

1.4 Aims and Objectives

The main aims of this study are to find the effect of temperature on mechanical behaviour of FRP composite materials applicable to modern wind turbine blades and modelling wind turbine blade structures using suitable composite materials for tropical wind farms.

Objectives:

1. Find the effect of temperature on FRP composite materials applicable for modelling the structures of the wind turbine blades using experimental, statistical and numerical analysis.
2. Develop NACA airfoil families, shape of the blade and determine the mechanical properties of blades using QBlade, SolidWork, Matlab and ANSYS fluent software to model horizontal axis wind turbine blades.
3. Determine the critical loadings on blade elements due to variable wind speeds using Blade Element Momentum Theory.
4. Characterize the FRP composite materials for each section of the blade using ANSYS software.
5. Evaluate simulation results of composite structures of wind turbine blades in particular, deformation, tip deflection and failure of wind turbine blade structures considering thermal and flap-wise loading conditions.
6. Identify the suitable materials in view of cost, strength and delay of failure of the blade structures under thermal and flap-wise loadings and model wind turbine blades suitable for tropical wind farms.

1.5 Methods and Materials

For modelling horizontal axis wind turbine blades suitable for tropical areas, unidirectional glass fibre, carbon fibre with Ampreg 21 polymer matrix were used for specimen preparation to test the behaviour of composite materials under increasing

temperatures. At the beginning, composite specimens were prepared by employing hand-layup techniques using the two unidirectional fibres and hybrid of these two materials to measure the static and mechanical behaviour under increasing temperature. Short Beam Shear (SBS) and Dynamic Mechanical Analysis (DMA) tests were conducted. The relation between rising temperatures and different composite specimens is determined. In addition, composite specimens are prepared by employing a vacuum infusion manufacturing process for further tensile testing using a LR30KN machine. To validate the experimental result, a 54m blade of Horizontal Axis Wind Turbine (HAWT) is developed. The total length of the wind turbine blade had circular cross-sections including three NACA airfoils families. The lift and drag coefficient of NACA airfoils were characterized using QBlade and ANSYS fluent software to select proper positions of the airfoils along the length of the wind turbine blade. Flap-wise loading on each section was calculated allowing for different wind speeds using the Blade Element Momentum Theory. Rectangular hollow shear webs were used in the inside parts along the length of the blade which was divided into three sections, the trailing edge, the leading edge and spar caps. Material modelling occurred on each blade section using ANSYS ACP (pre).

The behaviour of composite material under increasing temperature at specimen and structural levels was investigated using experimental and numerical methods. Mainly, simulation occurred using unidirectional GFRP, CFRP, carbon-glass/epoxy and glass-carbon/epoxy composite wind turbine blade structures under increasing thermal and flap-wise loading. Then, tip deflection, total deformation and failure of each section of the blade was analysed using Tsai-Wu failure criterion and proper composite material identified in light of cost and strength under variable thermal conditions. Finally, a composite structural wind turbine blade was developed using the candidate composite materials

1.6 Technical and Scientific Contributions

In most African countries, particularly in South Africa, the energy demand has rapidly increased. This growth rate, when viewed together with a large population base and high investment opportunities, makes the countries with fast growing power needs, suitable markets for all sources of electrical energy including the renewable ones. South Africa has imported the blades and given their installation and commission to German, French and Chinese companies. Present work can provide researchers with the knowledge an

knowhow to design and optimize the shape of large blades and model the wind turbine blades using FRP composite materials for various wind speeds.

1.7 Structure of the Thesis

The thesis begins with a literature review followed by seven chapters. Some of these chapters are reproductions of papers. A summary of all key findings is given in chapter 8. The chapters contained in the thesis are outlined below:

Chapter 2 presents a review of the literature relating to the main study areas.

Chapter 3 discusses the preparation of the specimens of the glass fibre, carbon fibre and hybrid of these two composite materials as well as different production techniques. It gives a brief outline of appropriate test methods implemented on this study.

Chapter 4 evaluates the influence of increasing temperatures on the static and dynamic mechanical properties of GFRP, CFRP and hybrid composite specimens using tests and numerical analysis.

Chapter 5 demonstrates the aerodynamic principles of converting energy from the wind and different parameters to choose airfoils to model the wind turbine blade. It gives a brief outline of linear momentum theory of Betz's, Glauert model and Blade Element Momentum theory applied to model the turbine blades. These techniques are to be used in order to maximize the power of airfoils and to determine the load distribution on blade sections.

Chapter 6 demonstrates the newly developed wind turbine blade profiles and structural modelling of wind turbine blade using GFRP, CFRP and hybrid composite materials. It furthermore demonstrates the validation of experimental and simulation results under thermal loading.

Chapter 7 critically discusses experimental and simulation results.

Chapter 8 discusses the key results of the previous chapters and makes recommendations for future research in this field of study.

Chapter 2

Literature Review

2.1 Wind Power Development and Effect of Temperature on FRP Materials

Because the earth revolves, the sun heats the earth's surface unevenly, this creates wind. Wind energy generates electricity, one of the renewable energy sources. It needs wind turbine blades to convert the kinetic energy from wind into mechanical power and generators convert the mechanical power into electricity. For many years coal, oil and natural gas were the main energy sources but they resulted in environmental pollutions. Hence, solar and wind energies are now the chosen energy sources in many countries.

Before Europeans started using wind as an energy source, Chinese farmers have been using wind wheels for centuries to drain rice fields Egyptians used windmills 3000 years ago to pump water. Professor James Blyth, a Scot, developed the earliest wind turbine using batteries to generate electricity in 1887 [7]. Then in 1888 the American, Brush developed a wind machine and his colleagues tested and used it on the Atlantic coast [8]. From then development of wind power technology improved. Between the 1920s and 1930s, small wind machines producing less than one kilowatt were developed by American researchers and then in 1941, the prototype of a horizontal axis wind turbine blade was built.

Currently, many countries are opening wind farms onshore and offshore with wind turbine blades which have a high generating capacity in order to meet the energy demand of these countries. The top five countries namely China, America, Germany, Spain and India have contributed a wind energy capacity worldwide. In 2003, the international wind energy market showed a total power of 8.3 GW installed globally [9]. In 2009, the wind power generating capacity increased and reached 158 GW, a difference of 31% more than 2008. The increase continued and data on the first half 2010 indicates that the capacity reached 175 GW, two years later 292 GW and 425 GW by 2015 [10]. Table 2.1 shows the overview of wind power installed in the years 2015 and 2016 globally, taken from The Global Wind Energy Council (GWEC).

Wind Power Development and Effect of Temperature on FRP Materials

Table 2. 1 Global installed wind power capacity (MW)-Regional distribution data [11].

AFRICA and MIDDLE EAST	Country name	Cumulative (End of 2015)	New installed (End of 2016)	Cumulative (End of 2016)
	South Africa	1,053	418	1,471
	Egypt	810	-	810
	Morocco	787	-	787
	Ethiopia	324	-	324
	Tunisia	245	-	245
	Jordan	119	-	119
	Other ¹	150	-	150
	Total	3,488	418	3,906
ASIA	PR China	145,362	23,328	168,690
	India	25,088	3,612	28,700
	Japan	3,038	196	3,234
	South Korea	835	201	1,036
	Taiwan	647	35	682
	Pakistan	308	282	590
	Thailand	223	-	223
	Philippines	216	-	216
	Other ²	253	25	278
	Total	175,970	27,679	203,649
EUROPE	Germany	44,941	5,443	50,384
	Spain	23,025	49	23,074
	UK	13,809	736	14,545
	France	10,505	1,561	12,066
	Italy	8,975	282	9,257
	Sweden	6,029	493	6,522
	Turkey	4,694	1,387	6,081
	Poland	5,100	682	5,782
	Portugal	5,050	268	5,318
	Denmark	5,064	220	5,284
	Netherlands	3,443	887	4,330
	Romania	2,976	52	3,028
	Ireland	2,446	384	2,830
	Austria	2,404	228	2,632
	Belgium	2,218	177	2,395
	Rest of Europe ³	7,220	1,077	8,297
	Total Europe	147,899	13,926	161,825
	Of which EU-28⁴	141,721	12,491	153,729
LATIN AMERICA AND CARIBBEAN	Brazil	8,726	2,014	10,740
	Chile	911	513	1,424
	Uruguay	845	365	1,210
	Argentina	279	-	279
	Costa Rica	278	20	298
	Panama	270	-	270
	Peru	148	93	241
	Honduras	176	-	176
	Dominican Republic	86	50	135
	Caribbean ⁵	164	-	164
	Others ⁶	335	24	359
	Total	12,218	3,079	15,297

Wind Power Development and Effect of Temperature on FRP Materials

NORTH AMERICA	Country name	Cumulative (End of 2015)	New installed (End of 2016)	Cumulative (End of 2016)
	USA	73,991	8,203	82,194
	Canada	11,219	702	11,900
	Mexico	3,073	454	3,527
	Total	88,283	9,359	97,642
PACIFIC REGION	Australia	4,187	140	4,327
	New Zealand	623	-	623
	Pacific Islands	13	-	13
	Total	4,823	140	4,963
	World total	432,681	54,601	487,282

Note: 1 Algeria, Cape Verde, Iran, Israel, Kenya, Libya, Nigeria. 2 Bangladesh, Mongolia, Sri Lanka, Vietnam. 3 Bulgaria, Cyprus, Czech Republic, Estonia, Finland, Faroe Islands, FYROM, Hungary, Iceland, Latvia, Liechtenstein, Lithuania, Luxembourg, Malta, Norway, Romania, Russia, Switzerland, Slovenia, Ukraine. 4 Austria, Belgium, Bulgaria, Cyprus, Croatia, Czech Republic, Denmark, Estonia, Finland, France, Germany, Greece, Hungary, Ireland, Italy, Latvia, Lithuania, Luxembourg, Malta, Netherlands, Poland, Portugal, Slovakia, Spain, Sweden, Uk. 5 Caribbean: Aruba, Bonaire, Curacao, Cuba, Dominica, Guadalupe, Jamaica, Martinica, Granada, St. Kitts and Nevis. 6 Bolivia, Colombia, Ecuador, Guatemala, Nicaragua, Venezuela.

According to the Global Wind Energy Council (GWEC) data at the end of 2016, China is leading USA on power production. China, USA, Germany, India and Spain made up 72.5 % of the global wind power installations in 2016. Figure 2.1 represents the amount of MW power capacity by these five countries in 2016.

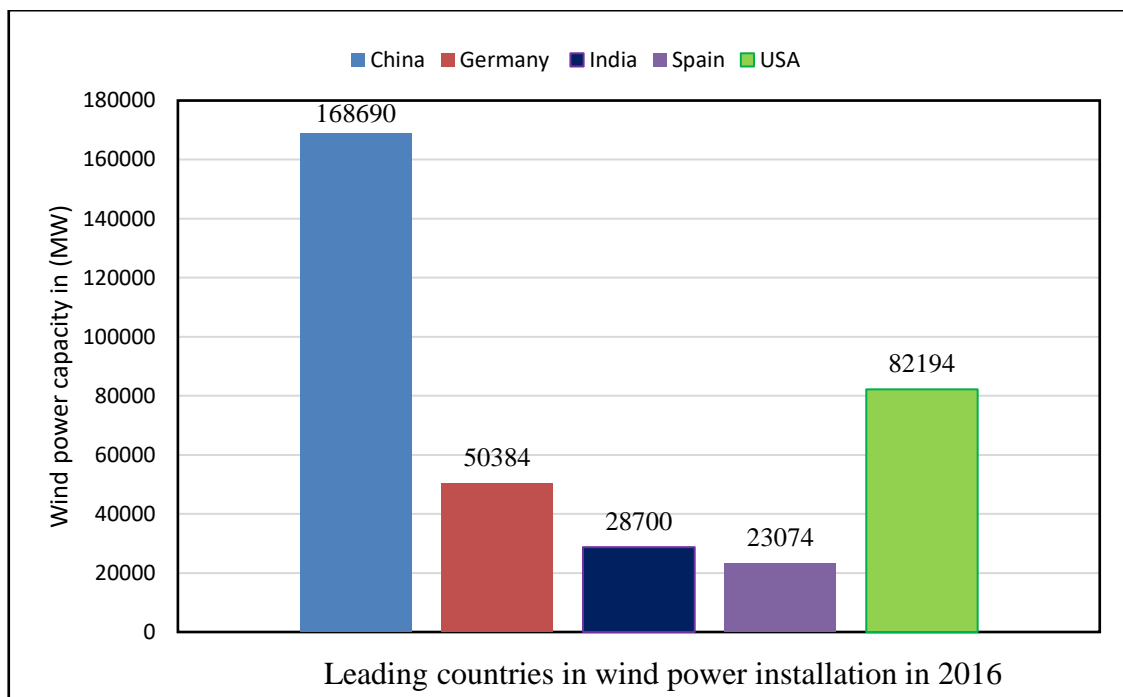


Figure 2. 1 Wind power capacity of the top five countries in 2016

In most African countries, installation of wind power is minimal. By the end of 2016 South Africa was the leader of wind energy in Africa producing 1471MW. Many

Wind Power Development and Effect of Temperature on FRP Materials

countries which have regions eminently suitable for generating wind energy require their leaders to commit to it. In particular, Northern African countries such as Algeria, Egypt, Morocco, Tunisia and Mauritania have the best wind resources in the coastal regions of the continent with an annual average wind speed of between 9.56 m/s and 11m/s at a height of 40m [12, 13]. The wind power capacities of the African and Middle Eastern countries are shown in Figure 2.2.

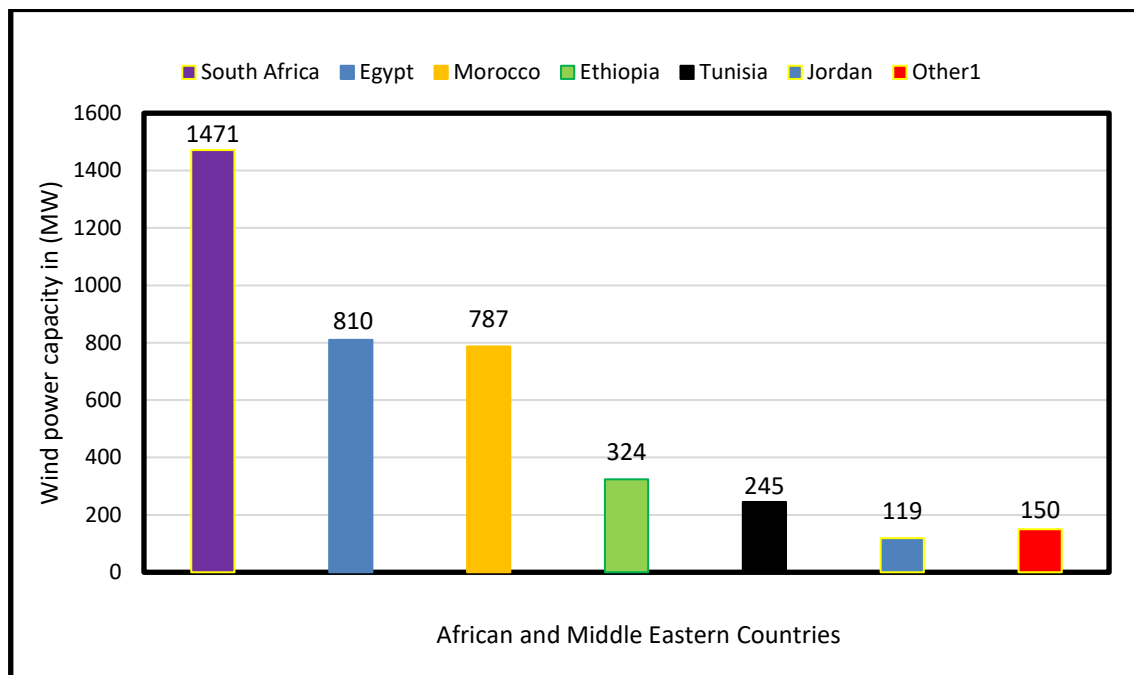


Figure 2. 2 Wind power capacity of African and Middle Eastern countries

The main components of a wind power generating plant are rotor, nacelle, tower and foundation. Blades are connected to the hub, which in turn, is attached to the main shaft. The amount of energy extracted from the wind depends on the size of the wind turbine blades. Most wind turbine manufacturers produce large wind turbine blades in increasing numbers. Formerly wind blades were manufactured from wood but they are now produced from composite materials.

2.2 Composite Materials for Construction of Wind Turbine Blades

Composite materials are produced by combining two or more materials such as polymers and fibres each of which have different mechanical properties. Fibre reinforced polymer composites consist of fibre and resin mixed together to produce a stronger material. Fibre Reinforced Polymeric (FRP) materials are used extensively in industries such as aerospace, transportation, construction, wind turbines, and marine products because of their properties which have a high load bearing capacity, high specific rigidity, high

Composite Materials for Construction of Wind Turbine Blades

specific strength, corrosion resistance and improved fatigue life [14, 15, 16]. The components used in aerospace industries and wind turbine blades are built using different fibres and thermoset or thermoplastic resins applicable to different working environments. The mechanical and physical properties of FRP composite materials are determined by fibre and resin type, fibre volume ratio, fibre orientations, ply stacking sequences and the number of layers. Nowadays, many wind turbine manufacturers use composite materials to build turbine blades and nacelles [17]. Particularly, unidirectional fibres ensure longitudinal rigidity and strength of the blade while the fracture toughness and delamination are determined by the matrix. The rigidity of the fibres and the fibre volume ratio determine the rigidity of the composites.

It is known that carbon fibres are the popular choice of industries requiring high rigidity and strength as they are light-weight in preference to the less expensive but heavier glass fibres. The use of carbon fibres allows thinner blades and better mechanical and physical properties [18]. Vestas and Gamesa wind turbine makers have used carbon composite on spar cap sections of wind turbine blades to reduce bending deformation of the blades. For large wind turbine blades, manufacturers prefer carbon fibre and hybrid composite materials to maximize the strength and to lower the weight of the blades [19].

Studies on the static structural analysis of composite wind turbine blades made of E-glass/epoxy with balsa cores in the shear web section computed the tip deflection, stress and strain of the blades with different ply arrangements [20]. Blade Element Momentum (BEM) modelling techniques were applied for the analysis of aerodynamic loads along the length of the composite blades. The results were found to be advantageous compared to the traditional blade materials. The generation of wind energy depends on the shape of the rotating blades [21]. The shape of the wind blades made of composites can be produced without complicated manufacturing processes.

The processes employed for wind turbine manufacturing using Fibre Reinforced Polymeric (FRP) composites were easier than those used for traditional materials such as steel and aluminium. Despite their advantages Fibre Reinforced Polymer (FRP) composites are susceptible to moisture and temperature when operating in adverse environmental conditions. This is due to the fact that water is absorbed from the environment and acts as plasticizers, softening the material. This can reduce matrix dominated properties such as transverse strength, fracture toughness and impact resistance [22, 23]. Consequently, the durability together with the safety of the structure

are affected due to the decreasing glass transition temperature (T_g) values of the polymeric matrix [24]. This, in turn, impacts on the fiber/matrix interfacial degradation, formation of residual stresses, fracture toughness, crack propagation, brittleness and ductility due to higher temperatures [25].

In the wind farms operating in Africa, wind turbine blades are affected by high temperatures during the service life of the blade [26]. Currently wind turbine blade manufacturers use E-glass and carbon fibres with thermoset resins for the construction of turbine blades. Meanwhile, there is a need to identify a FRP composite material which has superior static and dynamic mechanical properties under high temperatures. Previously research was conducted on the impact of temperature on the static and dynamic mechanical properties of fibre reinforced polymers. This work was directed towards determining the inter-laminar strength, tensile strength and delamination as well as the dynamic mechanical properties such as rigidity loss and glass transition temperature for various composite specimens. This experimental work will be discussed in detail in section 2.2.1.

2.2.1 Behavior of FRP Composite Material under High Temperatures

Fibre reinforced polymer composites are the preferred materials by most manufacturers of wind turbines, especially blade and nacelle sections. However, composites are affected by harsh environmental conditions when exposed to them for long periods [27]. Research findings indicate that cyclic heating can lower the static and dynamic mechanical behaviours of blades made of FRP composite materials. The results of studies on the behaviour of FRP composites subject to high and extreme temperatures are discussed next.

2.2.1.1 Strength Properties of FRP Materials under High Temperatures

The structural components of wind turbine blades have been designed using unidirectional GFRP and CFRP composite materials. The composite blades subject to high temperatures may lower the static and dynamic mechanical properties of the composite material due to the change of T_g of the polymer matrix. The influence of temperature on fibre/matrix interface may have a direct effect on the strength of the composite. Degradation due to elevated temperatures may occur along the fibre/matrix interface and can lead to residual stresses. This may lower the capacity of the polymer

Behavior of FRP Composite Material under High Temperatures

matrix to transfer the loads to fibre through the interface causing loss of strength of the composite material [28].

Springer [29] developed a model on the change of the mechanical behaviours involving tensile, compressive and shear strengths of FRP composites exposed to high temperatures. The model determines the decrease in the strength values as a function of the exposure time. Stress-strain responses of unidirectional GFRP composite materials tested at different temperatures are discussed [30]. Thomason and Yang [31, 32] investigated the interfacial shear strength of glass fibre reinforced with polypropylene thermoplastic resin in the temperature range of -40°C to 100°C . Moreover, the authors determined the interfacial shear strength of glass fibre/epoxy at a temperature range of 20°C to 150°C . A micro bond test was used to determine the relation between temperature and the interfacial shear strength of GFRP composite materials [31, 32]. Experimental results indicated that the interfacial shear strengths of GFRP composites have inverse relations with increasing temperature [31, 32].

Researchers examined the influence of temperature on the glass fibre/epoxy composite with the test temperatures changing from ambient temperature to lower temperatures. Torabizadeh [33] investigated the rigidity, strength and the failure strain of unidirectional GFRP composites with the temperature changing from room temperature to lower temperatures. In order to characterize the properties of unidirectional laminates, tensile, compressive and shear tests were performed using a universal test machine at temperatures 25°C , -20°C and -60°C . The experimental result indicated that low temperatures had a significant impact on the failure modes of fibre reinforced polymer composites. Furthermore, it was found that the strength and modulus values increase with decreasing temperature under tensile, compressive, and shear loads in longitudinal and transverse directions. On the other hand, low temperatures may lead to the formation of weak bonds between the fibres and the matrix causing crack propagation and catastrophic failure.

The [performance of FRP composites at high temperatures is of interest and is important in the design of engineering structures. Yunfu Ou and Deju Zhu [34] studied tensile properties of composite samples at different strain rates and temperatures to determine the mechanical behaviour of GFRP composites. Experimental results indicated that the tensile strength properties decrease as the test temperature increases.

Behavior of FRP Composite Material under High Temperatures

Similar investigations have been performed on CFRP and hybrid fibre/epoxy composites with increasing temperatures. Shenghu Cao et al [35] studied tensile properties of CFRP and hybrid CFRP-GFRP specimens at different test temperatures. The experimental results indicate that the tensile strength properties of CFRP specimens decrease significantly with the increase of test temperatures up to T_g of the polymer matrix and after that, the ultimate tensile strengths of the FRP specimens remain stable.

In addition, studies were conducted on the influences of higher temperatures on the failure modes of FRP composites. Chen et al [36] determined the failure behaviour and thermal stresses of graphite/epoxy specimens under combined mechanical and thermal loadings. The Finite Element Method (FEM) was used to examine the response of the specimens. The inter-laminar shear strength behaviour of CFRP under increasing temperatures was determined by a number of researchers. Detassis et al [37] studied the influence of temperature on the interfacial shear strength of CFRP composite materials with low T_g by fragmentation tests using a single fibre model composite. Experimental data indicated that the interfacial shear strength of CFRP decreases as the temperature approaches the T_g value of the polymeric matrix.

The research findings by most researchers on the behaviour of GFRP and CFRP composites found that the static mechanical properties like tensile and inter-laminar shear strengths of the composite were reduced under elevated temperatures.

2.2.1.2 Stiffness Properties of FRP Material under High Temperatures

FRP materials are used in a large number of structural applications that require good mechanical properties. Thermal and mechanical responses of FRP composite materials depend on the behaviour of polymer resins under high temperatures. Mainly, elastic modulus and strength of the polymeric matrix drop and the viscosity rises as the temperature increases and exceeds the T_g of the polymeric matrix. In order to model the structures made of fibre-reinforced composites, the material behaviour under increasing temperatures has to be investigated. Yu Bai et al [38] suggested a model of the rigidity of a composite material which depends on the temperature and viscosity of the polymer resin under increasing temperature. The elastic modulus values of fibre-reinforced polymer composites were analysed at different temperatures using Dynamic Mechanical Analysis (DMA). To determine the effect of temperature on FRP composite materials, specimens were prepared based on ASTM standards and loaded cyclically within the

Stiffness Properties of FRP Material under High Temperatures

elastic region. Stress-strain rate and the temperature were slowly increased at a constant rate. The sensors attached to the specimens measured the temperature, load and strain. The strain ε , is represented by:

$$\varepsilon = \varepsilon_0 \sin(\omega.t) \quad (2.1)$$

where ε_0 denotes the strain amplitude, ω and t represents circular frequency and time.

Stress, σ , under variable loading is calculated by:

$$\sigma = \sigma_0 \sin(\omega.t + \delta) \quad (2.2)$$

where σ_0 denotes the stress amplitude and δ represents the phase angle between the stress and strain. Storage modulus (E'), loss modulus (E'') and damping factor ($\tan \delta$) of the specimens are denoted by:

$$E' = (\sigma_0 / \varepsilon_0) \cos \delta \quad (2.3)$$

$$E'' = (\sigma_0 / \varepsilon_0) \sin \delta \quad (2.4)$$

$$\tan \delta = E'' / E' \quad (2.5)$$

The authors performed DMA using experimental results on pultruded glass fibre reinforced polyester laminates. The T_G and decomposition temperatures of polymeric matrix were determined from the test results. Additionally, the E' represents the elastic modulus under bending of the glass fibre specimen. As the temperature increases, E' of the GFRP composite specimens dropped rapidly. The loss modulus of viscoelastic material increased in response to increasing temperature and it dropped rapidly when the temperature exceeded the T_G of the polymeric matrix.

Damping factor of the composite specimens, that is, the ratio of E''/E' under increasing temperature was determined and the result indicated that it was similar to the loss modulus of glass fibre. Additionally, the authors determined the change of polymer material to a viscoelastic material under increasing temperatures using DMA. Changes of the material states of the glass fibre reinforced polymer composite are shown in Figure 2.3. At lower temperatures, the experimental results indicated that the E' is linearly constant. When the testing temperature increases, elastic modulus of the glass fibre composite is represented by a leathery state. In this state the E-modulus is lower than the one in the glassy state. The authors defined other material states. As temperatures rise,

Stiffness Properties of FRP Material under High Temperatures

the material state called rubbery state is reached which has a similar E-modulus to the leathery state. When the test temperature reaches a higher value, the intra-molecular bonds in the resin matrix are broken and the material is decomposed. This material state is named the decomposed state. This material, therefore, has four different states namely glass, leathery, rubbery and decomposed all of which were manifested under increasing temperatures.

Three transitions occurred on glass fibre specimen under DMA tests with increasing temperatures i.e., glass to leathery transition, leathery-to-rubbery transition and rubbery-to-decomposed transition.

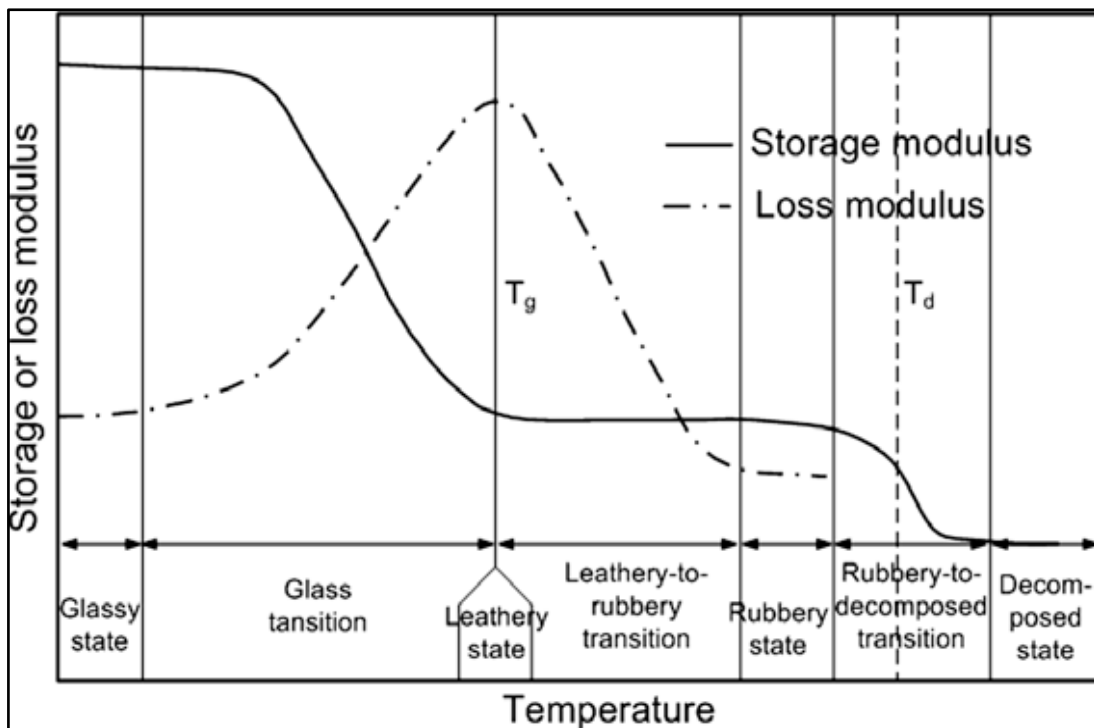


Figure 2.3 Definition of different material states and transitions under increasing temperatures

The mathematical modelling of the temperature-dependent elastic modulus is given next taking into account the change from the glassy to leathery state. Based on Arrhenius law, the authors presented the three transitions material states as:

$$\frac{d\alpha_g}{dt} = A_g \cdot \exp\left(\frac{-E_{Ag}}{RT}\right) (1 - \alpha_g)^n \quad (2.6)$$

where α_g represents the conversion degree of the glass transition, A_g denotes the pre-exponent factor, E_{Ag} represents the activation energy (a constant for specific process), R

Stiffness Properties of FRP Material under High Temperatures

is the universal gas constant ($8.314J / molK$), T denotes the testing temperature, and t is the time.

The constant heating rate which occurs on DMA testing machine can be represented as:

$$\frac{d\alpha_g}{dT} = \frac{A_g}{\beta} \exp\left(\frac{-E_{A,g}}{RT}\right) (1-\alpha_g)^n \quad (2.7)$$

Additionally, the heating rates for the leathery-to-rubbery transition and rubbery-to-decomposed transition can be computed as:

$$\frac{d\alpha_r}{dT} = \frac{A_r}{\beta} \exp\left(\frac{-E_{A,r}}{RT}\right) (1-\alpha_r)^n \quad (2.8)$$

$$\frac{d\alpha_d}{dT} = \frac{A_d}{\beta} \exp\left(\frac{-E_{A,d}}{RT}\right) (1-\alpha_d)^n \quad (2.9)$$

where α_r and α_d are the conversion degrees of leathery to rubbery and rubbery to decomposed transition. A_r and A_d represent the pre-exponential factors. $E_{A,r}$ and $E_{A,d}$ are the activation energies used for the leathery to rubbery transition and the rubbery to decomposed transition.

DMA testing results indicated that the properties of FRP materials depend on the temperatures to which they are exposed. Mechanical behaviour of FRP composites varies depending on the type of polymer matrix used in the composite. Various experimental models were developed to determine the mechanical properties of GFRP composite laminates at elevated temperatures using dynamic mechanical analysis [39, 40]. Di Landro and M. Pegoraro [41] studied the residual thermal stresses in the polymer matrix taking the viscoelastic properties of the matrix into account. The authors used shear and dynamic mechanical tests to investigate the viscoelastic behaviour of thermoplastic and thermoset polymers. The results give the processing temperatures and cooling rates expected for the formation of radial stresses at fibre/matrix interface for thermoset and thermoplastic polymers. These residual stresses contribute to the fibre-matrix adhesion and strongly influence the interface efficiency of the polymers. It was shown that when the interface efficiency decreases, the residual stress also decreases.

Generally, most authors argue that exposure of fibre-reinforced polymer composites to high temperatures for extended periods of time may lead to decay in the interface

Effect of Temperature on Impact Damages of FRP Material

efficiency and can have a strong impact on the change of the behaviour of the polymer even if the chemical adhesion of the fibres remains unaffected.

2.2.1.3 Effect of Temperature on Impact Damages of FRP Material

Structures made of composite materials are susceptible to damage under thermal loads. The nature of this damage along the transverse direction is different from the damage experienced by conventional metallic materials subject to thermal loads. Structural components made from fibre reinforced polymer composite materials, in particular, wind turbine blades, subject to low velocity impact loads may experience matrix crack, delamination, fibre fracture, debonding and fibre pull-out. This may also happen with tools dropping on the structure, hail stones and bird strikes.

Damage caused by low velocity impact is most detrimental to the strength and stiffness of the composite and it can also affect the service life of the component. Several studies have been done on the effect of impact loading on composites combined with the presence of high temperatures. The objective of these studies was to determine the properties of the FRP composite materials that have high impact resistance. Kwang-Hee Im et al [42] studied the effect of temperature on delamination and matrix cracking of composite laminates subject to impact loads. In the test specimens, the stacking sequences of CFRP materials were arranged as $[0_6/90_6]_s$ and $[0_4/90_4]_s$, and polyether ether ketone was used as the matrix material. A steel ball was used to generate the impact damage and scanning acoustic microscopy (SAM) was used to estimate the impact damage at various temperatures. The results show that when the temperature of laminates increases, the impact induced delamination area decreased. However, as the temperature of the laminates decreased, the delamination areas increased, while the occurrence of transverse cracks decreased. This indicated that delamination of CFRP laminates increases when temperature rises and the behaviour of the composite structure under thermal loads depends on the type of the polymer resin.

Lopez-Puente et al [43] investigated the influence of low temperatures on the damage experienced by CFRP materials under intermediate and high velocity impact loads. Tests were conducted on tape and woven fabric laminates at temperatures varying from 25°C to -150°C with the damage measured with a C- Scan machine. The results indicated that

Effect of Temperature on Impact Damages of FRP Material

damage is caused by temperature, impact velocity and the type of composite material used.

Benli and Sayman [44] determined the effect of temperature change and thermal residual stresses on the impact properties of unidirectional GFRP laminates. The laminates arranged on $[90/0/0/90]_s$, $[90/0/45/45]_s$, and $[0/90/45/45]_s$ were analysed considering at testing temperatures of 20°C, 90°C and -50°C using ANSYS software. Similarly, impact test applied on the samples range from 5J to 55J under specified temperatures. The result of the authors on thermal stress analysis and impact test indicates that the contribution of thermal residual stresses developed under variable temperature to impact damage of the laminates rises with decreasing temperature. In addition to this the authors found testing temperature and stacking sequence had considerable effect on the damaged areas.

Stress had a significant effect on the impact damaged areas of composite structures in a low temperature environment. Badawy [45] studied the impact behaviour of GFRP laminates exposed to temperatures -10°C, 20°C, 50°C and 80°C for one and three hour exposure periods. In the tests, unidirectional laminates were arranged as angle-ply and cross-ply laminates with various fibre volume fractions. The 6709 machine and hammer with a digital attachment were used for the impact tests and the energy absorption was measured at an impact speed of 3.46m/s. The test results indicated that the impact strength of GFRP laminates decreased with increasing temperatures for both unidirectional and cross-ply arrangements. The author also showed that with increasing fibre volume and proper ply arrangement, the impact strength of the laminates can be improved.

A similar research on carbon fibre composites was conducted to study their response to impact loading under different temperatures. Sayer et al. [46] investigated the effect of increasing temperatures on hybrid CFRP-GFRP composite laminates in a temperature range of -20°C to 60°C until complete perforation. In the experimental work, the impact tests were carried out by using an Instron-Dynatup 9250 HV model and the impact energy ranged from 10J to 35J until complete perforation. The results indicated that the impact energy absorption capacity of hybrid laminates at ambient temperatures was greater than at higher temperatures. Furthermore, perforation thresholds of hybrid CFRP-GFRP laminates were affected by temperature change. Salehi-Khojin et al. [47] investigated the role of variable temperatures on the impact loading behaviour of Kevlar/glass specimens.

Effect of Temperature on Impact Damages of FRP Material

The role of temperature on the maximum energy absorption, deflection, durability and compression after impact was investigated at 8J, 15J and 25J. The temperatures were between -50°C to 120°C in these tests. The results indicated that the impact performance of the hybrid composites were affected by increasing temperatures. The role of temperature was determined for hybrid Kevlar fibre and carbon fibre composite laminates [47]. Salehi-Khojin et al [48] studied the influence of temperature on sandwich composites with Kevlar and carbon fibre face sheets under the impact loading at temperatures ranging from -50°C to 120°C and subject to impact energies of 15J, 25J and 45J. Tested specimens contained urethane filled honey comb cores, four layers of Kevlar and carbon face sheets at the outer sides. The results show that the impact testing at room temperature was not enough to find the damage on sandwich composites but as the testing temperature increased the impact performance also changed. Mainly, the strength of the specimens was reduced due to the change of temperature and delamination failure which occurred as the test temperature increased.

Halvorsen et al. [49] determined the influence of temperature on sandwich composites with glass fibre face sheets under the impact loading and at temperatures ranging from -50°C to 120°C with impact energies of 20J, 30J and 45J. Test specimens contained urethane filled honey comb cores, four layers of fibre glass and Kevlar/fibre glass face sheets at the outer side. The results indicate that the impact performance of sandwich samples changes over a range of temperatures. Erickson et al. [50] compared the capacity of sandwich specimens to absorb impact energy using both foam-filled and non-filled honey comb core materials at different temperatures. The face sheets were manufactured from a cross-woven E-glass/epoxy matrix. The impact energy values were specified as 12J, 60J and 150J and test temperatures as -25°C, 25°C and 75°C. Experimental results indicated that temperature had a major effect on the energy that can be absorbed and the peak impact force that can be sustained by the samples. Delamination of the composite structures increased when the impact loading occurs at high and increasing temperatures.

2.2.1.4 Effect of Temperature on Fatigue Strength of FRP Material

Failure of fibre reinforced polymer composites was not dominated by a single crack or its propagation as is the case with metals, but rather by a combination of delamination, matrix failure, debonding, fibre pull-out and fibre failures. This results in the accumulation of damage to the composite materials. FRP materials meet different loading conditions under operational conditions. Fatigue is the most common cause of

Effect of Temperature on Fatigue Strength of FRP Material

structural failures in engineering structures, particularly with wind turbine blades subject to cyclic loading during their service life.

Among all material types, FRP composites have good fatigue strength properties. Miyano and Nakada [51] worked on the characterization of time and temperature dependence of fatigue strength of unidirectional CFRP composites. Epoxy resin impregnated with carbon fibre strands were used as test specimens. Three kinds of fatigue strengths, namely, strengths in the longitudinal, compressive and transverse directions were tested at various frequencies and temperatures. The results showed that fatigue strength in each direction had different behaviours. The tensile strength of CFRP composites in the longitudinal direction showed a moderate decrease. Compressive strength of CFRP composites in the longitudinal direction strongly decreased when the duration of tests and temperatures were increased. Using the same carbon fibre epoxy composite specimens, Ramanujam et al. [52] characterized the fatigue behaviour of CFRP composite laminates under thermal cycling. Experimentally, twenty-four carbon fiber/epoxy composite laminates were arranged as $[0_{12}^0 / 90_{12}^0]$ and were exposed to thermal cycling in an environmental chamber for different temperatures ranging from 30°C to 140°C. The result of the fatigue tests showed that there was a crack growth near the free surface-edges because of the thermal loading. Furthermore, under thermal cycling, fatigue crack growth may increase drastically. Mivehch and Varvani-Farahani [53] investigated the effect of temperature on the fatigue strength of FRP composites and on cumulative fatigue damage (D). The analysis included temperature-dependent parameters such as ultimate tensile strength (σ_{ult}), Young's modulus (E) and fatigue life (N_f). The authors found the same results as the other researchers for the mechanical properties of FRP composites which deteriorated as the test temperature increased. The temperature-dependent model was analysed with the help of six sets of damage data available in the literature. When comparing the Damage-Numbers of cycles (D-N curves) it was predicted that as the temperature increased, the cumulative fatigue damage also increased. Power-law stress-fatigue life relations were studied in [54] and the influence of temperature on the fatigue strength behaviour of FRP composites was investigated. Results showed that in the power-law S-N relation, both the coefficient and exponent of this relation were temperature-dependent. Coronado et al. [55] studied the effect of temperature on the process of mode-I delamination for unidirectional CFRP (AS4/3501-

Effect of Temperature on Fatigue Strength of FRP Material

6) composite with symmetrical configuration $[0^0]_{16/s}$ under static and fatigue loadings. Double cantilever beam (DCB) specimens were tested under static and fatigue loads and at temperatures 90°C, 50°C, 20°C, 0°C, -30°C and -60°C. The results of study on the static initiation of delamination indicates that the material stiffness is slightly decreased for maximum and minimum temperatures. However, the material exhibits better mechanical properties at a temperature of 9°C in the static initiation phase. During the initiation of fatigue delamination, the maximum delamination energy was required to start the crack. In general, Coronado et al. [55] showed that the properties of the material were influenced by the test temperature and represented a more brittle behaviour at low temperatures and high ductility at high temperatures. Ming-Hwa Jen et al [56] investigated the fatigue properties of APC-2 composite specimens under variable temperatures. In the experimental work, thermoplastic AS-4/PEEK cross-ply laminates were arranged as $[0/90]_{4s}$ and quasi-isotropic laminates were arranged as $[0/+45/90/-45]_{2s}$. Tests were conducted at temperatures 25°C, 50°C, 75°C, 100°C, 125°C and 150°C. The tension-tension (T-T) fatigue tests were done using MTS810 testing machine up to a maximum fatigue cycle of 10^6 . The results indicated that cross-ply laminates have a better ultimate tensile strength, longitudinal stiffness and fatigue strength as compared to the quasi-isotropic laminates. Mostly near to or above T_g of the thermoplastic matrix, mechanical properties deteriorated. Sjögren and Asp [57] investigated the inter-laminar toughness of $0^0/5^0$ layers for a Hexcel (HTA/6376C) CFRP specimen under fatigue loading at ambient and at a high temperature of 100°C. The inter-laminar toughness in pure Mode I fracture mode was measured using a Double Cantilever Beam (DCB) test. An end Notched Flexure (ENF) test was used to study the Mode II fracture. Mixed-Mode Bending (MMB) was used to study the mixed mode I and mode II fractures. The experimental results show that the strain energy release rate threshold values for delamination growth were significantly affected by fatigue loading, and the fatigue threshold at temperature 100°C was about 10% of the critical static values for all three modes tested. The delamination growth under mode II static loading at temperature 100°C differed from mode II static loading at room temperature. At temperature 100°C the crack jumped between the upper and lower fibre boundaries, while at room temperature the crack followed the upper fibre boundary. This may be due to a change of residual stress and matrix properties. The fatigue strength of bi-directional woven glass fibre composites under increasing temperatures was determined in [58]. Ferreira et al. [58] investigated the fatigue strength

Effect of Temperature on Fatigue Strength of FRP Material

and fatigue damage properties of woven bi-directional E-glass/polypropylene matrix laminates under increasing temperatures. Laminates used in these tests have different strengths and stiffness based on ply orientations. The authors showed that the fatigue strength of the laminates is strongly affected by layer arrangement and temperature on the surface of laminates which has a large effect on the failure.

Generally, mechanical properties of carbon and glass fibre reinforced polymeric resin composites decreased under increasing temperatures. This is due to low value of T_g for polymeric matrix. Properties of structures designed using FRP composite materials depend on the temperature and this is one of the drawbacks of composite materials used in the tropical regions for long service life like wind turbine blades in Africa (Sahara Desert, Chad, Sudan, Egypt, Morocco, and Ethiopia).

Despite the inherent advantages over traditional materials, FRP composite materials are affected by heat and moisture when composite structures operate in harsh environmental conditions over a long period of time. High temperatures and water absorption by composites lead to lower T_g and a softening of polymeric matrix. Moisture absorption weakens the matrix dominated properties such as the strength in the transverse direction, fatigue resistance, ILSS and impact tolerance. The effects of heat and moisture on composite materials have been investigated by researchers. Abdel-Magid et al. [59] studied E-glass/epoxy composite properties taking the effects of load, temperature and moisture. Specimens of E-glass epoxy composite of 52% of fibre volume fraction were submerged into distilled water at different temperatures and for different periods of time. Laminates were tested based on duration of time in distilled water at ambient and at a temperature of 65°C. The results indicated that for a duration of 500h submerged in distilled water at ambient temperature and subject to a tensile load, strength and strain failure values increased but stiffness decreased. Changes in the materials properties occur by fibre strengthening and matrix plasticization. For a duration of 3000h, the strength, elastic modulus and strain failure values decreased. The result indicated that cracks propagate along the interface and this made the material more brittle and less ductile. When the temperature approached 65°C for a duration of 1000h, strength and elastic modulus of the material decreased while the strain failure value increased. A tensile load has a positive effect on the material strength for short durations but the decrease in the value of the elastic modulus at higher temperatures, and longer duration of moisture results in catastrophic failure. High temperatures lead to ductile failure of the E-glass

Effect of Temperature on Fatigue Strength of FRP Material

epoxy laminated composite. Upadhyay et al. [60] investigated the impact of temperature and moisture on uniaxial fibre reinforced polymer under compressive loadings. Four types of FRP composites materials, namely, AS-graphite/epoxy laminate, T-300 graphite/epoxy laminates, boron/epoxy and E-glass/epoxy laminates were studied for micro buckling failure. Based on theoretical observations the results showed the effect of moisture absorption as well as temperature change on compressive strength. The hygrothermal effect lowered the compressive strength of polymer matrix composites by 15-20% with 2% moisture in the resin and at a temperature 50°C. This indicates that temperature had relatively more detrimental effect on the compressive strength compared to moisture. The hygrothermal impact on boron/epoxy laminates was much less compared to AS-graphite/epoxy laminates and E-glass epoxy laminates.

Cheng Xiaoquan et al. [61] investigated the hygrothermal properties of uniweave T300/QY9512 composite stitched laminates by experimental and analytical methods. Authors conducted compressive strength tests using a combination of heat and moisture at the ambient temperature. The test results showed that the hygrothermal environment has a severe impact on reducing the compressive strength of stitched composite laminates. Stitching might increase the compressive strength in view of different layup sequences of stitched laminates. Davidson et al. [62] studied the mode I toughness of T800H/3900-2 graphite/epoxy composite materials used in aircrafts and spacecraft under various environmental conditions. Moisture-saturated laminates at -43°C, 21°C and 98°C, and dry laminates at a temperature of 125°C were studied. All tests at temperature -43°C run in a freezer. The furnace was attached to the MTS servo hydraulic machine. The test results indicated that the specimen's toughness increased when test temperatures increased.

Different authors explained matrix viscosity, plasticization of resin and the development of the delamination of the specimens under increasing temperatures using a scanning electronic microscopy. The flexural properties of FRP composites under hygrothermal conditions were studied. Shiva Kumar and Shivarudraiah [63] studied the influence of temperature on the hygrothermal and flexural properties of GFRP samples. GFRP composite samples were exposed to temperatures 30°C, 50°C and 70°C and were kept in 95% relative humidity for 200 days. The results show moisture absorption in the sample increases with increasing temperature. A combination of temperature and

Effect of Temperature on Fatigue Strength of FRP Material

moisture led to a decrease in the flexural and interlaminar shear strength properties of the laminates. The thickness of specimens increased due to moisture and delamination.

Ellyin and Rohrbacher [64] determined the effect of an aqueous environment and temperature on the mechanical properties of GFRP laminates. Three types of arrangements were considered, namely, cross-ply, multi-directional and angle-ply. The laminates were dipped in distilled water at ambient temperature and at a temperature of 90°C for four months. Cyclic loading tests were conducted under a load control mode. The experimental results show that E-glass/epoxy laminates absorbed moisture and were influenced by the temperature of the distilled water. At a temperature of 20°C, moisture uptake approached the saturated state and the water content was about 0.8%. At a temperature of 90°C, no saturation state was observed, but crashes and blisters were observed on the surface of the laminates. The authors compared the fatigue strength of the specimens immersed in water at ambient temperature with dry specimens. Dry specimens had a higher fatigue strength. At a temperature of 90°C, the fatigue strength was reduced from 38% to 65% compared to dry specimens. Generally, swelling due to moisture lowered the stiffness of the composite laminates.

Mishra et al. [65] assessed the influence of thermal and cryogenic treatment on GFRP composite laminates in a hygrothermal environment for periods of four to sixty four hours at a temperature of 60°C with a relative humidity of 95%. Short beam shear (SBS) tests were conducted and analysed. The results indicated that the key factor for the reduction of the interlaminar shear strength (ILSS) was the duration of hygrothermal exposure. The authors observed fibre content had a significant impact on the static mechanical properties of the composite, in particular, the inter-laminar shear strength of the specimens. The ILSS of composite depends on the types of polymer resins not on the fibre strength of composite material.

The properties of hybrid composites were studied by a number of authors. Boualem and Sereir [66] evaluated the hygrothermal transverse stresses in UD-hybrid fibre reinforced polymer composites under cyclic environmental conditions. Both graphite epoxy hybrid composite AS/3501-5 laminates and T300/5208 laminates were tested. Saturation time and the quantity of water absorbed for six weeks, six days and six hours were recorded. The authors used the Fick equation and the Arrhenius law to describe the moisture concentration and to find the impact of temperature on moisture diffusion. The results showed that the use of hybrid FRP composite materials can lead to a reduction in

the hygrothermal transverse stresses. Qi and Herszberg [67] investigated the influence of hygrothermal cycling and impact on the residual compressive strength and damage resistance of carbon/epoxy laminates. The test specimens were made from plain-weave composite and contained four groups damaged by impacts of 0 to 6J energy at different hygrothermal environments. The experimental results concluded that the residual compressive strength of the laminate decreases because of matrix cracking due to hygrothermal cycling under impact loads.

Upadhyay et al. [68] studied the nonlinear flexural response of cross-ply and angle-ply laminated composite plates under hygrothermal conditions. The authors utilized various techniques in the formulation and the solution such as finite double Chebyshev series, von-Karman nonlinear kinematics, the higher order shear deformation theory (HSDT) and quadratic extrapolation techniques. The results indicated that the nonlinear flexural response of thick laminated plate is affected by hygro-thermo-mechanical loading. A rise in the temperature and moisture concentration become more detrimental as working temperatures approach glass transition temperature.

2.3 Summary of Review

Modern wind turbine blade manufacturing industries use large blades made from FRP composite materials because of their high stiffness, strength, and low weight as well as their facility to form intricate shapes to maximize the extraction of wind energy from the wind. However, change of temperature affects the physical and mechanical behaviour of FRP composites used in the wind turbine blades structural elements as the studies in the literature indicate. It is a shortcoming of polymeric resins in FRP composites that they are affected by high temperatures. Researchers studied the influence of temperature on FRP materials, in particular, on their stiffness, strength, impact resistance and fatigue strength as reviewed extensively in this chapter. The authors used different experimental tests and modelling techniques to investigate the effect of temperature on FRP materials. Increasing temperatures can lower fibre/matrix bonding strength and can lead to delamination. These are the main causes of degradation of FRP composite properties. When temperatures approach T_g of the polymeric resin, mechanical properties of the composite laminates are degraded. Several authors investigated the dependence of FRP composites on temperature.

It is important to investigate the effect of temperature on the mechanical behaviour of composite materials currently available for the modelling of wind turbine blades. Carbon, glass and the hybrid of these were selected and specimens were tested to investigate their response under various thermal conditions. Hand layup and resin infusion manufacturing processes were used to manufacture the specimens. Short beam shear tests, tensile tests and dynamic mechanical analysis under elevated temperatures were conducted to study the interlaminar shear strength, tensile strength and stiffness behaviour of composites to identify the correct materials for tropical wind farms.

In chapter 3, specimen preparation, description of different manufacturing techniques and test methods are discussed involving carbon/epoxy, glass/epoxy and hybrid composite materials.

Chapter 3

Materials and Testing Methods

3.1 Materials and Manufacturing Process

In the section below testing methods and the equipment used in the tests are discussed. The objective is to investigate the effect of temperature on the mechanical properties of fibre reinforced polymer composites materials. Materials used in the tests are T300 carbon fibre and E-glass fibre reinforced composites and their hybrids. Matrix material is Ampreg 21 epoxy resin premixed and homogenized with Ampreg 21 standard hardener with a mixing ratio of 10:2.6 by weight. Unidirectional and plain weave fibres, epoxy resin, peel ply, infusion mesh, spiral binder, perforated film, coremat and vacuum bags were purchased from AMT Company which distributes the Gurit products.

Composite specimens were prepared to determine the static and mechanical properties of the composites under thermal loading. For this purpose, Short Beam Shear (SBS) test and Dynamic Mechanical Analysis (DMA) test were conducted. Fibre volume ratio of the composite test specimens were specified as 50% and measured using matrix digestion based on ASTM 3171 standard [69]. The mechanical properties of the composites at room temperature are summarized in Table 3.1.

Table 3.1 Physical and mechanical properties of unidirectional glass fibre, carbon fibre and epoxy resin [70].

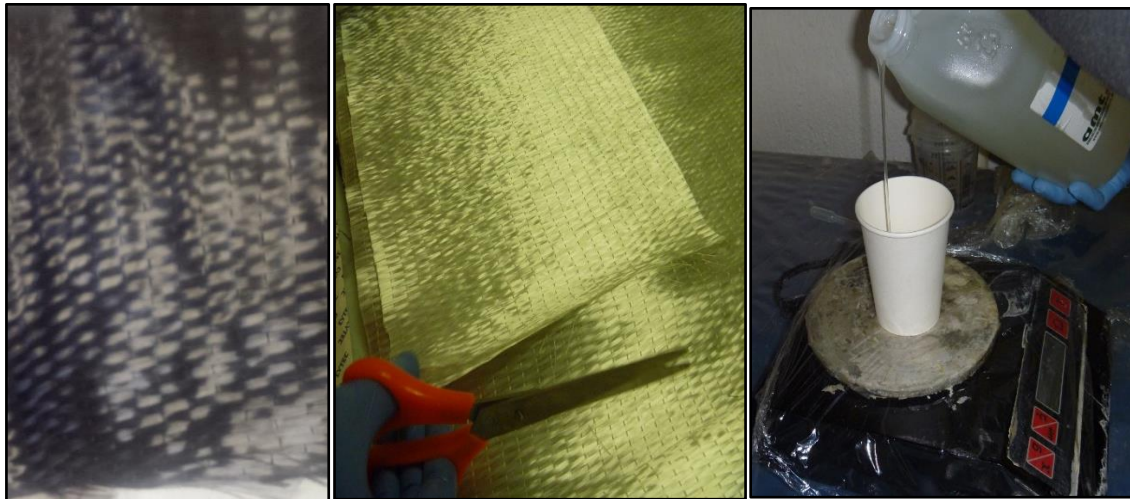
Materials	Young's Modulus [GPa]	Tensile strength [MPa]	Density [kg/m ³]	Poisson's ratio
E-glass	72.5	2350	2570	0.25
T-300 carbon	230	3530	1760	0.30
Epoxy	3.3	69.9	1100	0.36

3.2 Manufacturing Process of FRP Composite Specimens

Dimensions of the unidirectional carbon and glass fibre specimens were measured according to the required standards and cut using scissors as shown in Figure 3.1. For short beam shear and dynamic mechanical analysis tests, the specimens were prepared by hand-layup production techniques. For this purpose, wax, tacky tape, paint brushes, rollers, peel ply, perforated film and vacuum bag were used to prepare the specimens. Carbon fibre, glass fibre, glass-carbon fibre hybrid and carbon-glass fibre hybrid

Manufacturing Process of FRP Composite Specimens

composite materials were positioned manually on the glass table and then epoxy resin was poured on them, and subsequently a brush was used to prepare the specimens. Entrapped air was removed manually with rollers. The laminates were cured on the glass table at the ambient temperature for 24 hours and post cured in an oven for 16 hours at a temperature of 40°C. The composite laminates were cooled at room temperature before short beam shear and dynamic mechanical analysis tests. The hand lay-up manufacturing processes are shown in Figure 3.2.



(a) Unidirectional carbon fibre (b) Unidirectional glass fibre (c) Ampreg 21 epoxy resin
Figure 3. 1 Unidirectional carbon, glass fibre types and Ampreg 21 epoxy resin

Information on the sample codes, layer orientation of plies and total thicknesses of the laminates are shown in Table 3.2. The same thickness and orientations of plies were adopted in all composite specimens used in the tests. The total thickness of the hybrid specimens consisted of half carbon fibre reinforced composite and half glass fibre reinforced composite. Four composite specimens are shown in Figures 3.3 and 3.4. The test temperature for short beam shear tests increased from ambient temperature to 55°C and for dynamic mechanical analysis tests, it increased at a rate of 2°C/min to 140°C for all composite specimens.

Table 3.2 Sample code, layer configuration and thickness of laminates

Sample codes	Layer configurations fibres	Number of laminates	Total thickness [mm]
G-1	[0 ₇] _s G-1	7	3
C-2	[0 ₁₀] _s C-2	10	3
H-3	[0 ₂] _s G-1+[0 ₅] _s C-2+[0 ₂] _s G-1	9	3
H-4	[0 ₃] _s G-1 +[0 ₃] _s C-2+[0 ₃] _s G-1	9	3

Manufacturing Process of FRP Composite Specimens

G: glass fibre, C: carbon fibre, H-3: hybrid glass-carbon fibres and H-4: hybrid carbon-glass fibre composite specimens

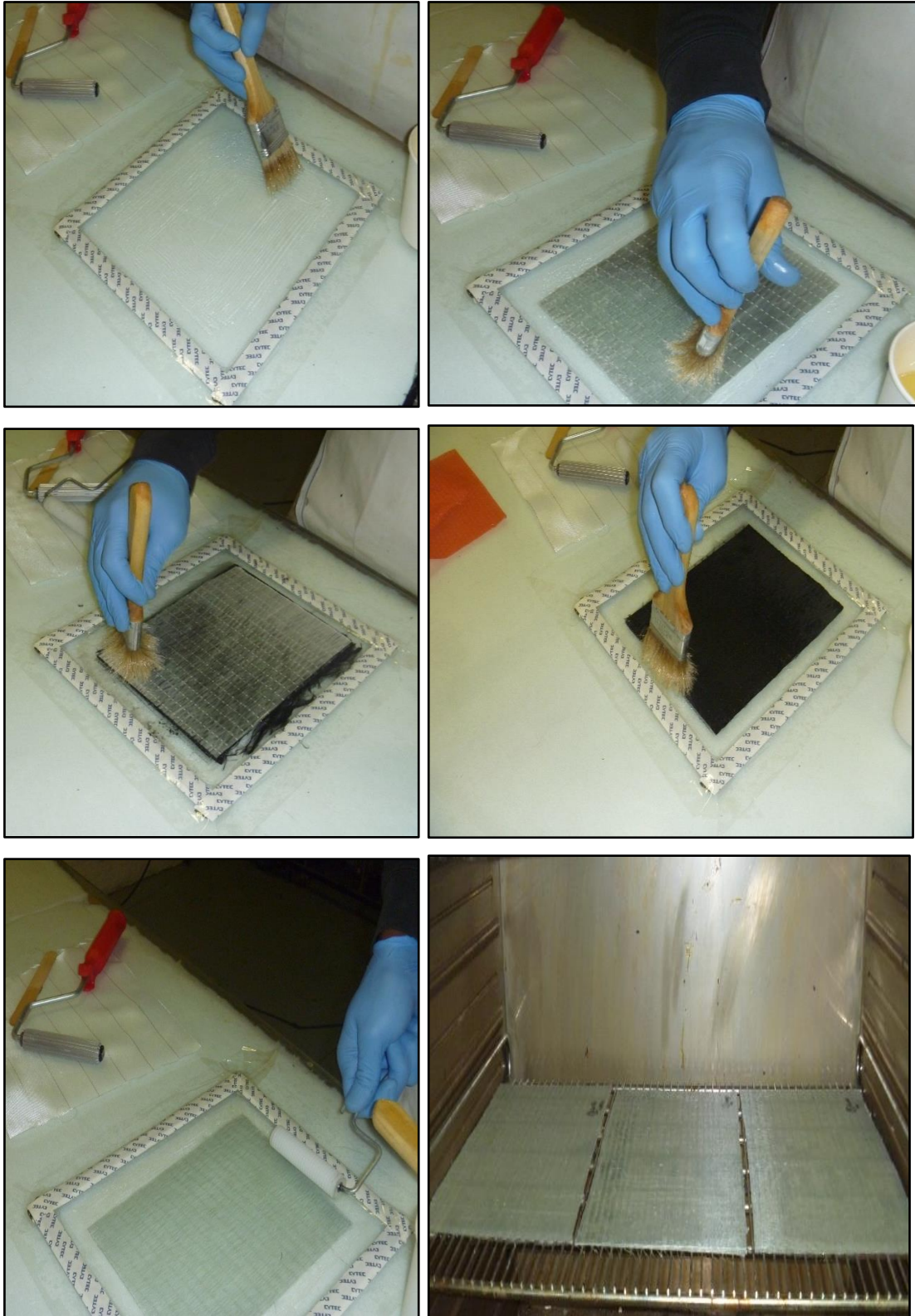


Figure 3. 2 Hand lay-up tools and lamination process of composite laminates

Manufacturing Process of FRP Composite Specimens

After curing the specimens, laminates were cut using a CNC machine with a tolerance of 0.02mm at a standard size for static and dynamic analysis under thermal loading.

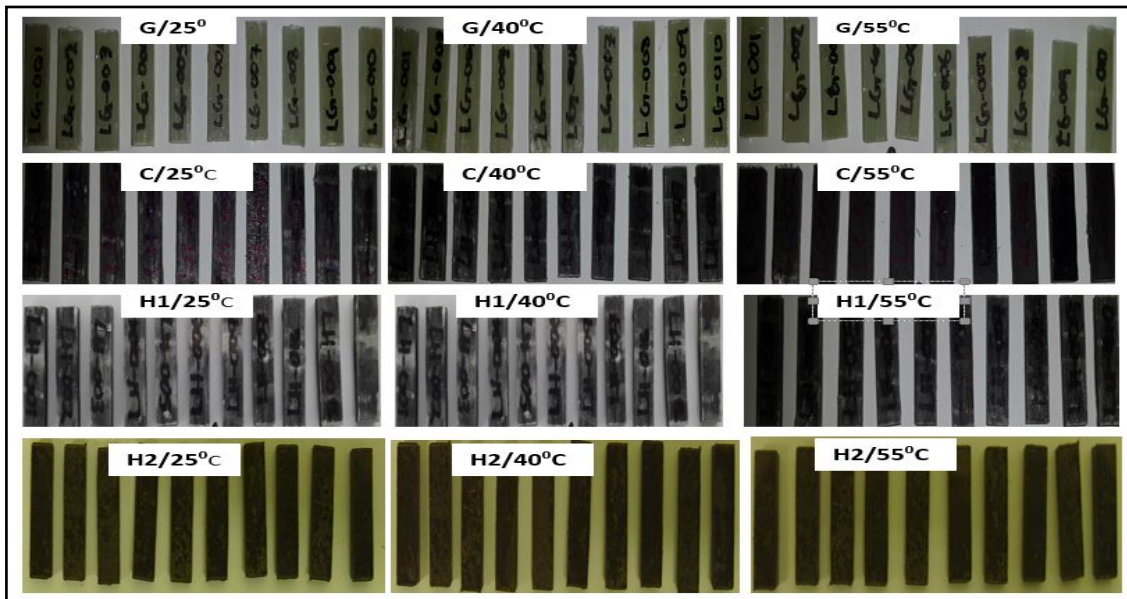


Figure 3.3 Unidirectional FRP composite specimens prepared for SBS testing

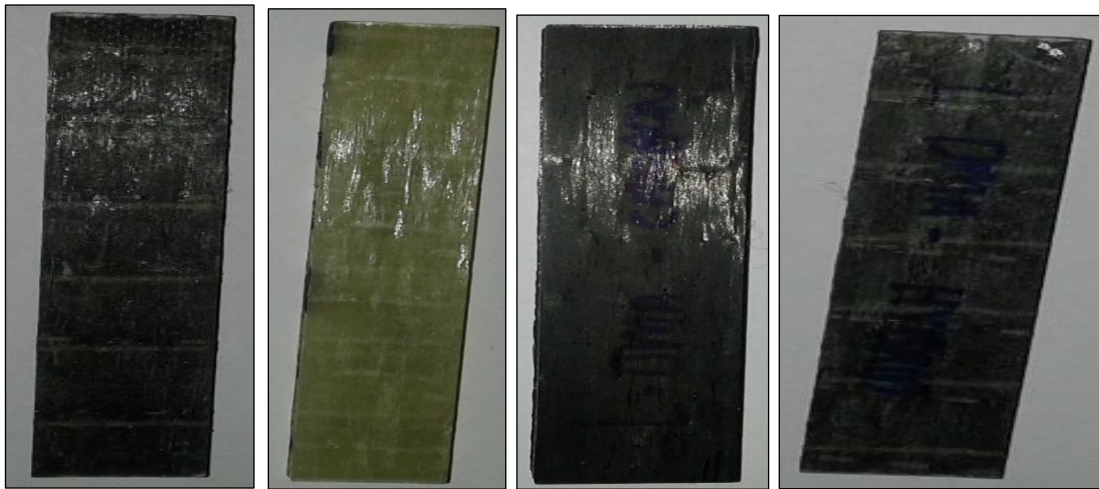


Figure 3.4 Unidirectional FRP composite specimens prepared for DMA testing

Additionally, tests were conducted to determine the impact of temperature on the mechanical behaviour of T300 CFRP, GFRP and hybrid GFRP-CFRP composite laminates. The same polymer resin was premixed and homogenized using Prime 20LV hardener at a mixing ratio of 10:2.6 by weight. The fibre volume ratio obtained for the glass/epoxy specimens was 55%. Above this value, the bonding strength between the fibres and matrix was less. Similarly the same procedure was followed to obtain the maximum combination of carbon/epoxy and glass-carbon fibre hybrid composite specimens. In these cases 60% fibre content was obtained in compliance with the ASTM

Manufacturing Process of FRP Composite Specimens

D 3171 standards. A vacuum resin infusion process was used to prepare the composite specimens. Layer orientations and thicknesses of the specimens are shown in Table 3.3.

Table 3.3 Sample code, layer configuration and thickness of composite laminates

Sample codes	Layer configurations fibres	Number of Laminates	Total thickness [mm]
G-1	[0 ₃] _s G-1	3	0.95±0.05
C-2	[0 ₃] _s C-2	3	0.95±0.05
H-3	([0 _s] G-1+[0 ₂] _s C-2+[0 _s] G-1	4	1.0±0.05

G: glass fibre, C: carbon fibre and H-3: hybrid glass-carbon fibres composite specimens

A vacuum resin infusion process uses vacuum to transfer the resin into fibre layers covered by the vacuum bag. Vacuum bag, peel ply, infusion mesh, core mat and spiral binders are used to prepare the specimens from three different composite materials. In the hand lay-up manufacturing process, fibres are laid on a glass table and the resin is applied using brushes. In the vacuum infusion process, fibres and the resin are placed in a vacuum bag and the air is sucked out of the bag through a tube. Currently the main components of helicopter blades, wind turbine blades, some automotive parts and certain parts used in aerospace industry are produced by this method. In the vacuum infusion process less epoxy resin is wasted and the resin is more evenly distributed in the composite products.

Vacuum created inside the bag helps to suck away the excess resin from the composite specimens. As a result, the fibre volume ratio of the composite can be in the range of 55% to 60% for the composite specimens. A detailed sequence to produce glass fibre composite laminates by vacuum infusion process is shown in Figures 3.5 and 3.6. As in the case of hand a lay-up manufacturing process, a glass table is first cleaned using ram wax. Subsequently peel ply, glass fibre, infusion mesh, core mat and spiral binder are placed on it before the epoxy resin is transferred to the fibres as shown in Figure 3.5 (a-f). Peel ply is a synthetic cloth that drapes over the flat glass table and on top of the glass fibres. It is used to create a smooth surface as well as to squeeze the trapped air form the specimens. When the peel ply is removed, the surface of the specimen is free from harmful sharp edges and spurs. In a vacuum infusion process, an infusion mesh or a flow media is used to make the resin enter the vacuum bag at a specific flow rate. As shown in Figure 3.5 (d) the infusion mesh is laid on the top of the glass fibres as a single layer. However, fibres can cause some resistance that can prevent the resin to flow freely. The presence of

Manufacturing Process of FRP Composite Specimens

the infusion mesh on the top surface of the composite ensures that the epoxy resin flows into the fibres efficiently. Figure 3.5 (e) shows the Coremat material used to prevent the formation of excessive resin around the specimens. The tube used to transfer the resin into the fibres and to apply vacuum is shown in Figure. 3.6 (a). The same tubing material is used to transfer the resin from the cup and to apply vacuum. A spiral binder is used for the resin infusion process to distribute the epoxy resin into the laminates. To achieve a widespread infusion of the polymeric resin, it is attached to the flange as shown in Figure 3.6. Once every material is positioned properly, tacky tape is placed around the material. A resin input pipe is inserted at the bottom of the material to draw the excessive resin. The air output/vacuum pipe is then inserted and it is connected to the vacuum pump to draw out the air and create suction. The vacuum bag is sealed around the material. It is important to ensure that there are no leaks or holes in the vacuum bag as any air drawn in could damage the laminate. As shown in Figure 3.6, the epoxy resin and hardener are mixed and left to stand for ± 20 minutes to de-gas. Once the required amount of resin is drawn into the laminate, the resin input pipe is closed off and the laminate is kept under vacuum until it is time to turn the vacuum off. The laminate is then left to cure for the remaining 24 hours. After 24 hours, the laminate is de-moulded and placed in an oven for post-curing for 16 hours.



(a) Peel ply on the glass table



(b) UD- glass fibre lay-up on the glass table



(c) Peel ply and fibre lay-ups for infusion



(d) Infusion mesh preparation



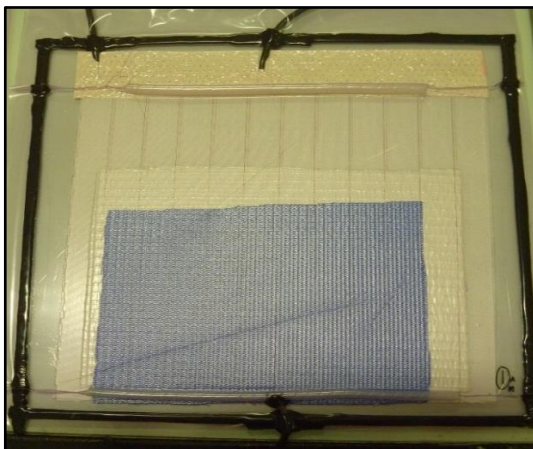
(e) Coremat for resin infusion



(f) Spiral binder

Figure 3. 5 Unidirectional fibre lay-up process before resin infusions

During vacuum infusion process, low viscosity epoxy resin is used to allow the resin to flow easily through the specimens.



(a) Resin feed and vacuum lines

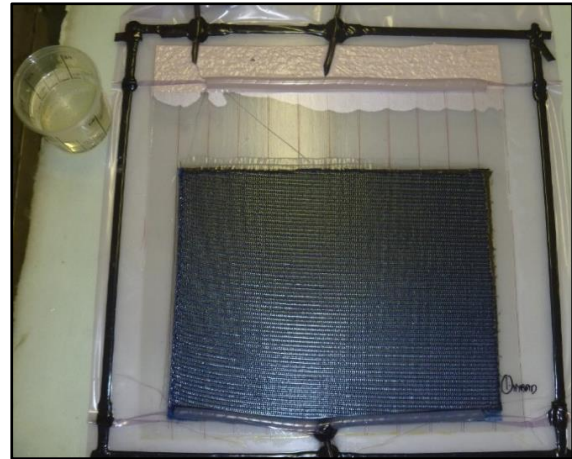


(b) Mixing of the resin

Manufacturing Process of FRP Composite Specimens



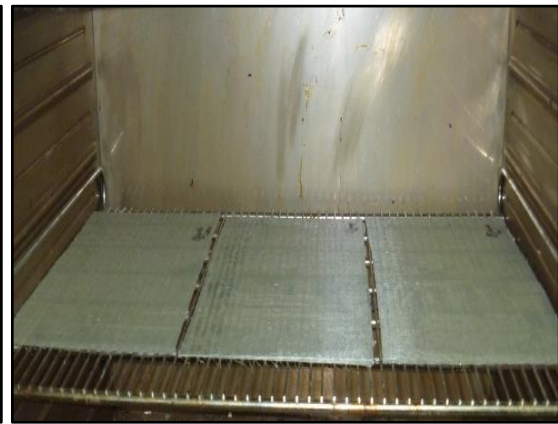
(c) Resin infusion



(d) Curing in the glass table



(e) demolded the glass specimens



(f) Curing in oven

Figure 3. 6 Vacuum resin infusion and curing process of glass fibre/epoxy specimens.

Similarly, the vacuum infusion process for carbon fibre specimens is shown in Figure 3.7 using unidirectional carbon fibres to prepare the specimens. Similar materials and tools are used to manufacture the carbon fibre specimens but permeability of the carbon fibre is lower and it tends to infuse slowly.



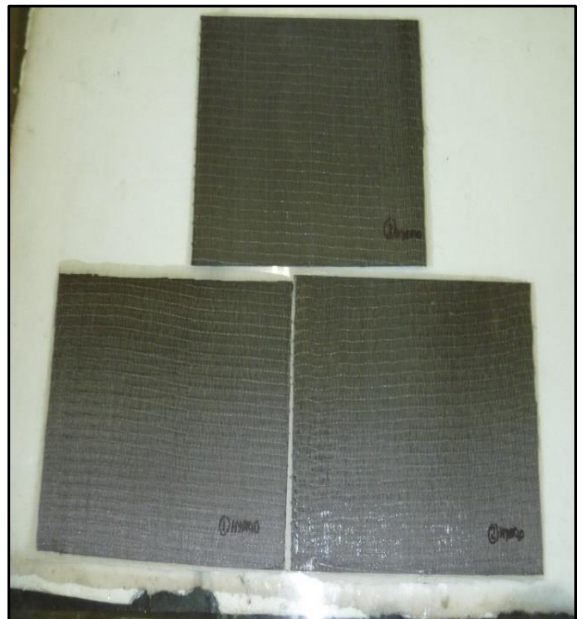
(a) Peel ply and fibre lay-ups for infusion



(b) Peel ply and fibre lay-ups for infusion



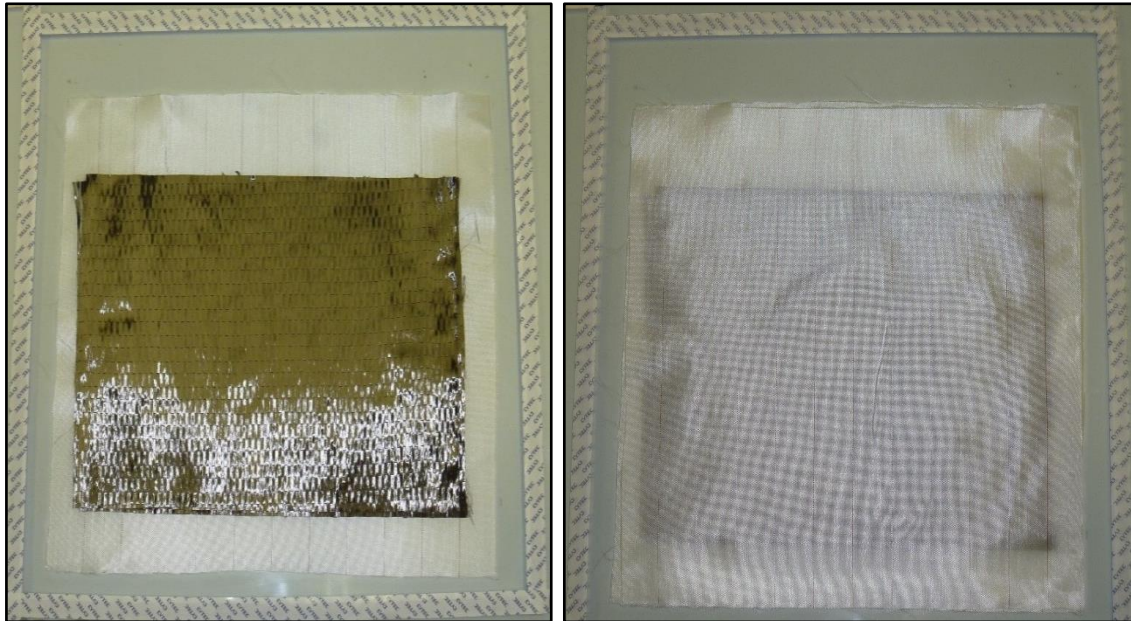
(c) Cure in the glass table



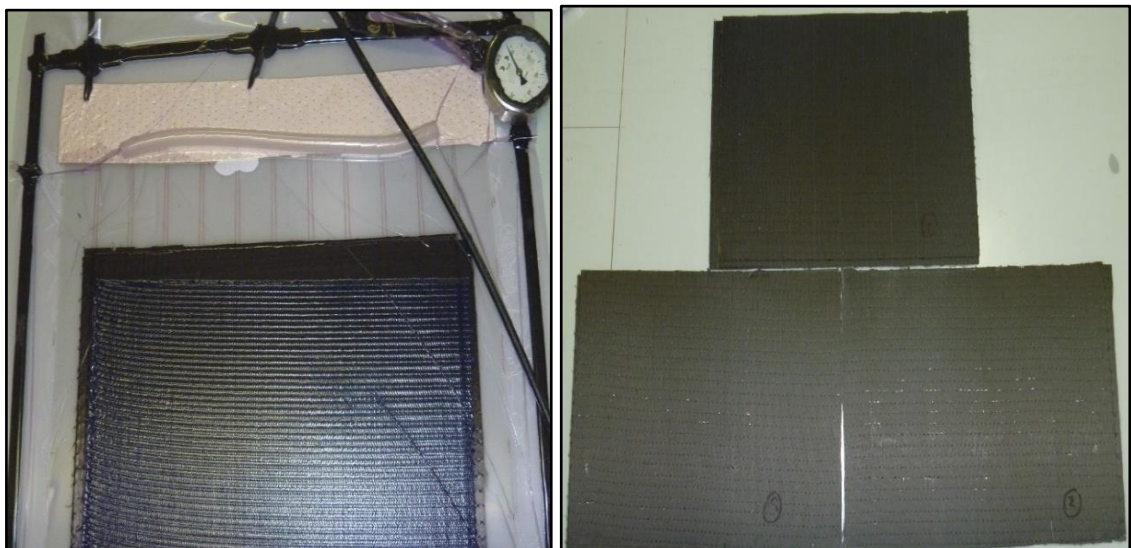
(d) Demolded the carbon specimens

Figure 3. 7 Resin infusion and curing process of carbon fibre/epoxy specimens.

Specimens were produced using a hybrid of the carbon and glass fibres with the carbon fibres in the middle section of the laminates. A vacuum infusion process used for this purpose is shown in Figure 3.8. The manufacturing steps and tools are similar to the ones used to manufacture glass fibre specimens. Permeability of the resin was the same in both cases.



(a) Peel ply and fibre lay-ups for infusion (b) Peel ply and fibre lay-ups for infusion



(c) Curing in the glass table (d) Demolded hybrid glass-carbon specimens

Figure 3. 8 Vacuum resin infusion and curing process for hybrid glass-carbon fibre/epoxy specimens.

The maximum thickness of the specimens manufactured by vacuum infusion process was approximately 1mm and it became challenging to hold it on the tensile testing machine. The tabs were produced using hand lay-up manufacturing employing 163g plain weave glass fibre, Ampreg 21 and Ampreg 21 standard hardener. The fibres in all panels were arranged in 0° , the tab sections were arranged in $\pm 45^{\circ}$ orientations and the nominal thicknesses used were based on ASTM standards. The specimens were cured for 24 hours

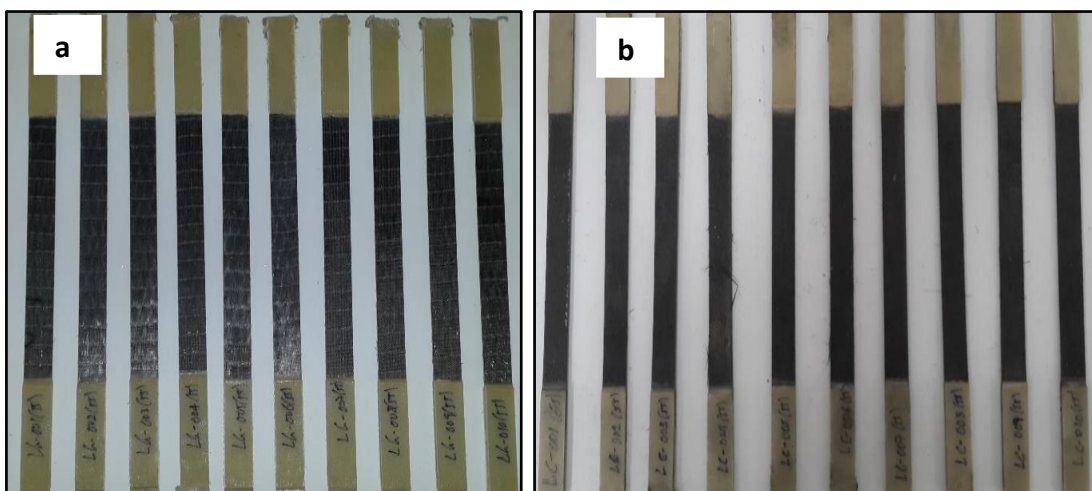
Manufacturing Process of FRP Composite Specimens

at room temperature followed by 16hour at 40°C in an oven. The bonding of the tap with the specimen is shown in Figure 3.9.



Figure 3. 9 Tab manufacturing process

Unidirectional CFRP, GFRP and hybrid GFRP-CFRP composite laminates were cured on a glass table at the ambient temperature for 24 hrs and demoulded for post curing in an oven for 16 hrs at 40°C. The composite laminates were cooled at room temperature, cleaned and flash was removed with sandpaper before testing. Specimens were measured and inspected for defects and placed into the laboratory for acclimatization for test purposes. After curing, the panels were cut using a CNC machine with a tolerance of 0.02 mm according to ASTM D 3039 standard as shown in Fig. 3.10.



(a) Unidirectional hybrid glass-carbon/epoxy (b) Unidirectional carbon/epoxy

Figure 3. 10 Composite specimens prepared for tensile tests

3.3 Testing Equipment and Experimental Methods

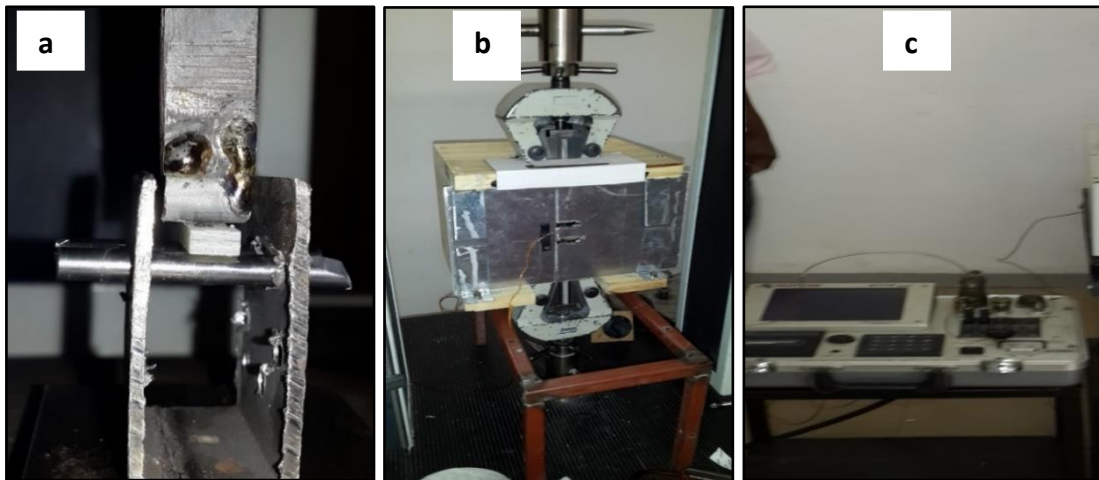
The composite specimens were prepared by hand lay-up and vacuum infusion manufacturing processes as outlined in the previous sections. Three types of tests were conducted to study the effect of temperature on fibre reinforced composites currently used in the construction of wind turbine blades. These are Short Beam Shear (SBS), Dynamic Mechanical Analysis (DMA) and tensile tests.

3.3.1 Short Beam Shear (SBS) Testing Method

SBS tests are used to determine the inter-laminar shear failure strength of FRP composites. Specimens were prepared according to the ASTM D 2344 standards. This is a well-known method to characterize the inter-laminar shear strength of unidirectional composites subject to ambient and high temperatures. The size of the specimen was 18mm×6mm×3mm. Short beam shear tests were conducted on a Lloyd LR 30K machine at a speed of 1mm/min at test temperatures 25°C, 40°C and 55°C. Before the tests, specimens were preheated for 2 hours in an oven and they stayed in the oven for a further 15 minutes. A sliding roller three-point bending fixture was used during the tests which included a loading nose with a diameter of 6mm and two support rollers with a diameter of 3mm. The loading nose moved down to apply load in the middle and create transverse load until the first failure happened. The oven used an infrared heater with a circular fan. A thermocouple was used to measure the exact temperature of the specimens before testing. Ten composite specimens were tested for each type of composite panel for the four different composites. The inter-laminar shear strengths (ILSS) of the composite specimens were calculated based on the load measured by the test equipment and the expression for ILSS is given by:

$$ILSS = \frac{0.75F_b}{bh} \quad (3.1)$$

where F_b is the load, b the width, h the thickness in mm and ILSS is in MPa.



(a) Bending fixture (b) Assembled oven to the machine (c) Thermocouple
Figure 3. 11 Tools and machine applicable for short beam shear testing.

3.3.2 Dynamics Mechanical Analysis (DMA) Testing Method

The viscoelastic behaviour of FRP composite specimens was studied using dynamic mechanical analysis (DMA) and the tests were performed as per ASTM: D5023 standard. DMA is applied to specimen's subject to oscillating loads, where it examines the reaction of the material within a given time interval. The size of the rectangular composite specimens was specified as 64mm×13mm×3mm. The composite specimens were tested under 3-point flexure using DMA Q 800 TA Instrument. The initial conditions for the tests were specified as a frequency of 1Hz at an amplitude of 15 μ m. The temperature in DMA tests increased at a rate of 2°C/min to 140°C and then the specimens were cooled.

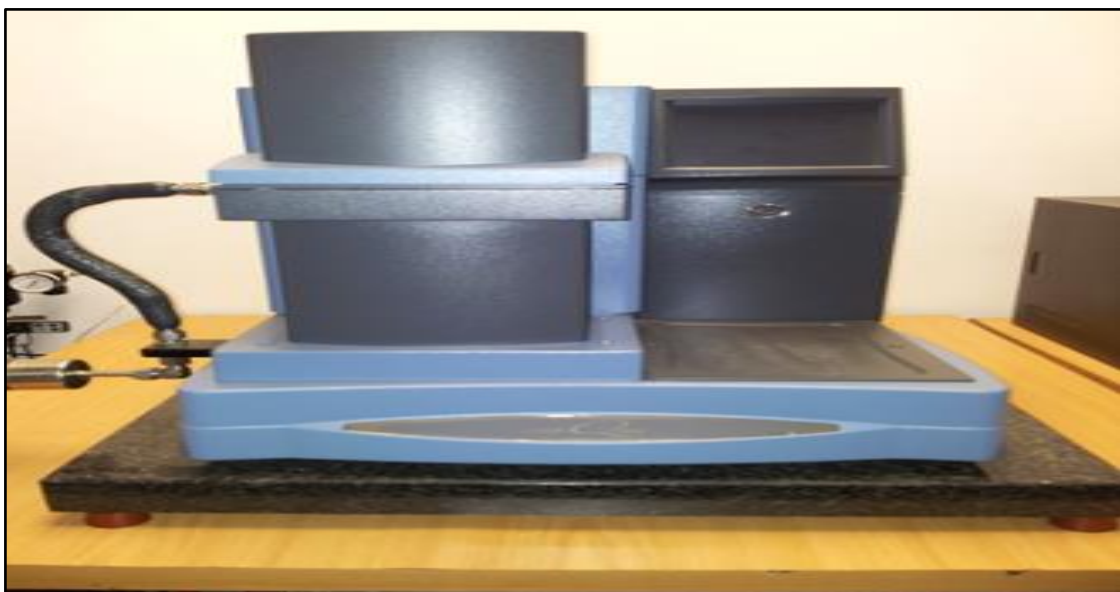


Figure 3. 12 Dynamic Mechanical Analyser (DMA)

3.3.3 Tensile Strength Tests

Tensile tests of the three specimens were carried out at temperatures of 25°C, 40°C and 55°C as per ASTM D3039 standard using Lloyd LR 30KN test equipment at a test speed of 2mm/min. Composite specimens were positioned vertically in the grip of the lower and upper jaws of the tensile testing machine.

Tabs were produced using plain weave glass fibre with Ampreg 21 as the standard hardener and were bonded on the sides of the specimens to provide a smooth load transfer from the jaws of the specimens up to the point of failure and also to reduce damage caused by the jaws. Before tensile testing, laminates were pre-heated for 2 hours in a binder oven and were left for a further 15 minutes in an attachable oven in the tensile test machine. The oven provided an infrared heater with a circular fan. A thermocouple was used to determine the temperatures of the specimens before the tests. Ten specimens were tested for each type of panel. The change in length during the tensile loading was determined using an Epsilon digital extensometer with a gauge length of 25 mm and a maximum travel of 2.5mm. A minimum of 10 specimens with approximate dimensions of 250mm × 15mm × 1mm [71] and gauge lengths of 150mm were prepared for each configuration. Tensile strength of specimens are given by

$$\sigma = P_{\max} / A \quad (3.2)$$

where σ , is the tensile strength (MPa), P_{\max} is the maximum load and A is the area of the specimen. The geometries of unidirectional specimens, ready for testing, are shown in Figure 3.13

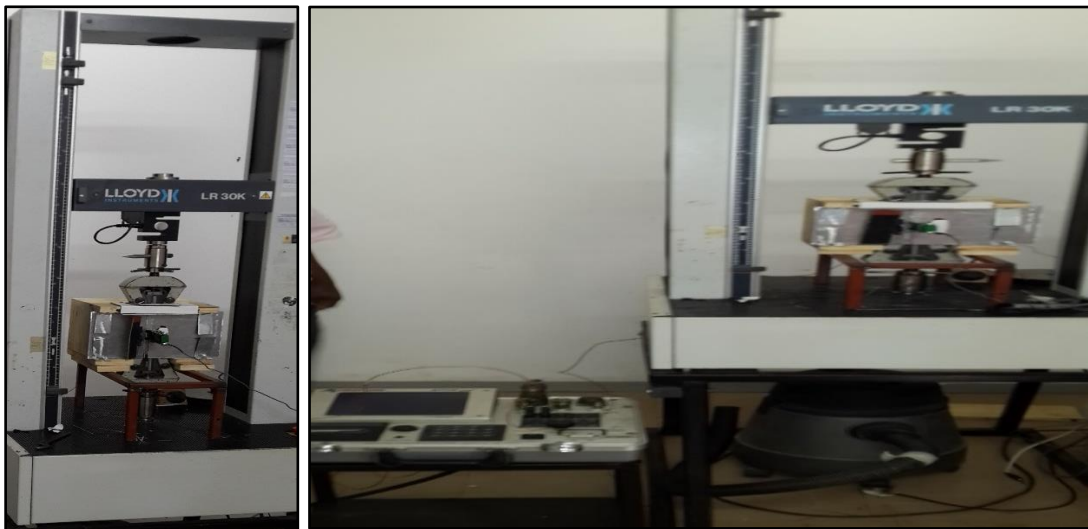


Figure 3. 13 Lloyd LR 30KN longitudinal tensile testing machine and assembled oven

3.3.4 Matrix Digestion Testing Methods

Fibre volume ratio of a composite material has a direct effect on the strength and stiffness of a composite structure. Consequently, the fibre content of composites is maximized to improve its properties. In the present study, fibre volume ratios of GFRP, CFRP and their hybrids have been maximized by trial and error in the hand lay-up and vacuum infusion manufacturing processes. Fibre volume ratios of GFRP specimens were approximately 55%, and those of CFRP and hybrid specimens were approximately 60%.

Matrix digestion using sulfuric acid and burr-off were used to determine the fibre volume ratios of specimens. Three specimens with dimensions 25 mm × 25 mm were cut from three different sections of each specimen. The specimens were then weighed and placed in a beaker. A minimum of 20-ml sulfuric acid was added until the colour of the solution darkened. Then, 35-ml of hydrogen peroxide was added and the fibres floated to the top of the solution. The beaker was removed from the hot plate and was allowed to cool. Finally, fibres were placed in an oven at 100°C for 1hr as indicated in Figure 3.14. The process of matrix digestion process was done according to the ASTM D 3171 standards.



Figure 3. 14 Matrix digestion process and tools

Fibre content in terms of weight percentage was determined using the expression

$$W_f = \frac{M_f}{M_i} \times 100 \quad (3.3)$$

where M_f and M_i are the mass of specimens after digestion and before digestion in grams. The fibre volume ratio of each specimen was determined assuming the void contents were minimal which is likely to be the case with vacuum infusion process. Fibre volume ratio of each specimen is given by the expression

$$V_f = \frac{\rho_r \times M_f}{(\rho_f \times M_r) + (\rho_r \times M_f)} \times 100 \quad (3.4)$$

where M_f is the mass of fibre, ρ_f density of the fibre, M_r mass of polymeric resin and ρ_r density of polymeric resin.

3.4 Numerical Analysis

To determine the effect of temperature on the static behaviour of FRP composites, experimental results are analysed using statistical methods. The most commonly used statistical distributions are implemented to model the static mechanical properties of composites under thermal loading. Failure of the composite specimens is studied using experimental and numerical results. For the most part, Chi-square and finite element methods are employed to obtain the numerical results.

3.4.1 Chi-square Test Methods

In the current study, three different statistical distributions are implemented, namely, normal, and log-normal. Using maximum likelihood procedures, parameters for each distribution are computed and their suitability is examined by a chi-square test. The Probability Distribution Function (PDF) and the Cumulative Distribution Function (CDF) for each specimen is given.

3.4.1.1 Normal Distribution

The mean and standard deviation parameters estimated by the maximum likelihood method are given by:

$$\mu = \frac{1}{N} \sum_{i=1}^N x_i, \quad \sigma = \sqrt{\frac{1}{N} \sum_{i=1}^N (x_i - \mu)^2} \quad (3.5)$$

where μ , σ and N are the mean deviation, standard deviation and sample size of the tests, respectively. Expressions for PDF and CDF are given by

$$\begin{aligned} \text{PDF: } f(x: \mu, \sigma) &= \frac{1}{\sigma\sqrt{2\Pi}} \exp\left[-\frac{(x-\mu)^2}{2\sigma^2}\right] \\ \text{CDF: } F(x: \mu, \sigma) &= \frac{1}{\sigma\sqrt{2\Pi}} \int_{-\infty}^x \exp\left[-\frac{(t-\mu)^2}{2\sigma^2}\right] dt \end{aligned} \quad (3.6)$$

3.4.1.2 Log-Normal Distribution

The parameters estimated by the log-normal distribution method are given by

$$\mu = \frac{\sum_{i=1}^N \ln x_i}{N}, \quad \sigma = \sqrt{\frac{1}{N} \sum_{i=1}^N (\ln x_i - \mu)^2} \quad (3.7)$$

Expressions for PDF and CDF are given by

$$\begin{aligned} \text{PDF: } f(x: \mu, \sigma) &= \frac{1}{\sigma x \sqrt{2\Pi}} \exp\left[-\frac{(\ln x - \mu)^2}{2\sigma^2}\right] \\ \text{CDF: } F(x: \mu, \sigma) &= \frac{1}{\sigma\sqrt{2\Pi}} \int_0^x \frac{1}{t} \exp\left[-\frac{(\ln(t) - \mu)^2}{2\sigma^2}\right] dt \end{aligned} \quad (3.8)$$

3.4.1.3 Weibull Distribution

The parameters estimated by Weibull distribution are obtained by solving the following set of equations:

$$\sigma^\eta = \frac{1}{N} \sum_{i=1}^N x_i^\eta, \quad \ln\left(\frac{1}{N} \sum_{i=1}^N x_i^\eta\right) - \frac{\eta}{N} \sum_{i=1}^N \ln x_i + \sum_{i=1}^N \left[\frac{x_i^\eta}{\sum_{i=1}^N x_i^\eta} \ln\left(\frac{N x_i^\eta}{\sum_{i=1}^N x_i^\eta}\right) \right] = 1 \quad (3.9)$$

where σ and η are Weibull distributions for shape and scale parameter of the short beam shear test data, respectively. Expressions for PDF and CDF are given by:

$$\begin{aligned} \text{PDF: } f(x: \eta, \sigma) &= \frac{\eta}{\sigma} \left(\frac{x}{\sigma}\right)^{\eta-1} \exp\left[-\left(\frac{x}{\sigma}\right)^\eta\right] \\ \text{CDF: } F(x: \eta, \sigma) &= 1 - \exp\left[-\left(\frac{x}{\sigma}\right)^\eta\right] \end{aligned} \quad (3.10)$$

3.4.1.4 Chi-Square Goodness of Fit Test Method

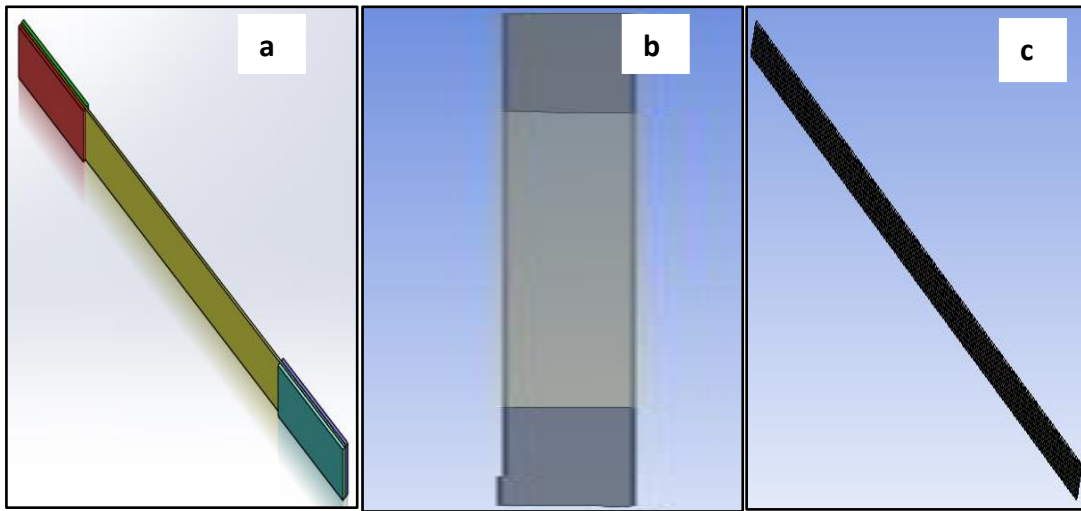
This method is used to assess accuracy of the experimental results and to make comparisons with the estimated probability distribution results. Chi-square goodness of fit test value, denoted by X^2 , is given by

$$X^2 = \sum (O - E)^2 / E \quad (3.11)$$

where O is the experimental result and E is the estimated value.

3.4.2 Finite Element Methods

A numerical analysis of the tensile tests was carried out using ANSYS finite element software, version 16.2 in order to compare experimental findings with computational results. First, the models of the specimens were prepared using the SolidWork software. These models were then exported to ANSYS as IGES files as shown in Figure 3.15. Subsequently, the solid models were implemented on ANSYS Design Modeller and were then divided into three sections involving the tab and tensile sections. The material properties were specified as orthotropic and the elastic properties of the materials were computed by the Rule of Mixtures (ROM). Composite specimens were modelled using ANSYS Composite Prep-Post software. For specimens 2688 meshing and 2925 nodes of shell, finite elements were used. The dimensions of the specimens, the boundary conditions and the loading conditions were specified as being the same as those in the experimental work. Maximum loads registered at the experimental tests were used in the FE simulations. Results obtained from the tensile tests were exported to ANSYS ACP for post-processing. Tsai-Wu failure criterion was used in the FE simulations to compute the failure index for each case.



(a) Solid model

(b) Surface model

(c) Meshed surface

Figure 3. 15 Geometries for tensile tests

3.5 Experimental Summary

Composite materials most often used in wind turbine blades were purchased and specimens were prepared for testing. The specimens were prepared using hand lay-up and vacuum infusion processes based on ASTM standards. A minimum of ten laminates were tested for each case to obtain reliable results. A numerical modelling of the specimens was done using SolidWork and ANSYS software and the numerical and experimental results were compared with each other.

Various test equipment was used and different numerical methods were implemented to obtain the experimental and numerical results. The data provided information on the effect of temperatures on the static and dynamic behaviour of composite materials used in wind turbine blades.

Chapter 4

Testing and Characterization of FRP Composite Materials at Elevated Temperatures

4.1 Testing Principles of FRP Composite Specimens

Superior mechanical properties of composites materials such as high rigidity and strength-to-weight ratios, corrosion and impact resistance, damping characteristics, etc. enable them to be used in diversified fields [72, 73]. During their service life, composite structures are exposed to harsh environmental conditions such as high temperatures. The static mechanical behaviour of composite specimens under high temperatures and tensile loading can be analysed using tensile testing machines. In the present Chapter, the stress-strain behaviours of different composite materials under increasing temperatures and loadings were assessed and compared with each other. Failure behaviours of unidirectional carbon, glass and hybrid composites were determined using tensile testing in the longitudinal direction of unidirectional fibres [74, 75, 76].

ILSS (interlaminar shear strength) of composite material is one of the measures of fibre/matrix bond strength. Different testing methods are available to find the ILSS of composites. The SBS (Short Beam Shear) test with three-point bending can be used to determine ILSS. In a SBS test, low span-to-thickness ratio reduces the bending stresses and allows through-thickness shear stress. This results in inter-laminar shear failure at the mid-plane. This test can be used to measure a composite specimen's mechanical behaviour at high temperatures [77, 78, 79]. In a SBS testing, composite laminates exhibit delamination in the mid-plane of the specimens. Occasionally, because of the effects of stress concentrations as well as voids, the delamination may shift to either side of the mid-plane [80]. In this case, delamination and matrix failure could lead to a reduction in the specimen's mechanical properties [81, 82]. In the present study, SBS and DMA tests were used to determine the static and dynamic mechanical properties of unidirectional GFRP, CFRP, hybrid GFRP-CFRP and hybrid CFRP-GFRP composites until delamination in the specimens occurred or the glass transition temperature was reached. The storage modulus, loss modulus, damping properties and T_g of specimens were used to analyse the rigidity and damping behaviour of the materials. A dynamic mechanical analyser was used to measure the response of the material to applied loads under increasing temperatures.

4.2 Short Beam Shear (SBS) Test Results

Unidirectional GFRP, CFRP, hybrid GFRP-CFRP and hybrid CFRP-GFRP composite laminates were tested by a Short Beam Shear test at temperatures 25°C, 40°C and 55°C with a dwell time of 15 minutes in the oven. Inter-laminar shear strengths were obtained from the tests and compared with the results obtained at the ambient temperature.

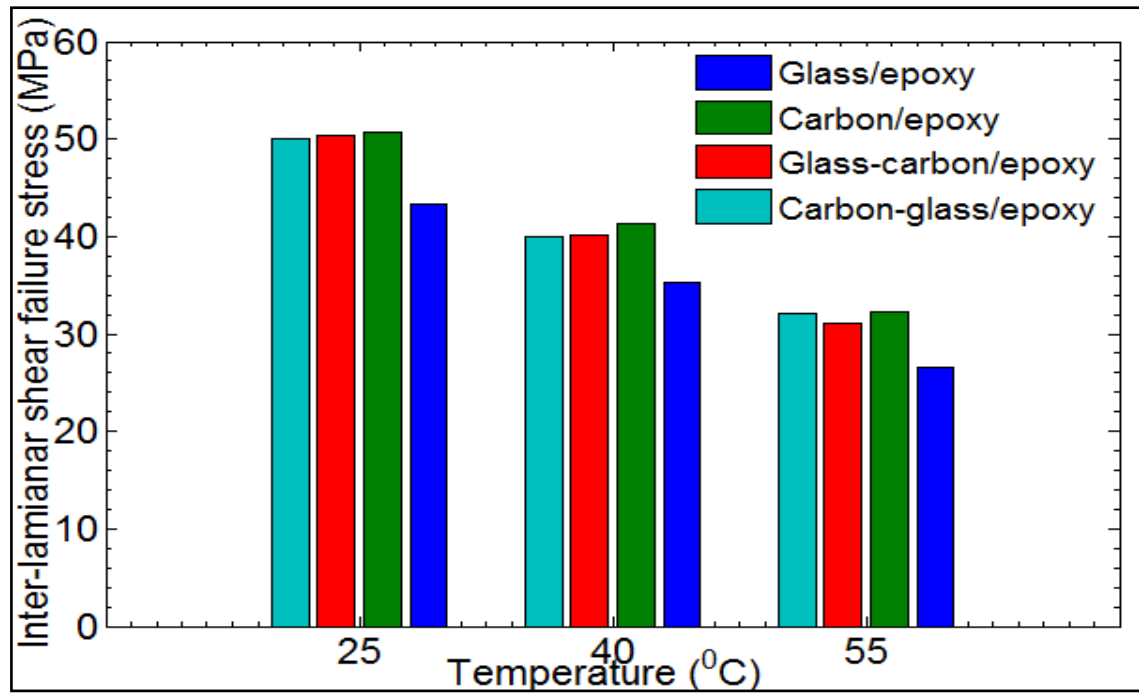


Figure 4.1 ILSS of unidirectional glass, carbon and hybrid composite laminates

As shown in Figure 4.1, the inter-laminar shear failure stresses of GFRP are lower by 18.47% and 38.70% at temperatures 40°C and 55°C, respectively, as compared to the values at the ambient temperature. The inter-laminar shear failure stress of CFRP decreased by 18.53% and 36.30% at temperatures 40°C and 55°C, respectively. Similarly, the inter-laminar shear failure stress of hybrid GFRP-CFRP composite decreased by 20.26% and 38.12%. ILSS of the hybrid CFRP-GFRP composite was lower by 20.00% and 35.96%.

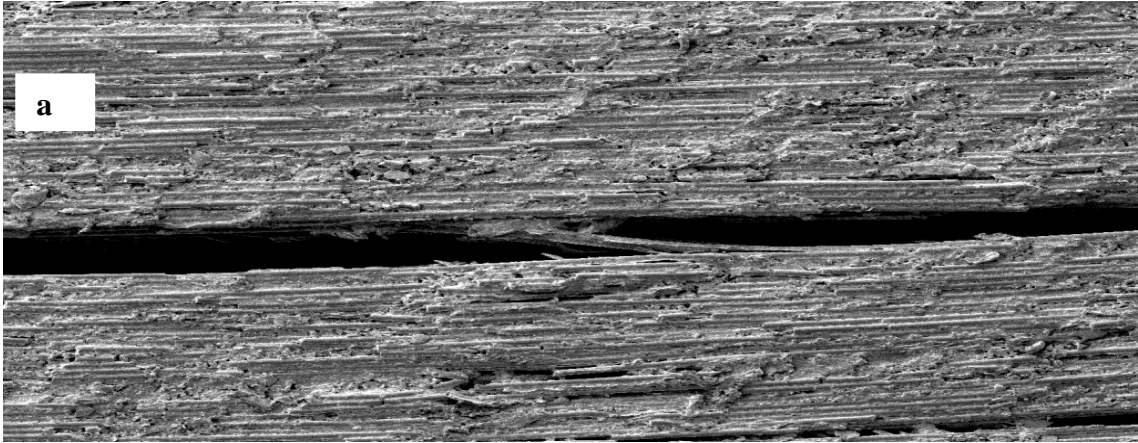
Experimental results shown in Figure 4.1 indicate that the ILSS of CFRP laminates was only slightly higher than the ILSS of hybrid composite laminates. The average ILSS values of the composite specimens and the coefficients of variation (COV) are given in Table 4.1. The coefficients of the variation of the four different specimens show that the variability in the ILSS increases as the testing temperature increases.

Testing Principles of FRP Composite Specimens

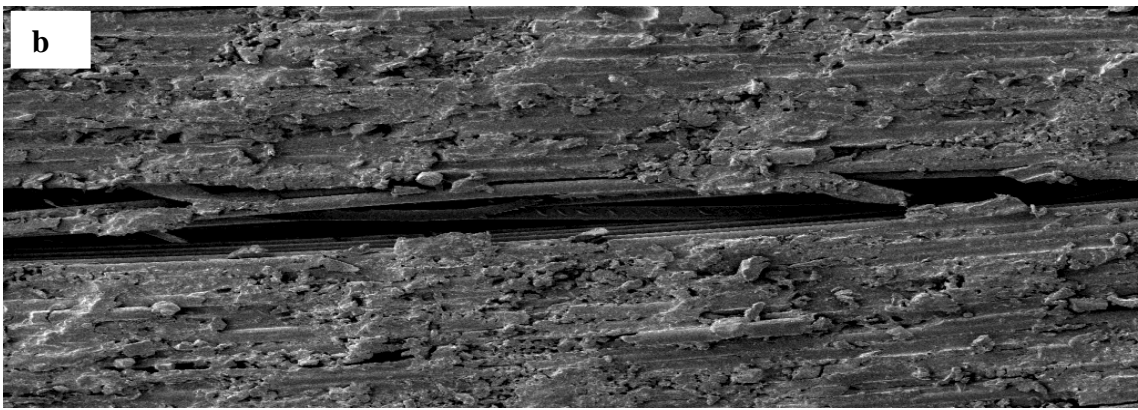
Table 4.1 The ILSS of unidirectional glass/epoxy, carbon/epoxy and hybrid/epoxy at temperatures 25°C, 40°C and 55°C measured by Short Seam Shear (SBS) tests

No	Specimen types	Temperature [°C]	Number of specimen	Average ILSS [MPa]	COV (%)
1	Glass/epoxy	25	10	43.36	2.48
2	Glass/epoxy	40	10	35.35	3.48
3	Glass/epoxy	55	10	26.58	5.16
4	Carbon/epoxy	25	10	50.77	2.73
5	Carbon/epoxy	40	10	41.36	5.60
6	Carbon/epoxy	55	10	32.34	7.16
7	Glass-carbon/epoxy	25	10	50.29	2.82
8	Glass-carbon/epoxy	40	10	40.10	5.31
9	Glass-carbon/epoxy	55	10	31.12	4.71
10	Carbon-glass/epoxy	25	10	50.00	6.18
11	Carbon-glass/epoxy	40	10	40.00	3.03
12	Carbon-glass/epoxy	55	10	32.02	3.16

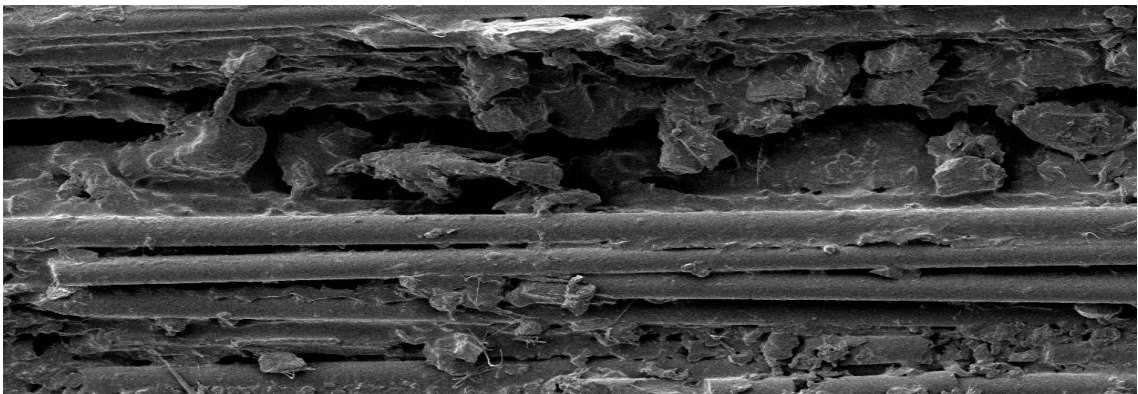
Micrographs of unidirectional failure modes of the specimens are shown in Figure 4.2 (a-c) which indicates that inter-laminar shear failure occurred with micro-cracking of the resin in the case of CFRP, GFRP and hybrid GFRP-CFRP composite laminates. Compression in the top layer and tension in the bottom layer of the specimens did not lead to the breaking of fibres during the test. Failure happens at the weak point of the resin between the plies. A strong interfacial bond between the layers makes the specimens more resistant to inter-laminar shear failure. During SBS tests, interfacial bond strengths of the composite specimens were directly related to the resistance of the specimens to shear failure. As indicated in Figure 4.2, the bond strength decreased at higher temperatures. At test temperatures of 40°C and 55°C, the experimental results indicate that composite specimens fail at a low loading rate. This may be due to susceptibility of fibre/matrix interface to degradation. Residual stresses in composite specimens cause initiation of micro-cracks in polymer resin and fiber/matrix interface which in turn leads to delamination.



(a) Unidirectional carbon/epoxy composite specimen under micro-cracking



(b) Unidirectional glass-carbon/epoxy Hybrid composite specimen under micro-cracking



(c) Unidirectional glass/epoxy composite specimen under micro-cracking

Figure 4. 2 SEM image of unidirectional delamination failure modes on FRP composite specimens.

4.2.1 Statistical Analysis of Experimental Results

As indicated above, unidirectional GFRP, CFRP, hybrids GFRP-CFRP and hybrid CFRP-GFRP composite laminates were tested to characterize the static mechanical properties, specifically, the inter-laminar shear strength at temperatures 25°C, 40°C and 55°C. Ten

experiments were conducted for each temperature for the four composite specimens, resulting in a total of 120 specimens tested.

The experimental results for the four composite specimens are shown in Table 4.1. Mean values and the coefficients of variation (COV) of the four composites are also shown in Table 4.1. The COV is the ratio of standard deviation to the mean value obtained for each test temperature. The inter-laminar shear failure stresses of the composites have coefficients of variation between 2.48% and 7.16% at the test temperatures. This might be an indication that the inter-laminar shear failure stresses are affected by the increase in the test temperatures.

The three distributions, afore mentioned, were selected for statistical modelling of the experimental results. Parameters for normal, log-normal and Weibull distributions are shown in Table 4.2.

Table 4. 2 Distribution parameters for ILSS [MPa] at temperatures 25°C, 40°C and 55°C.

No	Specimen types	Temperature [°C]	Normal		Log-normal		Weibull	
			μ	σ	μ of ln	σ of ln	η	σ
1	Glass/epoxy	25	43.37	1.08	3.77	0.027	44.62	43.93
2	Glass/epoxy	40	35.35	1.23	3.58	0.040	29.27	36.53
3	Glass/epoxy	55	26.58	1.37	3.29	0.055	21.67	27.58
4	Carbon/epoxy	25	50.77	1.39	3.94	0.035	33.66	52.13
5	Carbon/epoxy	40	41.36	2.32	3.71	0.079	14.95	42.36
6	Carbon/epoxy	55	32.35	1.23	3.50	0.047	25.13	33.75
7	Glass-carbon/epoxy	25	50.29	1.42	3.92	0.035	33.91	51.30
8	Glass-carbon /epoxy	40	40.11	2.13	3.70	0.064	18.44	41.61
9	Glass-carbon /epoxy	55	31.12	1.47	3.47	0.059	19.93	32.94
10	Carbon-glass /epoxy	25	49.92	3.09	3.92	0.071	16.81	50.49
11	Carbon-glass /epoxy	40	39.79	1.21	3.69	0.036	33.29	40.04
12	Carbon-glass /epoxy	55	35.54	1.12	3.58	0.039	30.07	35.82

To determine the validity of statistical distributions, a chi-square test is applied. Chi-square test results are shown in Table 4.3 which indicate that statistical distributions cannot be rejected at 5% significant level. In Table 4.3, a chi-square probability analysis result that fits better in each test temperature, is underlined. An estimate of correlation between experimental and theoretical data is computed from cumulative distribution

functions of normal, log-normal and Weibull distributions as shown in Table 4.4. The coefficients in Table 4.4 measure the linear correlation between the experimental and theoretical results.

Table 4.3 Chi-square test results

No	Specimen types	Temperature [°C]	Normal	Log-normal	Weibull
1	Glass/epoxy	25	0.896	<u>0.904</u>	0.852
2	Glass/epoxy	40	0.095	<u>0.407</u>	0.102
3	Glass/epoxy	55	<u>0.368</u>	0.326	0.157
4	Carbon/epoxy	25	0.182	<u>0.273</u>	0.144
5	Carbon/epoxy	40	<u>0.926</u>	0.602	0.705
6	Carbon/epoxy	55	0.073	<u>0.297</u>	0.115
7	Glass-carbon/epoxy	25	<u>0.684</u>	0.641	0.454
8	Glass-carbon/epoxy	40	0.886	<u>0.897</u>	0.697
9	Glass-carbon/epoxy	55	<u>0.556</u>	0.270	0.063
10	Carbon-glass/epoxy	25	0.681	0.943	<u>0.961</u>
11	Carbon-glass/epoxy	40	0.923	<u>0.958</u>	0.956
12	Carbon-glass/epoxy	55	0.681	0.943	<u>0.961</u>

Table 4.4 R-square values (Experimental data vs fitted responses)

No	Specimen types	Temperature [°C]	Normal	Log-normal	Weibull
1	Glass/epoxy	25	0.966	0.970	0.979
2	Glass/epoxy	40	0.868	0.894	0.841
3	Glass/epoxy	55	0.926	0.934	0.930
4	Carbon/epoxy	25	0.917	0.928	0.869
5	Carbon/epoxy	40	0.974	0.939	0.964
6	Carbon/epoxy	55	0.969	0.912	0.851
7	Glass-carbon/epoxy	25	0.950	0.961	0.957
8	Glass-carbon/epoxy	40	0.971	0.975	0.954
9	Glass-carbon/epoxy	55	0.942	0.858	0.843
10	Carbon-glass/epoxy	25	0.968	0.998	0.968
11	Carbon-glass/epoxy	40	0.990	0.987	0.960
12	Carbon-glass/epoxy	55	0.993	0.994	0.991

Comparisons of experimental and theoretical Cumulative Distributions Functions (CDF) for inter-laminar shear failure strengths are shown in Figures 4.3-4.6. Figure 4.3

shows CDF being plotted against inter-laminar shear strength for glass/epoxy specimens. Experimental values and theoretical cumulative distribution functions of normal, lognormal and Weibull distributions are shown in Fig. 4.3. A comparison of fits with experimental data, at temperatures 25°C and 40°C indicates that log-normal distribution was the best fit for the ILSS of the glass/epoxy specimens. Even though the normal and Weibull distributions do not match as well as the log-normal distribution with the test data, these distributions cannot be rejected at 5% significant level. For the test temperature of 55°C, the experimental data fits best with the normal distribution. The log-normal and Weibull distributions are also close to the experimental data.

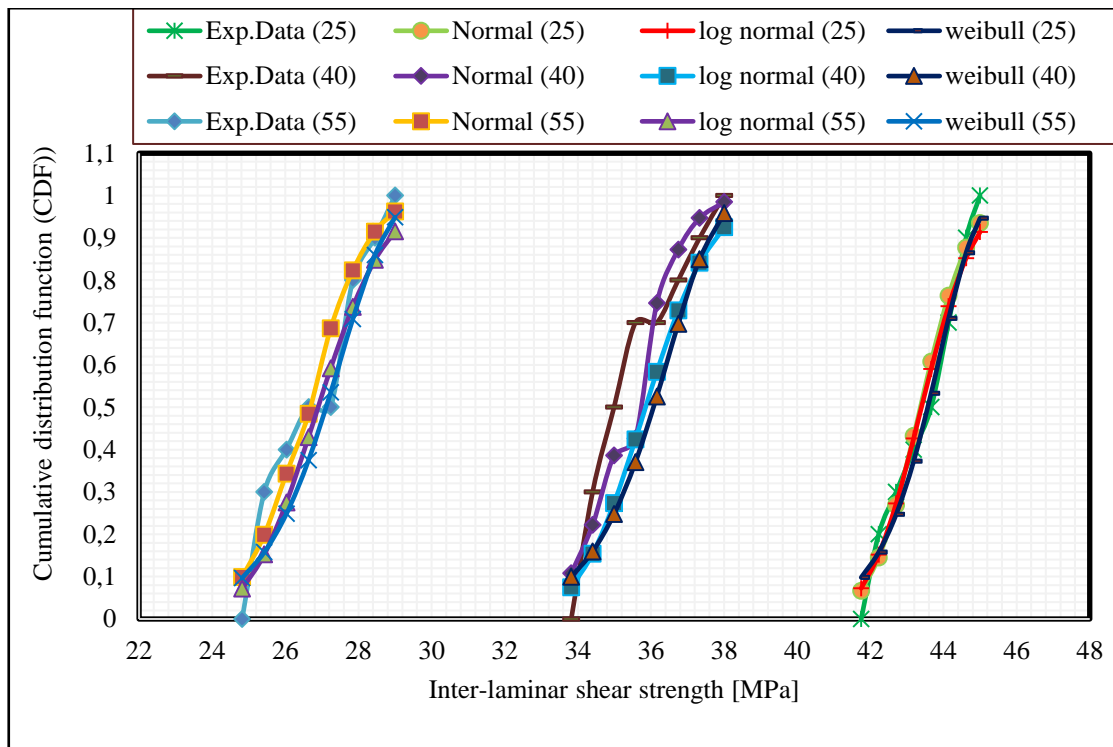


Figure 4.3 Comparison of experimental and theoretical results for inter-laminar shear strength of glass/epoxy specimens

Corresponding results for unidirectional CFRP specimens are shown in Figure 4.4. Comparisons of fits with the experimental data at temperatures 25°C and 55°C show that the log-normal distribution was the best fit for these cases. For the test temperature of 40°C, the best fit is given by the normal distribution. All distributions in the curves were also valid for the null hypothesis.

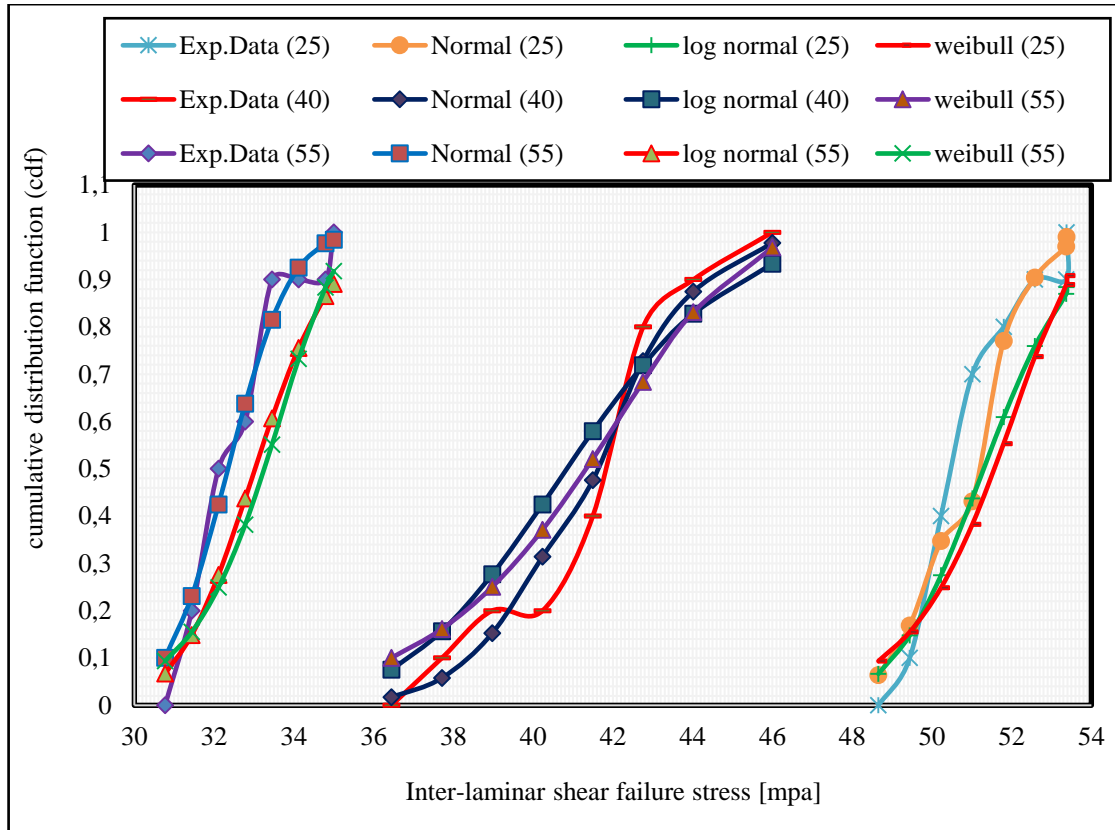


Figure 4.4 Comparison of experimental and theoretical results for inter-laminar shear strength for carbon/epoxy specimens

Corresponding results for hybrid GFRP-CFRP composite laminates are shown in Figure 4.5. For this case, the normal distribution gives the best fit with the experimental data at the test temperatures of 25°C and 55°C. Log-normal and Weibull distributions do not follow the experimental data closely, but they cannot be rejected at 5% significant level. For the test temperature of 40°C, the experimental data fits best with the log-normal distribution. The normal and Weibull distributions are also valid for the null hypothesis.

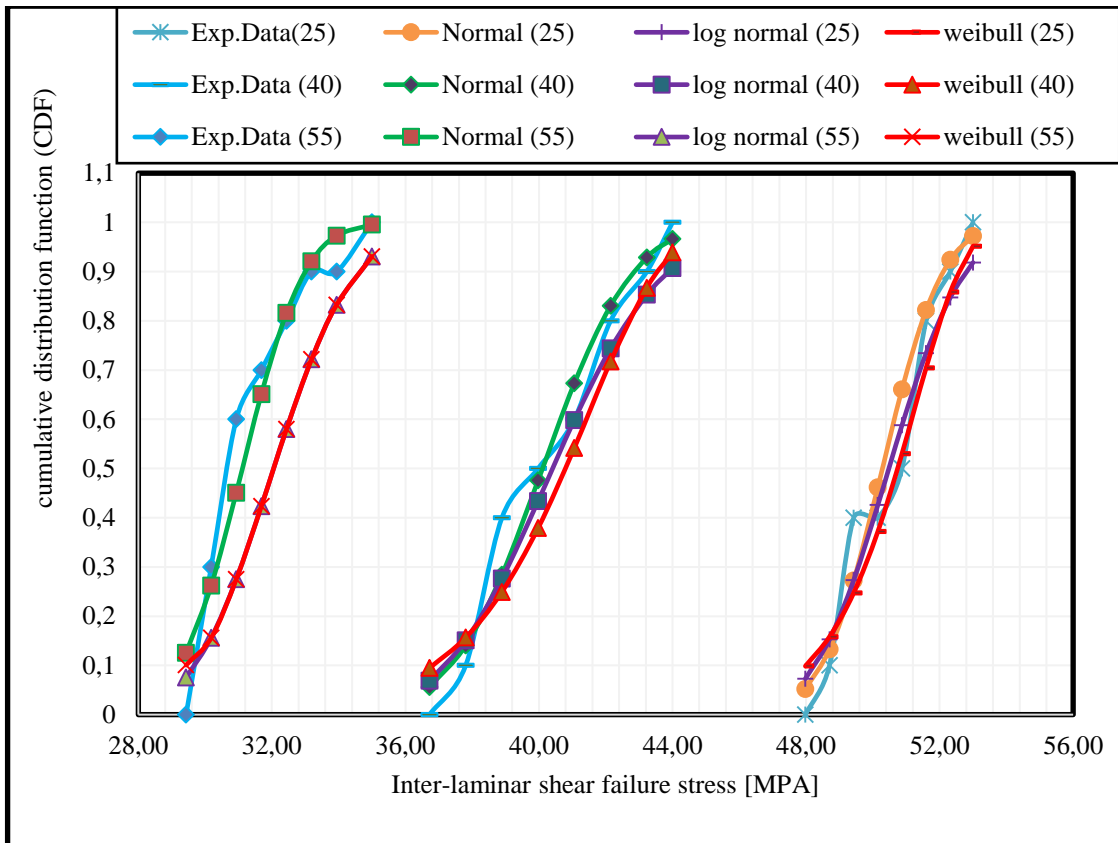


Figure 4.5 Comparison of experimental and theoretical results for inter-laminar shear strength for hybrid glass-carbon/epoxy specimens.

Corresponding results for hybrid CFRP-GFRP specimens are shown in Figure 4.6. A comparison of fits with the experimental data at temperatures 25°C and 40°C indicates that Weibull distribution is the best fit for ILSS of the specimens for this case. Even though normal and log-normal distributions do not follow the test data closely, they cannot be rejected at 5% significant level. For the test temperature of 55°C, the experimental data fits best with the log-normal distribution. The normal and Weibull distributions are also close to the experimental data.

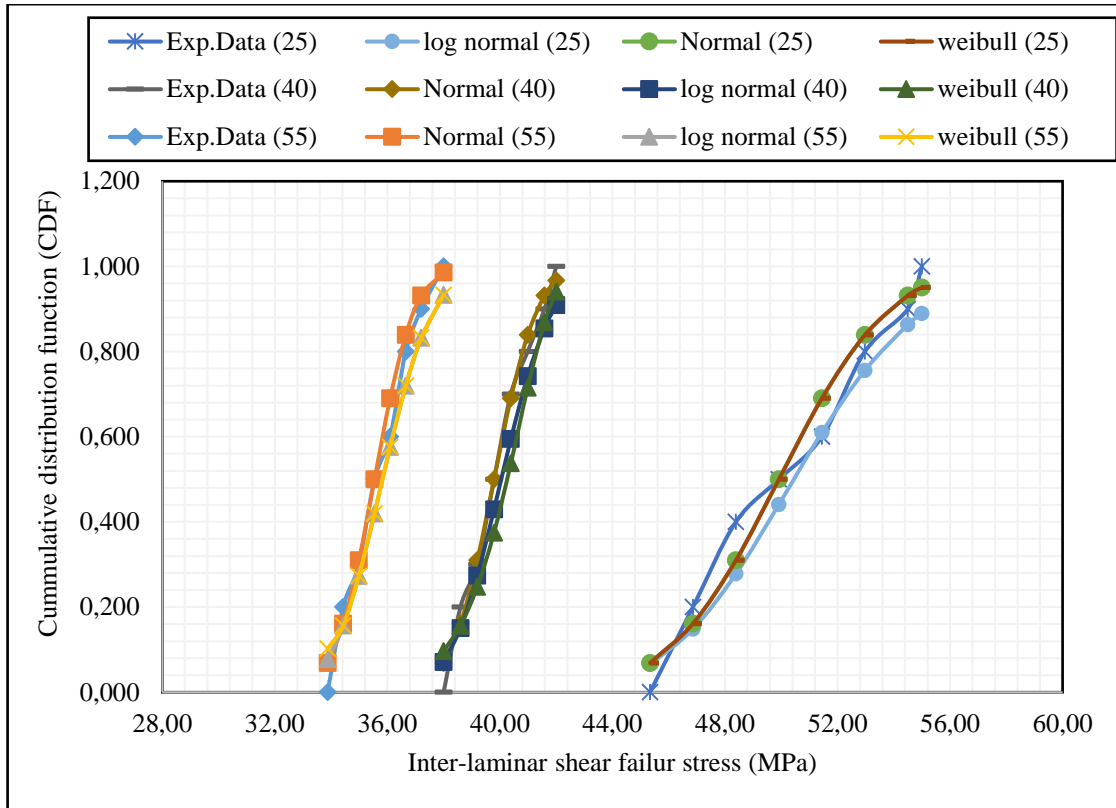


Figure 4.6 Comparison of experimental and theoretical results for inter-laminar shear strength for hybrid carbon-glass/epoxy specimens

The impact of elevated temperatures on ILSS for unidirectional GFRP, CFRP, GFRP-CFRP and CFRP-GFRP composite laminates were investigated at temperatures 25°C, 40°C and 55°C using the three-point SBS tests. Micro-cracks in the matrix were examined with a Scanning Electronic Microscope (SEM). Different failure modes were studied by SEM in different materials. It was observed that variations in ILSS largely depend on the level of bonding at the fibre/matrix interface. Plastic deformation of matrix was observed as the temperatures approached T_g of the polymeric resin.

4.3 Dynamic Mechanical Analysis (DMA) Test Results

Dynamic mechanical behaviour of composite specimens was studied at high temperatures based on ASTM standards. The studies included storage modulus (E'), loss modulus, (E'') loss factor ($\tan \delta$) and glass transition temperature (T_g) of composite materials. A knowledge of the behaviour of FRP composites, subject to harsh environmental conditions, is essential to design composite structures such as wind turbine blades. One of the main parameters that define the behaviour of polymer composites is T_g . Glass transition temperature T_g plays an important role in the strength of the bond between the

Dynamic Mechanical Analysis (DMA) Test Results

fibres and the matrix material. Experimental results obtained from DMA tests are useful to estimate the service life of composite structures working in higher temperature conditions.

The strength of FRP composites are affected by different factors such as fibre arrangement, fibre type and fibre-matrix bond. Dynamic mechanical analysis provides information on the viscoelastic properties of composites. Dynamic tests are used to analyse the glass transition and the relaxation of the matrix resin. Amorphous polymers have different glass transition temperatures denoted by T_g and above T_g the material changes to a rubbery state and the stiffness drops dramatically with increasing viscosity.

Storage modulus (E') is used to determine the load bearing capacity of fibre reinforced polymer composites at high temperatures. The values of the storage modulus for different composite specimens are shown in Figure 4.7. Glass transition temperatures (T_g), storage modulus (E') and the loss modulus (E'') values of composite laminates are shown in Table 4.5. Change in the dynamic storage modulus occurs due to the increase in the temperature which causes changes in the behaviour of the polymer matrix and fibre/matrix interface. There is a sharp drop in E' of the four FRP composite specimens as the test temperature approaches the glass transition temperature. This may happen because of the increase in the molecular mobility of polymer chains due to higher temperatures.

For CFRP composite specimens, a drop in storage modulus occurred at a glass transition temperature of 59.07°C. Similarly, a drop in storage modulus of GFRP, hybrid GFRP-CFRP and hybrid CFRP-GFRP composite laminates occurred at temperatures 63.17°C, 54°C and 64.36°, respectively. For composite structural designs, the storage modulus should be nearly constant and the range in which the storage modulus is constant is called the functional range of the material. For carbon/epoxy composite specimens, the functional range is up to a temperature of 40°C. After that, the storage modulus begins to increase and drops quickly once the temperature exceeds T_g .

Dynamic Mechanical Analysis (DMA) Test Results

GFRP and hybrid composite laminates reached the end of the functional range approximately at temperatures 57°C and 59°C, respectively. The storage moduli of hybrid CFRP-GFRP and CFRP composites were similar and the storage modulus of the hybrid CFRP-GFRP composite was higher. The data in Table 4.5 shows the differences in the viscoelastic behaviour of the composite specimens with increasing temperature.

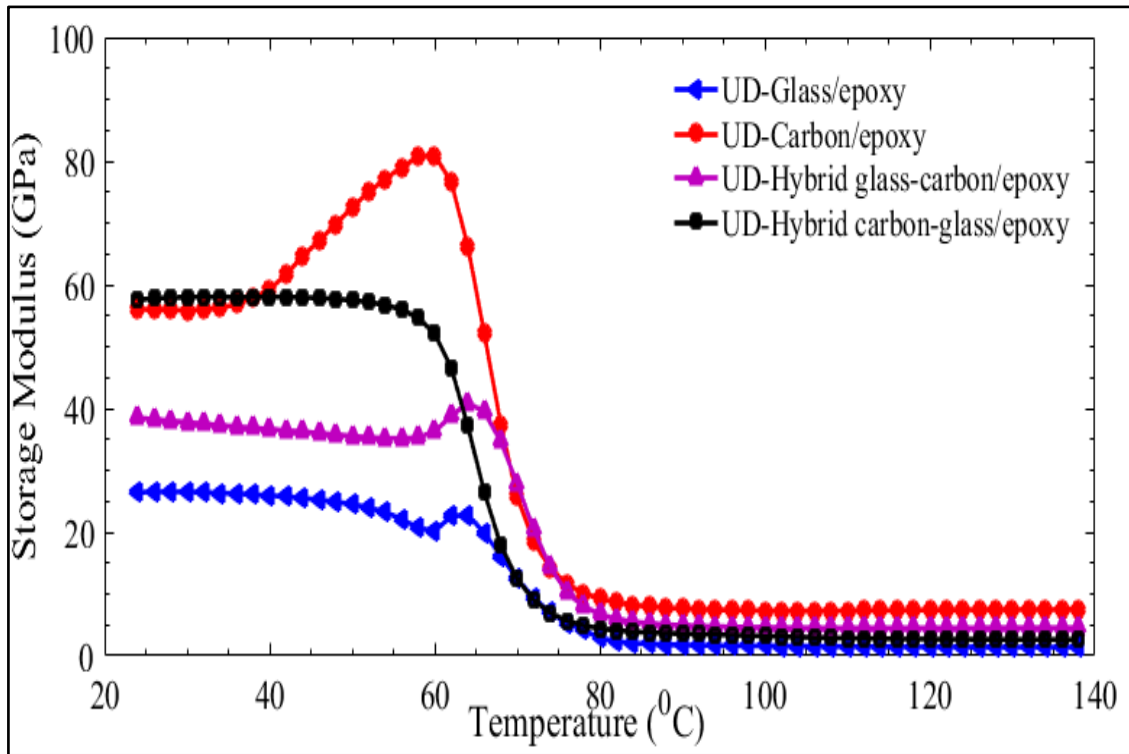


Figure 4.7 Storage modulus vs. temperature for glass/epoxy, carbon/epoxy and hybrid specimens

Loss modulus is used to determine the lost or dissipated energy per cycle in viscoelastic materials exhibiting a combination of elastic and viscoelastic behaviours under dynamic loads. Figure 4.8 shows the curves of loss moduli plotted against temperature for GFRP, CFRP, hybrid GFRP-CFRP and hybrid CFRP-GFRP composites. The maximum loss modulus occurs at T_g of the polymer matrix and these values are shown in Table 4.5. The higher loss modulus at T_g could be due to the increase in the internal friction which increases the dissipation of energy.

Maximum loss modulus for hybrid GFRP-CFRP composites is at the temperature of 71.27°C. For GFRP, CFRP and hybrid CFRP-GFRP composites, highest loss moduli are at temperatures 67.52°C, 66.69°C and 66°C, respectively. The maximum loss moduli values for hybrid composites lie between those of the CFRP and GFRP composites.

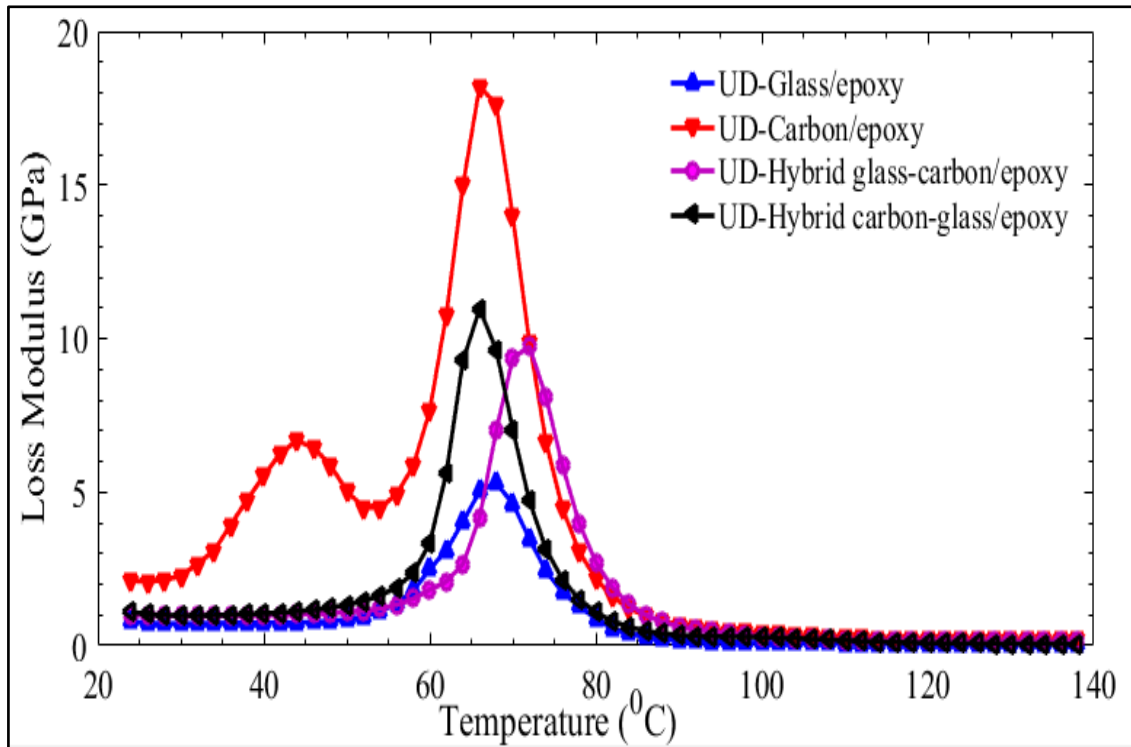


Figure 4.8 Loss modulus vs. temperature for glass/epoxy, carbon/epoxy and hybrid specimens

Loss factor ($\tan \delta$) is the ratio of E' / E'' . Figure 4.9 shows the loss factors for GFRP, CFRP, hybrid GFRP-CFRP and hybrid CFRP-GFRP composites as a function of the temperature.

As shown in the graph, loss factor increases as temperature increases, and the maximum damping values are at the temperature T_g . After this value, loss factors decrease as the rubbery region is approached. At temperatures below T_g , the chain segments of the polymeric resin are in a frozen state and damping values are low. Hence, the deformations are elastic and the molecular viscous flows are low. In the transition area, because of the initiation of the molecular chain segments and stress relaxation, damping values are high. However, in the rubbery region, the molecular chain segment is able to undergo a change and the damping values become minimum. Peak values of the loss factors are typical values for FRP composites used in structural applications. The loss factor ($\tan \delta$) for hybrid GFRP-CFRP composites was the highest compared to CFRP and GFRP composite specimens.

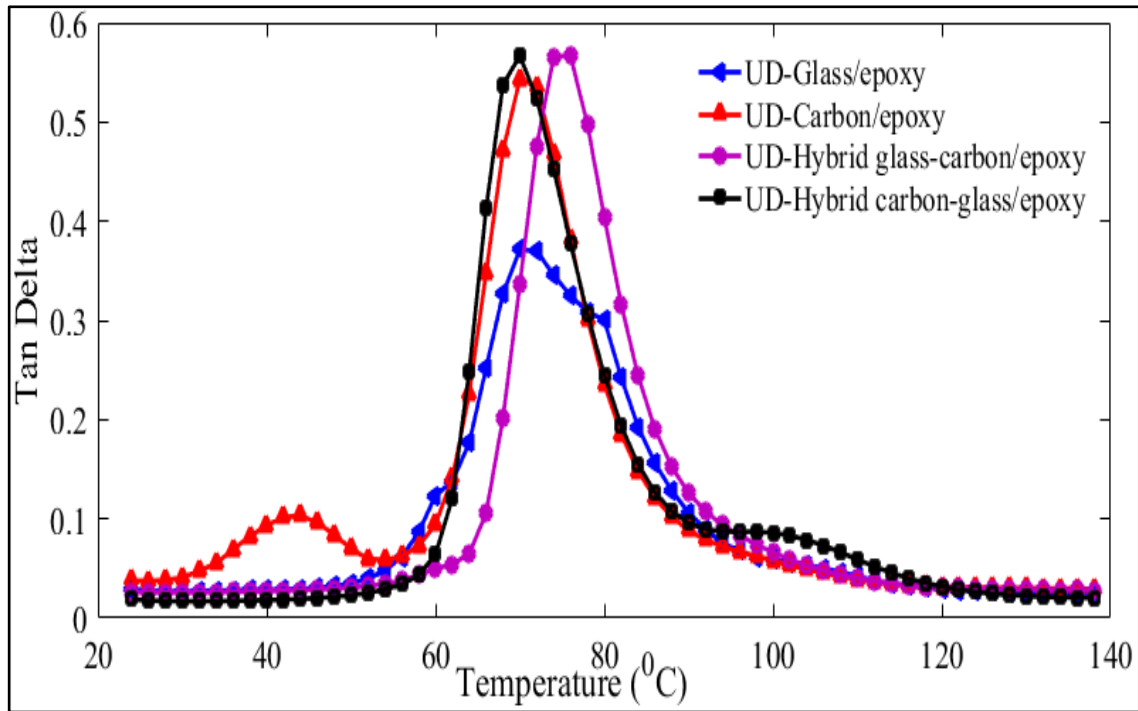


Figure 4.9 Loss factor vs. temperature for glass/epoxy, carbon/epoxy and hybrid specimens

Table 4.5 Storage modulus, loss modulus and T_g of GFRP, CFRP, hybrid GFRP-CFRP and CFRP-GFRP specimens

Specimen	Storage modulus [GPa]	Loss Modulus [GPa]	largest height of $\text{Tan } \delta$ curve	T_g from $\text{Tan } \delta$ [$^{\circ}\text{C}$]	T_g from E'_{max} [$^{\circ}\text{C}$]	T_g from E''_{max} [$^{\circ}\text{C}$]
Carbon/epoxy	80.925	18.20	0.5356	70.77	59.07	66.69
Glass/epoxy	22.823	5.29	0.3701	70.97	63.17	67.52
Glass-carbon/epoxy	40.933	9.74	0.5669	75.04	64.36	71.27
Carbon-glass/epoxy	56.744	10.96	0.5667	70.00	54.00	66.00

Figure 4.10 shows Cole-Cole graphs for unidirectional GFRP, CFRP, hybrid GFRP-CFRP and hybrid CFRP-GFRP composites. E' is plotted against the E'' to measure the viscoelastic behaviour of the specimens. Cole-Cole plots for polymeric materials are nearly semi-circular curves. It helps to determine the molecular relaxation behaviour with temperature variation and, more specifically, the linear viscoelastic properties of polymers in the vicinity of the glass transition region. It shows that the hybrid specimens have strong fibre/matrix interfacial bonds. It is observed from Figure 4.10 that the Cole-Cole graph of hybrid CFRP-GFRP composites is close to that of carbon/epoxy composite

specimens. Dynamic mechanical analysis (DMA) test results show that CFRP composites have a higher dynamic storage modulus, loss modulus and lesser loss factor compared to the hybrid composite specimens. However, hybrid composites could be a better alternative when vibration and noise control are important factors.

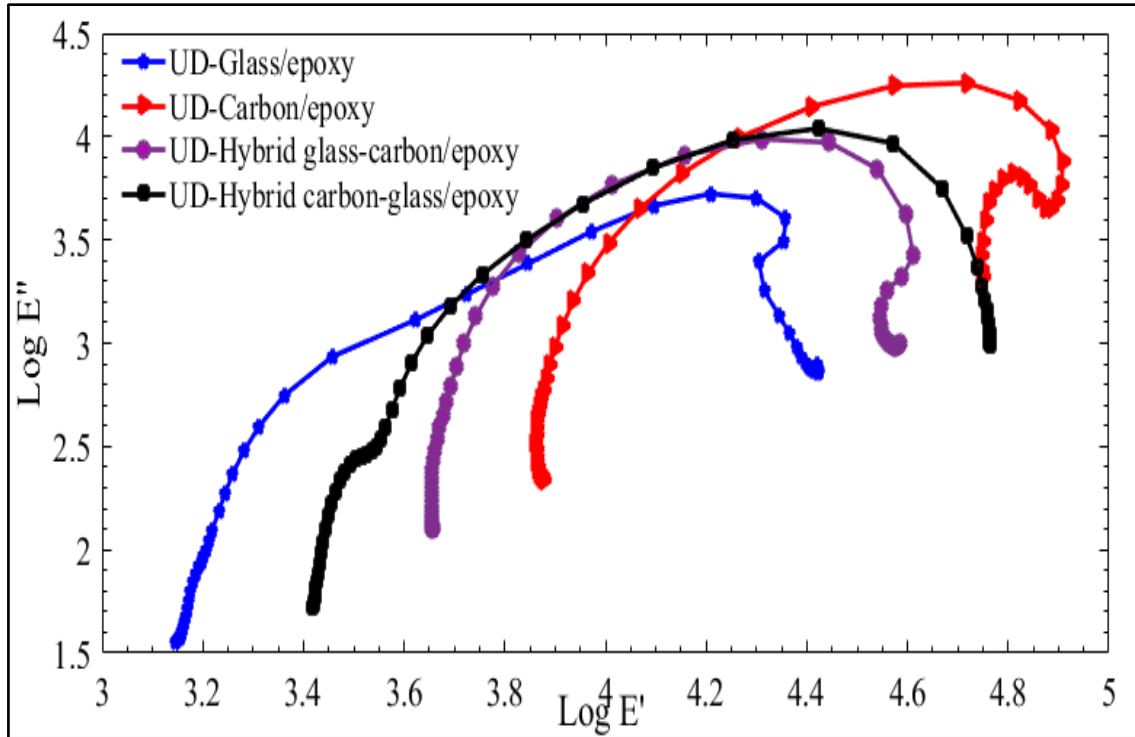


Figure 4.10 Cole-Cole graphs of GFRP, CFRP and hybrid composite specimens

The viscoelastic behaviours of composite specimens are investigated by Dynamic Mechanical Analysis (DMA). Results showed that the suitable operating range of unidirectional CFRP composite was up to 40°C and after that the storage modulus of the specimen became nonlinear. However, storage modulus of hybrid GFRP-CFRP composite laminates was nearly constant up to 59°C. Moreover, T_g and damping behaviours of hybrids were better than those of CFRP laminates. Experimental results on the static and dynamic behaviour of hybrid composites indicated that they may be more suitable for wind turbine blade structures because of high damping properties and high ILSS values before the temperature reaches the glass transition temperature. Vibration and noise are critical issues for the design of wind turbine blades and high damping ratios are desirable to counter these problems.

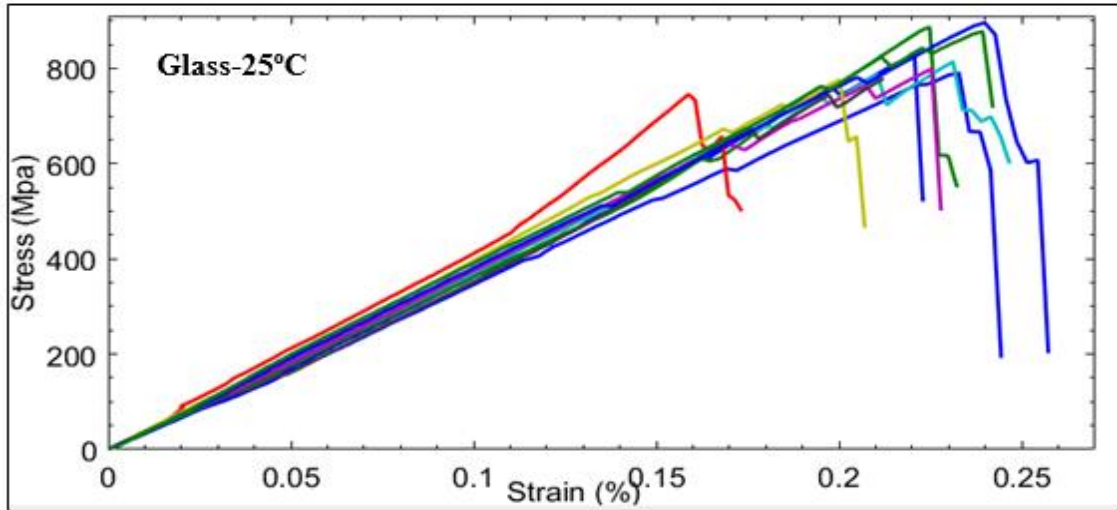
4.4 Principles of Tensile Strength Testing and Results

Failure of unidirectional fibre reinforced polymer composite material is a complex phenomenon. Initially all fibres are intact and capable of carrying applied loads. The following parameters are important for load transfer to fibres:- strength, bondage at the fibre/matrix interface. Fibre volume ratio, matrix cracking and regularity of fibre spacing. As the applied load increases, the weakest fibres will eventually fail. The loads released by broken fibres are transferred to other fibres and possibly to the matrix. The resulting stress concentrations increase and this leads to the development of clusters of broken fibres. At some point the composite structures as a whole becomes unable to carry the load and the structure failure occurs [83] [84] [85] [86] [87] [88].

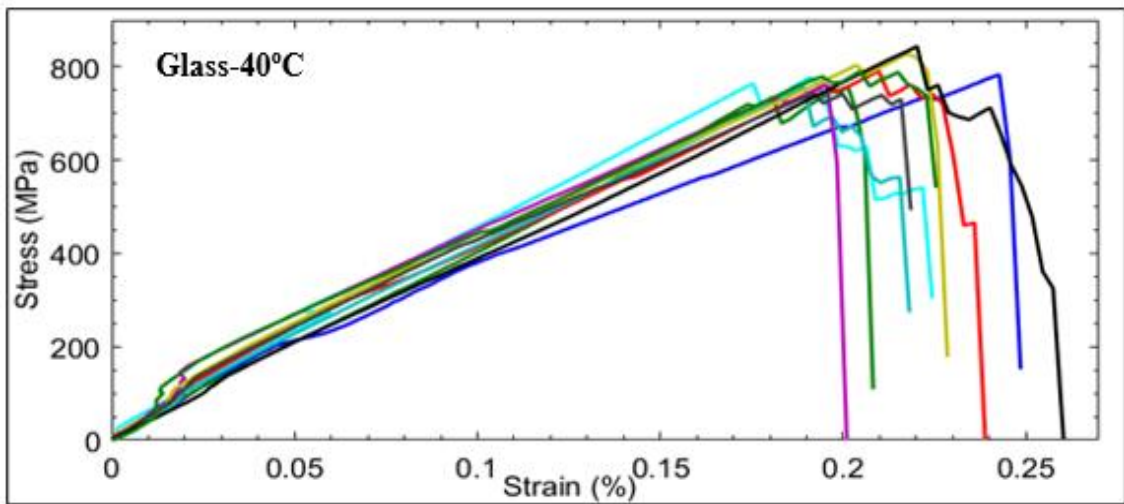
Hybridization using two materials can influence the fibre failure process due to the changes in stress concentrations and stress recovery at broken fibres. This is due to the difference in neighbouring fibres which have different stiffness properties [89] [90]. The properties of fibre-reinforced composites depend on the stability of the interfacial region between the fibre and the matrix. When this interface is intact, the matrix plays a significant role in determining the magnitude of stress concentration in nearby fibres. Finite Element Methods (FEM) can be used to find the stress distribution around fibres [91]. The matrix-to-fibre stress transfer is an important issue for fibre composite materials. The strength of these composites depends on the load-bearing ability of the fibre, strength of fibre-matrix interface and mechanical properties of the matrix [92] [93].

Epoxy resins have been used extensively in the design of wind turbine blades due to their mechanical properties and their high glass transition temperature. In composite structures, there is a high variation in the mechanical properties of the fibre and the matrix. Moreover, the yield behaviour of the viscoelastic matrix material is highly dependent on the temperature. Therefore, it is essential to investigate the stress-strain behaviour of fibre reinforced polymer composites under elevated temperatures.

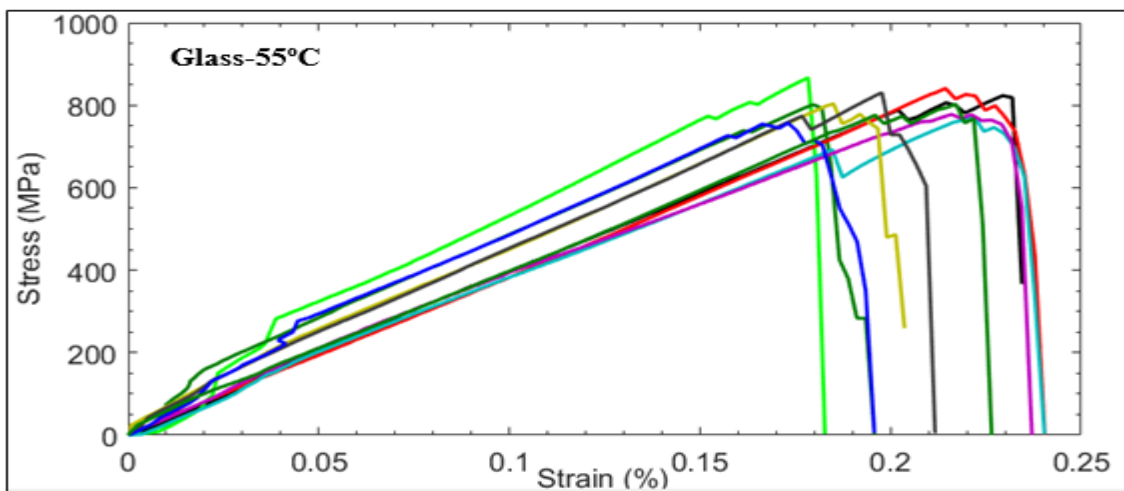
Figure 4.11 shows the stress-strain curves of unidirectional glass/epoxy composites at temperatures 25°C, 40°C and 55°C. The stress-strain curves show a linear elastic range behaviour up to a specific strain value. This is followed by non-linear behaviour, stiffness loss and finally failure. The slope of stress-strain curves decreases after the yield point and the specimen fails gradually after reaching the maximum stress.



(a) Stress vs. strain curves of glass/epoxy specimens at temperature 25°C



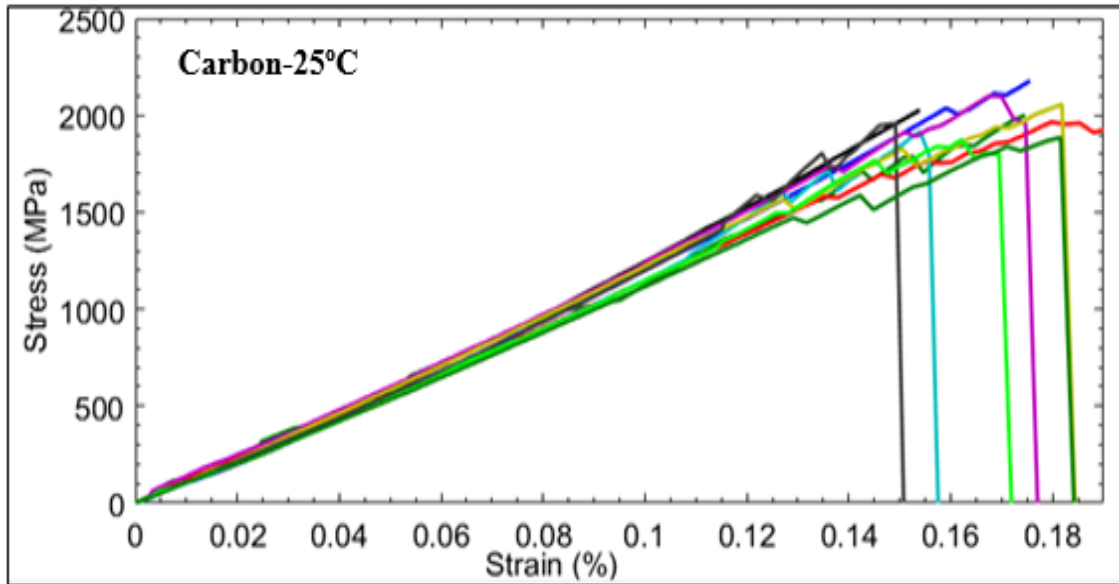
(b) Stress vs. strain curves of glass/epoxy specimens at temperature 40°C.



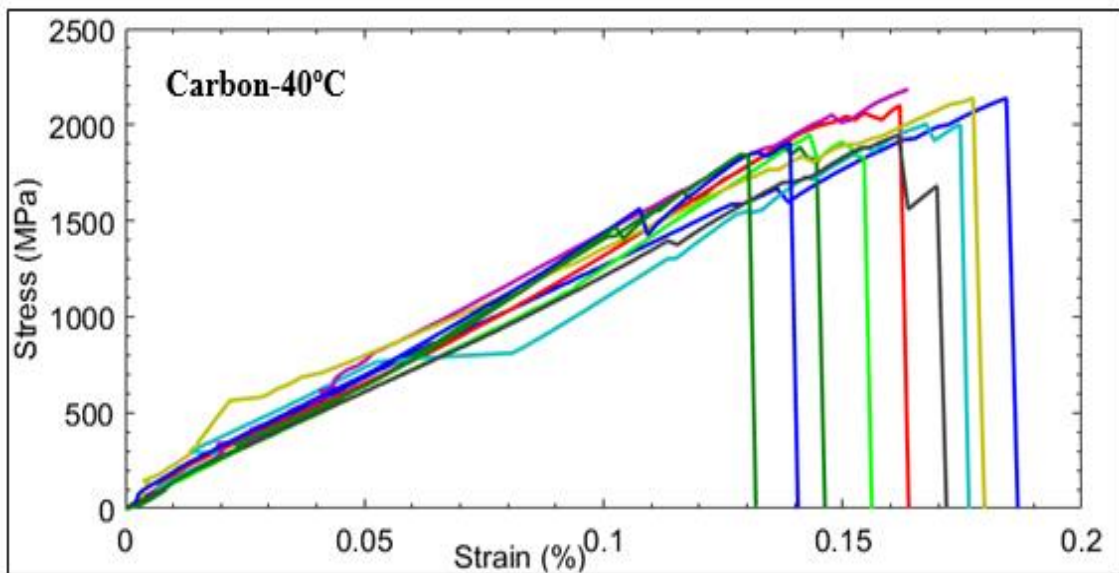
(c) Stress vs. strain curves of glass/epoxy specimens at temperature 55°C.

Figure 4.11 Stress vs strain curves of glass/epoxy specimens at various temperatures.

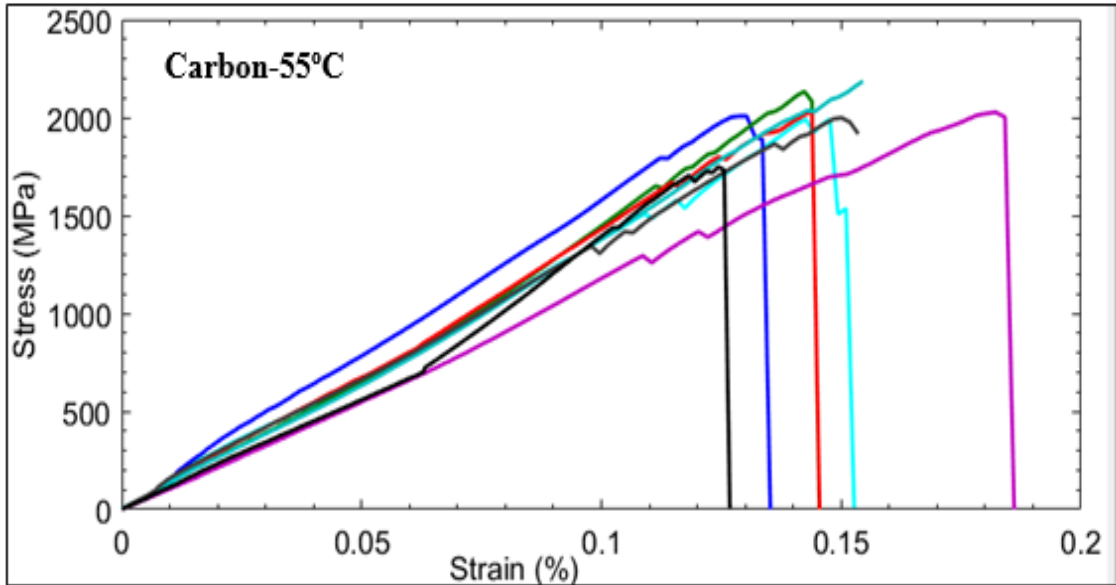
Figure 4.12 shows stress-strain curves for CFRP specimens at different temperatures. The slope of stress-strain curves of carbon/epoxy specimen exhibits a linear elastic behaviour until catastrophic failure occurs and the tensile strength difference is less than 1.7% at various temperatures.



(a) The stress vs. strain curves of carbon/epoxy specimens at temperature 25°C.



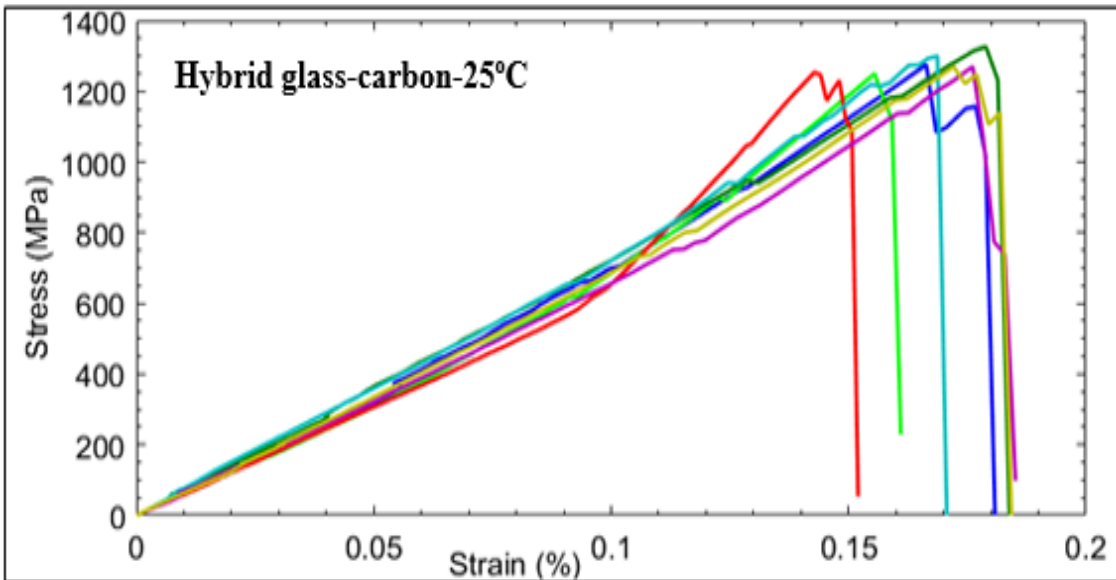
(b) The stress vs. strain curves of carbon/epoxy specimens at temperature 40°C.



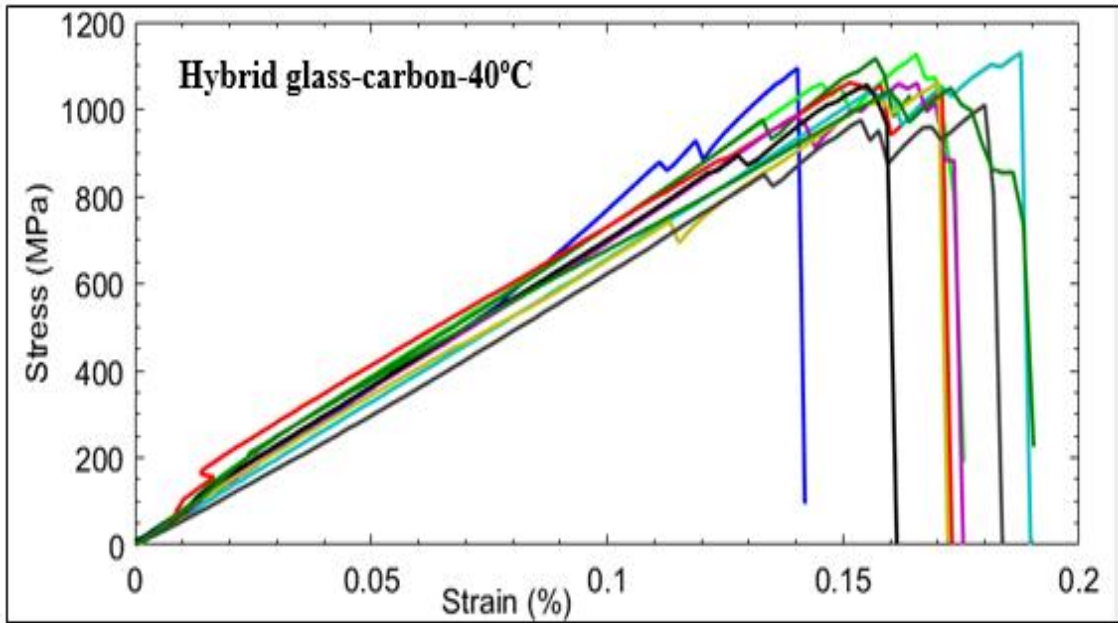
(c) The stress vs. strain curves of carbon/epoxy specimens at temperature 55°C

Figure 4.12 Stress vs. strain curves of carbon/epoxy specimens at various temperatures

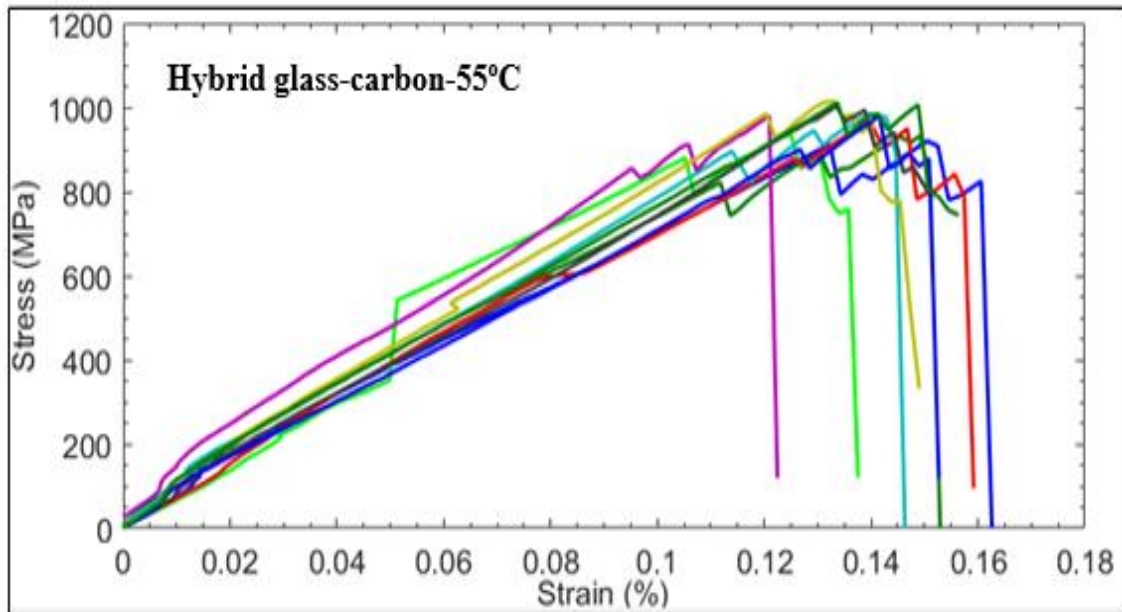
Figure 4.13 shows the stress-strain curves of hybrid glass-carbon specimens. In this case failure behaviour is ductile rather than brittle. The tensile strength of the specimen decreases as the temperature increases. This may be due to the stiffness difference between the two fibres.



(a) The stress vs. strain curves of hybrid glass/carbon specimens at temperature 25°C.



(b) The stress vs. strain curves of hybrid glass/carbon specimens at temperature 40°C.



(c) The stress vs. strain curves of hybrid glass/carbon specimens at temperature 55°C.

Figure 4.13. Stress vs. strain curves of hybrid glass/carbon specimens at various temperatures

Average tensile strengths of the three composite laminates are shown in Figure 4.14. Coefficients of variation of the composite laminates are shown in Table 4.6. It is observed that the tensile strength of GFRP specimen was the smallest at temperature 40°C. This may have happened due to thickness difference or formation of voids in the panels during

the vacuum infusion manufacturing process. The changes in tensile strengths of carbon/epoxy and glass/epoxy are minimal (approximately 4%).

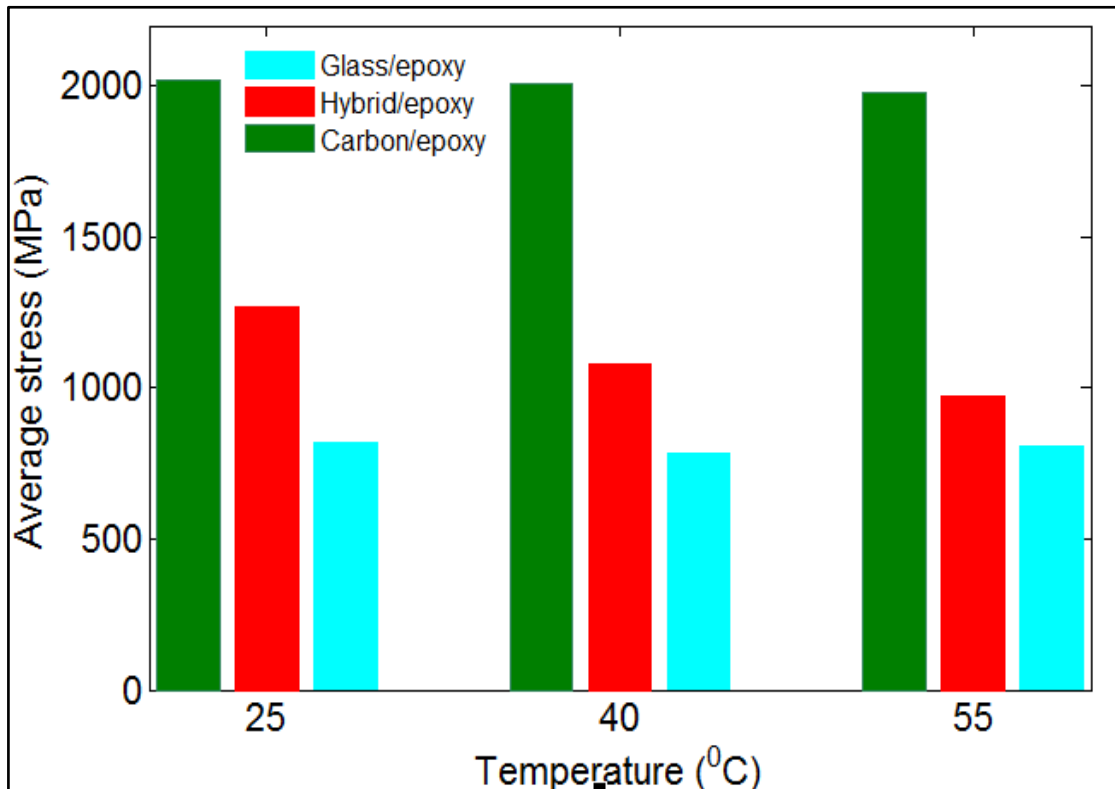
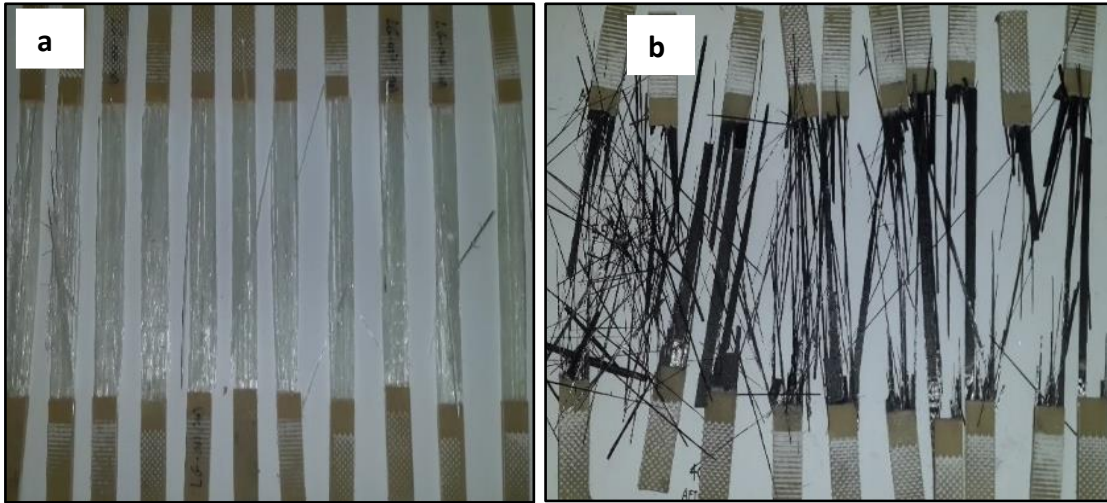


Figure 4.14 Average experimental tensile strength vs. temperature

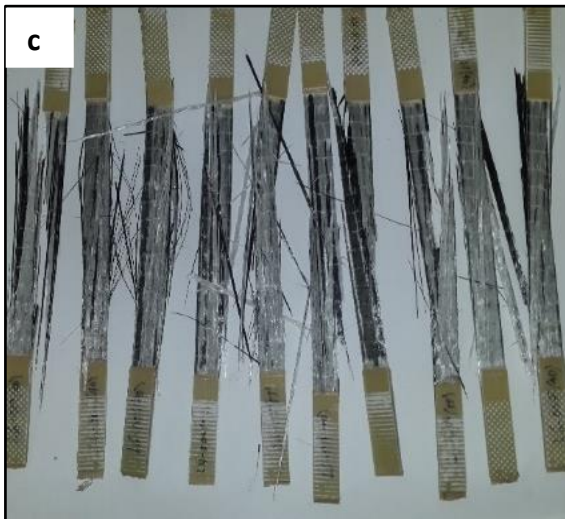
The comparison of failure strains indicates that glass/epoxy specimens have the highest failure strains compared to other composites. Carbon fibre/epoxy specimens have the lowest failure strains and the failure is brittle. The low failure strain of carbon/epoxy makes it unsuitable to be used in the wind turbine blade manufacturing. The failure strain of composite specimens can be increased by using hybrids of two different composites as shown in Figure 4.14(a-c). The hybrid specimens made by a vacuum infusion process satisfied the failure criteria stipulated by the ASTM D3039 standard. The failure region of the failed specimens is shown in Figure 4.15 (a-c). Specimens did not fail by shear or by the debonding of fibres at the interface between the laminate and tab.

Figure 4.15 (a-c) illustrates different failure types of the three composite specimens. An experimental study helps to investigate the types of failure modes which can happen if the wind turbine blades are manufactured out of unidirectional carbon, glass or a hybrid of the two. Figure 4.16 shows fibre fracture and debonding which occurred under tensile testing. There was a high dispersion in the failure stress levels of carbon/epoxy specimens.



(a) Unidirectional glass/epoxy

(b) Unidirectional carbon/epoxy

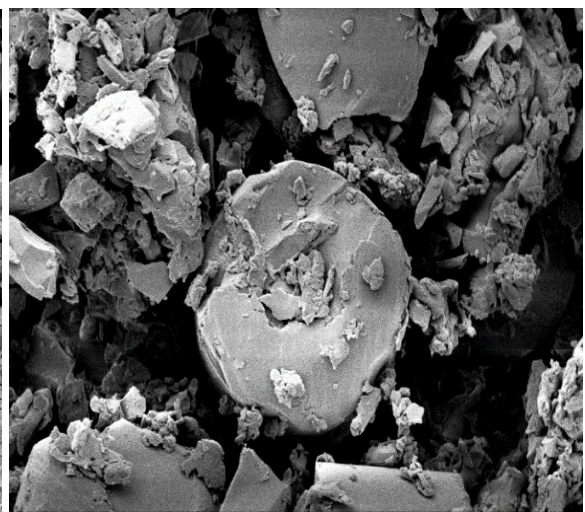


(c) Unidirectional hybrid glass-carbon/epoxy

Figure 4.15 Failure specimens collected after testing of the three composite specimens



(a)



(b)

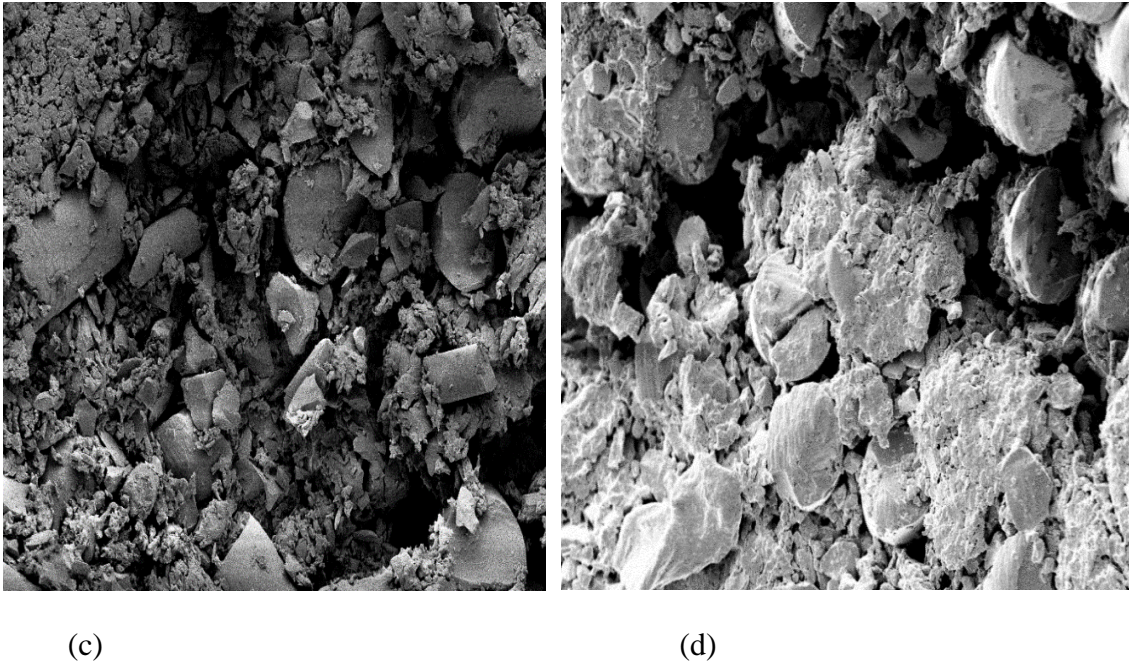


Figure 4.16 SEM image of composite specimens after failure (a) carbon/epoxy (b) glass/epoxy (c) carbon fibre in hybrid/epoxy (d) glass fibre in hybrid/epoxy

Table 4. Six strength values for unidirectional GFRP, CFRP and hybrid/epoxy at testing temperatures 25°C, 40°C and 55°C based on ten specimens for each case.

No	Specimen types	Temperature (°C)	Number of specimen	Average load (N)	Average strain (%)	Average stress value (MPa)	COV (%)
1	Glass/epoxy	25	10	9823	0.22	818.579	6.30
2	Glass/epoxy	40	10	9456	0.21	783.193	4.11
3	Glass/epoxy	55	10	9634	0.20	807.695	4.13
4	Carbon/epoxy	25	10	27219	0.17	2017.730	5.52
5	Carbon/epoxy	40	10	27137	0.15	2010.130	6.05
6	Carbon/epoxy	55	10	26880	0.14	1975.930	7.15
7	Hybrid/epoxy	25	10	19081	0.18	1270.800	1.70
8	Hybrid/epoxy	40	10	16239	0.16	1076.520	3.60
9	Hybrid/epoxy	55	10	14620	0.15	972.742	3.48

4.4.1 Finite Element Modeling Methods and Results

Tensile strength behaviour of FRP composite specimen, subject to thermal loading, was studied by finite element methods. The density, strength and moduli for unidirectional composite laminates were calculated using Rule of Mixtures (ROM) and employing the material properties shown in Table 3.1. Theoretical analysis is given in Appendix B. The fibre volume fractions used in FE simulations are the same as the test specimens manufactured by vacuum infusion processes. Material modelling for each composite was done on ANSYS ACP (pre), and was then transferred to ANSYS static structural module. The specimens were fixed at one end and loaded on the other end using thermal loading. Figure 4.17 shows the tensile testing process under different temperatures and forces using ANSYS software.

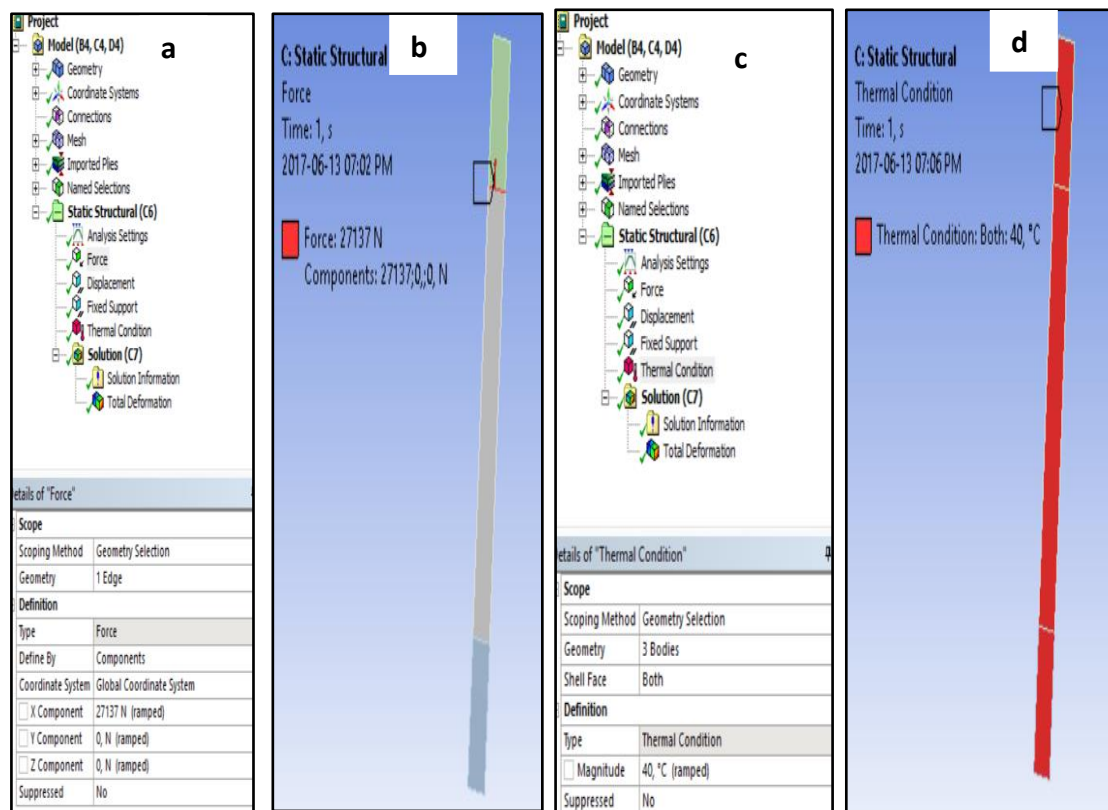


Figure 4.17 Tensile tests using ANSYS software (a) input parameters (b) fixing the specimen and applying force (c) thermal loading (d) force and thermal loading.

To detect the failure load for each specimen under different loads, the results from static structure were transferred to ANSYS ACP (post). Figure 4.18 (a-c) illustrates the maximum stress distribution at the top ply of the carbon/epoxy specimen at different temperatures. The simulation results show that the stress increases as the test temperature increases from ambient to 40°C and 55°C.

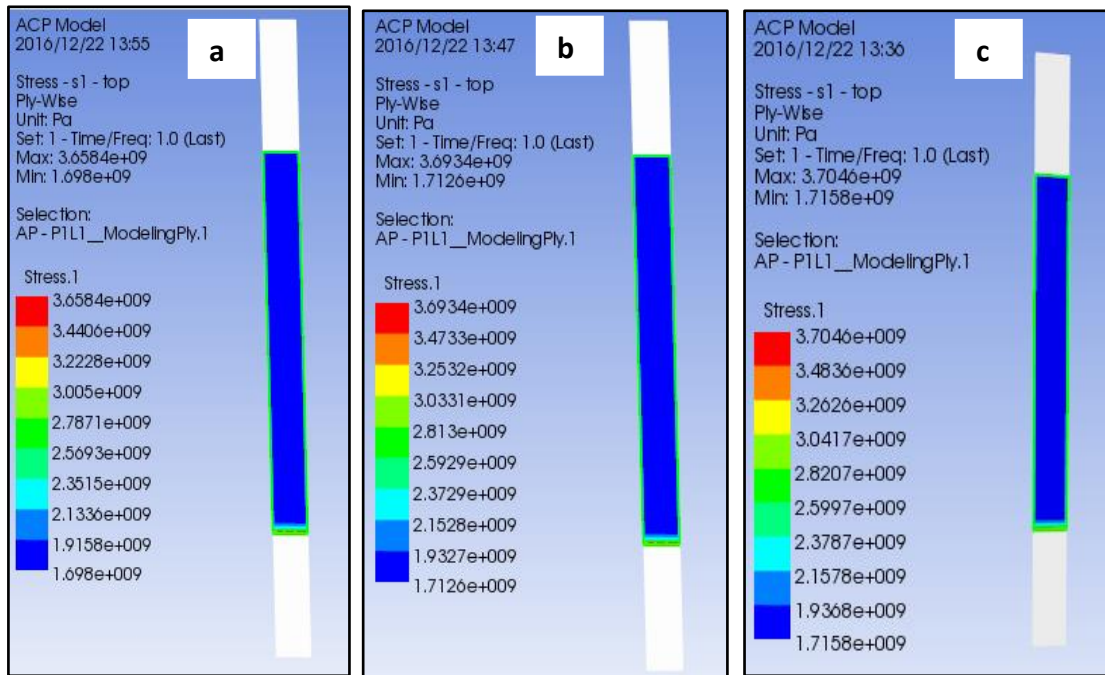


Figure 4.18 Stress distribution in the top ply of carbon/epoxy specimens at temperatures 25°C, 40°C and 55°C.

Simulation results show that the maximum stress occurs at top ply of the composite specimens. Distribution of stress in each layer was analysed by ANSYS software. The simulation results for glass/epoxy specimens are shown in Figure 4.19 (a-c). It is observed that the stress on the top layer of the specimens increases as temperature increases.

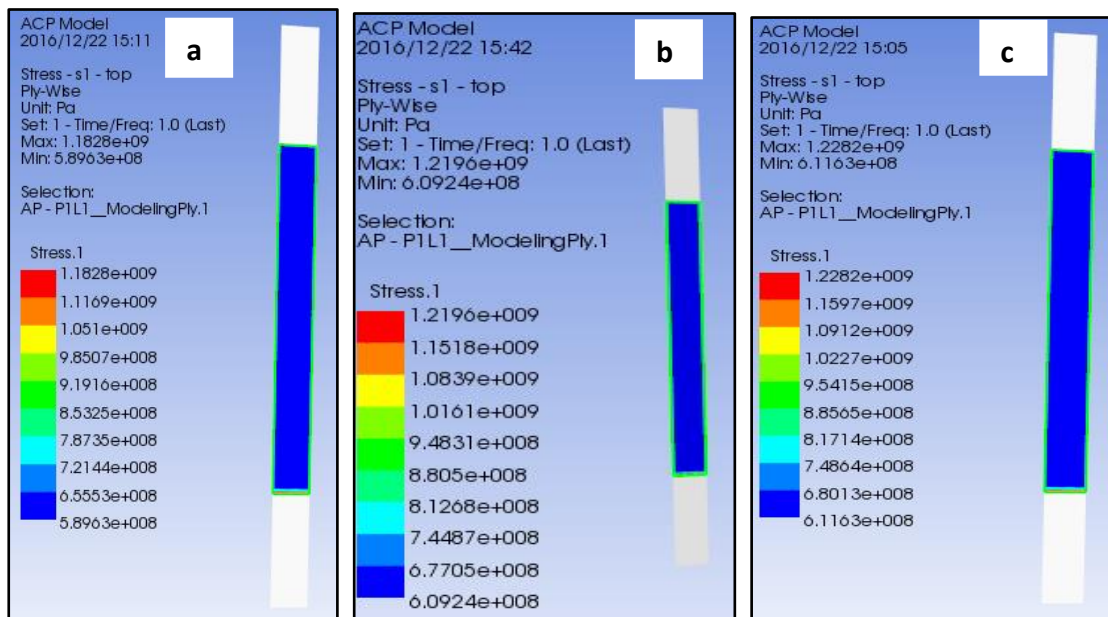


Figure 4. 19 Stress distribution at the top ply of glass/epoxy specimens at temperatures 25°C, 40°C and 55°C.

Stress on the top layer of hybrid specimens are shown in Figure 4.20 where the top layer is carbon/epoxy. Stress distribution in each laminate was analysed using ANSYS software.

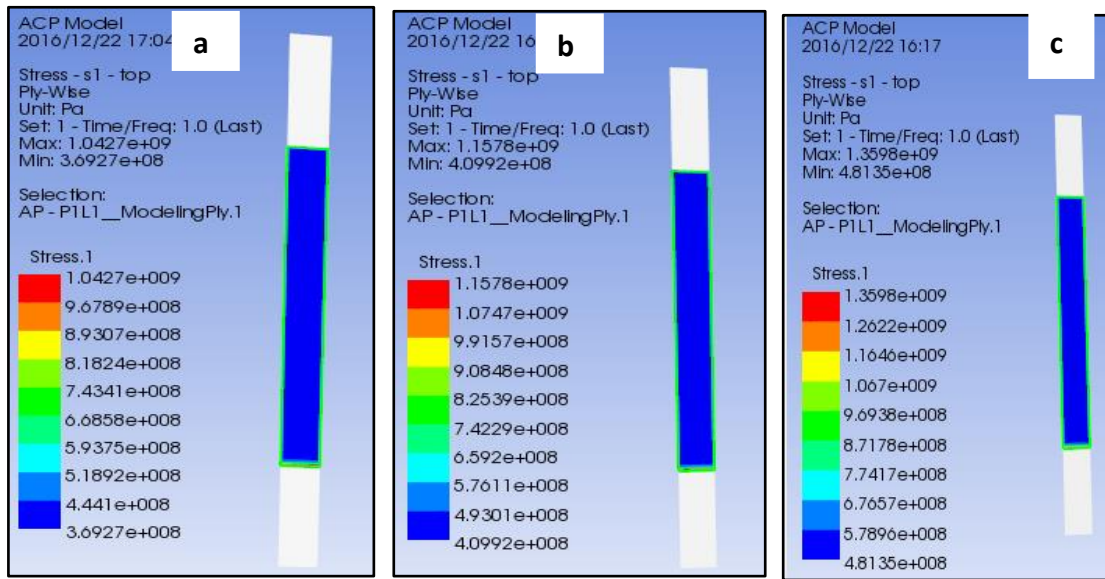


Figure 4. 20 Stress distribution at the top ply of hybrid glass-carbon specimens at temperatures 25°C, 40°C and 55°C.

The average stress at different temperatures is shown in Figure 4.21. The change in the stress in the fibre direction is minimal for carbon and glass specimens but a slight change occurs on the top layer of the hybrid/epoxy. Simulation results show that there is a decrease in the static mechanical properties in the fibre direction before the glass transition temperature is reached.

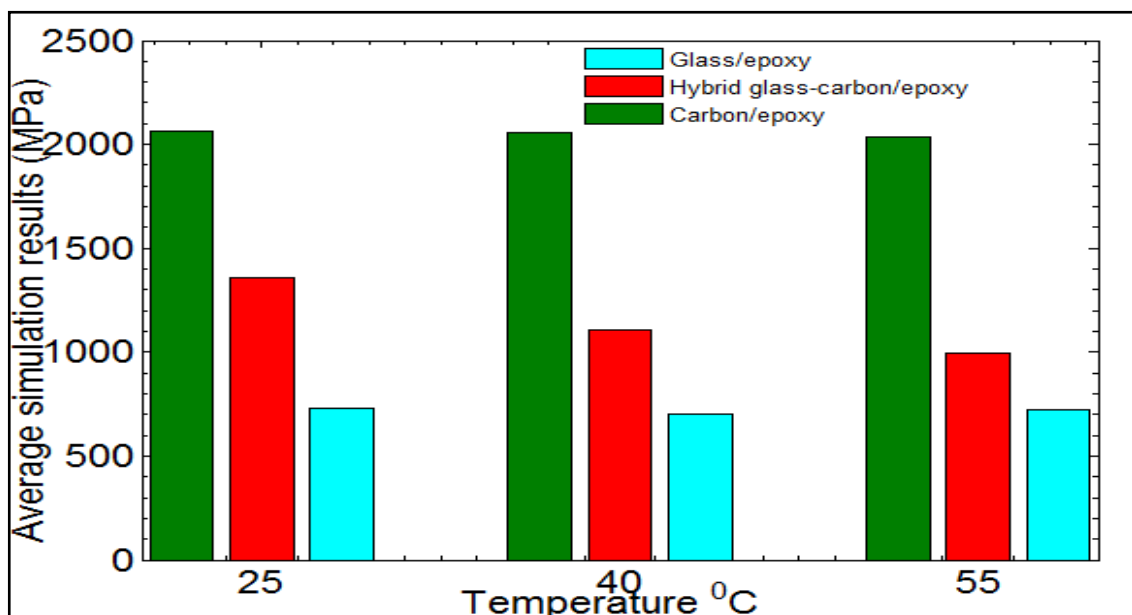


Figure 4.21 Simulation on tensile stress vs. variable testing temperature

Failure analysis was conducted using ANSYS software and the results were transferred to ANSYS ACP (post) as shown in Figures 4.22, 4.23 and 4.24. In the finite element analysis, Tsai-Wu failure criteria was used which is shown in Appendix B. The simulation results shown in Figure 4.22 (a-d) show that the failure index of glass/epoxy composite exceeds the failure limit of Tsai-Wu failure criterion ($Fi \leq 1$) and the failure occurs near to the tab section.

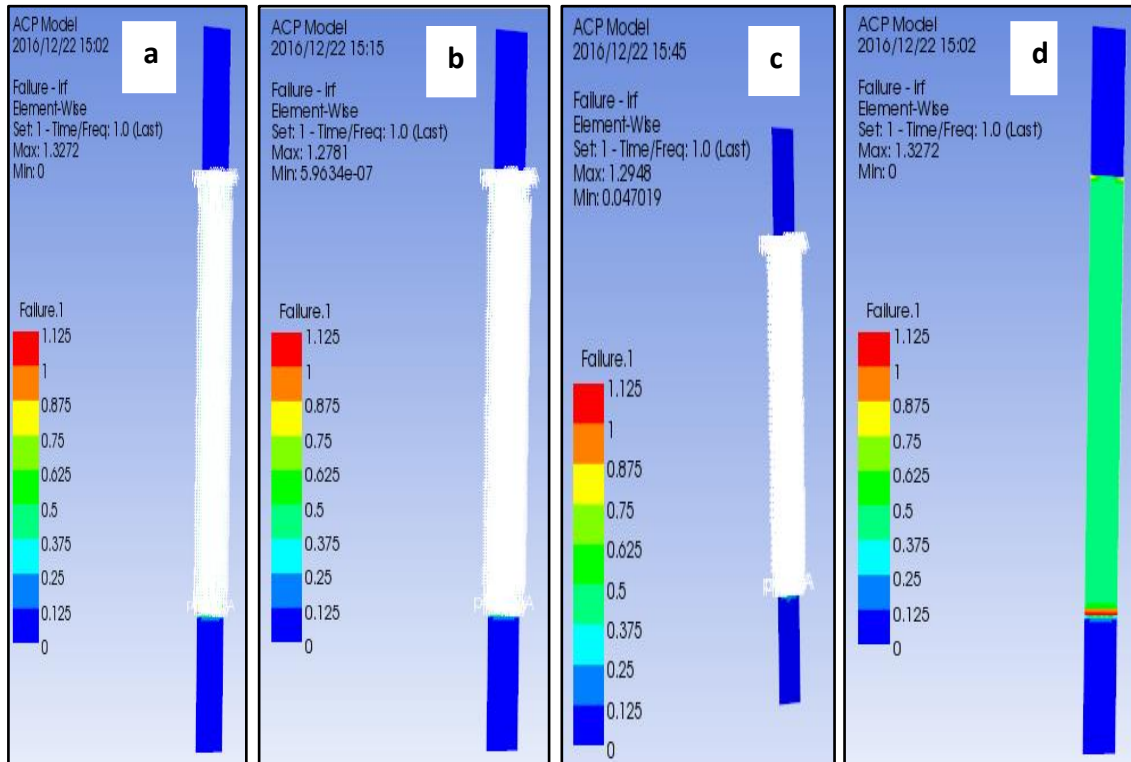


Figure 4.22 Glass/epoxy failure index values at temperatures (a) 25°C, (b) 40°C, (c) 55°C (d) location of failure

Simulations are shown in Figures 4.23 (a-d) and 4.24 (a-d) for carbon/epoxy and hybrid/epoxy laminates. Failure indexes of these two composites exceed the failure limit of Tsai-Wu failure criterion ($Fi \leq 1$) and failures occur near the tab section. Thus the three composite specimens failed as it was also the case in the experimental studies.

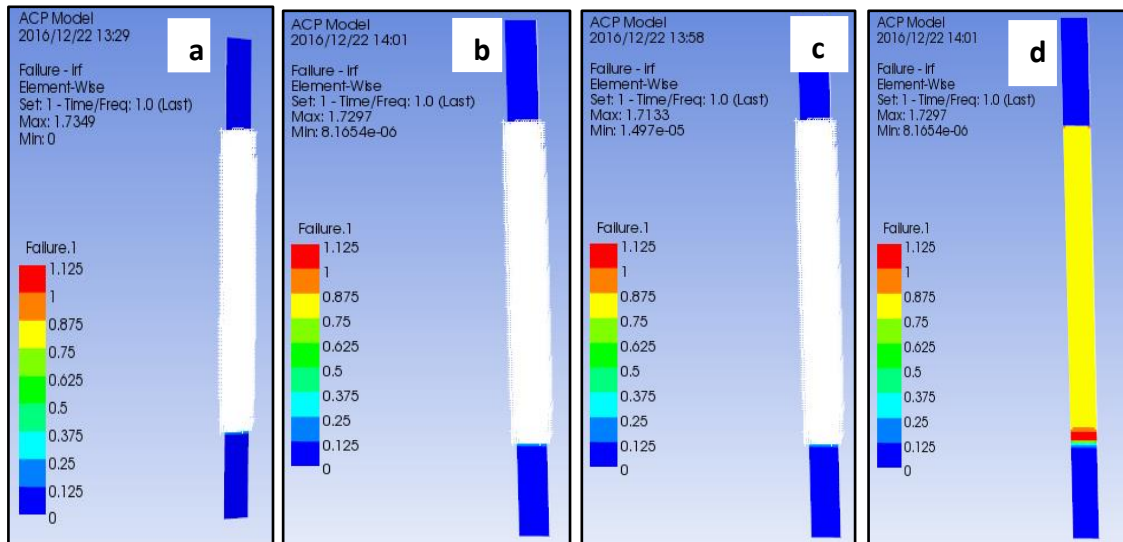


Figure 4.23 Carbon/epoxy failure index values at temperatures (a) 25°C, (b) 40°C, (c) 55°C, d) location of failure

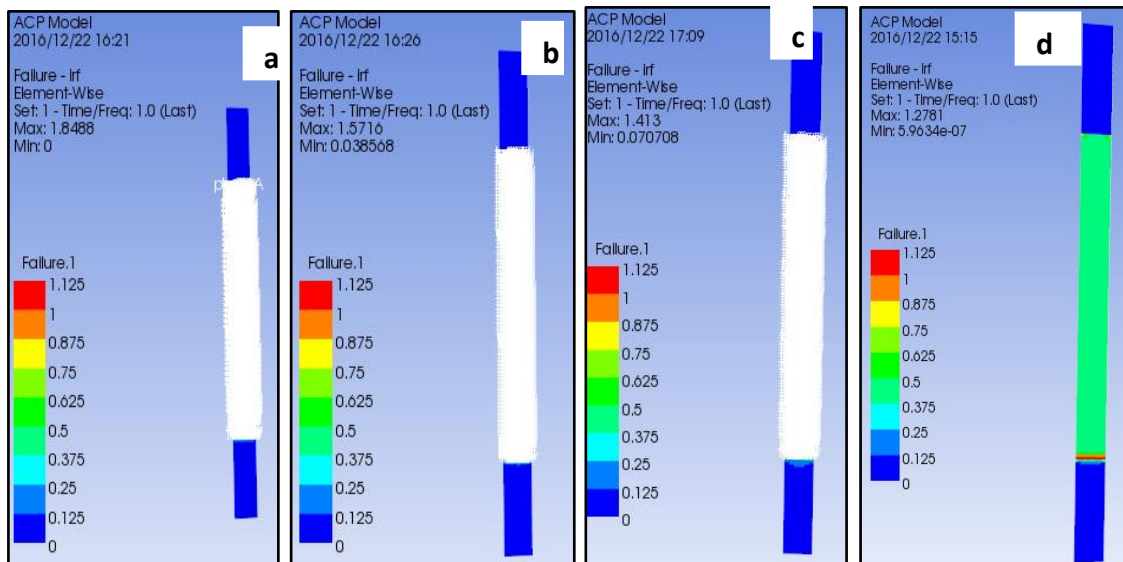


Figure 4.24 Hybrid glass-carbon/epoxy failure index values at temperatures (a) 25°C, (b) 40°C, (c) 55°C d) location of failure

4.4.2 Comparison of Experimental and FEA on Tensile Testing

Finite element simulations were performed to compare the numerical results with the experimental results. The magnitudes of the applied loads and temperatures are shown in Table 4.7 for each simulation. Three plies were used for the simulation of glass/epoxy and carbon/epoxy composite specimens, while four plies were used for hybrid glass-carbon/epoxy specimens. The largest differences between FEA and experimental results are for glass/epoxy composites and the percentages of the differences are between 10% and 11%. Smallest differences are for carbon/epoxy specimens and they are between

Comparison of Experimental and FEA on Tensile Testing

2.2% and 2.9%. For hybrid specimens the percentages of the differences were between 2.3% and 6.5%. Comparative results between the simulations and test results are shown in Figure 4.25. The simulation results show that GFRP specimens fail at a lower stress compared to the values obtained in the tests. However, simulation results indicate a higher failure stress for CFRP and hybrid composites as compared to the failure stress obtained from tests as shown in Figure 4.25.

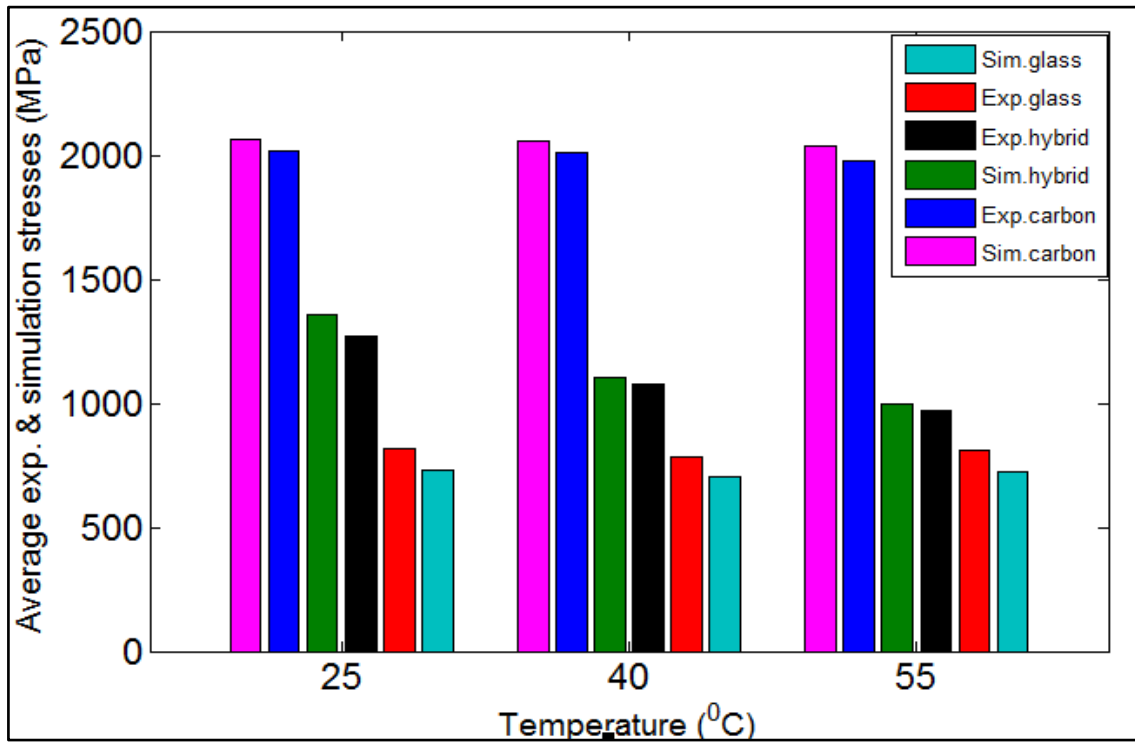


Figure 4.25 Average experimental and simulation failure stresses vs. temperature.

Table 4. 6 Average values of the experimental and simulation results at temperatures 25°C, 40°C and 55°C.

No	Specimen types	Temperature (°C)	Average applied load (N)	Average stress simulation results (MPa)	Average exp. stress results (MPa)	Error (%)	Failure index
1	Glass/epoxy	25	9823	727.73	818.579	11.0	1.327
2	Glass/epoxy	40	9456	700.08	783.193	10.6	1.278
3	Glass/epoxy	55	9634	720.24	807.695	10.8	1.295
4	Carbon/epoxy	25	27219	2062.17	2017.730	2.2	1.735
5	Carbon/epoxy	40	27137	2055.2	2010.130	2.2	1.730
6	Carbon/epoxy	55	26880	2034.81	1975.930	2.9	1.713
7	Hybrid/epoxy	25	19081	1358.75	1270.800	6.5	1.849
8	Hybrid/epoxy	40	16239	1106.95	1076.520	2.7	1.572
9	Hybrid/epoxy	55	14620	995.58	972.742	2.3	1.413

4.4.3 Statistical Analysis of Test Results for Tensile Strength

Tensile strengths at different temperatures were determined by conducting 10 experiments for each temperature with three different composites resulting in 90 laminates tested. Results of these tests are presented in Table 4.6 where mean values and Coefficients of Variation (COV) are shown for each temperature. Tensile strengths of the three specimens show coefficients of variation between 1.70% and 7.15%. This is an indication that the strength properties are affected by temperature.

For statistical analysis of the results, normal, log-normal and Weibull distributions were selected. Parameters for each distribution are shown in Table 4.8.

Table 4.7 Distribution parameters for tensile strength (MPa) values at temperatures 25°C, 40°C and 55°C.

No	Specimen types	Temperature (°C)	Normal		Log-normal		Weibull	
			μ	σ	μ of ln	σ of ln	η	σ
1	Glass/epoxy	25	818.58	51.58	6.720	0.069	17.12	844.76
2	Glass/epoxy	40	783.19	32.16	6.683	0.048	24.55	801.28
3	Glass/epoxy	55	807.70	33.39	6.707	0.051	23.22	829.06
4	Carbon/epoxy	25	2017.73	111.37	7.622	0.056	21.05	2070.0
5	Carbon/epoxy	40	2010.13	121.51	7.618	0.063	18.73	2069.4
6	Carbon/epoxy	55	1975.93	141.20	7.595	0.084	14.11	2051.1
7	Hybrid/epoxy	25	1270.80	21.59	7.150	0.025	46.12	1289.4
8	Hybrid/epoxy	40	1076.52	38.76	6.982	0.043	27.78	1098.1
9	Hybrid/epoxy	55	972.742	33.84	6.881	0.037	31.71	990.18

In order to test the accuracy of statistical distributions, the chi-square fit method is selected. The chi-square test results are presented in Table 4.9 which indicates that statistical distributions cannot be rejected at the 5% significant level. In Table 4.9, statistical distribution which fits the experimental data best is underlined. Estimates of correlation between the experimental and theoretical data as functions of normal, log-normal and Weibull distributions are shown in Table 4.10. The coefficients in Table 4.10 measure the linear correlation between the experimental and theoretical results.

Statistical Analysis of Test Results for Tensile Strength

Table 4.8 Chi-square test results

No	Specimen types	Testing temperature (°C)	Normal	Log-normal	Weibull
1	Glass/epoxy	25	0.747	0.784	<u>0.880</u>
2	Glass/epoxy	40	<u>0.310</u>	0.159	0.200
3	Glass/epoxy	55	0.327	<u>0.823</u>	0.263
4	Carbon/epoxy	25	<u>0.813</u>	0.644	0.499
5	Carbon/epoxy	40	<u>0.611</u>	0.598	0.413
6	Carbon/epoxy	55	<u>0.315</u>	0.225	0.187
7	Hybrid/epoxy	25	<u>0.837</u>	0.505	0.451
8	Hybrid/epoxy	40	<u>0.721</u>	0.656	0.697
9	Hybrid/epoxy	55	0.409	<u>0.436</u>	0.061

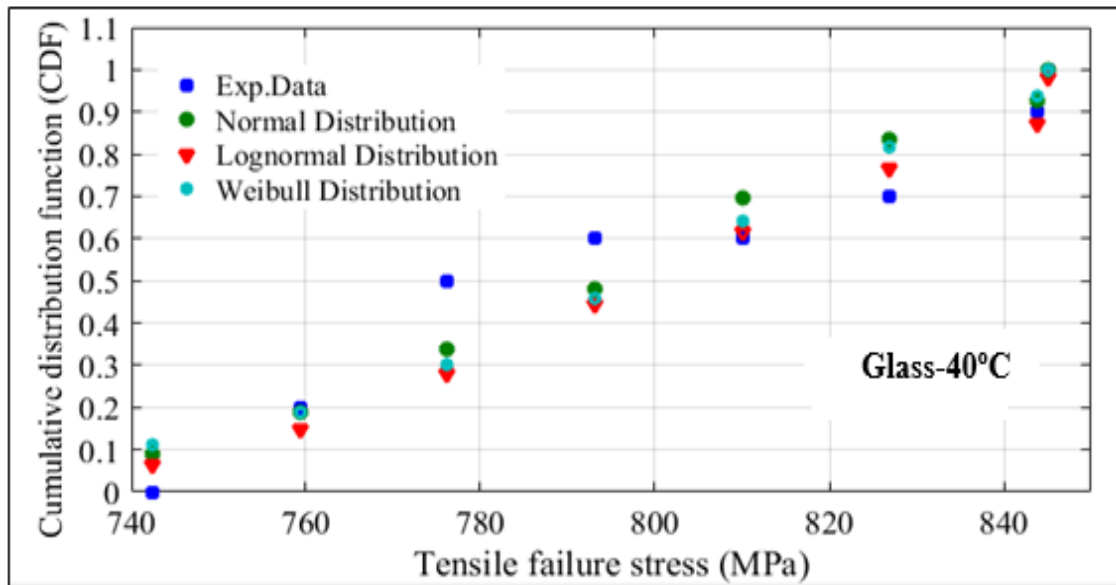
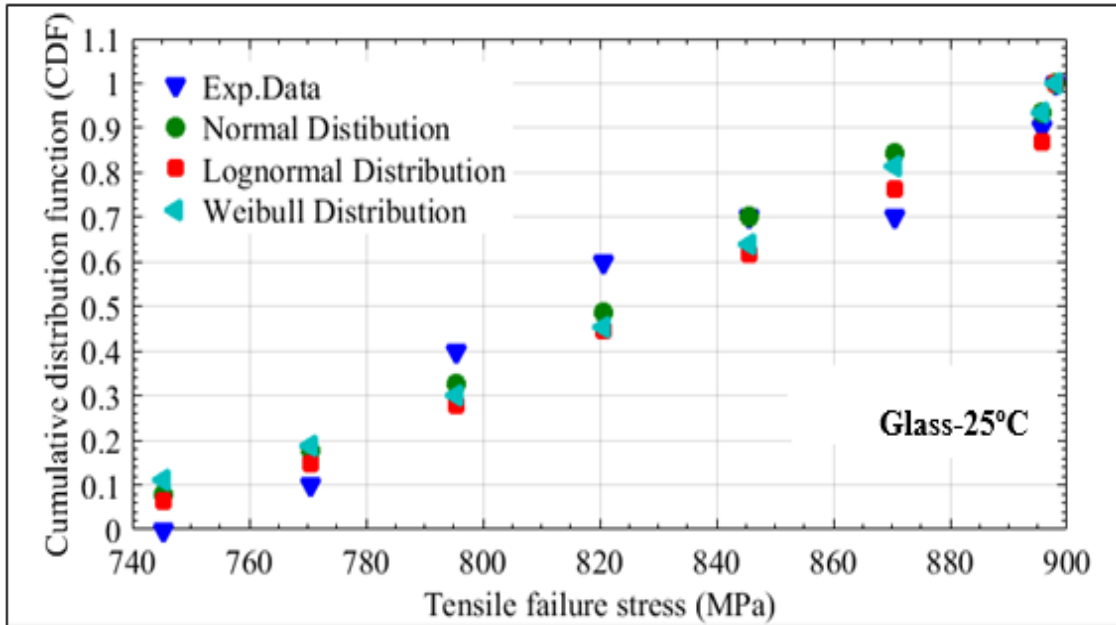
Table 4.9 R-square values (Exp. Data vs fitted responses)

No	Specimen types	Testing Temperature (°C)	Normal	Log-normal	Weibull
1	Glass/epoxy	25	0.945	0.943	0.924
2	Glass/epoxy	40	0.925	0.860	0.874
3	Glass/epoxy	55	0.964	0.963	0.958
4	Carbon/epoxy	25	0.970	0.960	0.955
5	Carbon/epoxy	40	0.909	0.912	0.893
6	Carbon/epoxy	55	0.945	0.941	0.937
7	Hybrid/epoxy	25	0.975	0.961	0.958
8	Hybrid/epoxy	40	0.955	0.960	0.938
9	Hybrid/epoxy	55	0.955	0.958	0.955

Comparisons of the Cumulative Distributions Functions (CDF) based on experimental and theoretical results are shown in Figures 4.26, 4.27 and 4.28 for different temperatures. In Figure 4.26, the experimental and theoretical cumulative distribution functions for tensile strengths of glass/epoxy are shown for normal, lognormal and Weibull distributions at temperatures 25°C, 40°C and 55°C. A comparison of fits with the experimental data at 25°C indicates that Weibull distribution is the best fit. Even though the normal and lognormal distributions do not follow the experimental data closely, they

Statistical Analysis of Test Results for Tensile Strength

cannot be rejected at 5% significant level. At temperatures 40°C and 55°C, normal and lognormal distributions give the best fit for the experimental data.



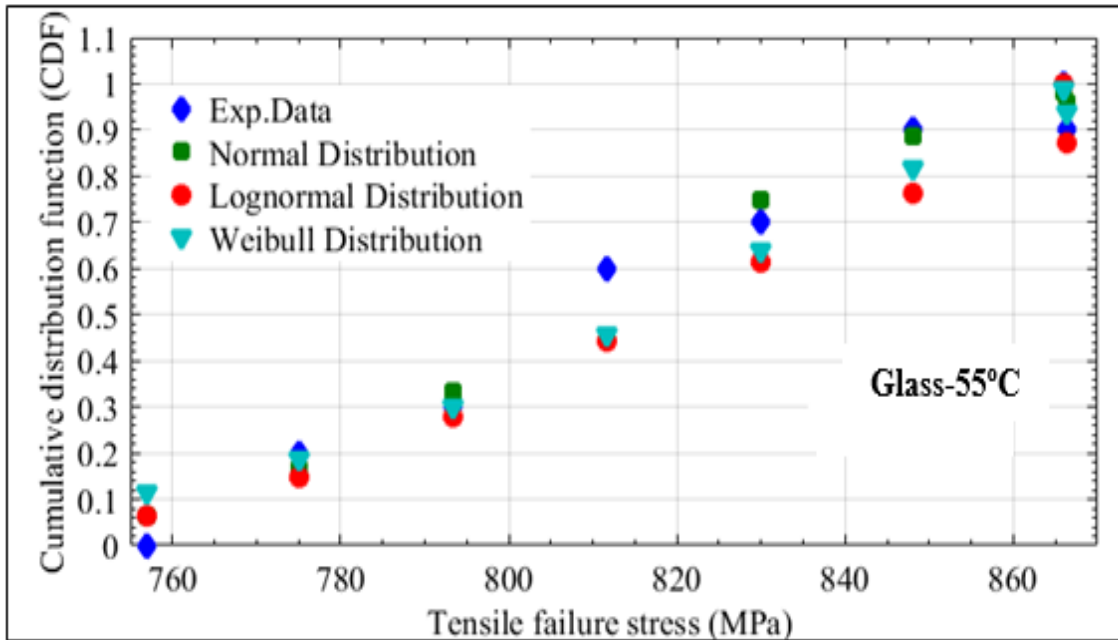
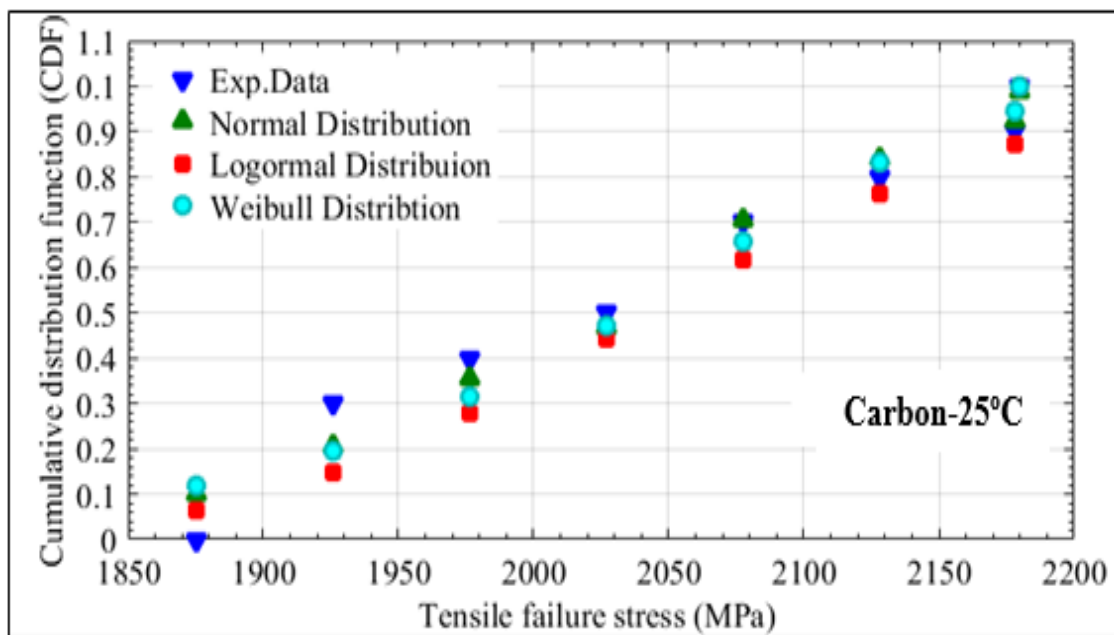


Figure 4.26 Comparisons of experimental and theoretical results for tensile strengths for glass/epoxy at temperature 25°C, 40°C and 55°C.

Corresponding results for carbon/epoxy are shown in Figure 4.27. A comparison of fits with the experimental data indicates that the normal distribution is the best fit in this case for all testing temperatures. Even if the normal and Weibull distributions do not follow closely with the experimental data, one cannot reject these distributions at 5% significant level.



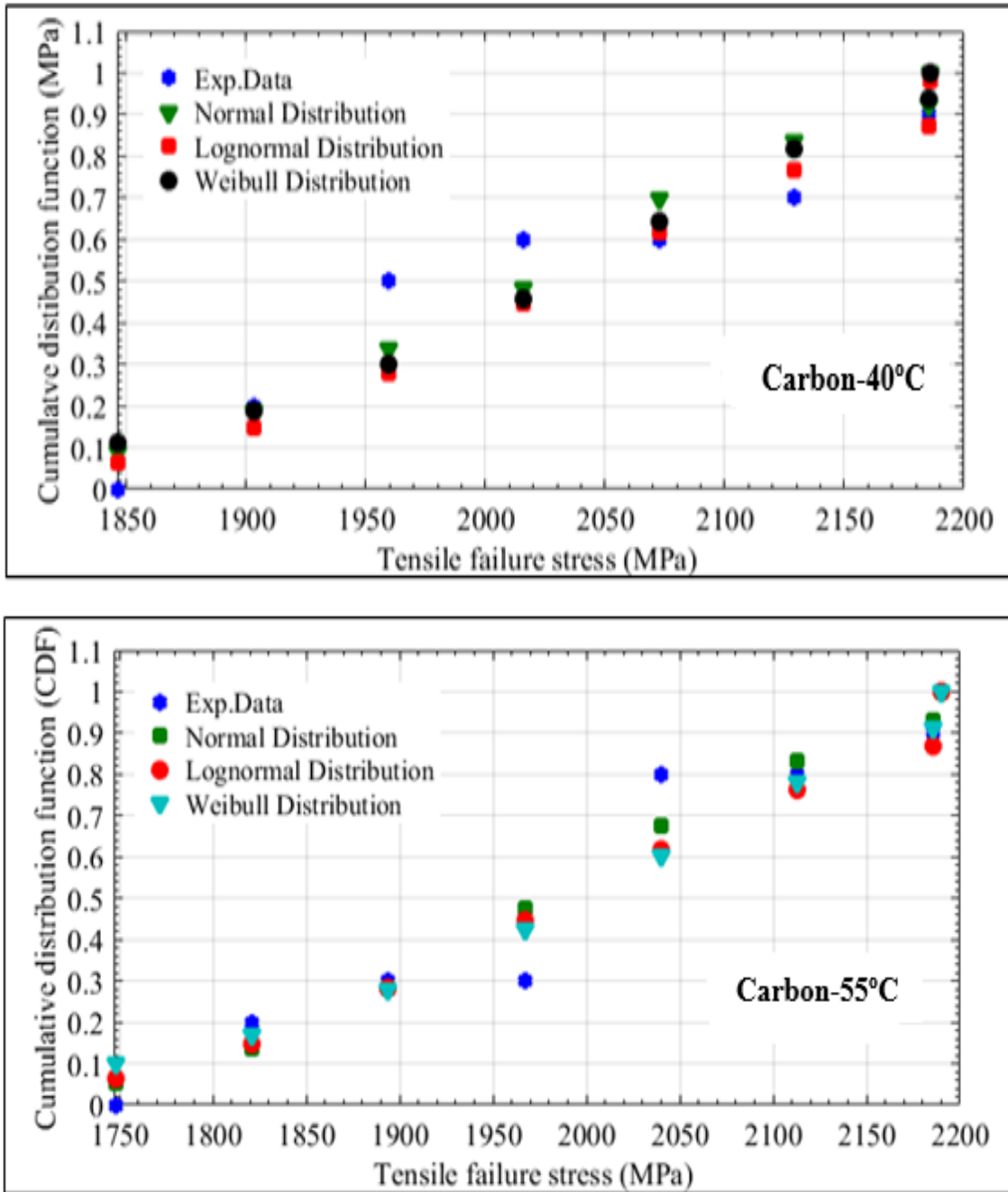


Figure 4.27 Comparisons of experimental and theoretical results for tensile strength for carbon/epoxy at temperatures 25°C, 40°C and 55°C.

Corresponding results for hybrid/epoxy are shown in Figure 4.28. For this case, normal distribution gives the best fit with the experimental data for 25°C and 40°C. The log-normal and Weibull distributions do not follow the experimental data closely, but cannot be rejected at 5% significant level. For temperatures 55°C, the experimental data fits best to the log-normal distribution. The normal and Weibull distributions are also valid for the null hypothesis.

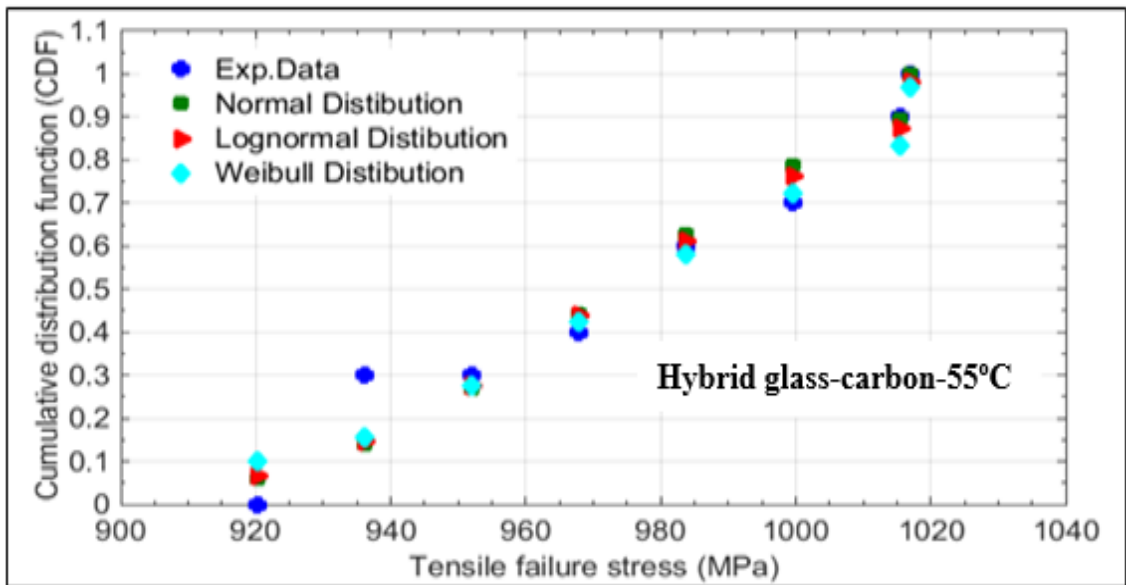
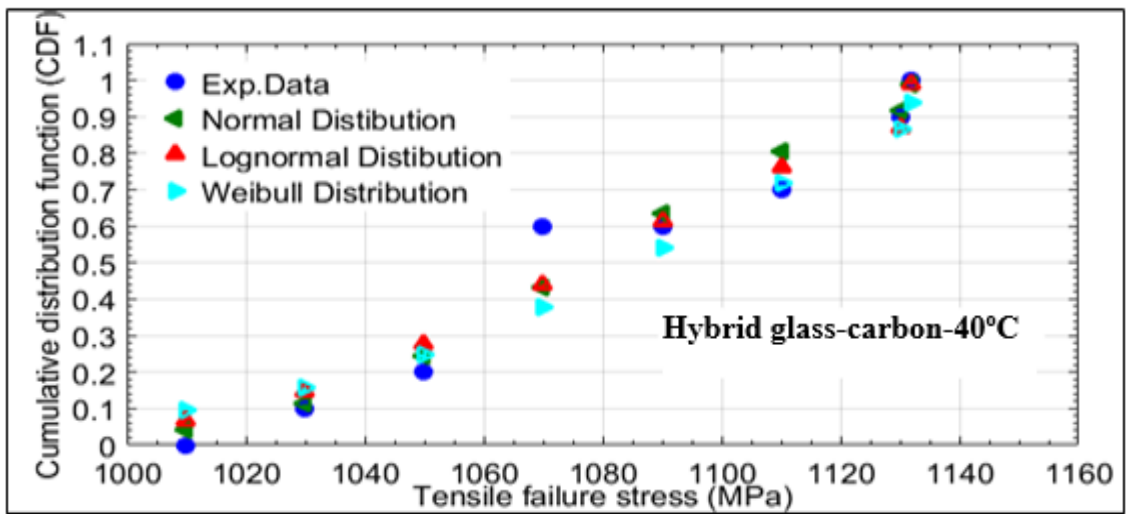
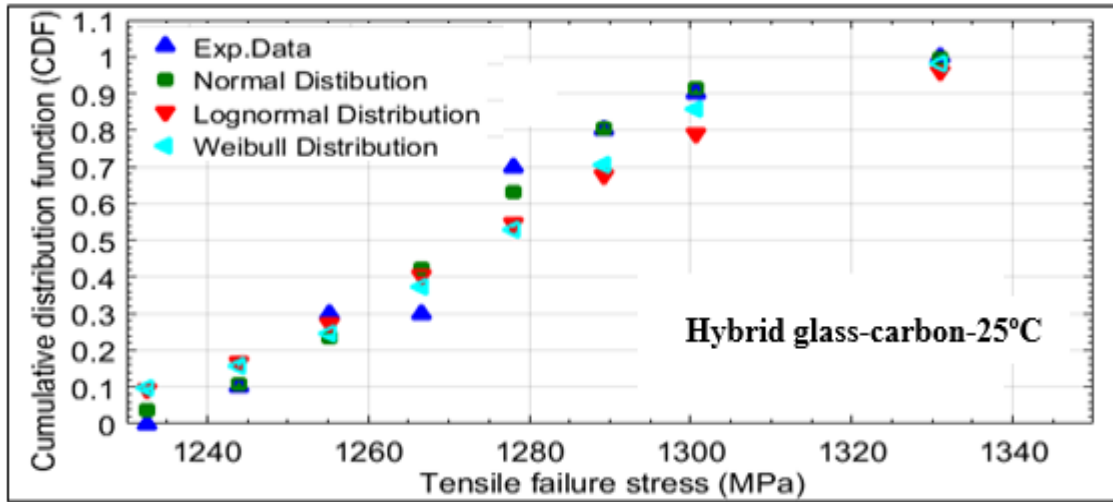


Figure 4.28 Comparisons of experimental and theoretical results for tensile strength for hybrid glass-carbon/epoxy at temperatures 25°C, 40°C and 55°C

4.5 Test Summary

Carbon fibre, glass fibre and hybrids fibre composite specimens were tested using short beam shear tests, dynamic mechanical analysis and tensile tests under various temperatures. The static mechanical properties of composites were determined by Short Beam Shear (SBS) tests. The inter-laminar shear failure strength of the composite specimens was measured at elevated temperatures. Delamination of the specimens occurred at lower stress levels as the temperature increased.

Dynamic Mechanical Analysis (DMA) revealed that the stiffness of the specimens decreased with increasing temperatures. Tests were used to measure the storage moduli and T_g of polymer matrix.

Composite specimens were tested under tensile loading and numerical simulations were performed to correlate the experimental and theoretical results. The results show that mechanical properties of the composite specimens change when they are subjected to thermal loading. The experimental and numerical results show that the mechanical properties of composite specimens are degraded under increasing temperatures due to the material properties being temperature dependent.

This study was conducted using composite test specimens. However, it is necessary to study the response of composite materials at the structural level. In Chapter 5, airfoil profiles are studied, and the design and development of optimized blade shapes are discussed. In particular, NACA airfoils are investigated using different parameters to maximize the power coefficient of 54m horizontal axis wind turbine blades. These blades can generate 2MW power on tropical wind farms.

Chapter 5

Development of Airfoil Profiles to Model Optimized Shapes of HAWT Blades

5.1 Principles of a Wind Turbine Energy Conversion System

A wind turbine power generation depends on the interaction between the wind and the rotor. The performance of wind turbine blades mainly depends on the wind speed, airfoil geometry and rotor characteristic which are some of the factors that determine the efficiency of power production. The primary function of a wind turbine's rotor is to convert the energy in the wind to kinetic energy, i.e. rotating the hub. The starting point of the design of wind turbine blades is the actuator-disk concept developed by Rankine and extended by Froude to develop marine propellers. Albert Betz (1926) recognized that mechanical energy can be extracted from air stream passing through a given cross-sectional shape [94]. The analysis assumes a stream tube and two cross-sections of the stream tube as control volume boundaries as shown in Figure 5.1.

5.2 Betz's Elementary Momentum Theory

Figure 5.1 shows a stream tube with an actuator disk representing the wind turbine blades which creates a discontinuity of pressure in the stream tube of air flowing through it.

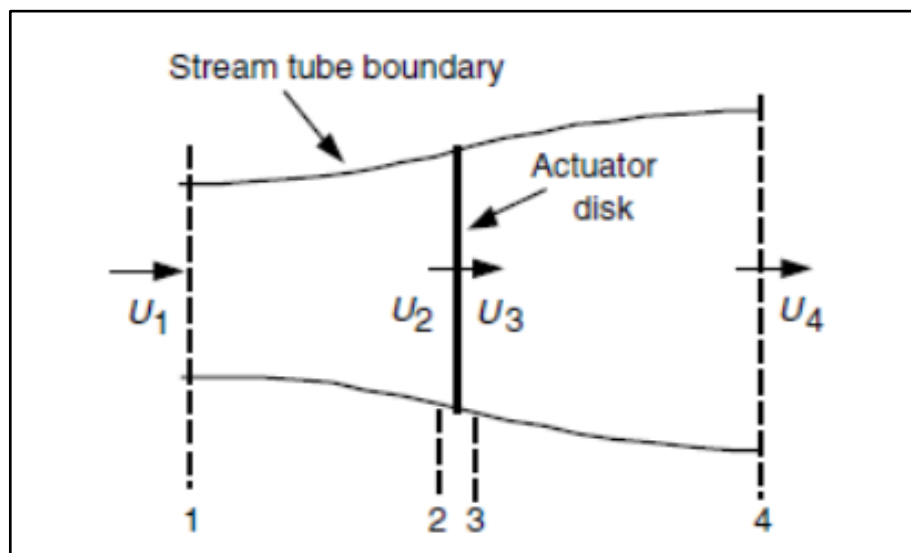


Figure 5. 1 An actuator disc model of a wind turbine; U is air velocity; 1, 2, 3, and 4 indicate locations (McGowan, 2009)

Kinetic energy of air can be expressed as

Principles of a Wind Turbine Energy Conversion System

$$K.E = \frac{1}{2}mU^2 \quad (5.1)$$

where m is the mass and U is the air velocity. A cross-sectional area of the actuator disk is denoted as A . Air passes through it with the same velocity U_2 and U_3 , represented by U . Air density is denoted by (ρ) . The air mass is given by

$$\dot{m} = \rho UA \quad (5.2)$$

Conservation of linear momentum can be applied to the control volume of a one-dimensional, incompressible, time-invariant flow. The force of the wind on the wind turbine blades is equal and opposite to the thrust (T) which can be expressed as

$$T = U_1(\rho AU)_1 - U_4(\rho AU)_2 \quad (5.3)$$

The subscripts indicate the values at the numbered cross-sections in Figure 5.1. For steady state flow, the mass flow rates at the inlet and exit are the same. Therefore, the thrust on the wind blade is given by

$$T = \dot{m}(U_1 - U_4) \quad (5.4)$$

The thrust is positive since the value of U_4 is less than the free stream velocity U_1 . The value of the thrust is maximum when U_4 zero, that is, is when the air is stationary at the convertor. Nevertheless, the result is not physically meaningful as no work is done on either side of the wind turbine rotor. A physically meaningful result is given by the ratio of U_4 / U_1 . The Bernoulli equation can be used in the upstream of the actuator disc and can be expressed as

$$P_1 + \frac{1}{2}\rho U_1^2 = P_2 + \frac{1}{2}\rho U_2^2 \quad (5.5)$$

This equation is given by

$$P_3 + \frac{1}{2}\rho U_3^2 = P_4 + \frac{1}{2}\rho U_4^2 \quad (5.6)$$

in the downstream of the actuator disc. It is assumed that the pressures at the far upstream and the downstream are equal ($P_1 = P_4$) and the air velocity across the disc is the same ($U_2 = U_3$). The thrust on each side of the disc is

$$T = A_2(P_2 - P_3) \quad (5.7)$$

Solving for ($P_2 = P_3$) and using equations (5.6), (5.7) and (5.8), the thrust can be found as

Principles of a Wind Turbine Energy Conversion System

$$T = \frac{1}{2} \rho A_2 (U_1^2 - U_4^2) \quad (5.8)$$

Taking into account the law of conservation of momentum, the force applied on the rotor plan by the air can be expressed as:

$$F = \dot{m}(U_1 - U_4) \quad (5.9)$$

This force must be counteracted by an equal force exerted by the rotor on the airflow. The thrust pushes the air mass at a velocity U_2 . The power required for this movement can be calculated as

$$P = FU = \dot{m}(U_1 - U_4)U_2 \quad (5.10)$$

The power extracted from the air flow can be derived from the energy difference between the end points of the rotor. Equating these two analytical expressions gives the relationship for the flow velocity U_2 ,

$$\begin{aligned} \frac{1}{2} \dot{m}(U_1^2 - U_4^2) &= \dot{m}(U_1 - U_4)U_2 \\ U_2 &= \frac{1}{2}(U_1 + U_4) \end{aligned} \quad (5.11)$$

Wind velocity through the rotor is equal to the arithmetic mean of (U_1, U_4) [95]

$$U_2 = \frac{1}{2}(U_1 + U_4) \quad (5.12)$$

The axial induction factor (a), that is, the fractional decrease in wind velocity between the free [96] stream and the rotor is determined by

$$a = \frac{(U_1 - U_2)}{U_1} \quad (5.13)$$

The wind velocity at section (U_2) can be expressed as

$$U_2 = U_1(1 - a) \quad (5.14)$$

The wind velocity at the exist (U_4) is

$$U_4 = U_1(1 - 2a) \quad (5.15)$$

The induced velocity at the rotor $(U_1 a)$ is a combination of the free stream and induced wind velocity. As the axial induction factor increases and approaches to $a = 0.5$, the wind

Principles of a Wind Turbine Energy Conversion System

velocity at the exist goes to zero and the theory no longer applies. The power, using this model is the thrust times the velocity at the disc and is given by

$$P = \frac{1}{2} \rho A_2 (U_1^2 - U_4^2) U_2 = \frac{1}{2} \rho A_2 U_2 (U_1 + U_4)(U_1 - U_4) \quad (5.16)$$

By substituting (U_2) and (U_4) from equations (5.15) and (5.16), the power, based on the Betz model, can be computed as

$$P = \frac{1}{2} \rho A U^3 4a(1-a)^2 \quad (5.17)$$

The power coefficient (C_p) of the wind turbine rotor is the ratio of the actual power developed by the rotor to the free stream energy flux through a disk of the same area as swept out by the rotor and can be computed as

$$C_p = \frac{\text{Rotor power}}{\text{Power in the wind}} = \frac{\frac{1}{2} \rho A U^3 4a(1-a)^2}{\frac{1}{2} \rho A U^3} \quad (5.18)$$

The non-dimensional power coefficient of the wind turbine rotor is given by

$$C_p = 4a(1-a)^2 \quad (5.19)$$

Figure 5.2 shows that as the axial induction factor increases, the power coefficient also increases as it approaches $a=1/3$. Substituting this value in equation (5.20), the maximum power coefficient found as $C_{p,\max} = 0.5926$. This is called the Betz limit. Similarly, the axial thrust on the disk is:

$$T = \frac{1}{2} \rho A U^2 [4a(1-a)] \quad (5.20)$$

The thrust coefficient is given by

$$C_T = \frac{\text{Thrust force}}{\text{Dynamic force}} = \frac{\frac{1}{2} \rho A U^2 4a(1-a)}{\frac{1}{2} \rho A U^2} = 4a(1-a) \quad (5.21)$$

The thrust coefficient has the maximum value of 1.0 when the axial induction factor is ($a=0.5$) and the downstream velocity is zero. The value of the thrust when the power coefficient reaches the maximum is $=0.89$ and the velocity behind the rotor is $U_4 = 0$ and the value of the induction factor $a=0.5$.

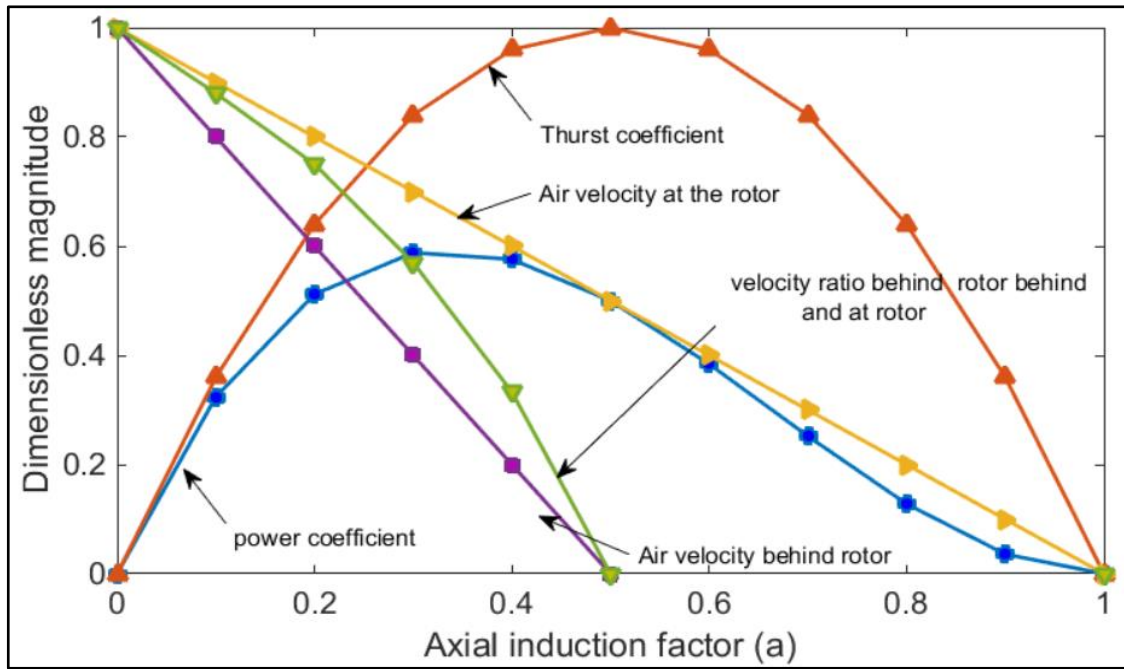


Figure 5. 2 Operating parameters for a Betz wind turbine model

The overall wind turbine efficiency is a function of both mechanical and rotor power coefficients and is given by

$$\eta_{overall} = \frac{P_{out}}{\frac{1}{2}\rho AU^3} = \eta_{mech} Cp \tag{5.22}$$

The power can be expressed as

$$P_{out} = \frac{1}{2}\rho AU^3 (\eta_{mech} Cp) \tag{5.23}$$

By taking the derivative of equation (5.20), the axial induction factor can be computed to determine the other parameters which can be used to design the structural components of wind turbine blades.

5.3 Flow through Horizontal-Axis Wind Turbine with Wake Rotation

The linear momentum theory of the previous section is used in Betz’s idealized theory, but has a number of strong assumptions. In reality, a rotating rotor of a wind turbine may impart a rotating motion or a spin to the rotor wake, which can rotate opposite to the torque of the rotor. Betz model focuses on the axial momentum theory and neglects rotational components (ω) of the flow after passing through the actuator disk. The theory was examined by Glauert [96] who noted that the angular velocity of the air relative to

Flow through Horizontal-Axis Wind Turbine with Wake Rotation

the angular velocity of the wind turbine blade increases from Ω to $\Omega + \omega$. The reason is that the axial component of the velocity remains constant. In the case of a horizontal axis wind turbine rotor, the flow behind the rotor rotates in the direction opposite to the rotation of the rotor. This is due to the reaction to the torque exerted by the flow on the rotor. The addition of a vortex component reduces the torque and the power coefficient of the rotor according to Betz model. This happens because of the generation of rotational kinetic energy in the wake. The power coefficient depends on the ratio between the energy components due to rotation and translational motion of the air stream. This ratio depends on the tangential velocity of the wind turbine rotor in relation to undisturbed axial wind velocity and it is called the tip speed ratio (λ) given by

$$\lambda = \Omega R / U \quad (5.24)$$

where Ω is the rotor angular velocity and R is the rotor radius. A higher tip speed ratio increases the efficiency of the power output but the noise levels increase. The magnitude of the tip speed ratio is based on the speed of the wind turbine. The recommended tip speed ratio for wind turbines operating at low wind speeds is between 1 and 4 and the ones operating at high wind speeds is above 5. The relation between rotational speed and tip speed ratio is given by

$$\lambda = \frac{2\pi nr}{60U} \quad (5.25)$$

where n is the rotational speed. The angular induction factor (a') is given by

$$a' = \frac{\text{angular velocity of wind at the rotor}}{\text{twice the angular velocity of the rotor}} = \frac{\omega}{2\Omega} \quad (5.26)$$

The thrust on the wind turbine rotor when wake rotation is included can be expressed as

$$dT = 4a'(1+a')\frac{1}{2}\rho\Omega^2 r^2 2\pi r dr \quad (5.27)$$

Based on linear momentum analysis, the thrust on the annular cross-section that uses axial induction factor can be expressed as

$$dT = 4a(1-a)\frac{1}{2}\rho U^2 2\pi r dr \quad (5.28)$$

Equating the thrust given by equation (5.21) based on the linear momentum analysis and the thrust on the annular cross-section given by equation (5.27), the local speed ratio (λ_r) is computed as

Flow through Horizontal-Axis Wind Turbine with Wake Rotation

$$\frac{a(1-a)}{a'(1+a')} = \frac{\Omega^2 r^2}{U^2} = \lambda_r^2$$

$$\lambda_r = \frac{\Omega r}{U} = \frac{\lambda r}{R} \quad (5.29)$$

(λ_r) is the ratio of the rotor speed at some intermediate radius to the wind speed. Applying the conservation of angular momentum to the torque exerted on the wind turbine rotor denoted by (Q) , the change in the angular momentum of the wake is computed as

$$dQ = d\dot{m}(\omega r)(r) = (\rho U_2 2\pi r dr)(\omega r)(r) \quad (5.30)$$

Considering the axial and induction factors, U_2 can be expressed as

$$U_2 = U(1-a) \text{ and } a' = \omega / 2\Omega \quad (5.31)$$

Using the relation $(U_2 = U)$, the change in the angular momentum can be computed as

$$dQ = 4a'(1-a) \frac{1}{2} \rho U \Omega r^2 2\pi r dr \quad (5.32)$$

The power generated at each element, using this model, is given by

$$dP = \Omega dQ \quad (5.33)$$

The power coefficient with a rotational component is obtained as

$$dC_p = \frac{8}{\lambda^2} a'(1-a) \lambda_r^3 d\lambda_r \quad (5.34)$$

Introducing the local speed ratio, and solving for angular induction factor (a') , the following relation can be derived:

$$a' = -\frac{1}{2} + \frac{1}{2} \sqrt{1 + \frac{4}{\lambda_r^2} a(1-a)} \quad (5.35)$$

The rotor power is a function of the angular and axial induction factors including the tip speed ratio of the wind turbine rotor and is given by

$$dP = \frac{1}{2} \rho A U^3 \left[\frac{8}{\lambda^2} a'(1-a) \lambda_r^3 d\lambda_r \right] \quad (5.36)$$

The aerodynamic conditions for maximum power production in each annular ring can be determined by the expression

$$a' = \frac{1-3a}{4a-1} \quad (5.37)$$

The physical laws based on Betz and Glauert models on the airflow around a wind turbine rotor with and without a wake can be used to determine the maximum power that can be extracted from the wind. The axial induction factor developed by Betz is one of the critical parameters to model the shape of a wind turbine blade. It can be applied to determine the blade geometry for the design of horizontal axis wind turbine blades and the angular induction factors to maximize the power on each airfoil.

5.4 Airfoil Characterization and Non-Dimensional Parameters

Wind turbine blades uses airfoils which have the shape of a blade in cross-section and generates mechanical forces because of the relative motion of the airfoil around the air. The geometric shapes of airfoils are designed to maximize the power production. The shape of an airfoil is shown in Figure 5.3. The straight line joining the leading and trailing edges of the airfoil is called the chord line. The most forward and backward points of the airfoil connect the mean camber line and are named leading and trailing edges. The thickness of the airfoil is the maximum distance between the lower and upper surfaces, measured perpendicular to the chord line. The camber is the distance between the chord line and the mean camber line of the airfoil, measured perpendicular to the chord line. The Angle of Attack (AOA) of an airfoil is defined as the relative angle (α) between the chord line and the incoming airflow.

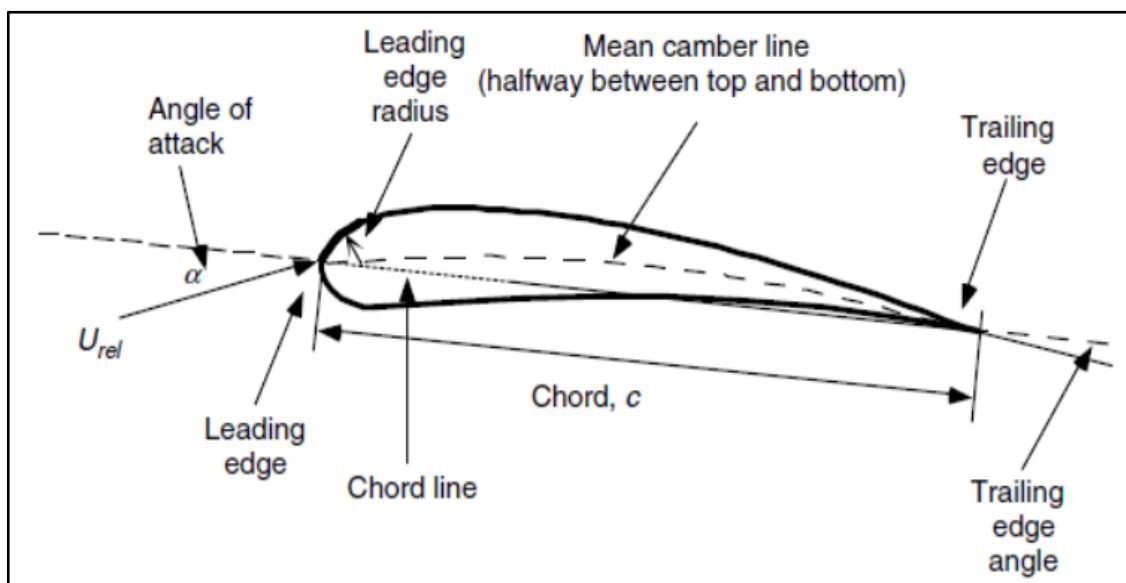


Figure 5.3 Airfoil nomenclature (McGowan, 2009)

5.5 Lift, Drag and Moment Coefficients Analysis of a Turbine Blade

Air flow over an airfoil produces distribution of forces over the entire airfoil surface. Because of this, two forces and one moment are created on the surface of the airfoil. The lift force is perpendicular to the direction of the incoming air flow and is primarily the result of the angle of attack. It occurs due to the unequal pressures on the top and bottom surfaces of the airfoil. The force which is parallel to the direction of the oncoming air flow is the drag force. The primary objective when designing wind turbine airfoil shapes is to generate more lift force with less drag force. Figure 5.4 shows the force distribution and the moment acting at a distance $(C / 4)$ from the leading edge.

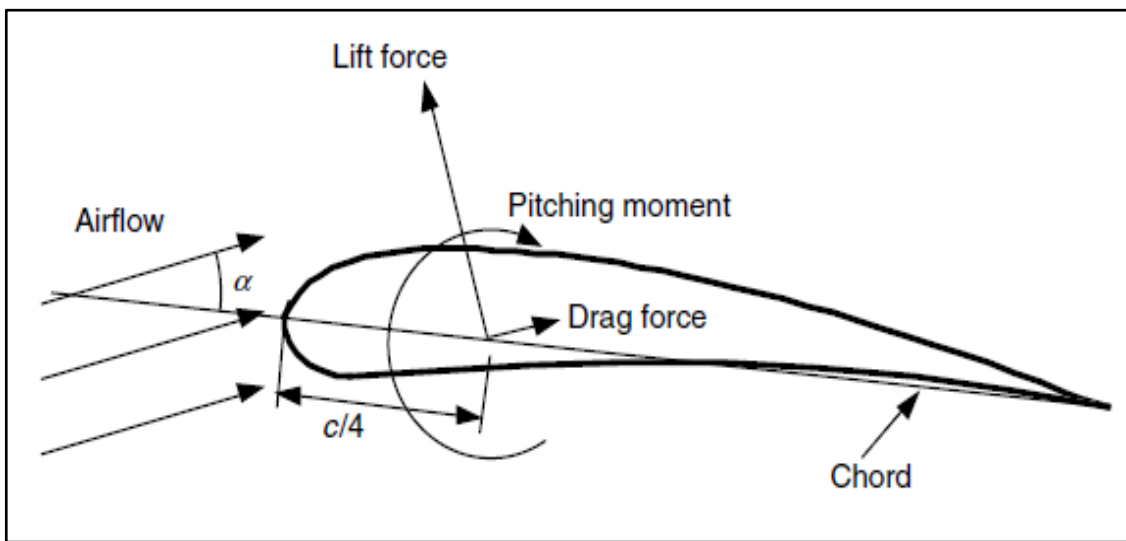


Figure 5. 4 Forces and moments on an airfoil section (McGowan, 2009)

Theoretical analysis to compute the lift coefficient C_l is presented next. Chord length of the airfoil C_l is given by

$$C_l = \frac{F_L}{1/2\rho U^2 c} \quad (5.38)$$

Drag coefficient C_d can be expressed as

$$C_d = \frac{F_D}{1/2\rho U^2 c} \quad (5.39)$$

Pitching moment coefficient C_M is given by

$$C_M = \frac{M}{1/2\rho U^2 A c} \quad (5.40)$$

where A is the projected airfoil area ($Chord \times Span$). The most important non-dimensional parameter for fluid flow also used to measure the lift and drag coefficients of air flow is the Reynolds number Re given by

$$Re = \frac{UL}{\nu} = \frac{\rho UL}{\mu} = \frac{\text{Inertial force}}{\text{Viscous force}} \quad (5.41)$$

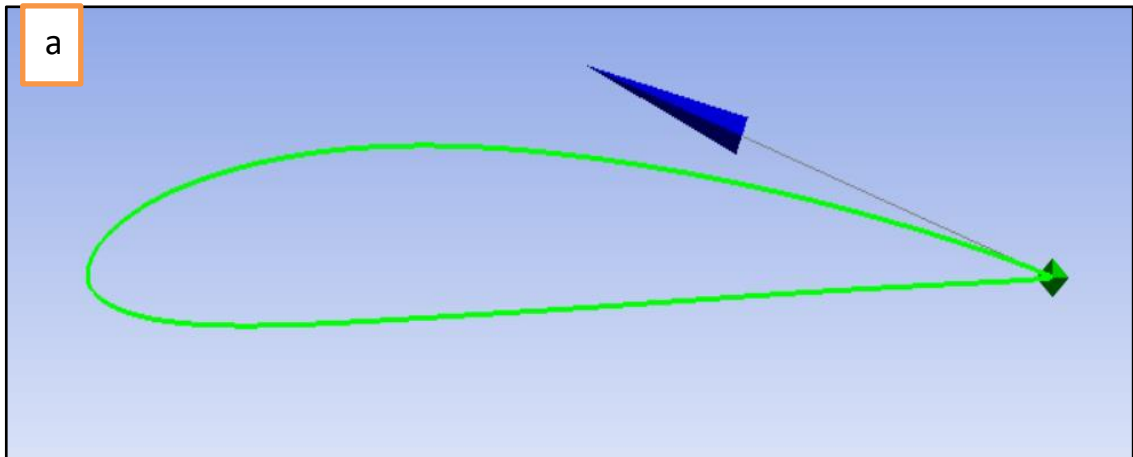
where μ is air viscosity, $\nu = \frac{\mu}{\rho}$ is the kinematic viscosity, U is undisturbed air flow velocity and L is the chord length of the airfoil.

5.5.1 Parameters Considered on Modelling Wind Turbine Airfoils

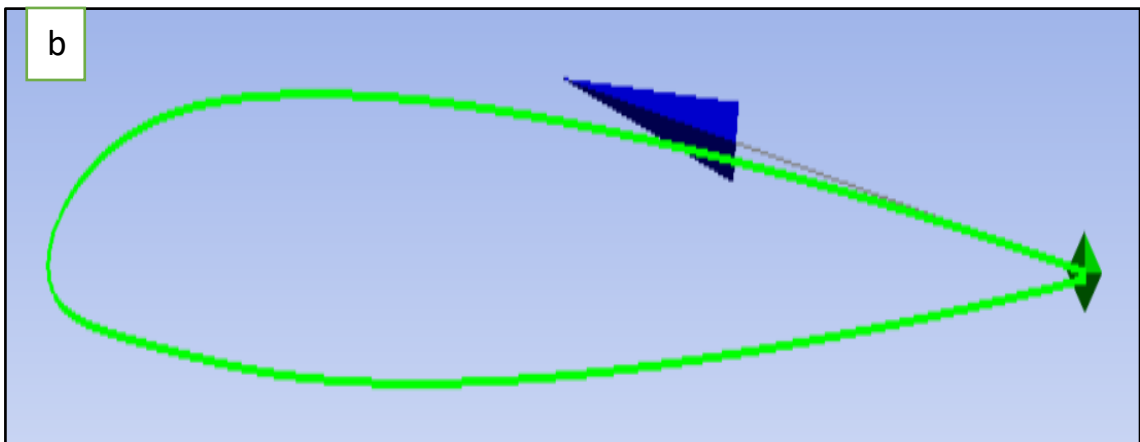
One important key element for the design of wind turbines is to choose the right airfoil to convert the kinetic energy of the airflow into mechanical energy in an inexpensive and efficient way. Currently, there are different types of airfoils for wind turbine blades such as NACA airfoils, NREL airfoils and RISO airfoils. Airfoil properties for wind turbine blades include structural and aerodynamic characteristics.

The maximum airfoil thickness in the outer part of a blade is one of the parameters considered from a structural point of view. For an aerodynamic point of view, to improve the wind turbine performance, the aerodynamic efficiency (L/D) at the tip should be as high as possible. The sections of wind turbine airfoils are root, middle and the tip sections. An important point to consider in a blade design is that they do not lose their efficiency due to dust, dirt and ice accumulations on the leading edge and other sections of the blade. Moreover, low airfoil noise is an important parameter for the outer part of the blades, especially for onshore wind turbines.

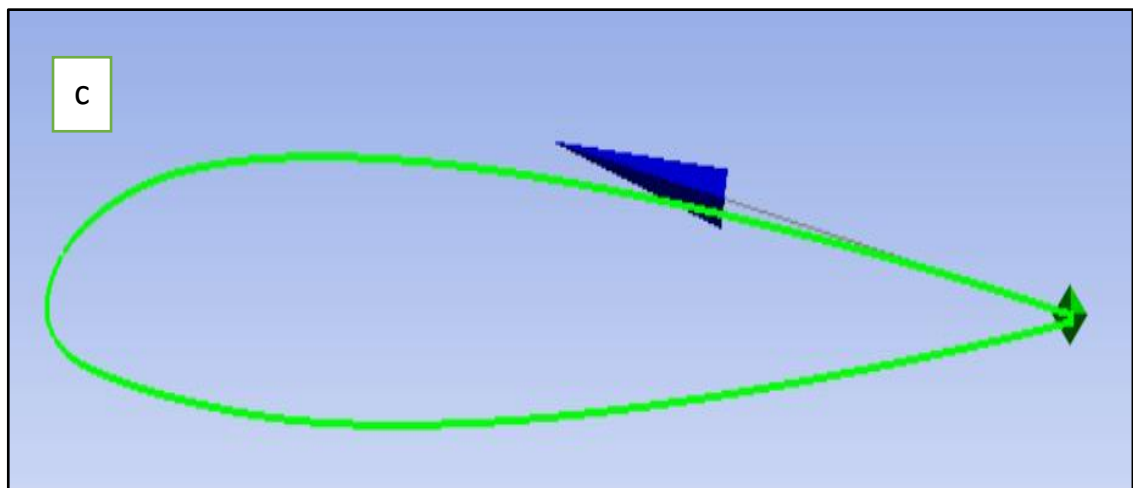
The performance of the Horizontal Axis Wind Turbine (HAWT) mainly depends on the type of airfoil, angle of attack and pitch angle. Before modelling and investigating the aerodynamic properties of wind turbine blades, it is necessary to find the aerodynamic behaviour of the airfoil taking into account different angles of attack and other parameters. To do this, aerodynamic characteristics of NACA 4415, NACA 23012 and NACA 23015 airfoils are selected to investigate. Results are given for five different Reynolds numbers and nominal angles of attack of 0° to 12° . Geometry of the three NACA airfoils are shown in Figure 5.5(a-c).



(a) NACA 4415 airfoil



(b) NACA 23012 airfoil



(c) NACA 23015 airfoil

Figure 5.5 Different NACA airfoils

Airfoil Characterization and Non-Dimensional Parameters

The aerodynamic efficiency (L/D), the lift coefficient and drag coefficient of each airfoil are determined using QBlade and XFOIL software's. Figure 5.6 shows L/D values for NACA 4415 airfoil for a range of Reynolds numbers. The results show that the maximum aerodynamic efficiency for NACA 4415 was about 175 at an angle of attack approaching 5° .

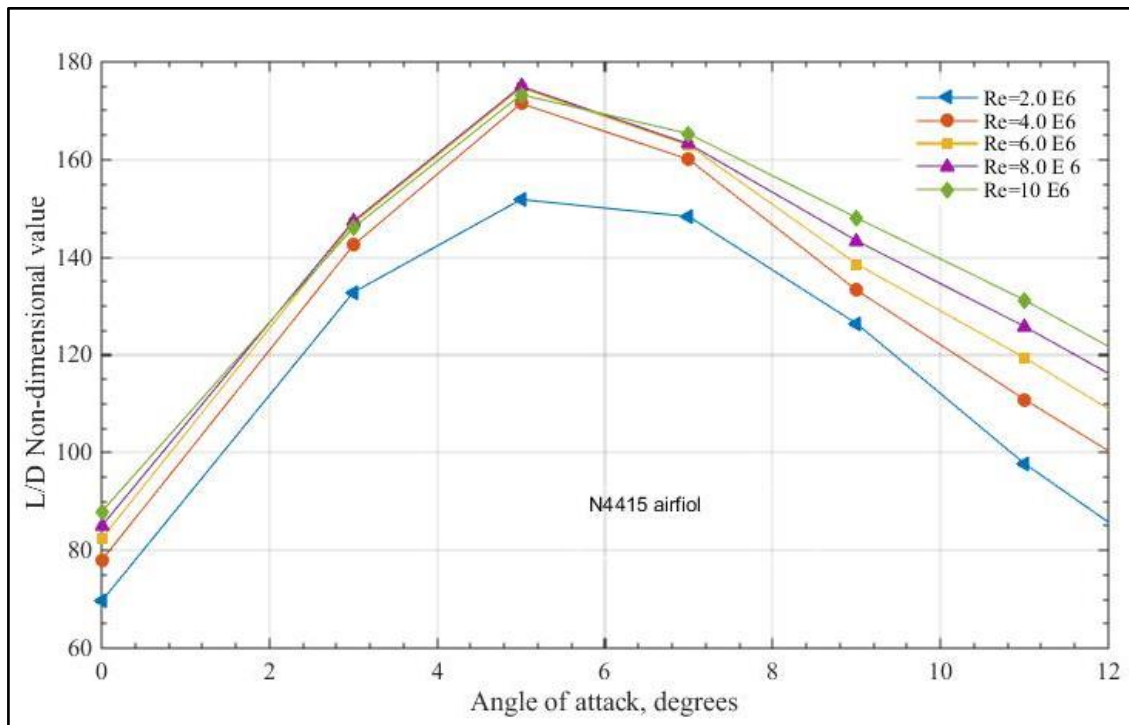


Figure 5.6 Non-dimensional parameters vs. angle of attack for NACA 4415 airfoil at different Reynolds numbers

Similarly, Figure 5.7 shows the aerodynamic efficiency of NACA 23012 airfoil for a range of Reynolds numbers. The results illustrate that the aerodynamic efficiency of NACA 23012 reaches about 155 with the angle of attack approaching 9° . This is a 11.43 % decrease as compared to NACA 4415 airfoil.

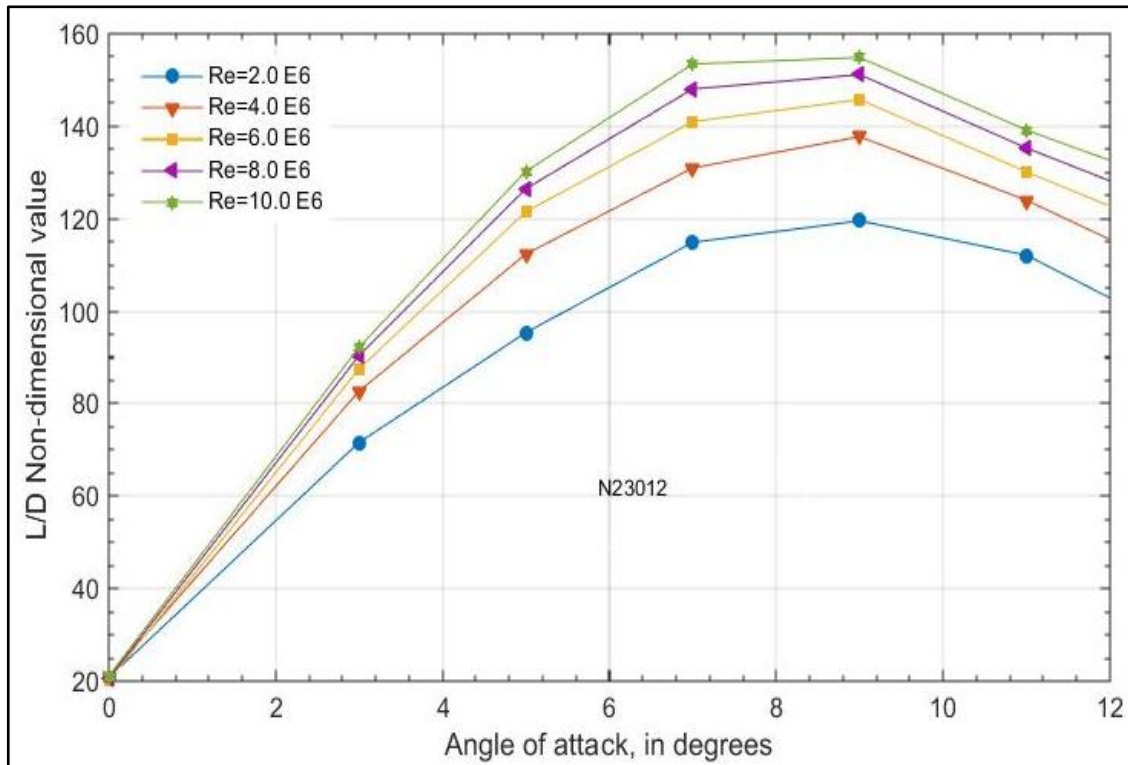


Figure 5.7 Non-dimensional parameters vs. angle of attack for NACA 23012 airfoil at different Reynolds numbers

Figure 5.8 shows the corresponding results for NACA 23015. The results indicate that the maximum aerodynamic efficiency for NACA 23015 is about 160 with the nominal angle of attack approaching 9° . Aerodynamic efficiency of this airfoil is reduced by 8.6% as compared to NACA 4415 airfoil. Considering the results from the three airfoils, it is observed that the aerodynamic efficiency depends on the angle of attack.

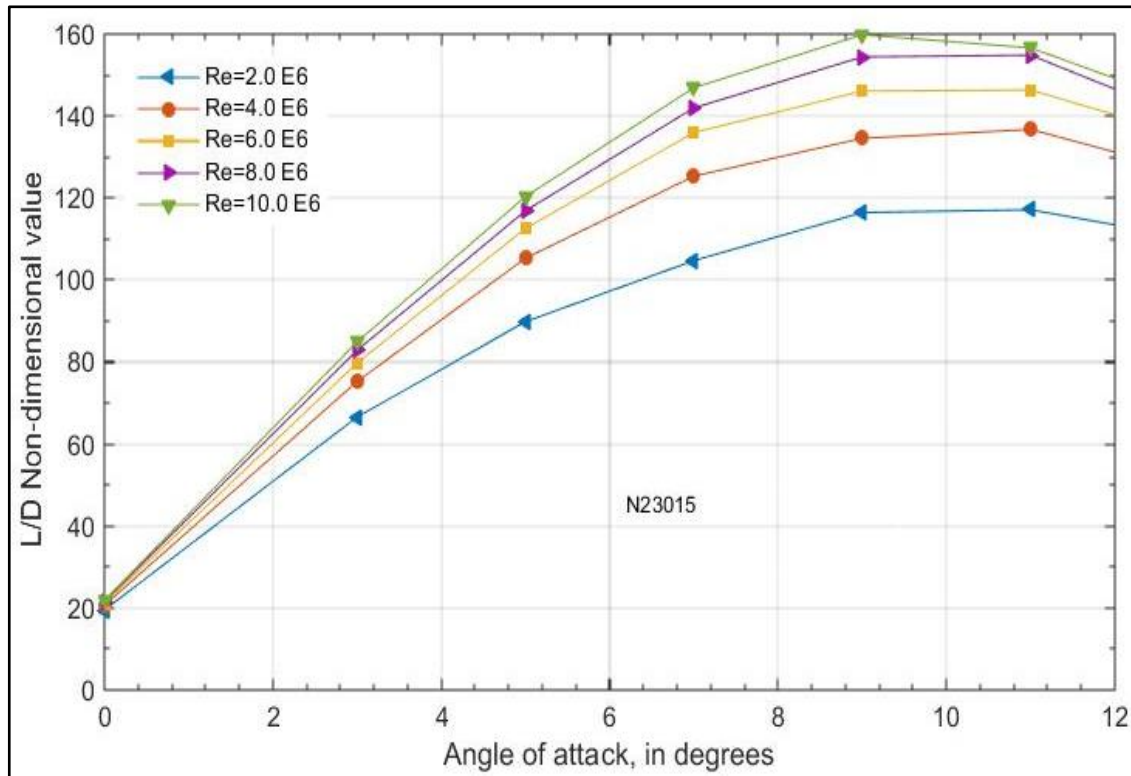


Figure 5.8 Non-dimensional parameters vs. angle of attack for NACA 23012 airfoil at different Reynolds numbers

The results obtained from the three airfoils are not enough to determine the position of the airfoils along the length of the blades in order to maximize the power output. It is necessary to consider the lift and drag coefficients of the three airfoils.

5.5.1.1 Modelling and Selection of Airfoils using QBlade/XFoil Techniques

There are different types of airfoil families which can be used to design horizontal axis wind turbines. Among them, NACA airfoils are the ones used most by wind turbine manufacturing industries. Each airfoil family is based on the shapes of the airfoils, the lift and drag coefficients and as such each one is different. It is important to select airfoils which have high lift and low drag coefficients. For this purpose, QBlade and XFoil open software packages are used. Figure 5.9 shows the lift coefficients of the three airfoils at various angles of attack (AOA) at a Reynolds number ($6e^6$). It is observed that at low angle of attacks, the lift coefficient (C_L) increases linearly and the maximum lift coefficient occurs at an angle attack of about 20° . Beyond this critical value of the angle of attack, the lift coefficient decreases with increasing AOA. The lift coefficients of

Airfoil Characterization and Non-Dimensional Parameters

NACA 23012 and NACA 23015 are nearly the same for AOA values, less than the critical value of the angle of attack. NACA 4415 airfoil has a better lift coefficient compared to the NACA 23012 and NACA 23015 airfoils.

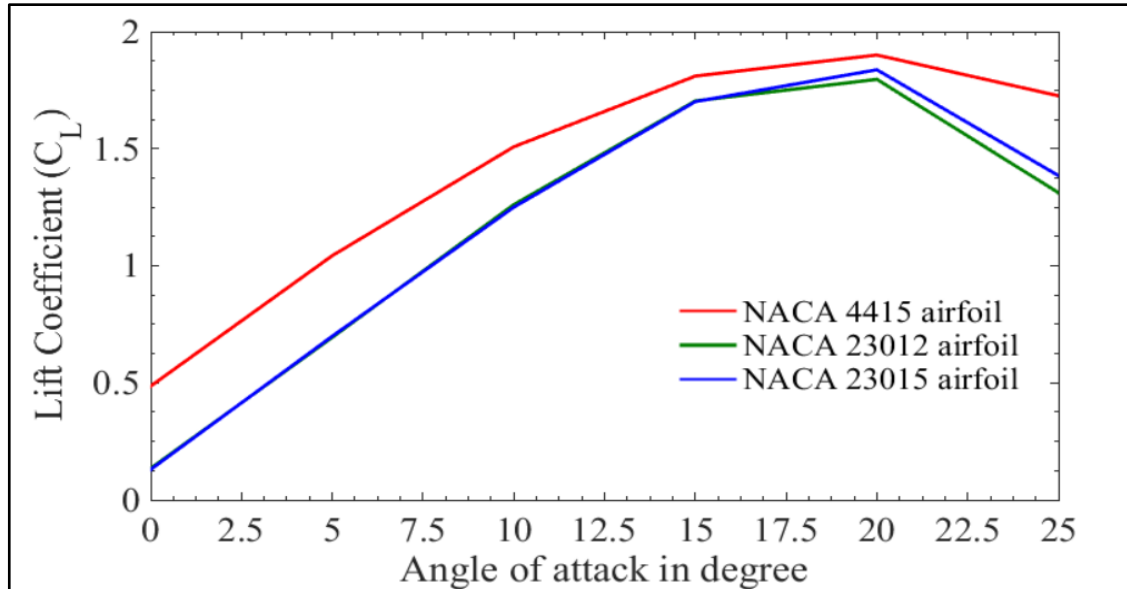


Figure 5.9 Lift coefficient vs (AOA) at Reynolds number ($6e^6$)

Figure 5.10 shows the drag coefficients of the three airfoils versus the angle of attack for the above airfoils at the Reynolds number ($6e^6$). The results show that these three airfoils have low drag coefficients for AOA values in the range 0° to 6° . When the AOA increases above 6° , the drag coefficients increase and NACA 4415 airfoil has a higher drag coefficient when the angle of attack is between 6° and 20° . The change in drag coefficients of NACA 23012 and NACA 23015 airfoils are nearly similar for the angle of attack values between 6° and 15° . NACA 23012 and NACA 23015 airfoils have low drag coefficients for AOA values between 6° to 20° . As such these airfoils are the better choice in this range of the angle of attack values. The properties of each airfoil vary with respect to lift and drag coefficients and it is important to investigate the parameters for the design of airfoils.

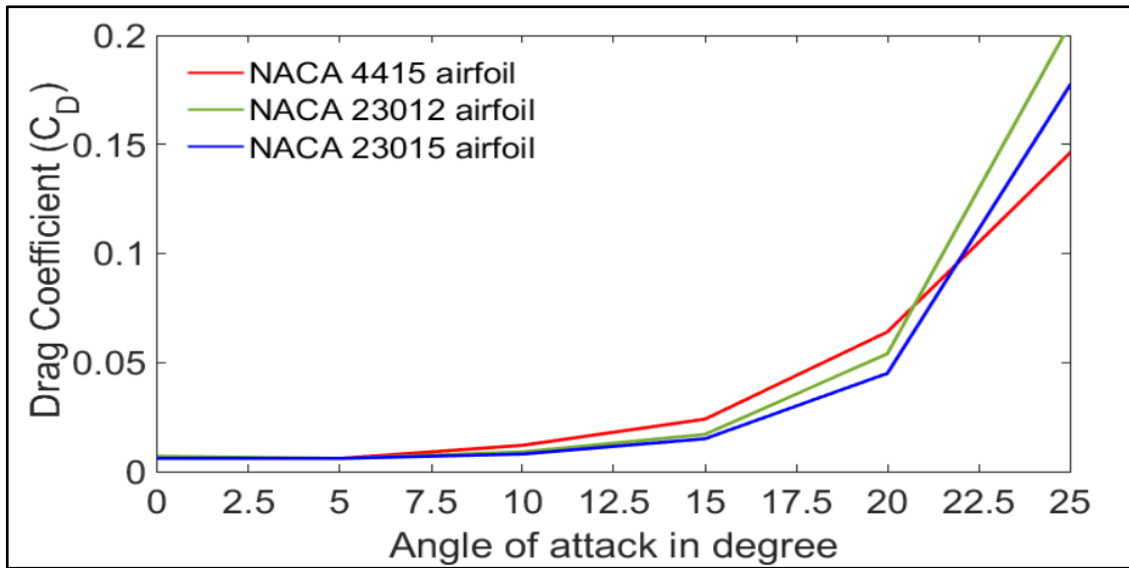


Figure 5.10 Drag coefficient model vs. (AOA) at Reynolds number ($6e^6$)

The ratio of lift to drag coefficient versus AOA is shown in Figure 5.11 at a Reynolds number ($6e^6$). It is observed that the maximum lift to drag coefficient of NACA 4415 airfoil is about 173 when the angle of attack approaches 5° and after this value of AOA this coefficient decreases substantially. The maximum lift to drag coefficients of NACA 23012 and NACA 23105 airfoils are about 140 and 156, respectively, at an angle of attack with values of approximately 10° . These values are 19% and 9.8% less than the corresponding value for NACA 4415 airfoil.

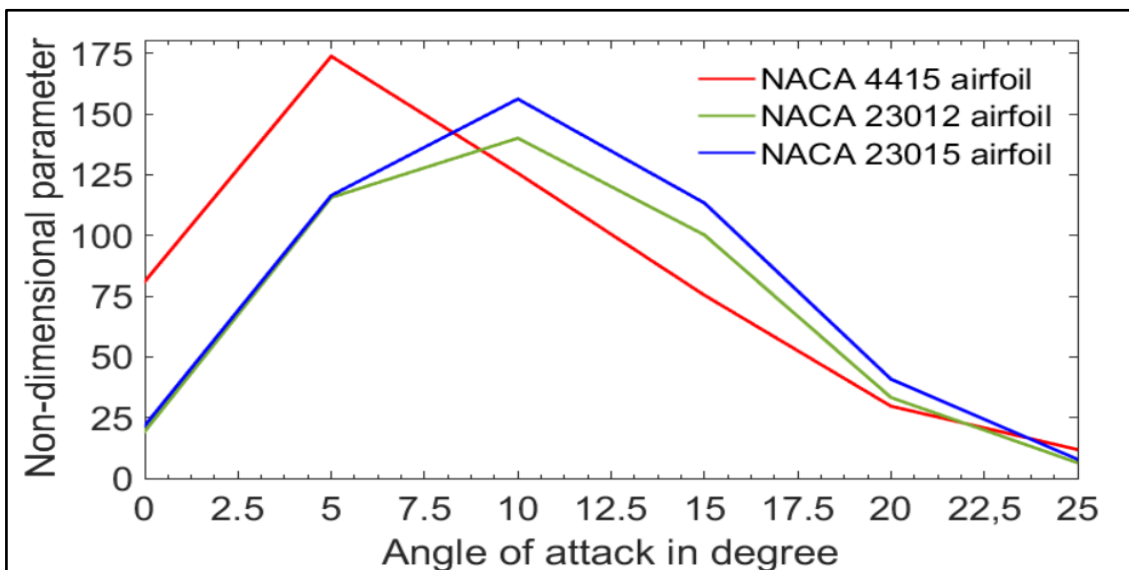


Figure 5.11 Ratio of lift to drag coefficient vs. (AOA) at Reynolds number ($6e^6$)

Airfoil Characterization and Non-Dimensional Parameters

Figure 5.12 shows the non-dimensional aerodynamic efficiency ratio denoted by (L/D) plotted against the angle of attack. The maximum aerodynamic efficiency (L/D) of NACA 4415 airfoil is about 177 at an angle of attack of 5° and this value decreases afterwards. The maximum aerodynamic efficiency of NACA 23012 is about 122, and that of NACA 23015 is about 112.6. These values are 31% and 36.38% less than the corresponding value for NACA 4415 airfoil. As the angle of attack increases and approaches 10° , the maximum aerodynamic efficiency of NACA 23012 airfoil is about 129.8 representing a 6% increase. The maximum aerodynamic efficiency NACA 23015 airfoil is about 147.8 representing a 23.8% increase. The aerodynamic efficiency of NACA 4415 airfoil is about 129.8 at an AOA of 10° representing a 26.6% decrease as compared to its value at 5° .

These non-dimensional parameters, as discussed above, indicate that aerodynamic behaviours of airfoils depend on the angle of attack. The non-dimensional parameters are used to determine the most suitable airfoil model and its position. In the above figures the angle of attack values ranged from 5° to 10° and the three airfoils had similar aerodynamic efficiency values at an angle of attack 8.5° .

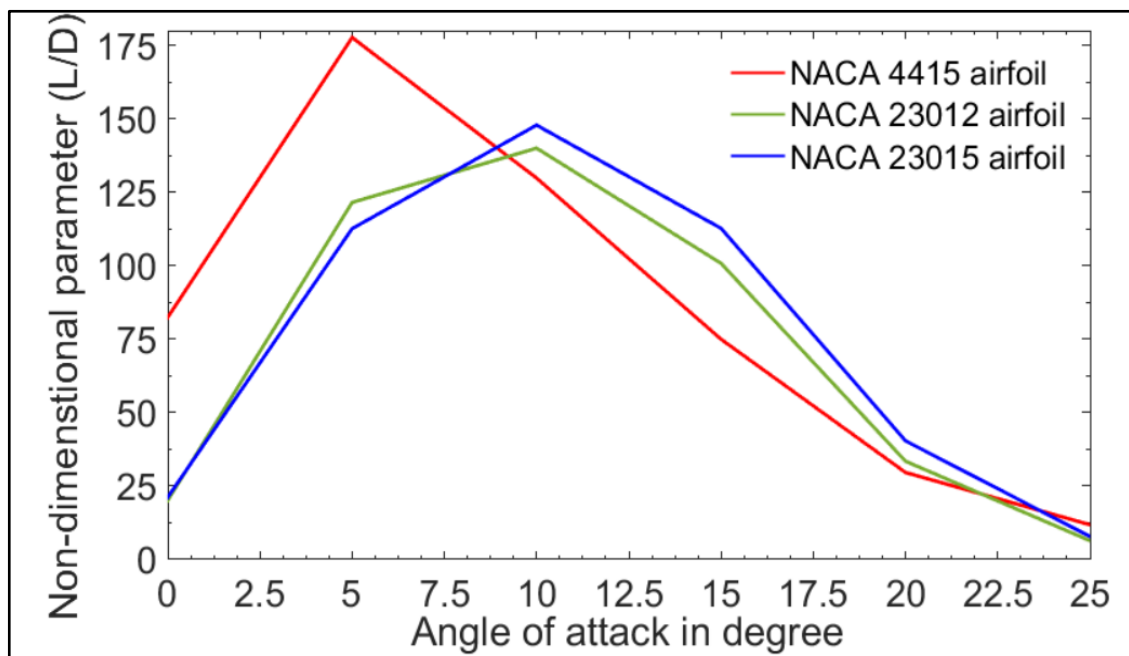


Figure 5.12 Non-dimensional parameter (L/D) ratio vs. (AOA) at Reynolds number $(6e^6)$

Airfoil Characterization and Non-Dimensional Parameters

Figure 5.13 shows the lift coefficient versus drag coefficient at Reynolds number ($6e^6$) for NACA 4415, NACA 23012 and NACA 23015 airfoils. The lift coefficient of NACA 4415 airfoil is approximately 1.043. The drag coefficient is about 0.006 for an AOA of 5° . The angle of attack changes to 10° as the lift and drag coefficients increase by 30.83 % and 50%. The lift coefficient of NACA 23012 airfoil is about 0.694 and its drag coefficient is about 0.006 when the AOA is 5° . The lift and drag coefficients increase by 44.96 % and 33.3% as AOA becomes 10° . The lift and drag coefficients of NACA 23015 airfoil are 0.699 and 0.006 at an angle of attack of 5° . These values change by 44 % and 25% when AOA is 10° .

The results for the three airfoils indicate that NACA 4415 airfoil has high lift and low drag coefficients and the other two airfoils have lower lift coefficients as compared to NACA 4415 airfoil. These two airfoils have lower drag coefficients and the increase is less as AOA increases as compared to NACA 4415 airfoil. To maximize the power output of a wind turbine, high lift coefficients and low drag coefficients are needed.

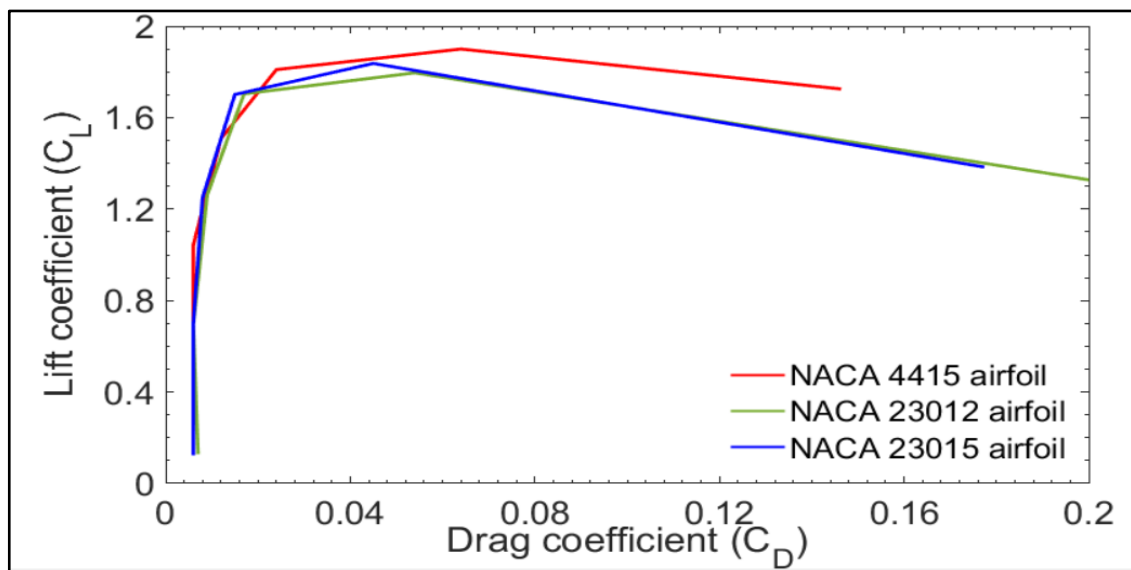


Figure 5.13 Lift coefficient vs. drag coefficient at Reynolds number ($6e^6$)

In Figures 5.14, 5.15 and 5.16, simulation results are given for the three airfoils to determine the pressure distributions and aerodynamic efficiencies (L/D) at an angle of attack of 8.5° . The results show that the lift and drag coefficients, and the aerodynamic efficiencies of the airfoils are different. These three airfoils are selected to model the

Airfoil Characterization and Non-Dimensional Parameters

geometries of wind turbine blades using QBlade/XFoil software. Table 5.1 describes the aerodynamic behaviours of the three airfoils at Reynolds number ($6e^6$).

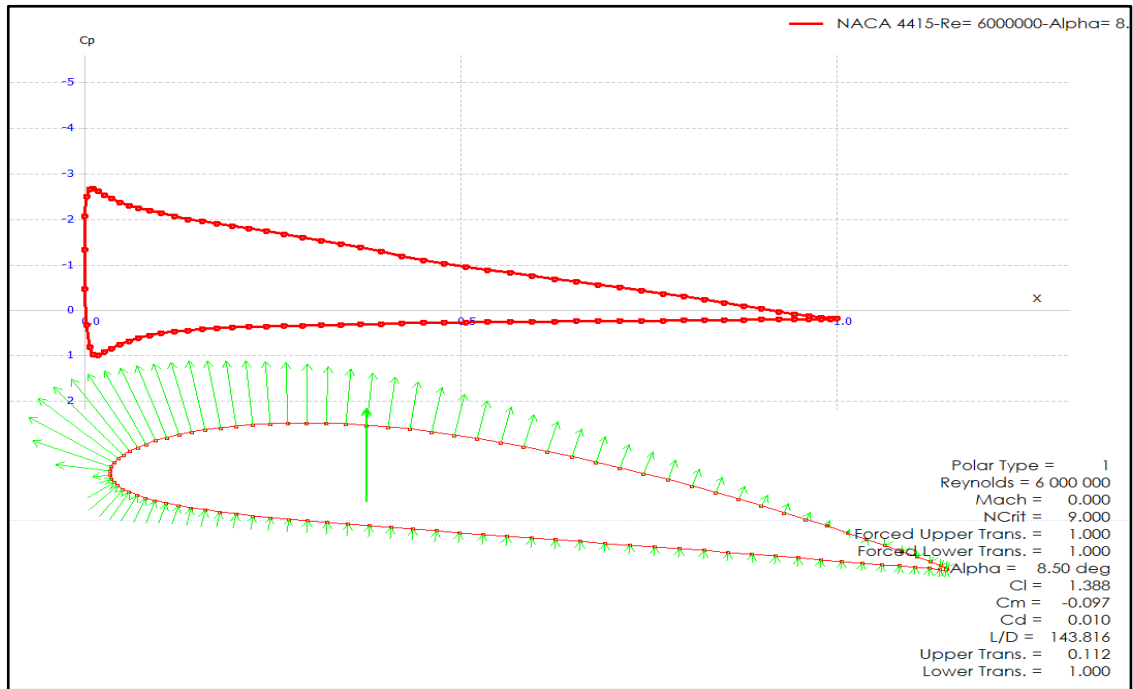


Figure 5.14 Pressure coefficient vs angle of attack at Reynolds number ($6e^6$) for NACA 4415 airfoil

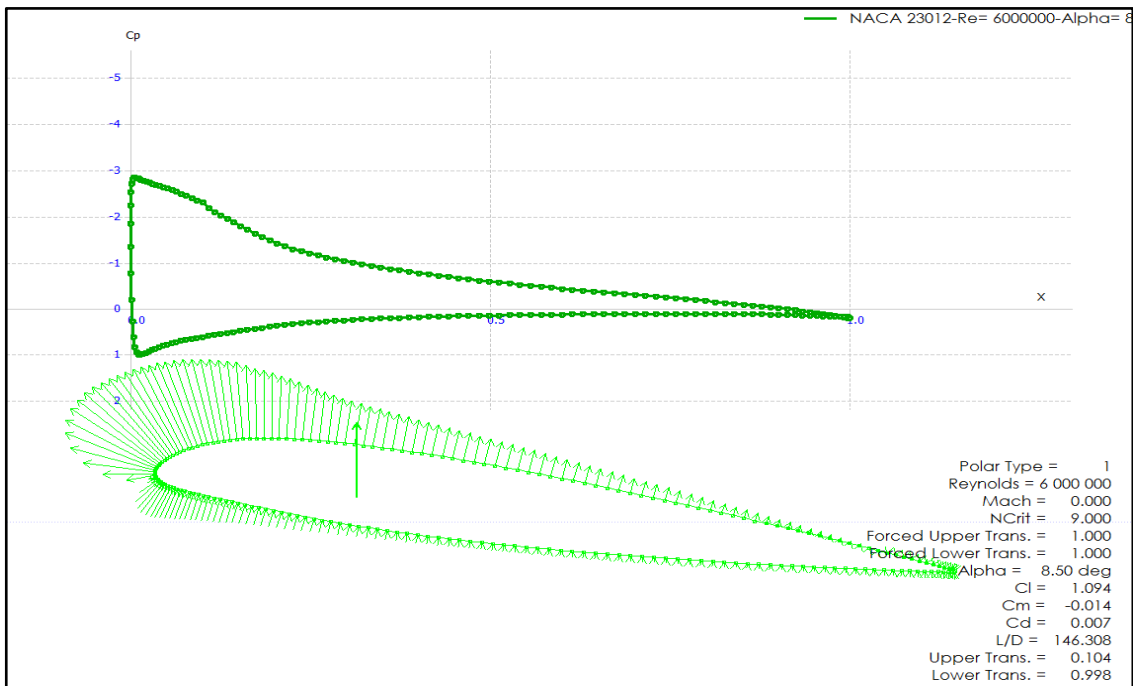


Figure 5.15 Pressure coefficient vs angle of attack at Reynolds number ($6e^6$) for NACA 23012 airfoil

Airfoil Characterization and Non-Dimensional Parameters

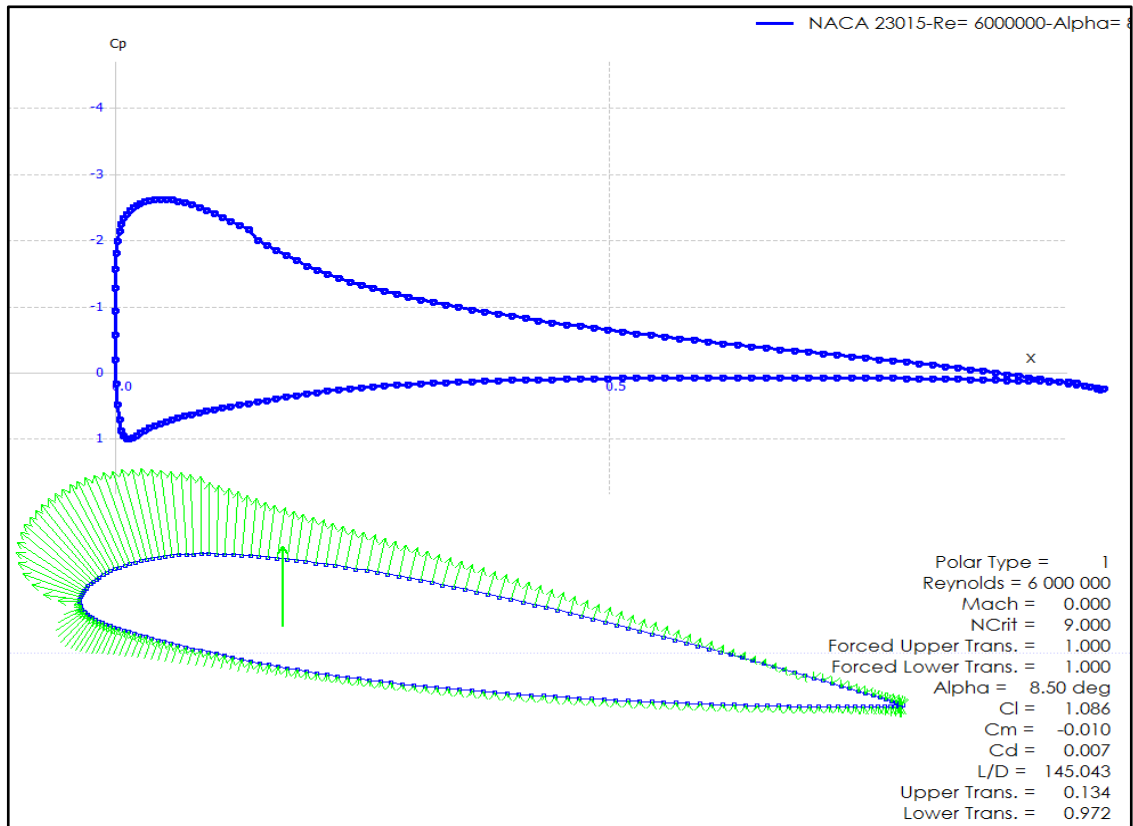


Figure 5.16 Pressure coefficient vs. angle of attack at Reynolds number ($6e^6$) for NACA 23015 airfoil

Table 5.1 Aerodynamic behaviour of NACA airfoils used as wind turbine blades

Airfoil types	Angle of attacks in degrees					
	0	5	10	15	20	25
NACA 4415 (C_L)	0.486	1.043	1.508	1.810	1.90	1.726
NACA 23012 (C_L)	0.135	0.694	1.261	1.704	1.796	1.312
NACA 23015 (C_L)	0.130	0.699	1.250	1.701	1.837	1.385
NACA 4415 (C_d)	0.006	0.006	0.012	0.024	0.064	0.146
NACA 23012 (C_d)	0.007	0.006	0.009	0.017	0.054	0.205
NACA 23015 (C_d)	0.006	0.006	0.008	0.015	0.045	0.177
NACA 4415 (L/D)	82.378	177.643	129.804	74.959	29.616	11.831
NACA 23012 (L/D)	20.078	121.520	139.987	100.788	33.44	6.406
NACA 23015 (L/D)	21.181	112.608	147.830	112.714	40.379	7.830
NACA 4415 ($C_L C_d$)	81.00	173.83	125.66	75.42	29.69	11.82
NACA 23012 $C_L C_d$	19.29	115,67	140.11	100.24	33.26	6.4
NACA 23015 $C_L C_d$	21.67	116.5	156.25	113.4	40.82	7.82

5.5.1.2 Modelling and Selection of Airfoil using CFD Technique

There are many types of airfoils available for horizontal-axis wind turbine blades. NACA airfoils are used widely by most manufacturing industries. In the present study, QBlade/XFoil open software is used in order to investigate the aerodynamic behaviours of NACA 4415, NACA 23012 and NACA 23015 airfoils. The accurate aerodynamic modelling of airfoils is important to improve the efficiency of wind turbines. For this purpose, Computational Fluid Dynamics (CFD) is employed. Specifically, CFD analysis using shear stress transport (SST) $k - \omega$ model is used in the study of NACA 4415, NACA 23012 and NACA 23015 airfoils. Non-dimensional parameters such as lift coefficient, drag coefficient and pitching moment coefficient are computed at an angle of attack of 8.5° . Velocity and pressure distributions along the surface of the airfoils are computed and compared to determine the location of the airfoils along the length of the blades. Comparisons of the CFD simulations with QBlade simulations are made to assess the accuracy of parameters for modelling the wind turbine blades. For 2-D analysis of steady and incompressible flow, the continuity equation is given by

$$\nabla \cdot (\rho V) = \frac{\partial(\rho u)}{\partial x} + \frac{\partial(\rho v)}{\partial y} = 0 \quad (5.42)$$

The momentum equation for viscous flow in the x direction is

$$\rho \frac{Du}{Dt} = -\frac{\partial p}{\partial x} + \frac{\partial \tau_{xx}}{\partial x} + \frac{\partial \tau_{yx}}{\partial y} + \frac{\partial \tau_{zx}}{\partial z} + \rho f_x \quad (5.43)$$

where u is the velocity component in the x direction, p is the pressure, τ 's represent normal and shear stresses acting on the surface of the fluid particle, and f_x represents the body forces per unit length in the x direction. In the continuity equation for 2D flow, the term $\frac{\partial(\rho w)}{\partial z}$ is dropped. In the momentum equation, the term $\frac{\partial \tau_{zx}}{\partial z}$ is dropped. All airfoil simulations were performed using (SST) $k - \omega$ model. A flow domain was developed surrounding the NACA 4415, NACA 23012 and NACA 23015 airfoils. The chord length (C) of the NACA airfoils is taken as 1m. The upstream and downstream of the domains were taken at about 10 times the chord length of the airfoils. A fully turbulent flow solution was used in ANSYS Fluent 16.2 where (SST) $k - \omega$ model was employed to represent turbulent viscosity. ANSYS 16.2 fluent launcher was utilized in the simulations. This software has a density based solver and absolute velocity

Modelling and Selection of Airfoil using CFD Technique

formulation for 2D domains. Implicate solver and Roe-flax type were available and green-gauss cell was used for the gradient option. For discretization, kinetic energy of the flow and the dissipation rate were set to second order upwind. Angle of Attack (AOA) was taken as 8.5° and the speed of the air was specified as 9.56m/s and 25m/s. Figure 5.17 shows the boundary of the airfoil after a Boolean operation and the projection of the area of the airfoils.

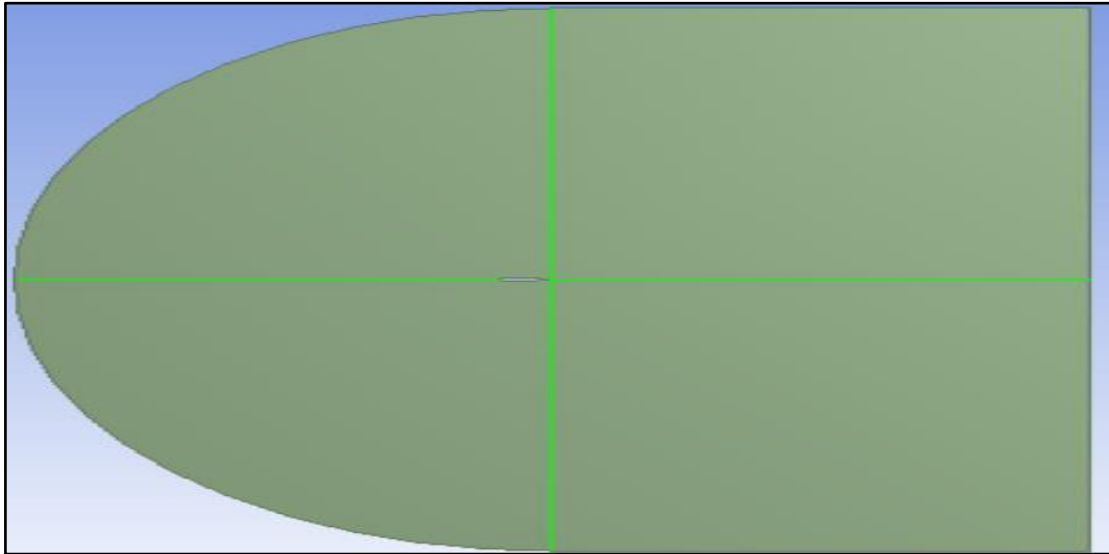


Figure 5.17 Boundary of the airfoils

A large number of grids around the aerofoil surfaces was used to capture the pressure gradients accurately at the boundary layer. Next, a mesh was generated for the airfoil geometries. Resolution of the mesh needed great accuracy in the areas surrounding the leading and trailing edges. In the far-field areas of the airfoils, the mesh resolution became progressively coarser since the flow gradients approach was close to zero in these areas. Figure 5.18 shows the mesh for the NACA 4415 airfoil consisting of 29538 nodes and 29153 elements.

Modelling and Selection of Airfoil using CFD Technique

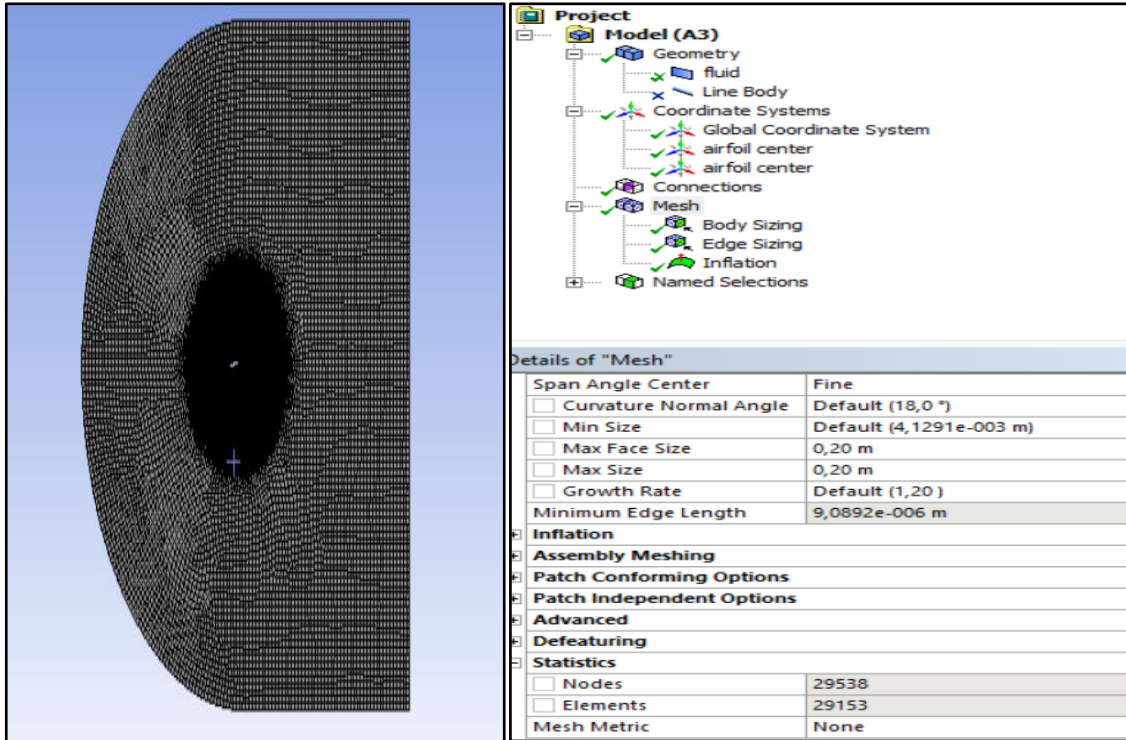


Figure 5.18 Mesh around NACA 4415 airfoil and the data

Figure 5.19 shows the mesh for NACA 23012 airfoil consisting of 29825 nodes and 29435 elements.

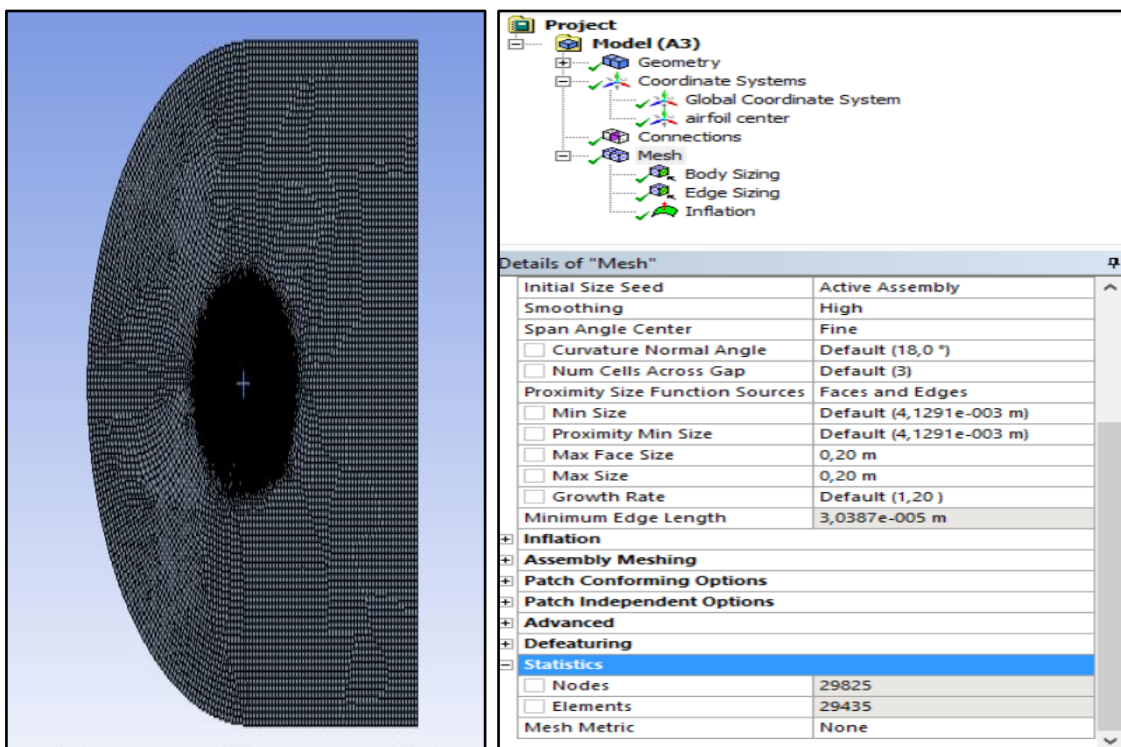


Figure 5.19 Mesh around NACA 23012 airfoils geometry and data

Modelling and Selection of Airfoil using CFD Technique

Figure 5.20 shows the mesh for NACA 23015 airfoil consisting of 29837 nodes and 29456 elements. Aerodynamic parameters were computed at wind speeds of 9.56m/s and 25m/s.

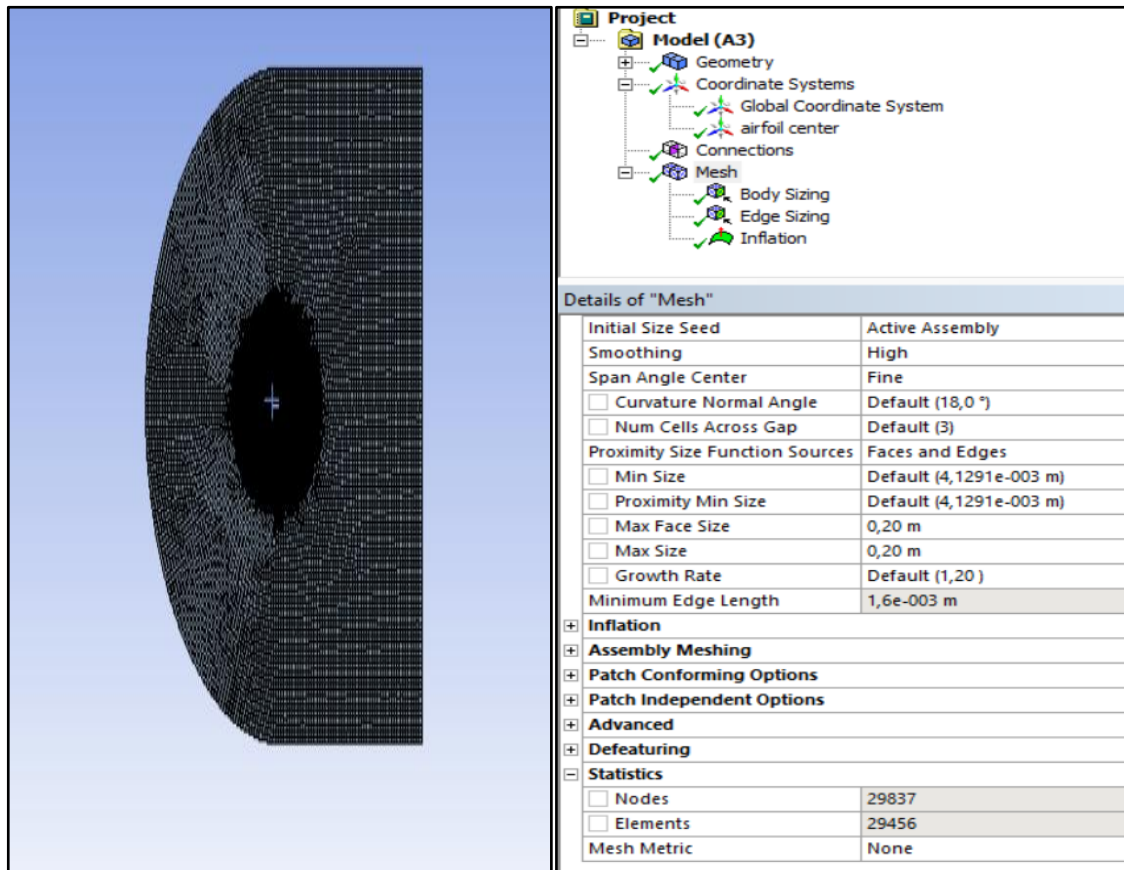


Figure 5.20 Mesh around NACA 23015 airfoils geometry and data

An aerodynamic study of NACA airfoils using CFD was performed by numerically solving the Reynolds Average Navier-Stokes (RANS) equations using the accompanying turbulence model. Figure 5.21 shows the polar curve of the lift coefficient for NACA 4415 airfoil after 2000 iterations to determine the location of the airfoil along the length of the wind turbine blade. Simulation results show that the lift coefficient of NACA 4415 airfoil decreases and the lowest value is about 0.775. After this value, the lift coefficient increases to approximately 0.850 and keeps stable.

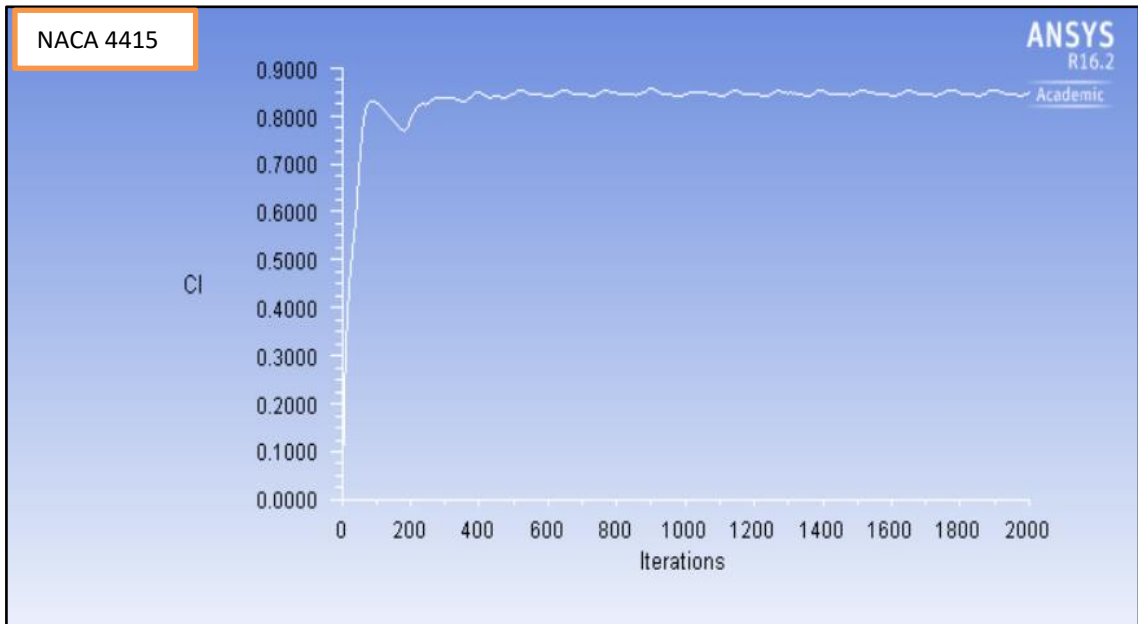


Figure 5.21 Lift coefficient vs the number iterations for NACA 4415 airfoil

Simulation results for NACA 23012 airfoil show that the lift coefficient decreases and the lowest value is approximately 0.550 after 200 iterations. Subsequently, it increases to a value of 0.690 and keeps stable after 2000 iterations. The lift coefficient of NACA 23012 is 18.8% less than that of NACA 4415 airfoil.

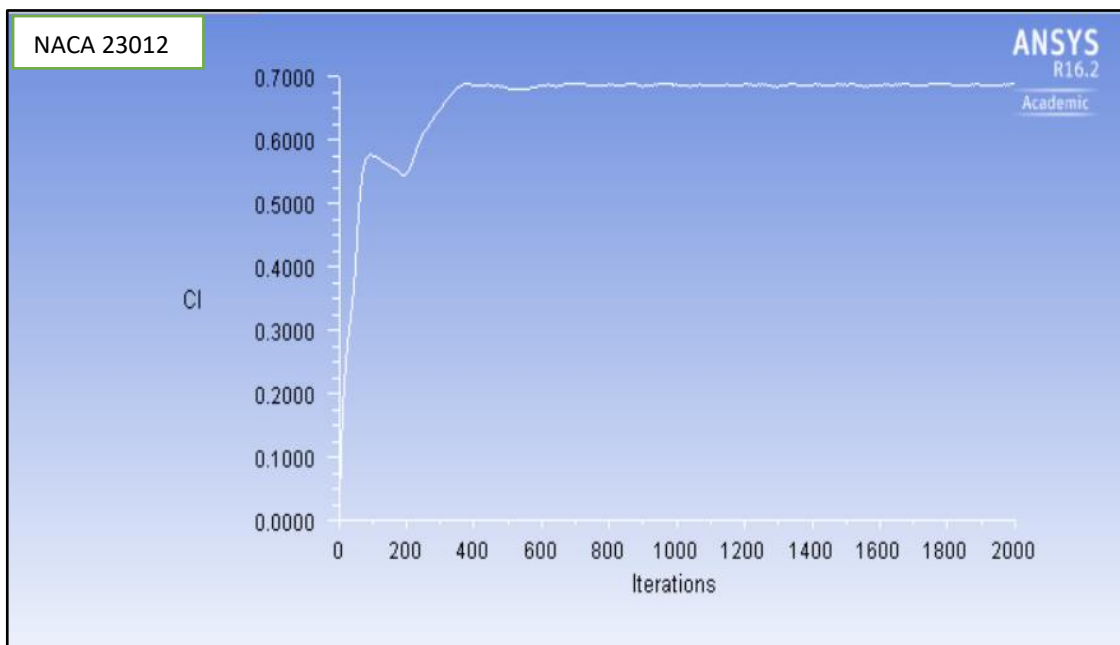


Figure 5.22 Lift coefficient vs the number of iterations for NACA 23012 airfoil

Modelling and Selection of Airfoil using CFD Technique

The lift coefficient of NACA 23015 airfoil is approximately 0.525 after 200 iterations, increases to 0.660 and stays stable after 2000 iterations. The lift coefficient of NACA 23015 airfoil is 4.35% less than that of NACA 23012 airfoil and 22.35% less than that of NACA 4415 airfoil. NACA 4415 airfoil gave the highest lift coefficient value as compared to other airfoils.

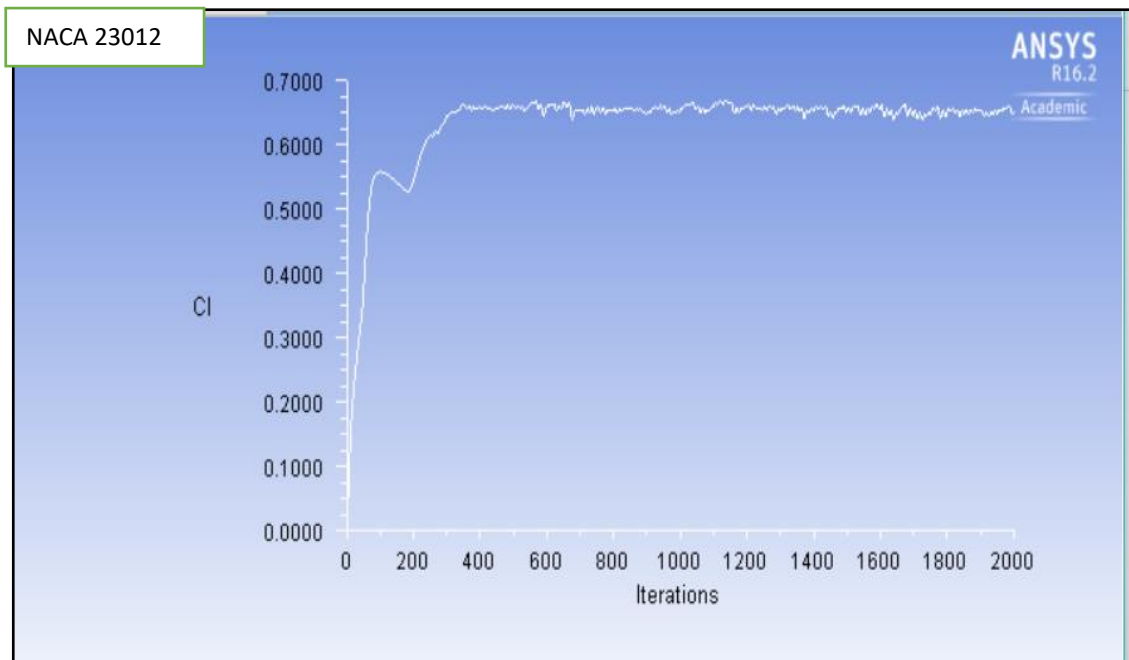


Figure 5.23 Lift coefficient values vs the number of iterations for NACA 23015 airfoils

Next, the drag coefficients of NACA 4415, NACA 23012 and NACA 23015 airfoils were computed to determine the airfoil with the lowest drag coefficient. Figure 5.24 shows the polar curve of drag coefficient for NACA 4415 airfoil. The simulation results indicate that the drag coefficient of NACA 4415 airfoil increases and the highest value is 0.0838 after 50 iterations. After that, the drag coefficient decreases to a value of 0.0550 after 200 iterations and keeps stable at 0.060 after 2000 iterations.

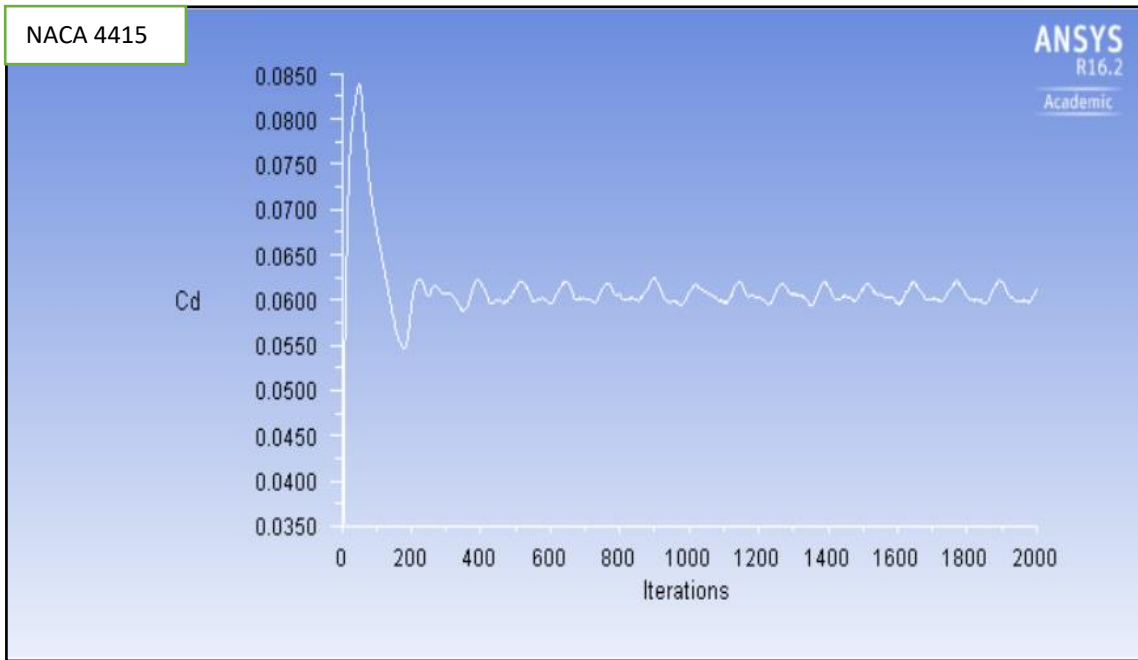


Figure 5.24 Drag coefficient vs the number of iterations for NACA 4415 airfoil

The highest value of the drag coefficient for NACA 23012 airfoil was computed as 0.0563 after 50 iterations as shown in Figure 5.25. It decreases to a value of 0.0425 after 200 iterations and keeps stable at 0.0513 after 2000 iterations. This indicates that the drag coefficient NACA 23012 is 14.5% less than that of NACA 4415 airfoil.

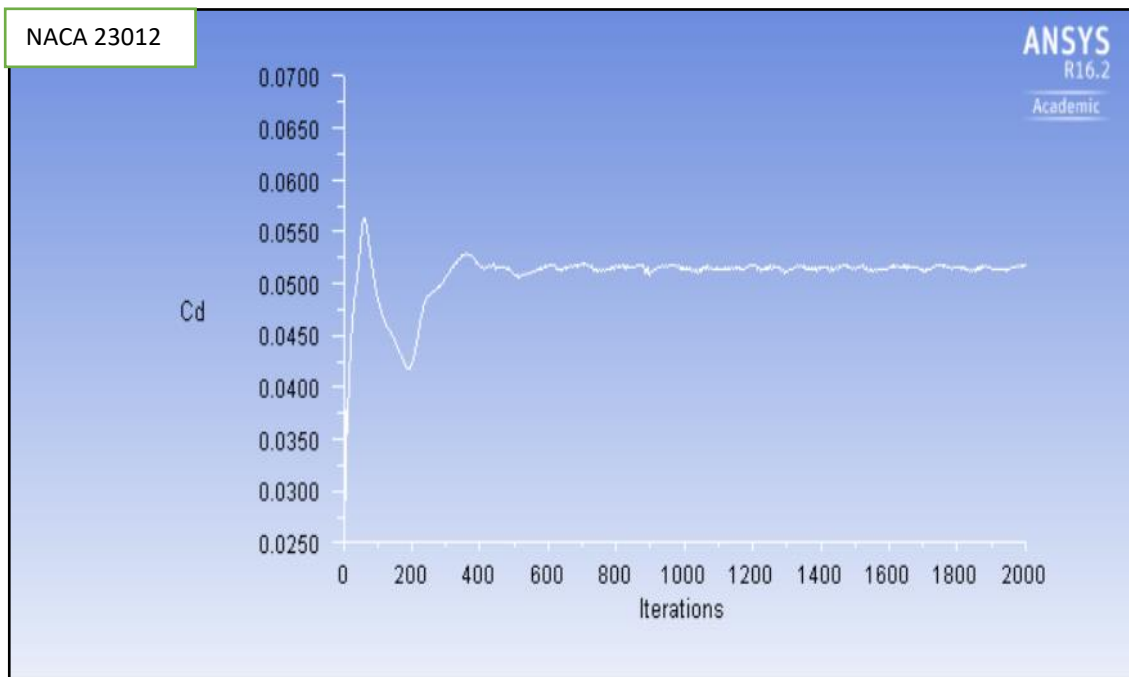


Figure 5.25 Drag coefficient vs the number of iterations for NACA 23012 airfoil

Modelling and Selection of Airfoil using CFD Technique

The drag coefficient of NACA 23015 airfoil reaches a value of 0.0550 after 50 iterations as shown in Figure 5.26. After this value, it decreases to 0.0413 after 200 iterations and keeps stable at 0.0500 after 2000 iterations. The drag coefficient of this airfoil is 16.67% less than that of a NACA 4415 airfoil.

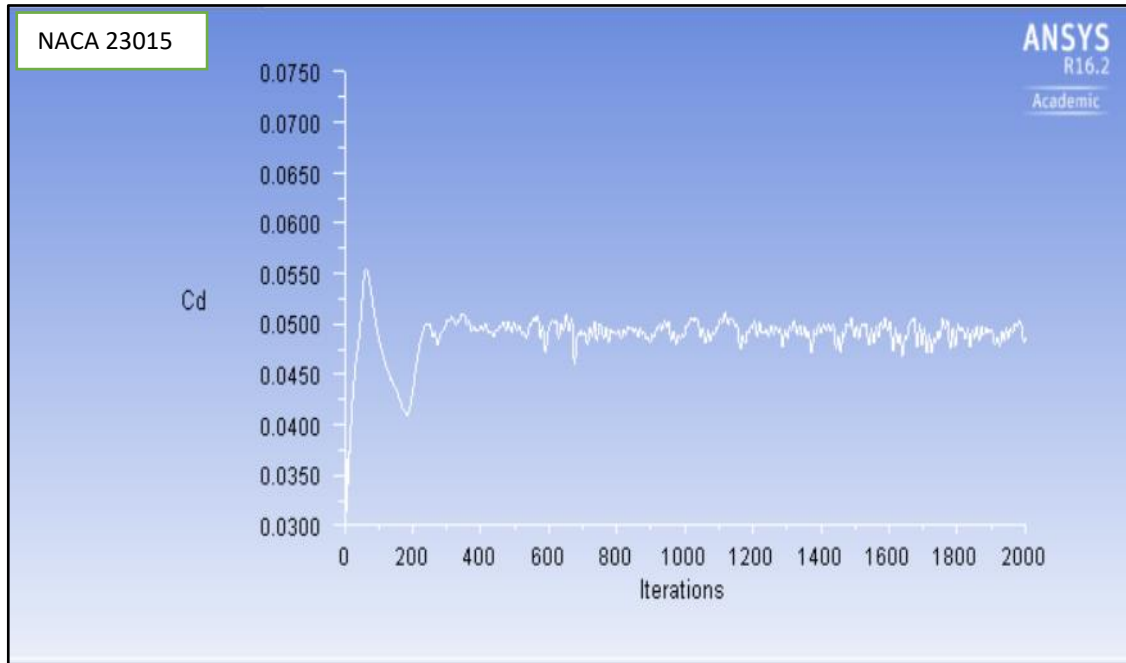


Figure 5.26 Drag coefficient vs the number of iterations for NACA 23015 airfoils

Results indicate that NACA 23015 airfoil has the lowest drag coefficient and NACA 4415 airfoil has the highest one. Wind speeds of 9.56m/s and 25m/s at an angle of attack 8.5° were used in the CFD simulations to compute the velocity and pressure differences for the three airfoils under consideration. Figure 5.27 shows the airflow around NACA 4415 airfoil at a wind speed of 9.56m/s and at an angle of attack of 8.5° . It is observed that the air velocity is faster on the upper surface as compared to the lower surface and the maximum velocity reaches 14.9m/s.

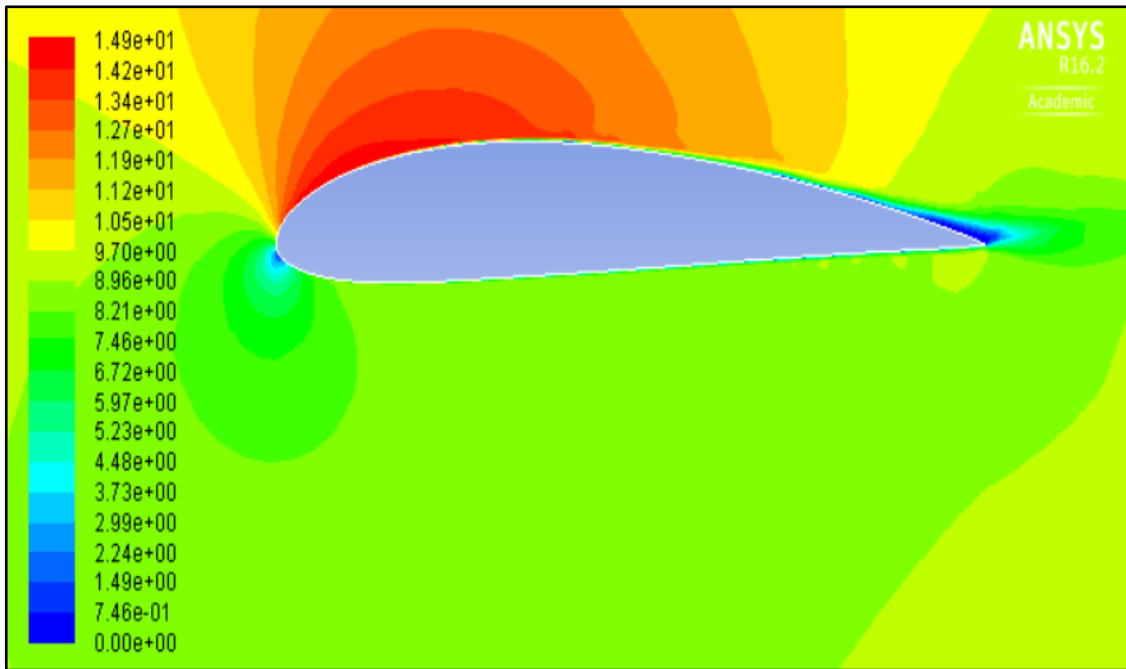


Figure 5.27 Contours of the velocity of the airflow around NACA 4415 airfoil

Figure 5.28 shows the airflow around NACA 23012 airfoil. It is noted that the maximum air velocity at the top surface reaches 15.2m/s. There is a 2% velocity difference between NACA 23012 and NACA 4415 airfoils.

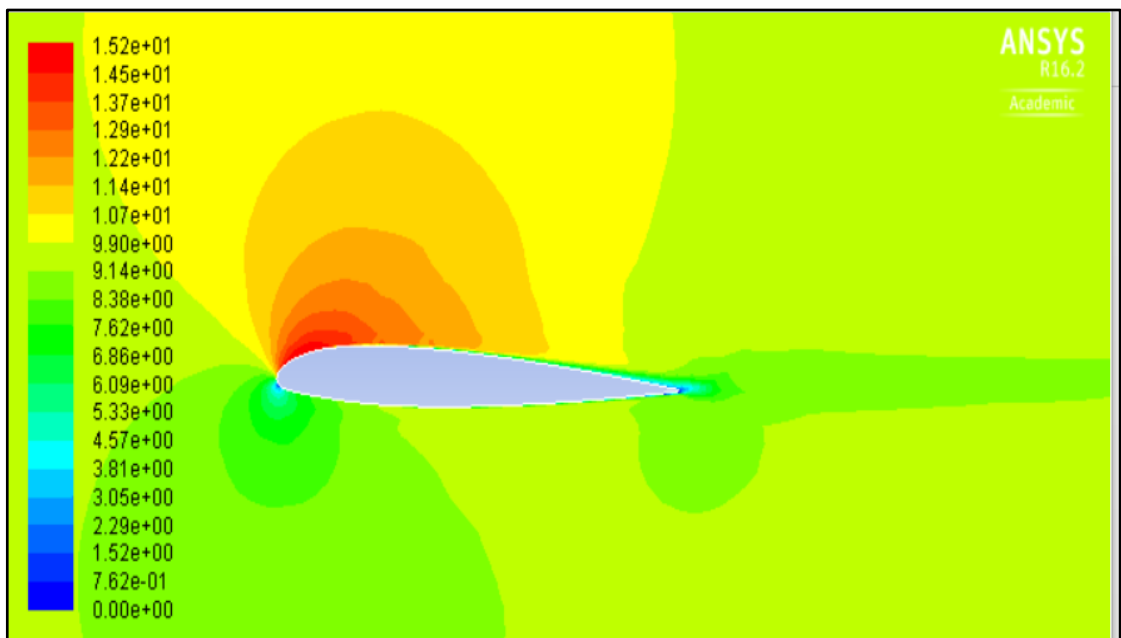


Figure 5.28 Contours of the velocity of the airflow around NACA 23012 airfoil

Figure 5.29 shows the airflow around NACA 23015 airfoil at the same wind speeds and angle of attack as in the above figures. In this case, the maximum air velocity at the upper surface is 15.1m/s and there is a 1.3% velocity difference between this airfoil and NACA 4415 airfoil.

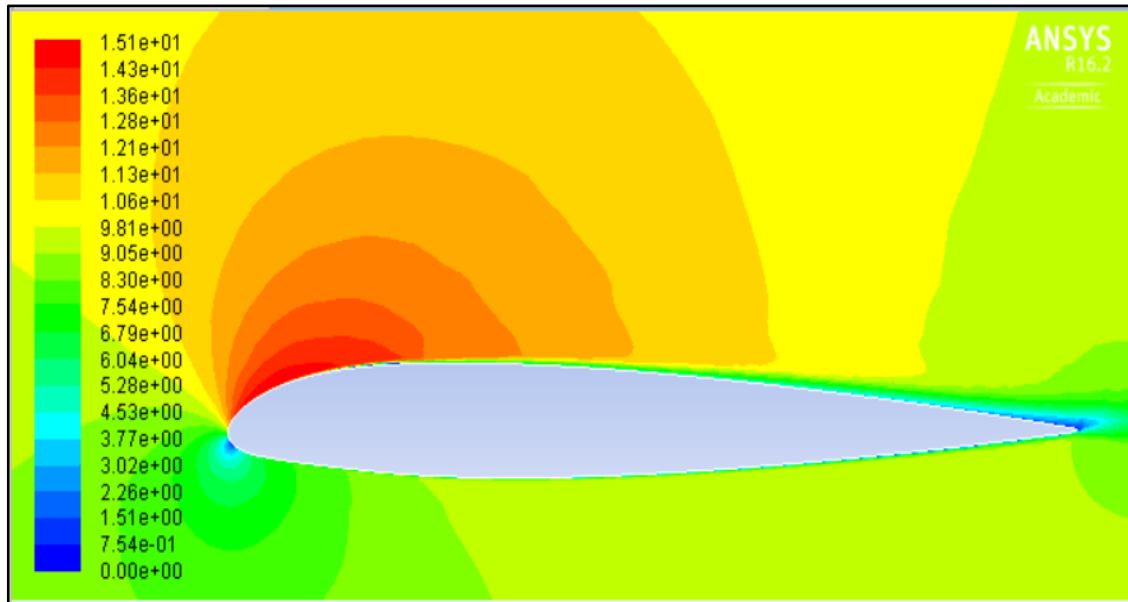


Figure 5.29 Contours of the velocity of the airflow around NACA 23015 airfoil

Next the wind speed in CFD simulations was increased to 25m/s with the value of the angle of attack kept at 8.5° and the velocity distributions on the top and bottom surfaces of airfoils were computed. Figures 5.30, 5.31 and 5.32 show the air flows around NACA 4415, NACA 23012 and NACA 23015 airfoils at a wind speed of 25m/s. Results show that the air speed increased at the top surface and the maximum air velocities reached 38.8m/s, 38.6m/s and 39m/s for the three airfoils under consideration. This result indicates that the velocity distributions on the three airfoils are nearly the same as the velocity distributions at higher wind velocities.

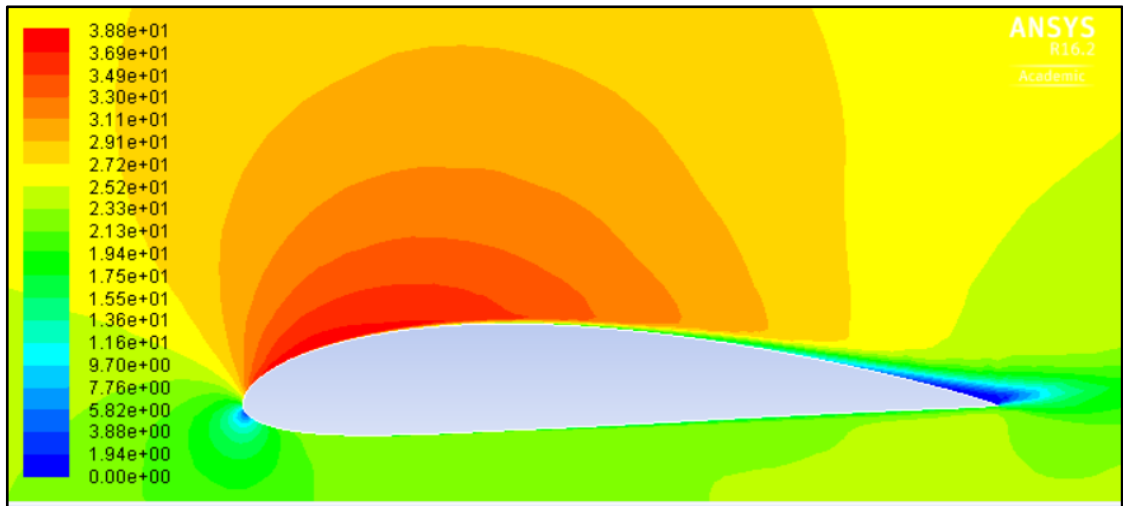


Figure 5.30 Contours of the velocity of the airflow around NACA 4415 airfoil

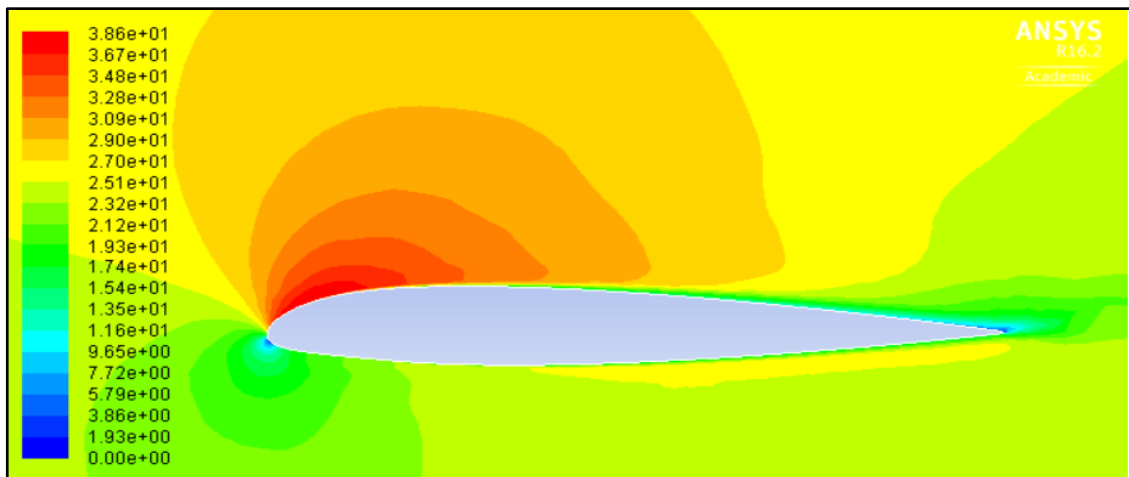


Figure 5.31 Contours of the velocity of the airflow around NACA 23012 airfoil

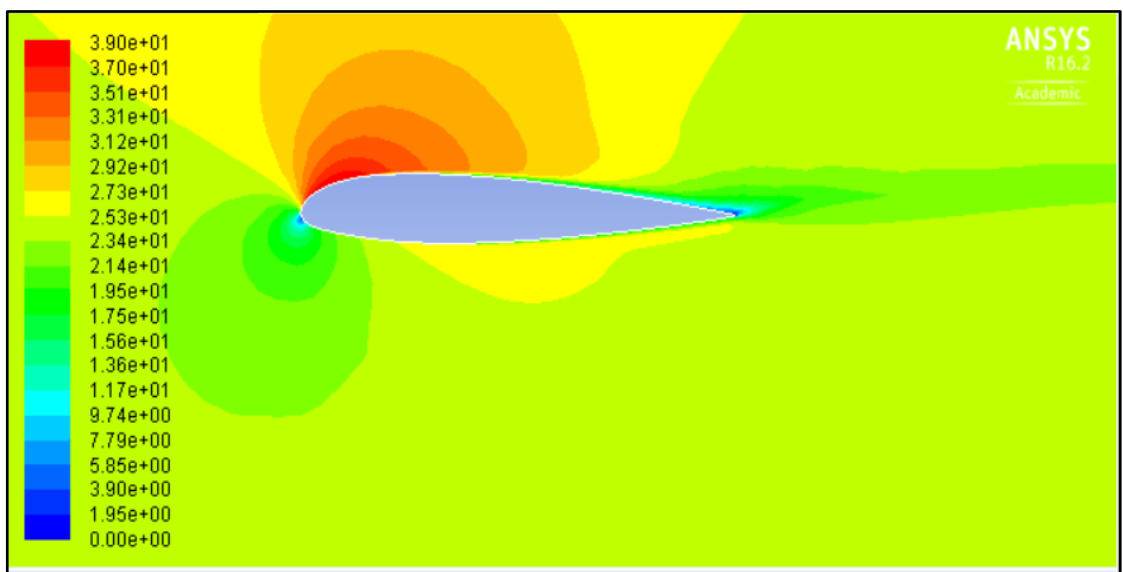


Figure 5.32 Contours of the velocity of the airflow around NACA 23015 airfoil

Next pressure distributions on NACA airfoils are studied to determine the positions of the airfoils along the length of the blades and to maximize the energy output. Figures 5.33, 5.34 and 5.35 show the pressure distributions on NACA 4415, NACA 23012 and NACA 23015 airfoils at a wind velocity of 9.56m/s and at an angle of attack of 8.5° . The results for the three airfoils indicate that the pressures on the bottom surfaces are greater than the ones on the top surfaces. Maximum static pressure of 44.4 Pascal is located at the lower surface of the leading edge of NACA 4415 airfoil. The maximum static pressures for NACA 23012 and NACA 23015 airfoils are 45.5 Pascal and 44.3 Pascal, respectively. The pressure distributions on the three airfoils are nearly similar on the lower leading edges as well as the minimum static pressures on the upper surfaces.

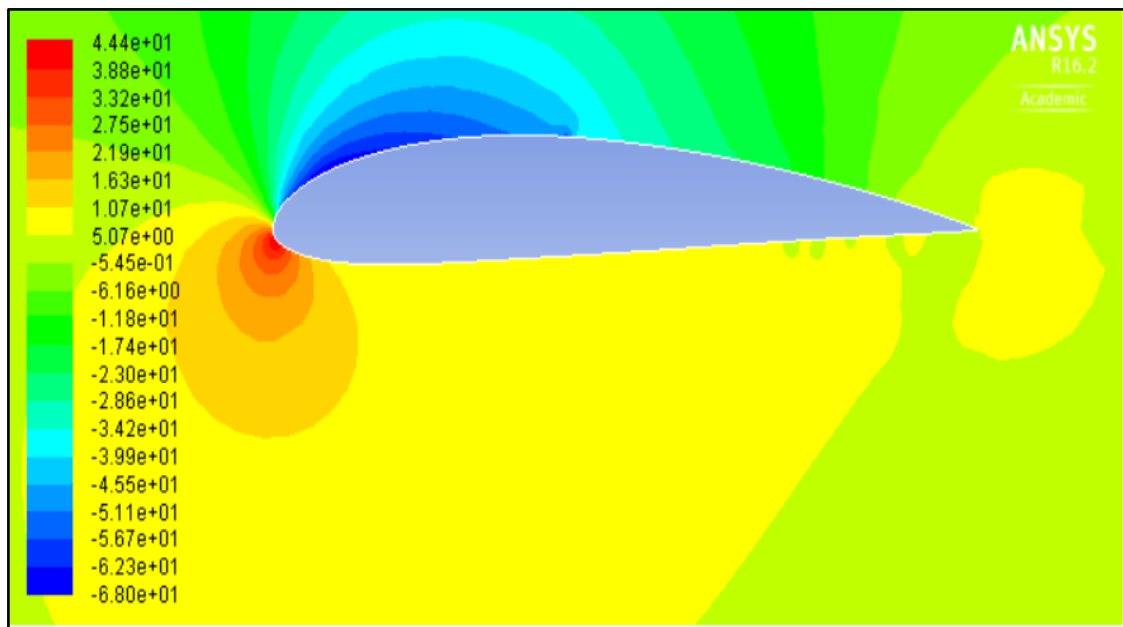


Figure 5.33 Contours of static pressure (Pascal) on NACA 4415 airfoil

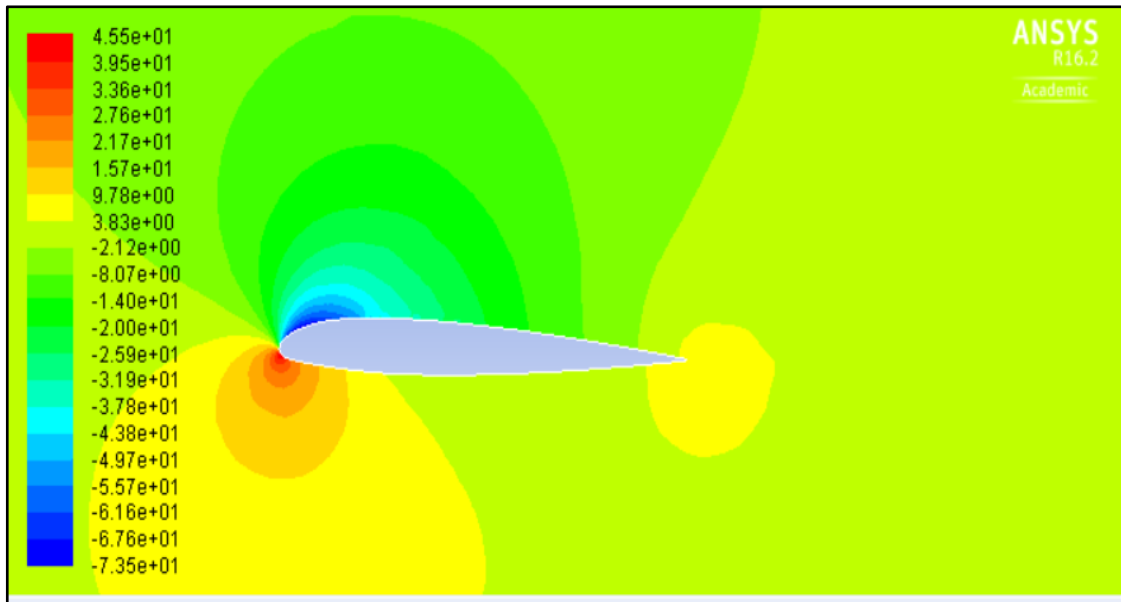


Figure 5.34 Contours of static pressure (Pascal) on NACA 23012 airfoil

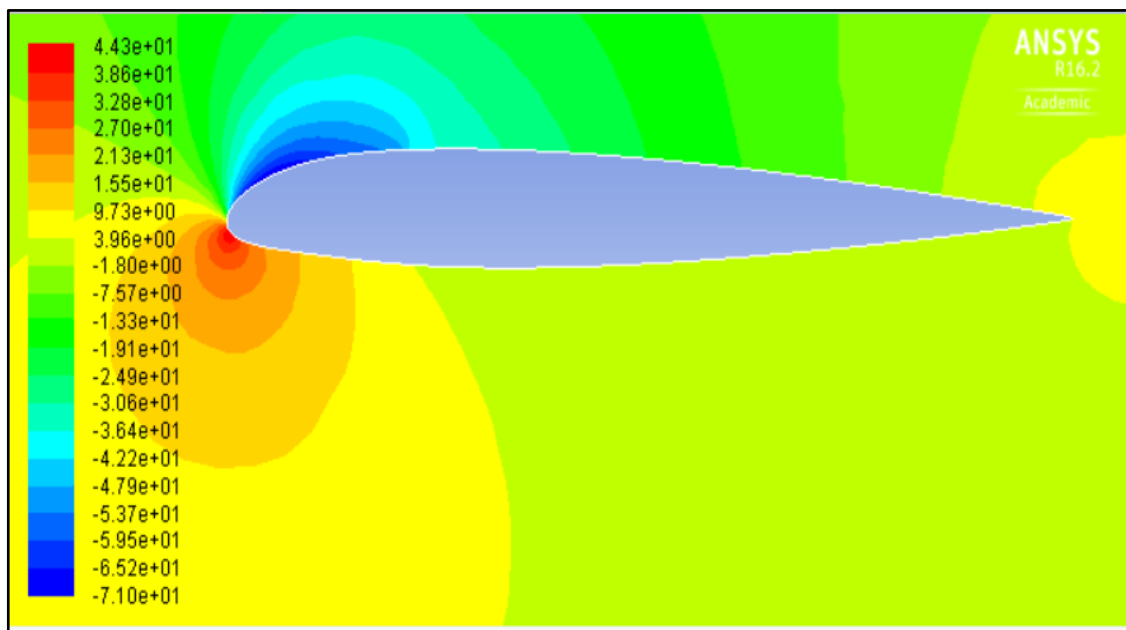


Figure 5.35 Contours of static pressure (Pascal) on NACA 23015 airfoil

Pressure differences at a wind velocity of 25m/s and at an angle of attack 8.5° were studied to assess the performance of the airfoils. Figures 5.36, 5.37 and 5.38 show the pressure distributions over NACA 4415, NACA 23012 and NACA 23015 airfoils. The pressure on the bottom surface of NACA 4415 airfoil is larger than the one on the top surface and the pressure on the lower surface of the leading edge reaches 304 Pascal.

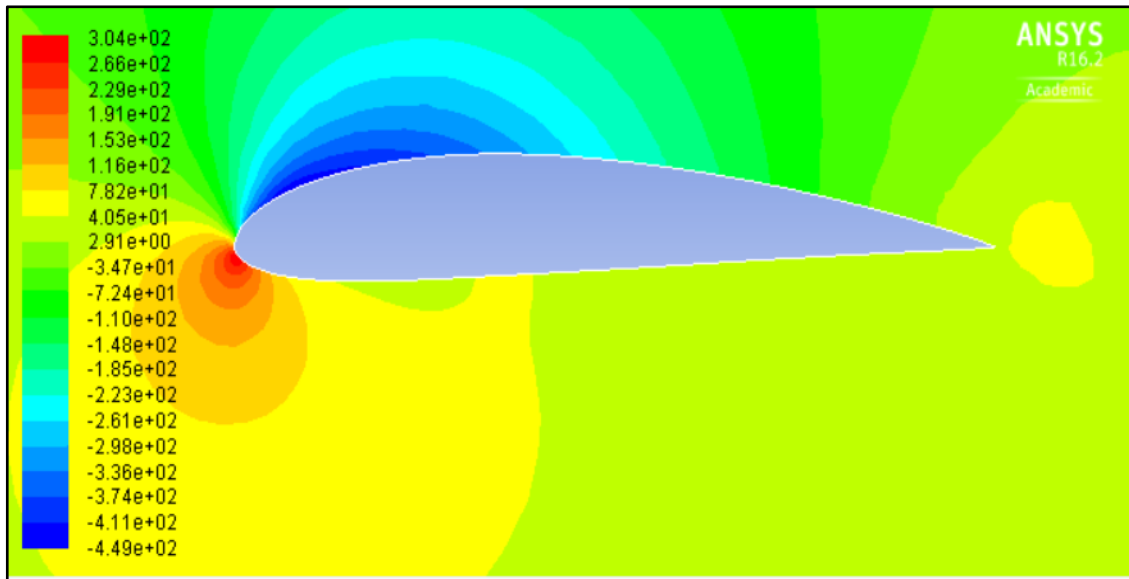


Figure 5.36 Contours of static pressure (Pascal) on NACA 4415 airfoil

Corresponding pressures on the lower surfaces of NACA 23012 and NACA 23015 airfoils reach 308 and 302 Pascal. The pressure differences for the three airfoils are less than 2% and shows similar differences when the wind velocity increases from 9.56m/s to 25m/s. The pressure distributions on both sides of the airfoils contribute to the lift.

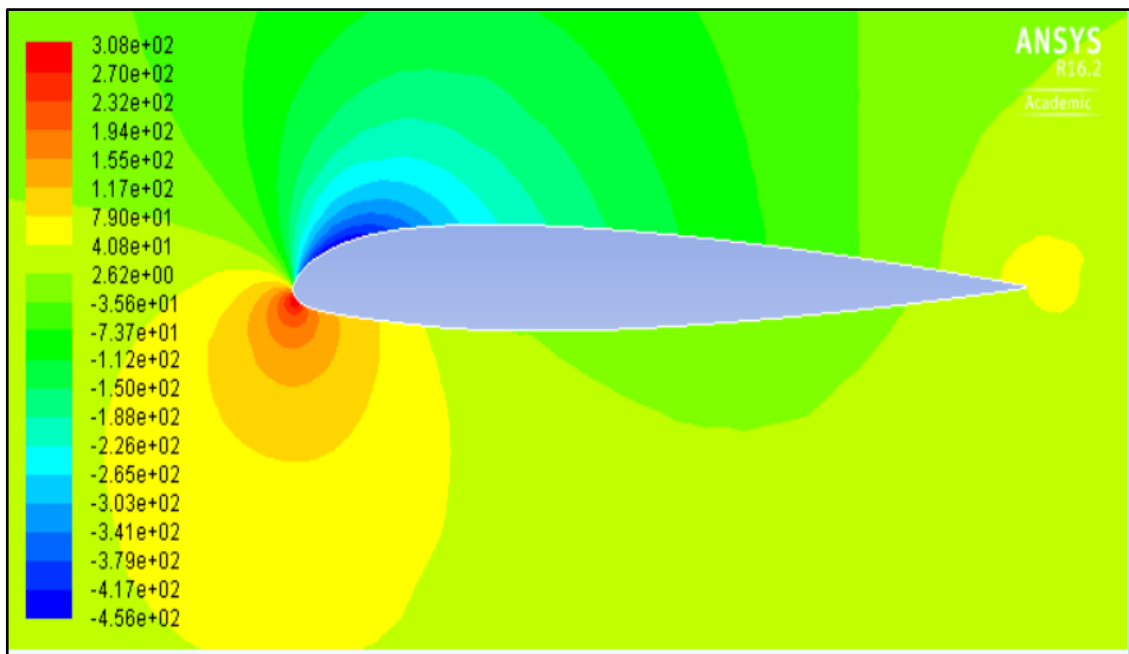


Figure 5.37 Contours of static pressure (Pascal) on NACA 23012 airfoil

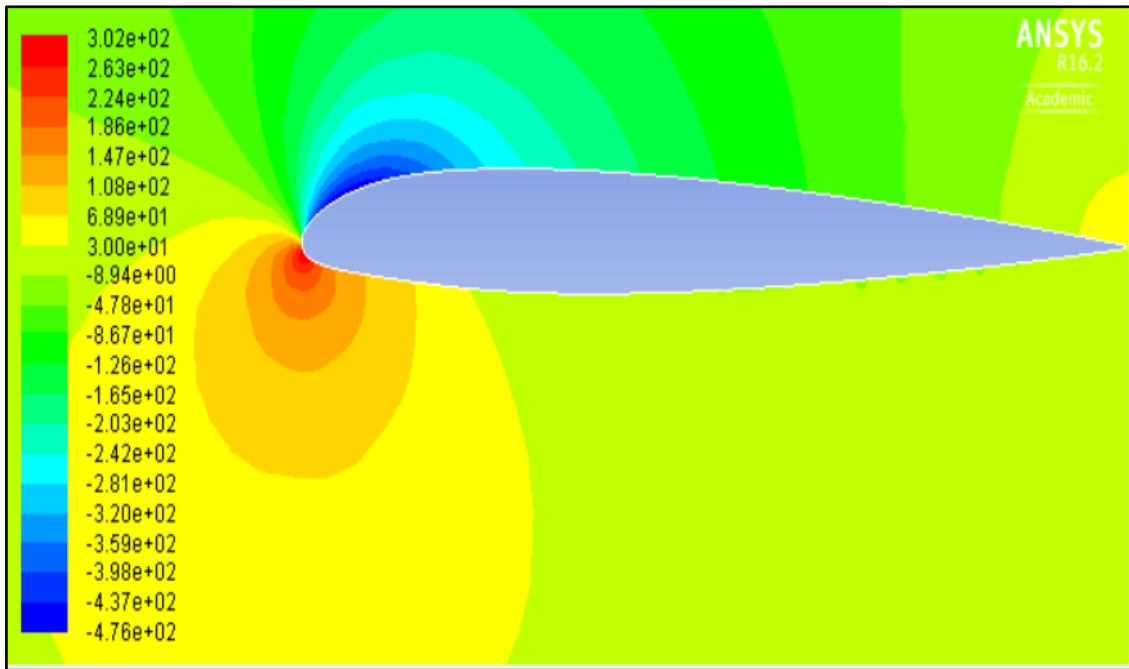


Figure 5. 38 Contours of static pressure (Pascal) on NACA 23015 airfoil

Next CFD simulations are used to investigate the kinetic energy extracted from the airflow on the airfoils at a wind velocity of 9.56m/s and at an angle of attack of 8.5° .

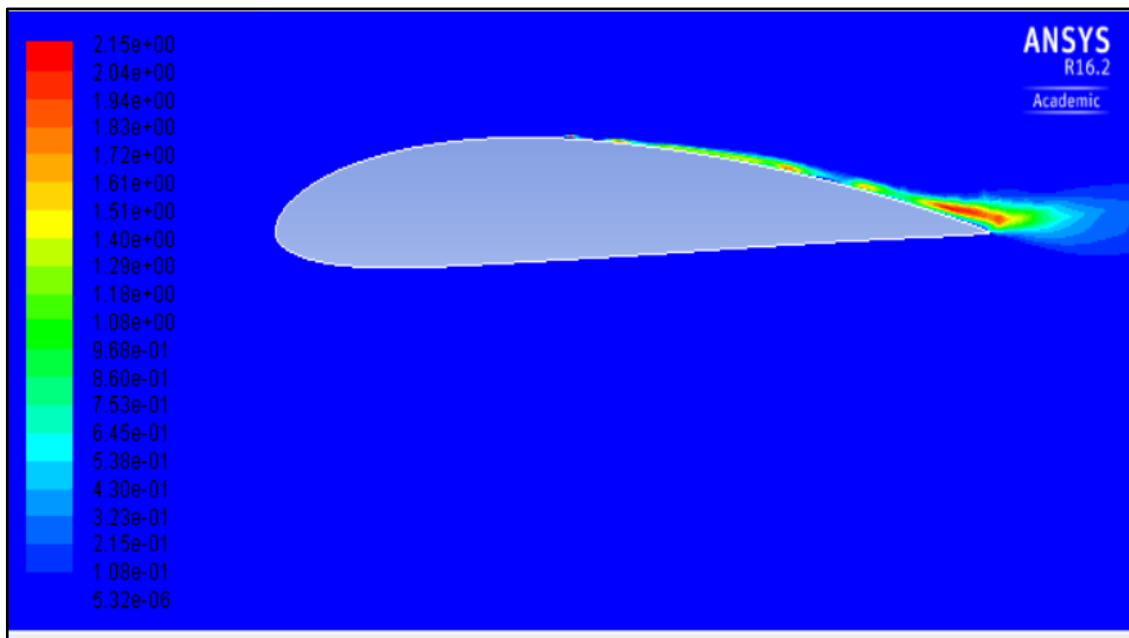


Figure 5.39 Contours of turbulence kinetic energy on NACA 4415 airfoil at a wind velocity of 9.56m/s.

Figures 5.39, 5.40 and 5.41 show the turbulence kinetic energy over NACA 4415, NACA 23012 and NACA 23015 airfoils. It is observed that the turbulence kinetic energy on the upper trailing edge of NACA 4415 airfoil is greater than the one on the lower surface and the greatest turbulence kinetic reaches approximately 2.15 %.

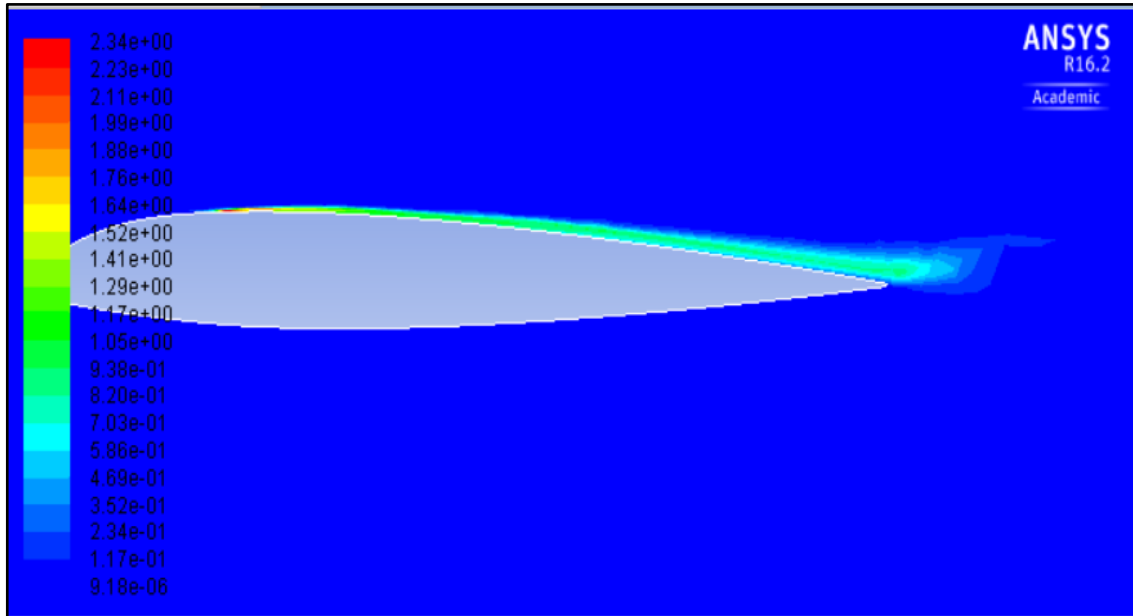


Figure 5.40 Contours of turbulence kinetic energy on NACA 23012 airfoil at a wind velocity of 9.56m/s

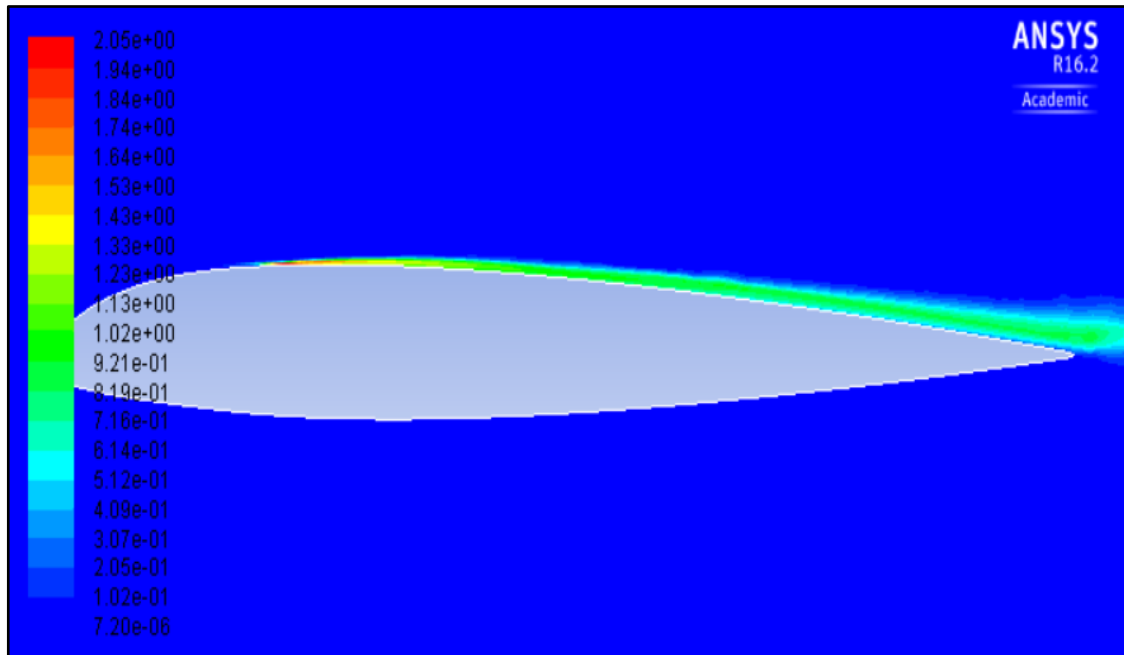


Figure 5.41 Contours of turbulent kinetic energy on NACA 23015 at wind velocity 9.56m/s

Maximum turbulence kinetic energy for NACA 23012 airfoil is larger than the ones for others airfoils due to the curves of airfoils on the trailing edges. Next, CFD simulations are employed to determine the turbulence kinetic energy extracted from the flow at a wind velocity of 25m/s and at an AOA of 8.5°. Figures 5.42, 5.43 and 5.44 show the turbulence kinetic energies over the three airfoils. The simulation results show that the maximum kinetic energy on NACA 4415 airfoil reaches 12.6% at the top trailing edge of the airflow.

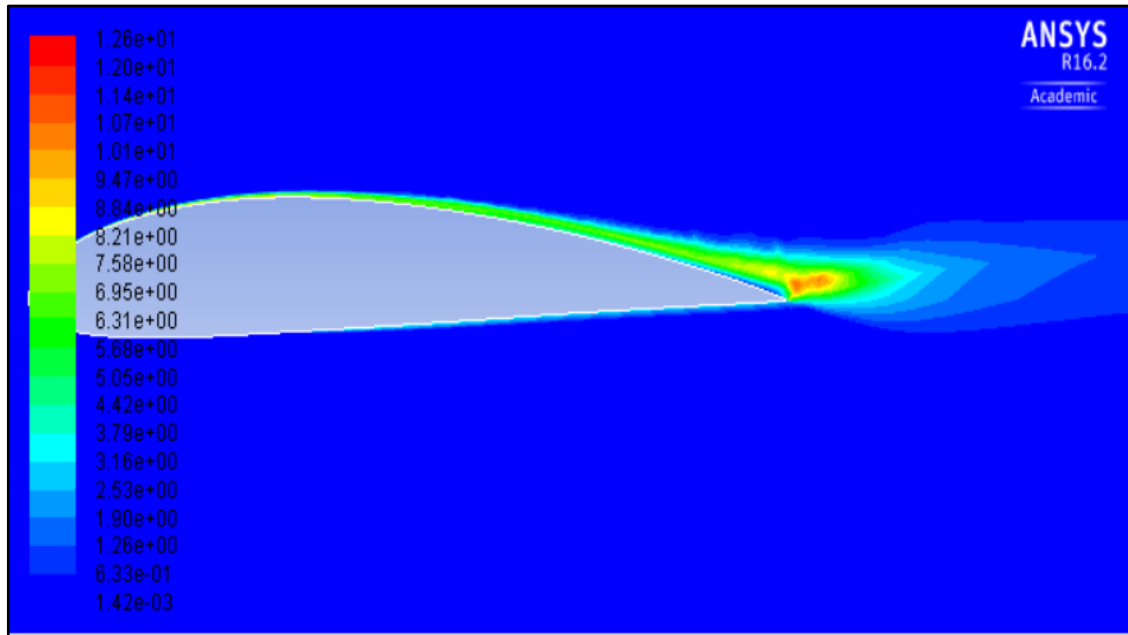


Figure 5.42 Contours of turbulence kinetic energy on NACA 4415 airfoil at a wind velocity of 25m/s.

The maximum kinetic energies on NACA 23012 and NACA 23015 are about 12.3% and 14%. The turbulence kinetic on NACA 4415 and NACA 23012 airfoils are approximately the same when the wind velocity is 25m/s. The turbulence kinetic energy extraction is higher for the NACA 23015 airfoil. Results indicate that the turbulence kinetic energy depends on the curve of the trailing edge of the airfoil and the wind velocity.

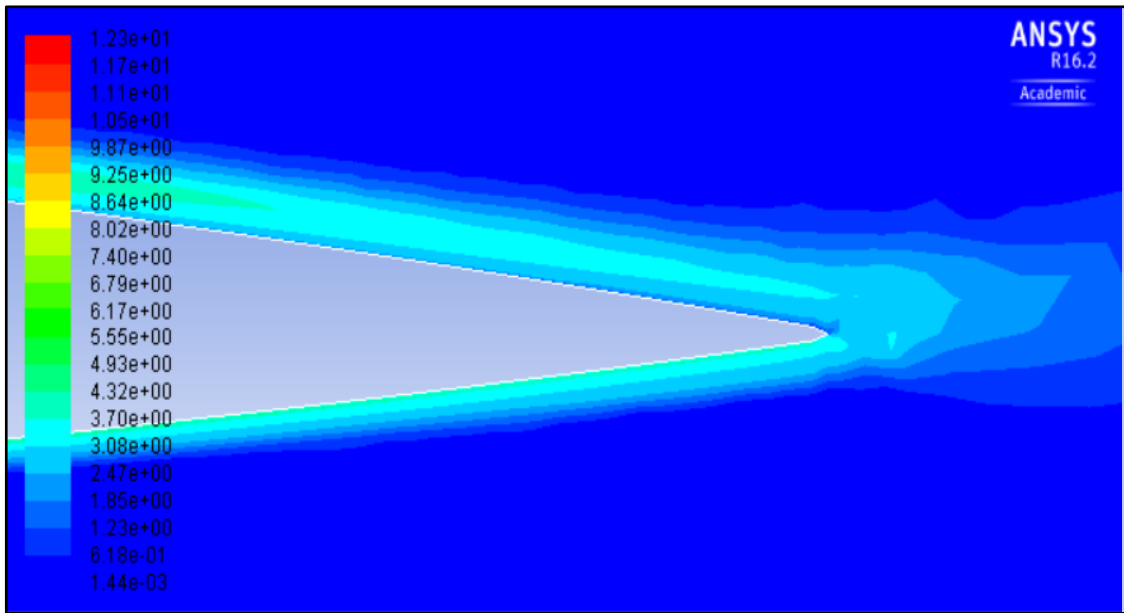


Figure 5.43 Contours of turbulence kinetic energy on NACA 23012 airfoil at a wind velocity of 25m/s

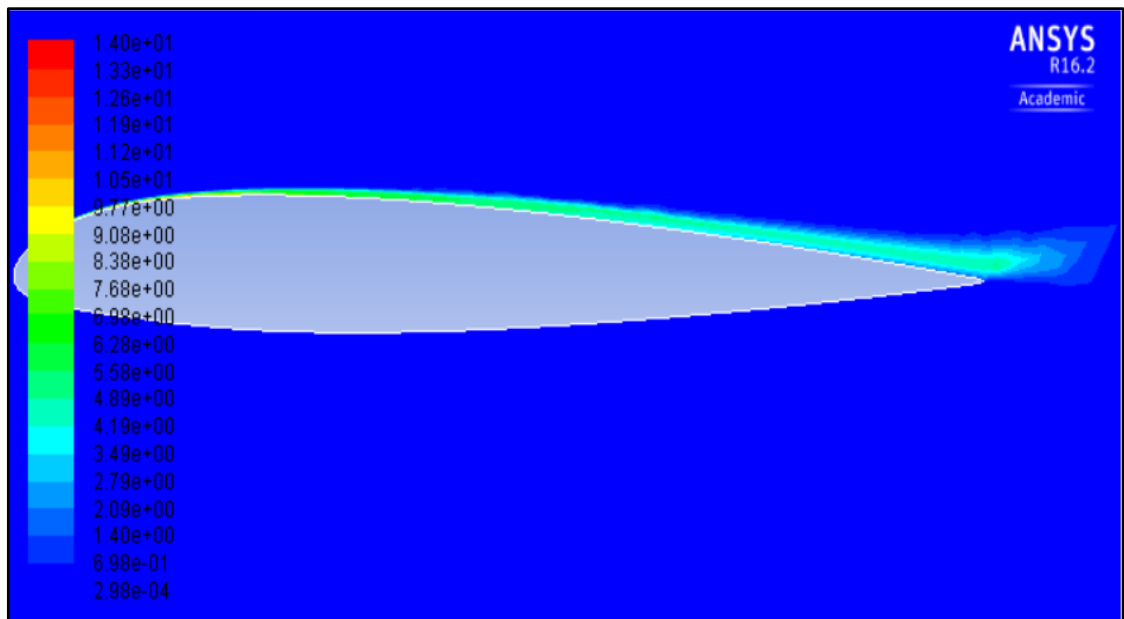


Figure 5.44 Contours of turbulence kinetic energy on NACA 23015 airfoil at a wind velocity of 25m/s

Three NACA airfoils were studied to assess the aerodynamic efficiency and positions of the airfoils on the wind turbine blades using QBlade and CFD simulation results. Simulation results were used to investigate the velocity, pressure and turbulence kinetic energy distributions. Curves of the trailing edges indicate the existence of turbulence kinetic energy on the wind turbine blades. The software packages were used to calculate

Momentum Theory and Blade Element Theory for Modelling Blades

the loads along the airfoils to assess the aerodynamic efficiency of the airfoils. The lift and drag coefficient for three NACA airfoils were determined using the simulations.

Lift and drag coefficients were calculated by QBlade software to model the shape of the horizontal-axis wind turbine blades. Forces generated at different wind speeds were investigated using the BEM theory based on the steady state behaviour of the airfoils and the wind turbine rotor.

5.6 Momentum Theory and Blade Element Theory for Modelling Blades

A horizontal-axis wind turbine rotor consists of one or more blades. The flow along the blades is characterized by a which is a function of the rotor power extraction and thrust. The analysis of the force applied on wind turbine blades uses a momentum theory and a blade element theory. The principles of the momentum theory use the conservation of linear and angular momentum to analyse the forces on the wind turbine blades. The blade element theory is used to evaluate the force at a section of the blade as a function of the wind turbine blade geometry. The wind turbine blades are modelled as a collection of several minuscule strips with width ' dr ' that are connected from tip to tip.

5.6.1 Momentum Theory

The classical momentum theory has a number of simplifying assumptions. The flow is assumed to be inviscid, incompressible and irrotational. The velocity and the static pressure are uniform over the cross section of the disk and stream-tube. The forces and flow conditions on the rotor are derived by considering conservation of momentum noting that force is the rate of change of momentum. This theory took into account the annular control volume as shown in Figure 5.45. Axial and angular induction factors are assumed to be a function of the radius.

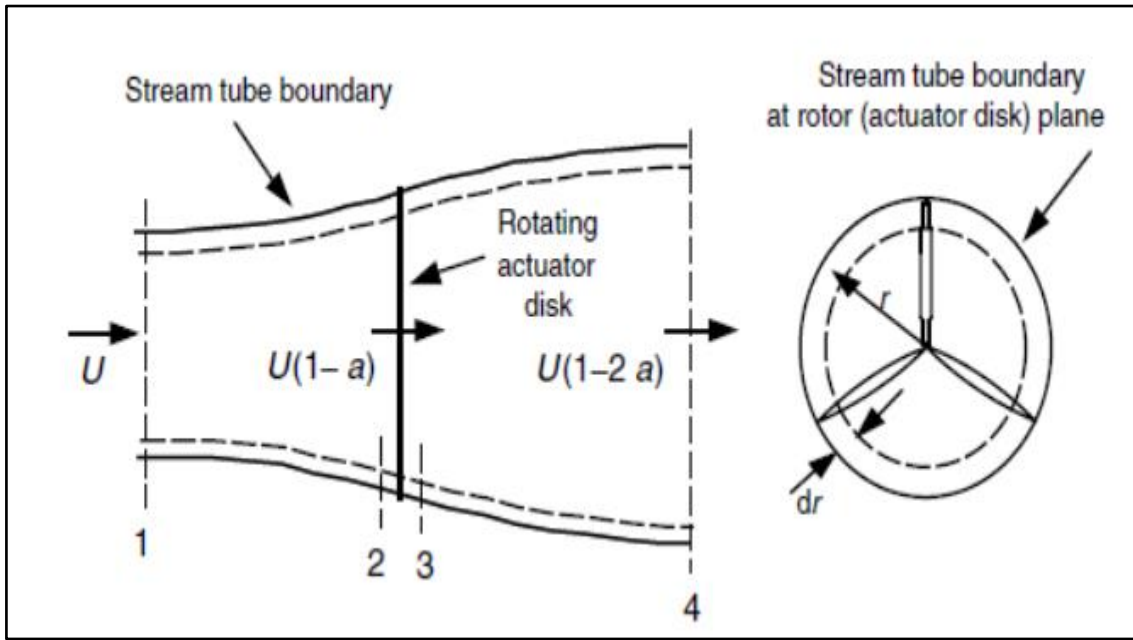


Figure 5.45 Geometry of rotor (McGowan, 2009)

Applying the linear momentum to the control volume of radius r , one obtains

$$dT = \rho U^2 4a(1-a)\pi r dr \quad (5.44)$$

Similarly, based on conservation of angular momentum, the differential torque is given by

$$dQ = 4a'(1-a)\rho U \pi r^3 \Omega dr \quad (5.45)$$

5.6.2 Blade Element Theory

The blade element theory involves dividing a blade into ten to twenty elements to calculate the forces at each section of the blade and each of the sections has a different flow due to different rotational speeds (Ωr), different chord lengths (c) and twist angles (φ) along the length of horizontal axis of the wind turbine. Furthermore, the following assumptions apply: there is no aerodynamic interaction between the elements and the forces which are determined by the lift and drag behaviour of the airfoils. The blade elements are shown in Figure 5.46.

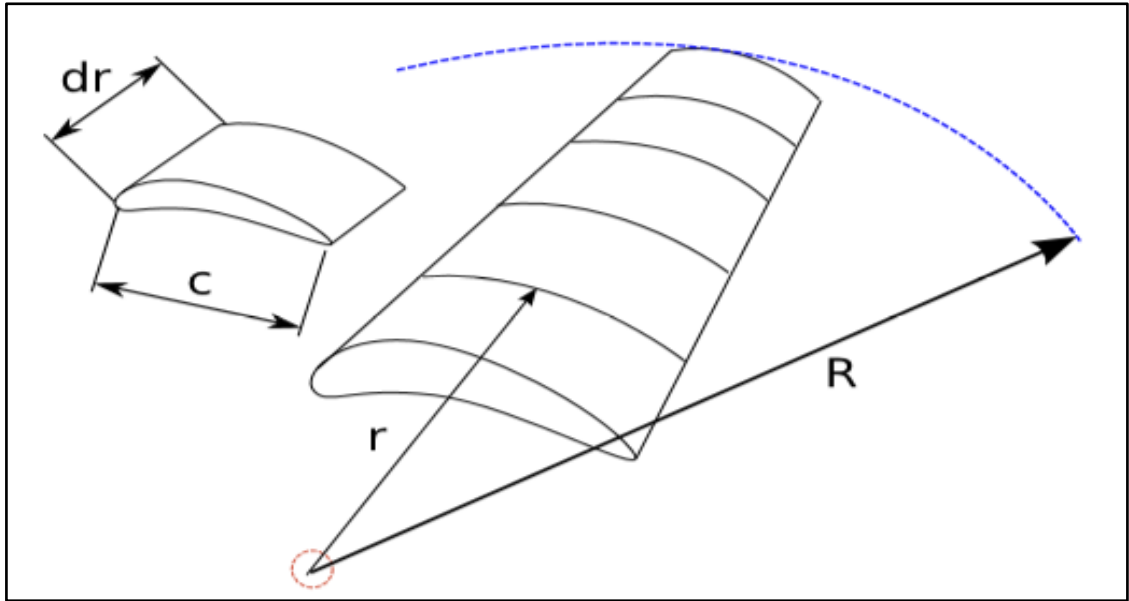


Figure 5.46 Schematic of blade element model; C airfoil chord length; dr radial lengths of elements; r radius of elements; R rotor radius (Grant Ingram, 2011)

The lift and drag forces generated on each section of the blades must be perpendicular and parallel, respectively, to the relative wind velocity which is the vector sum of the wind velocity at the rotor and the wind velocity due to the rotation of the wind turbine blade. The wind turbine blade rotates with an angular speed of Ωr . The angular velocity of the blades is $\omega r/2$. The average tangential velocity of the blade given by

$$\Omega r + (\omega/2)r = \Omega r + \Omega a' r = \Omega r(1 + a') \quad (5.46)$$

Noting that

$$U_2 = U(1 - a) \quad (5.48)$$

the following equation is obtained

$$\tan \varphi = \frac{U(1 - a)}{\Omega r(1 + a')} = \frac{1 - a}{(1 + a')\lambda_r} \quad (5.47)$$

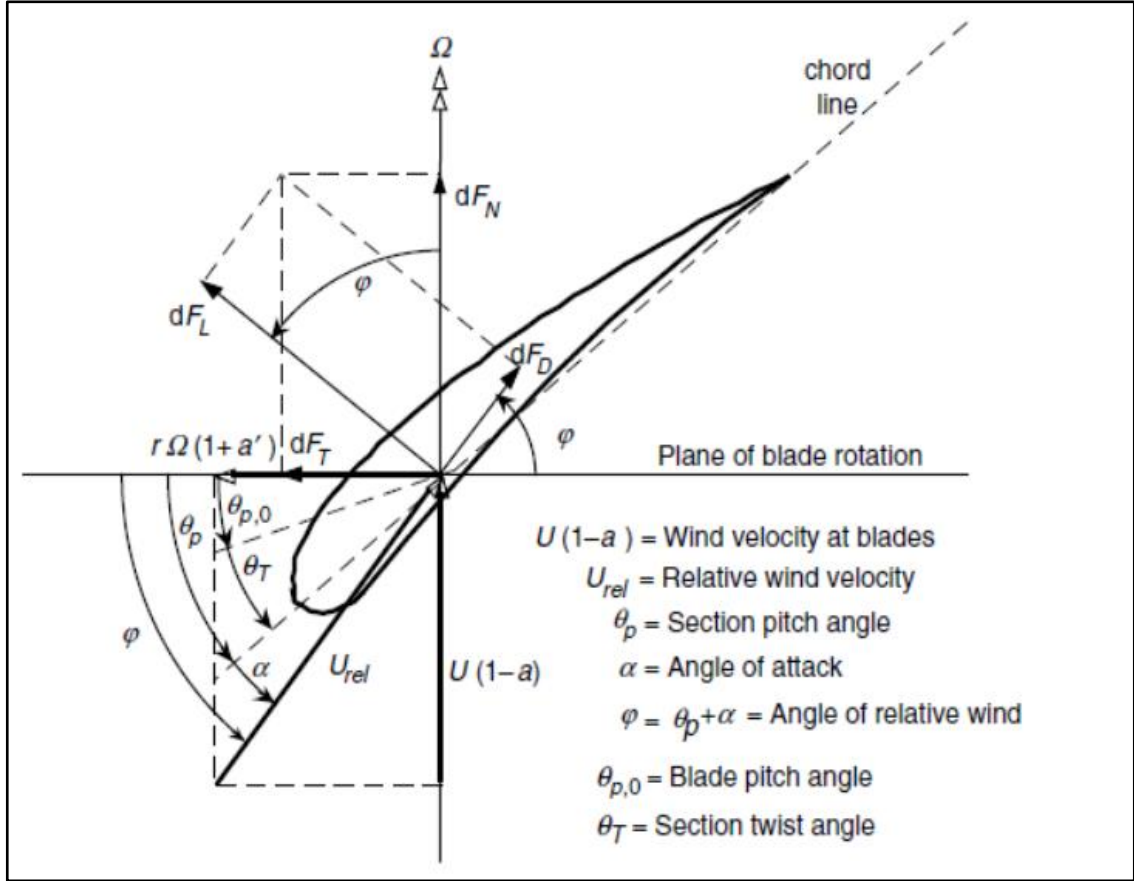


Figure 5.47 Blade geometry for analysis of forces on wind turbine blade (McGowan, 2009)

The value of ϕ will vary from blade element to blade element along the length of the blade. From Figure 5.47 the relative wind velocity is obtained as

$$U_{rel} = U(1-a) / \sin \phi \quad (5.48)$$

The lift dF_L and the drag force dF_D on the blade element along its length can be computed based on the lift coefficient C_l and the drag coefficient C_d of the airfoils. Their values on each section of the blades can be calculated as follows:

$$dF_L = C_l \frac{1}{2} \rho U_{rel}^2 c dr \quad (5.49)$$

$$dF_D = C_d \frac{1}{2} \rho U_{rel}^2 c dr \quad (5.50)$$

The forces on the blade section are shown in Figure 5.47. The normal force dF_N and the tangential forces dF_T on each section of the blades can be found as

Momentum Theory and Blade Element Theory for Modelling Blades

$$dF_N = dF_L \cos \varphi + dF_D \sin \varphi \quad (5.51)$$

$$dF_T = dF_L \sin \varphi - dF_D \cos \varphi \quad (5.52)$$

If there are B blades, the total normal force and tangential force in the section at a distance r from the centre are given by

$$dF_N = B \frac{1}{2} \rho U_{rel}^2 (C_l \cos \varphi + C_d \sin \varphi) c dr \quad (5.53)$$

$$dF_T = B \frac{1}{2} \rho U_{rel}^2 (C_l \sin \varphi - C_d \cos \varphi) c dr \quad (5.54)$$

The differential torque on an element is

$$dQ = B \frac{1}{2} \rho U_{rel}^2 (C_l \sin \varphi - C_d \cos \varphi) c r dr \quad (5.55)$$

Based on the blade element theory, the normal force (thrust) and tangential force (torque) on an annular rotor section of the airfoils are obtained. An increase in thrust force has an impact for lowering the torque (power output) of the wind turbine blade. The normal and tangential forces can be more useful by noting the relative velocity (U_{rel}) in terms of induction factor. Substituting and carrying out some algebra gives

$$dF_N = \sigma' \pi \rho \frac{U^2 (1-a)^2}{\sin^2 \varphi} (C_l \cos \varphi + C_d \sin \varphi) r dr \quad (5.56)$$

$$dQ = \sigma' \pi \rho \frac{U^2 (1-a)^2}{\sin^2 \varphi} (C_l \sin \varphi - C_d \cos \varphi) r^2 dr \quad (5.57)$$

where σ' is the local solidity and is defined as

$$\sigma' = Bc / 2\pi r \quad (5.58)$$

5.6.3 Combined Blade Element Momentum Theory for Modelling Blades

The Blade Element Momentum Theory uses the two equations (5.46) and (5.47) from the momentum theory which are the axial thrust and torque in equations. Two equations from the blade element theory involve the axial force and the torque involving the lift and drag coefficients (eqs. 5.58 and 5.59). The combined theory is used to calculate the induction factors, a and a' for airfoils with low drag coefficients. The torque equations (5.47) and (5.59) computed from the blade momentum theory can be written as:

$$a' (1-a) = \sigma' C_l / (4\lambda_r \sin \varphi) \quad (5.59)$$

Momentum Theory and Blade Element Theory for Modelling Blades

By equating the normal force from the momentum theory in equation (5.46) and the blade element theory in equation (5.58), the following expression is obtained

$$a / (1 - a) = \sigma' C_l \cos \varphi / (4 \sin^2 \varphi) \quad (5.60)$$

Equations (5.61) and (5.62) are the parameters for modelling the wind turbine blades. Based on a combination of the momentum theory and the blade element theory, the shapes of the blades can be modelled. The maximum power coefficient assuming no wake rotation ($a' = 0$) or drag ($C_d = 0$), and taking the axial induction factor $1/3$, the thrust force is computed from equation (5.46) as

$$dT = \rho U^2 4 \left(\frac{1}{3} \right) \left(1 - \frac{1}{3} \right) \pi r dr = \rho U^2 (8/9) \pi r dr \quad (5.61)$$

For a drag coefficient of $C_d = 0$, the normal force given by equation (5.56) is

$$dF_N = B \frac{1}{2} \rho U_{rel}^2 (C_l \cos \varphi) c dr \quad (5.62)$$

The relative velocity of the wind turbine blade given by equation (5.50) in terms of the maximum linear induction factors ($1/3$) can be expressed:

$$U_{rel} = U(1 - a) / \sin \varphi = \frac{2U}{3 \sin \varphi} \quad (5.63)$$

By combining the equations from the momentum theory and the blade element theory and using the equations (5.63), (5.64) and (5.65), one obtains

$$\frac{C_l B c}{4 \pi r} = \tan \varphi \sin \varphi \quad (5.64)$$

Equation (5.49) with $a' = 0$ and $a = 1/3$ becomes

$$\tan \varphi = \frac{2}{3 \lambda_r} \quad (5.65)$$

Equating equations (5.66) and (5.67) gives

$$\frac{C_l B c}{4 \pi r} = \left(\frac{2}{3 \lambda_r} \right) \sin \varphi \quad (5.66)$$

The local tip ratio $\lambda_r = \lambda(r/R)$ of the wind turbine section can be calculated after determining the tip speed and the radius of the wind turbine blade. Considering equations

(5.67) and (5.68), the angle of relative wind velocity and the chord length c of each section of the ideal blade are given by

$$\varphi = \tan^{-1} \left(\frac{2}{3\lambda_r} \right) \quad (5.67)$$

$$c = \frac{8\pi r \sin \varphi}{3BC_l \lambda_r} \quad (5.68)$$

A linear distribution of chord along the length of the blade may be considered easy to make. The model is based on an ideal wind turbine blade shape derived with wake rotation and zero drag. These equations provide an initial guess after determining the angle of relative wind velocity (Equation 5.69) to calculate the rotor performance and to modify the design if necessary. This is an iterative process and is analysed using the following value of a :

$$a = 1 / \left[1 + 4 \sin^2 \varphi / (\sigma' C_l \cos \varphi) \right] \quad (5.69)$$

The angular induction factor given by equation (5.39) is used to maximize the power production. The results using the linear and angular induction factors a, a' and the angle of relative wind velocity on each element of the airfoil is calculated iteratively to improve the twist and chord distributions. The airfoil performance and the position along the length of the blades are determined using QBlade/ XFOil and CFD analysis using ANSYS 16.2 Fluent software. The airfoils used for baseline horizontal axis wind turbine blades are shown in Figure 5.48. The total length (radius) of this wind turbine blade is 54m and uses three airfoils. The distribution of NACA 4415 airfoil begins from 20% radius R , NACA 23015 airfoil from 55% radius R and NACA 23012 airfoil from 75% radius R . The remaining part of the region between the root and the greatest chord position evolves circular sections.

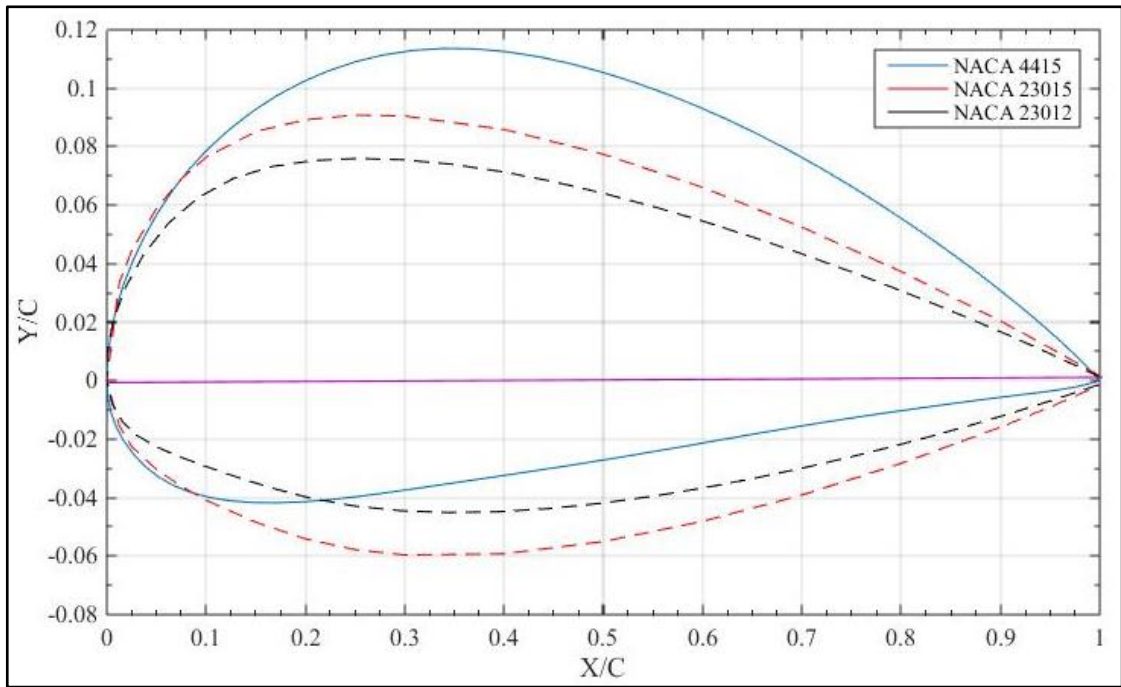


Figure 5.48 Airfoils used for baseline blade model

The greatest chord length (c_{max}) is set as 7.5% of the blade length and is located at 20% of the blade radius R . Chord of blade at tip is 20% of the largest chord length and the distribution of the chord is linear from the chord location to the blade tip. The hub radius is set as 4.5% of the rotor radius and the wind turbine blade root diameter is fixed as 60% of the largest chord length (c_{gre}). The tip speed ratio λ and AOA (α) are 9 and 8.5° , respectively. The largest twist value is 18° at the largest chord value of 20% of the wind turbine rotor radius R . The values decrease at each section and finally becomes 0° at the tip of the blade. Chord distribution along the length of the wind turbine blade is shown in Figure 5.49.

Distribution of applied loads on the wind turbine blades is calculated considering the BEM theory with the cut-in wind speed of 3m/s and the cut-out wind speed of 25m/s. Distribution of the flap-wise shear force along the length of the blade is shown in Figure 5.50. It could be observed that the flap-wise shear force is higher at the root section and this value decreases as it approaches the tip of the blade. The magnitude of flap-wise shear force distribution on the blade depends on the wind velocity. The shear force on the blade is higher at the cut-out wind speed. The geometry of the wind turbine blades are developed considering the flap-wise shear loads [97].

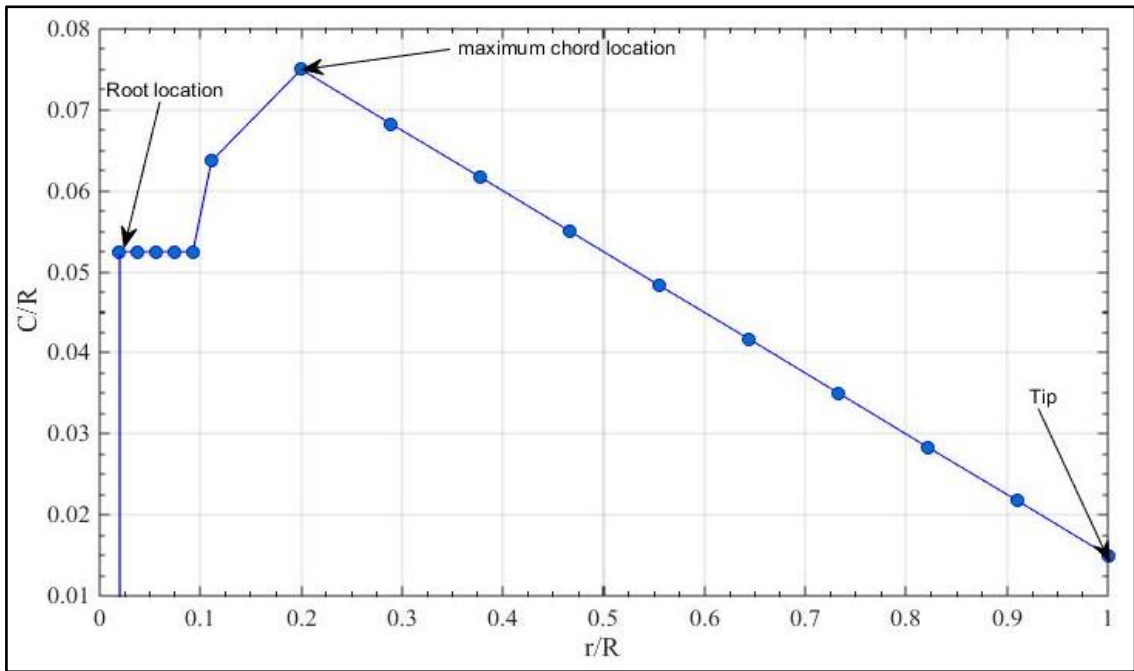


Figure 5.49 Chord length distribution along the length of wind turbine blade

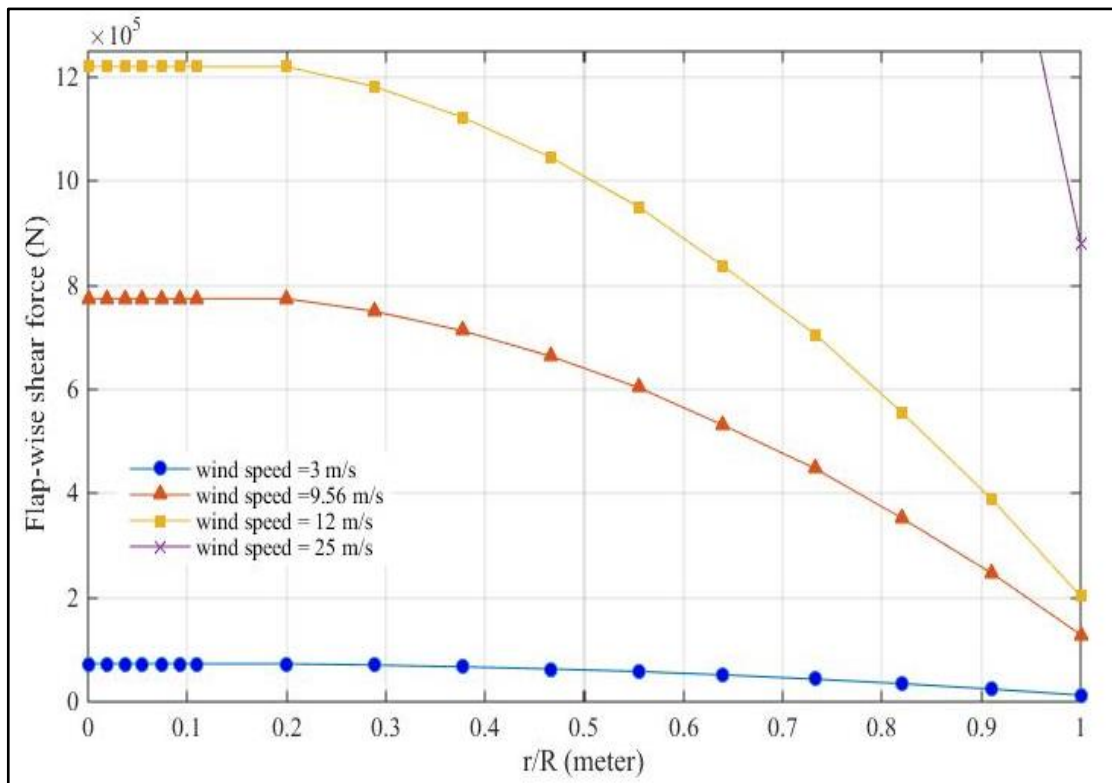


Figure 5.50 Flap-wise shear force distribution at various wind speeds

The flap-wise moments on 54m wind turbine blades at cut-in wind speeds of 3m/s and 25m/s are shown in Figure 5.51. It indicates that the flap-wise moment is higher near the

root section of the turbine blade and this value increases as the wind speed changes. Blade modelling uses the flap-wise bending moment to estimate the spar-cap and web thickness of the blades under different loading conditions.

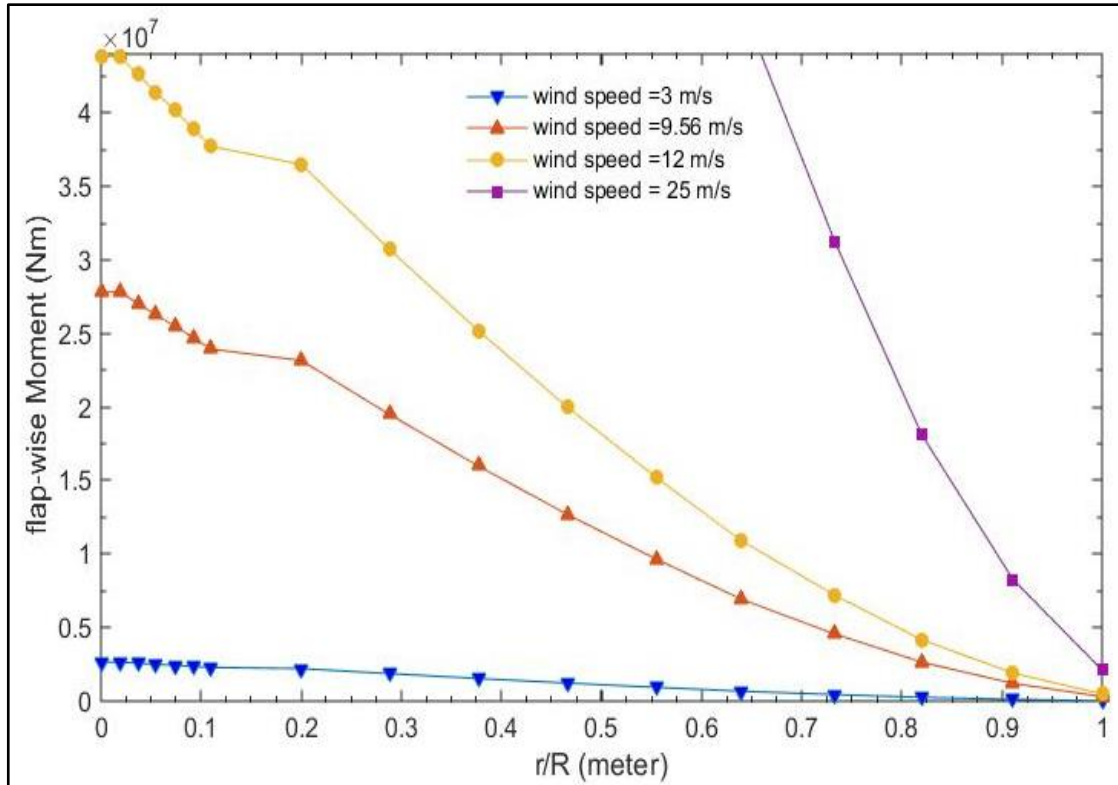


Figure 5.51 Flap-wise moment distribution at various wind speeds

5.7 Summary of Chapter

Aerodynamic principles and theoretical modelling of horizontal-axis blades are employed to model the geometry of blade elements. NACA airfoils were selected to model the horizontal-axis blades which can increase the efficiency of energy extraction capacity from the wind flow. To design this blade, Betz’s and Glaunt modelling techniques were used to find the linear and angular induction factors along the length of the blades to maximize the power output. Several iterations were performed on NACA airfoils using Xfoil/QBlade and ANSYS software’s at Reynolds number ($6e^6$) and three NACA airfoils were selected. Velocity, pressure and turbulence distributions on each airfoil were analysed using ANSYS CFD fluent simulation under different wind speeds to determine the locations of the airfoils in order to maximize the power output. Based on this, locations of the three airfoils along the length of the blades were identified and the chord

length of each airfoil was determined. Locations of NACA 4415, NACA 23015 and NACA 23012 airfoils are 20%, 55% and 75% of the full length of the blade. The remaining portion of the region between the root and the maximum chord is covered with a circular profile. The greatest chord length (c_{gre}) was set to 7.5% of the blade length and was located at 20% of the rotor radius R . The chord of the blade at the tip was 20% of the largest chord length and the distribution of the chord was linear from the largest chord position to the tip of the blade. The hub radius of the blade was set as 4.5% of the rotor radius and the blade root diameter was set as 60% of the maximum chord length. The tip speed ratio λ and angle of attack α were set as 9 and 8.5° , respectively. The greatest twist value reached 18° at 20% of the wind turbine rotor radius R and this value decreased on each section finally reaching 0° at the tip of wind turbine blade. The cut-in and the cut-out wind speeds were between 3m/s to 25m/s. The load distribution analysis was done using Blade Element Momentum (BEM) theory. The total length of the blade was divided into sixteen parts to determine the bending moment, flap-wise loading and the shear force along the length of 54m blade. The wind loading and all other parameters were used to determine the shape of the blades which are given in Appendix A.

In Chapter 6, using different parameters and theories discussed in Chapter 5, modelling of the wind turbine blades is given involving the shear webs, trailing and leading edges and spar caps. Composite materials used in short beam shear tests, dynamic mechanical analysis and tensile testing are applied to model the elements of the wind turbine blades and the effect of temperature on the structure is studied. The thickness of the material on each element is estimated based on the flap-wise and thermal loading at wind speeds of 3m/s, 6m/s and 9m/s and at temperatures 25°C , 40°C , 55°C and 70°C . The failure behaviour of each section of the blade is studied under increasing temperatures. Issues related to the tip deflection, total deformation and failure behaviour optimization are discussed in Chapter 6.

Chapter 6

Development of Composite Wind Turbine Blade Structures

6.1 Elements of Modern Wind Turbine Blades

Wind turbine blades, nacelle and tower are the three basic components of wind turbines. Blades are the most important components for extraction of kinetic energy from the wind which is converted to mechanical torque and finally to electrical energy. The most commonly used wind turbines in various wind farms are the horizontal axis wind turbines. Over the year's wind turbine blades have grown in size as well as in power generation capacity. As the diameter of a wind turbine blade increases, the weight of the blade also increases. Researchers are working on increasing the aerodynamic performance, proper structural design and optimum material selection applicable to the structural design of horizontal-axis wind turbine blades.

The leading edge, trailing edge, shear webs and spar caps are the components of modern wind turbine blades. In the present study, to validate the experimental findings on the effect of temperature on FRP composite materials, the elements and geometry of the horizontal axis wind turbine blades were developed in accordance with IEC 61400-2 standards. The objective is to increase the efficiency and to optimize the structural components to make them as strong and as light as possible under different loading conditions.

Three NACA airfoils were used to model the geometry along the span of a 54m horizontal axis wind turbine blade using SolidWork and ANSYS software. Rectangular shear webs were divided into three parts along the length of blade. To characterize and optimize the structural components of composite blades and to find the right material in warm climates, the wind turbine blade was divided into 46 sections for simulation. Materials used in the experimental tests were specified in the computer simulations. The response of each section of the blade under flap-wise and thermal loadings was computed to validate the experimental results.

6.2 Micromechanical Modelling of Material for Wind Turbine Blade

Modern wind turbine blade manufacturing industries shifted to manufacture the blades from Fibre Reinforced Polymer (FRP) composite materials which have good mechanical

properties compared to traditional materials [98]. The lifetime and failure of the blade depend on the type of material used to manufacture it. In the present study, composite wind turbine blades are manufactured using GFRP, CFRP and a hybrid of these two composite materials. Composite materials consist of two or more chemically dissimilar constituents with superior mechanical behaviour, like high stiffness, high strength and low weight as compared to traditional materials. Carbon fibre is a stiffer, stronger and lighter material [99, 100]. Glass fibre stretches more before it breaks and can be used for structural design of wind turbine blades.

For modelling composite blade structures, ROM was applied to determine the mechanical properties of FRP composites with 60% fibre volume fraction. The micromechanical analysis to determine the physical and mechanical properties of the composites is shown in Appendix B. The data was used as the input for ANSYS 16.2 material database. Tables 6.1 and 6.2 show the mechanical properties of the GFRP, CFRP and the PVC foam used to model the elements of composite wind turbine blade.

Table 6.1 Mechanical properties of GFRP and CFRP composites

Stiffness and strength of GFRP and CFRP lamina	Glass/epoxy	Carbon/epoxy
Longitudinal modulus E_1 (GPa)	41.3	139.2
Transverse modulus E_2 (GPa)	9.0	8.076
In-plane shear modulus G_{12} (GPa)	4.7	5.00
Longitudinal tensile strength X_1^T (MPa)	1340	3128.2
Longitudinal compressive strength X_1^C (MPa)	541.0	1616.4
Transverse tensile strength X_2^T (MPa)	288.0	1227.4
Transverse compressive strength X_2^C (MPa)	100	680
In-plane shear strength, S_{12} (MPa)	60.0	80.0
Poisson's ratio (ν_{12})	0.30	0.324
Longitudinal thermal expansion coefficient $\alpha_1 [1/^\circ C \times 10^{-6}]$	5.50	2.50
Transverse thermal expansion coefficient $\alpha_2 [1/^\circ C \times 10^{-6}]$	-45.00	30.083

Table 6. 2 Properties of PVC foam

Property	Value	unit
Density	119.7	kg/m ³
Young's modulus	102	MPa
Poisson's ratio	0.3	-
Bulk modulus	85	MPa
Shear modulus	39.231	MPa

Wind blades are often exposed to extreme heat and high loads during their service life. The blades have to operate and withstand any external loads that may come up. To enable this, each component of the blade has to be designed adequately. Typically, flap-wise and edgewise loads acting on a blade cause stress on the cross-section and dimensional change. The optimal aerodynamic shape, contact with the turbine tower, minimum gravity loads and longer service life are the basic properties of composite materials to be considered for modelling the blades [101, 102]. Blade materials for warm areas are not given much attention by most design engineers. Most design engineers do not focus on blade materials for warm climate areas. In the present study, the impact of temperature variation is studied on deformation, deflection and failure of blade structures.

Next, the blade structures made from unidirectional CFRP, GFRP and hybrid CFRP-GFRP and hybrid GFRP-CFRP composite materials are studied. The unidirectional FRP composite laminates can provide the required bending stiffness for rotating structural components like wind turbine blades, helicopter blades and robotic arms. The spar-caps and shear webs made from PVC foam and unidirectional laminates were arranged at (0^0) and ($-45^0/0^0/45^0$) orientations on different elements of the blade. The presence of the sandwich materials can increase the bending strength of each section and can be used for modelling the blades. The thickness of the shear web was considered a well as the length of the blades. The thickness of the spar-caps was taken between 40mm to 100mm. The face of the blades was specified as 10mm. The leading and trailing sections of the blades were specified as having thicknesses of between 30mm to 70mm. Figure 6.2 shows the main components of the blade such as shear webs, spar-caps and the aerodynamic shell. Horizontal axis wind turbine blades have two faces on the suction side and the pressure side connected with a box beam. The shear web modelling along the span of the blade is shown in Table 6.3.

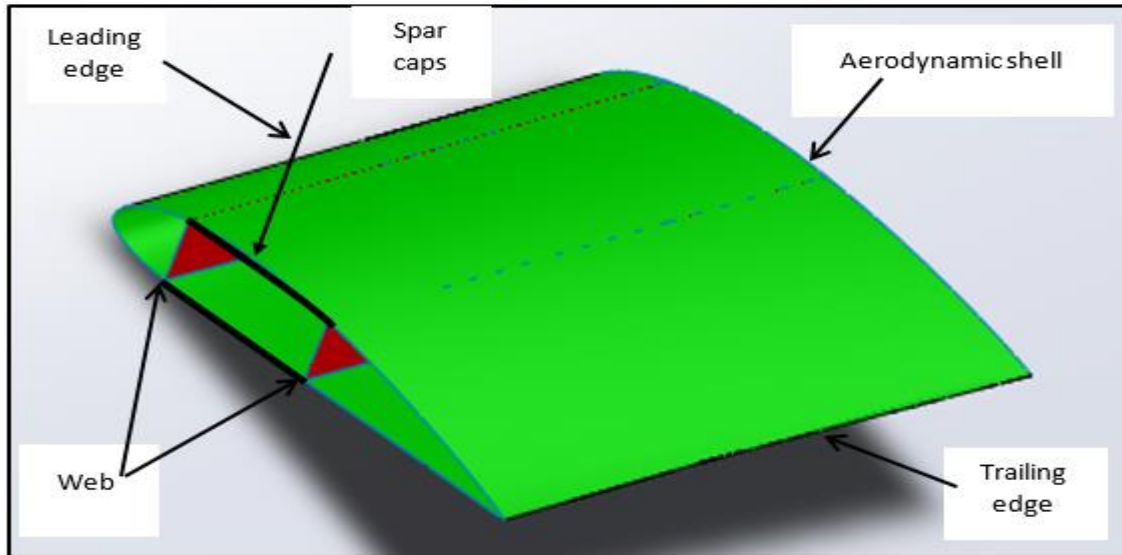


Figure 6.1 Structural components of horizontal axis wind turbine blade

Table 6.3 Rectangular shear web distribution on the airfoil and circular cross sections

No.	Blade families	Chord distance (mm)	Shear web from leading edges (25%*chord length) (mm)	Shear web from leading edges (75%* and 55% chord length) (mm)	Distance between shear webs (mm)
1	Circular	2430	607.5	1822.5	1215
2	Circular	2430	607.5	1822.5	1215
3	Circular	2430	607.5	1822.5	1215
4	Circular	2430	607.5	1822.5	1215
5	Circular	2430	607.5	1822.5	1215
6	Circular	2430	607.5	1822.5	1215
7	Circular	2430	607.5	1822.5	1215
8	N4415	4050	1012.5	2227.5	1215
9	N4415	3690	922.5	2029.5	1107
10	N4415	3330	832.5	1831.5	999
11	N4415	2970	742.5	1633.5	891
12	N23015	2610	652.5	1435.5	783
13	N23015	2250	562.5	1237.5	675
14	N23012	1890	472.5	1039.5	567
15	N23012	1530	382.5	841.5	459
16	N23012	1170	292.5	643.5	351
17	N23012	810	202.5	445.5	243

Comparison were done on the mass of the wind turbine blades built from CFRP, GFRP, hybrid CFRP-GFRP and hybrid GFRP-CFRP composites. In all cases, the thickness of the blades in each element was the same. The weight of the hybrids is similar

Micromechanical Modelling of Material for Wind Turbine Blade

and hybrid glass-carbon was selected for comparisons. The PVC foam is used for shear web and spar-caps and are the same for all blades. The elements of the three blades and thicknesses are shown in Tables 6.4, 6.5 and 6.6.

Table 6.4 Elements of the blade and its mass using carbon/epoxy

No	Elements of the blade	Carbon/epoxy			
		Thickness (mm)	Weight /area(kg/m ²)	Surface area of each element (m ²)	Mass of each element (Kg)
1	Section-2	100	176	7.6314	1343.1264
2	Section-3	100	176	7.6319	1343.2144
3	Section-4	100	176	7.631	1343.056
4	Section-5	100	176	7.6346	1343.6896
5	Section-6	100	176	7.606	1338.656
6	Section-7	100	176	7.5563	1329.9088
7	Section-8	100	176	37.626	6622.176
8	Section-9 Top	90	141.6	6.7952	962.20032
9	Section-9 bottom	90	141.6	7.0207	994.13112
10	Section-9 left	70	123.2	8.9645	1104.4264
11	Section-9 right	70	123.2	16.18	1993.376
12	Section-10 Top	90	141.6	6.161	872.3976
13	Section-10 bottom	90	141.6	6.2545	885.6372
14	Section-10 left	70	123.2	8.1633	1005.71856
15	Section-10 right	70	123.2	13.889	1711.1248
16	Section-11 Top	70	106.4	5.5959	595.40376
17	Section-11 bottom	70	106.4	5.6667	602.93688
18	Section-11 left	70	123.2	7.1603	882.14896
19	Section-11 right	70	123.2	12.943	1594.5776
20	Section-12 Top	70	106.4	4.8303	513.94392
21	Section-12 bottom	70	106.4	4.8753	518.73192
22	Section-12 left	60	105.6	6.5872	695.60832
23	Section-12 right	60	105.6	11.352	1198.7712
24	Section-13 Top	70	106.4	4.1826	445.02864
25	Section-13 bottom	70	106.4	4.21	447.944
26	Section-13 left	60	105.6	5.8077	613.29312
27	Section-13 right	60	105.6	10.065	1062.864
28	Section-14 Top	70	106.4	3.6034	383.40176
29	Section-14 bottom	70	106.4	3.6155	384.6892
30	Section-14 left	60	105.6	4.8682	514.08192
31	Section-14 right	60	105.6	8.4882	896.35392
32	Section-15 Top	65	106.00	3.0741	325.8546
33	Section-15 bottom	65	106.00	3.0781	326.2786
34	Section-15 left	60	105.6	3.953	417.4368
35	Section-15 right	50	88.00	6.8124	599.4912
36	Section-16 Top	50	88.00	2.6909	236.7992
37	Section-16 bottom	50	88.00	2.6924	236.9312
38	Section-16 left	50	88.00	2.8351	249.4888
39	Section-16 right	70	123.2	5.1284	631.81888
40	Section-17 Top	40	70.4	1.9229	135.37216
41	Section-17 bottom	40	70.4	1.9221	135.31584
42	Section-17 left	30	52.8	2.0922	110.46816
43	Section-17 right	30	52.8	3.8504	203.30112
44	Section-17 face	10	17.6	0.054017	0.9506992
45	Beam 1-right	130	212.0	29.85953	6330.22036
46	Beam m2-left	105	176.4	32.66255	5761.67382

Micromechanical Modelling of Material for Wind Turbine Blade

Table 6.5 Elements of the blade and its mass using glass/epoxy

No	Elements of the blade	glass/epoxy			
		Thickness (mm)	Weight /area(kg/m ²)	Surface area of each element (m ²)	Mass of each element (Kg)
1	Section-2	100	257	7.6314	1961.2698
2	Section-3	100	257	7.6319	1961.3983
3	Section-4	100	257	7.631	1961.167
4	Section-5	100	257	7.6346	1962.0922
5	Section-6	100	257	7.606	1954.742
6	Section-7	100	257	7.5563	1941.9691
7	Section-8	100	257	37.626	9669.882
8	Section-9 Top	90	206.4	6.7952	1402.52928
9	Section-9 bottom	90	206.4	7.0207	1449.07248
10	Section-9 left	70	179.9	8.9645	1612.71355
11	Section-9 right	70	179.9	16.18	2910.782
12	Section-10 Top	90	206.4	6.161	1271.6304
13	Section-10 bottom	90	206.4	6.2545	1290.9288
14	Section-10 left	70	179.9	8.1633	1468.57767
15	Section-10 right	70	179.9	13.889	2498.6311
16	Section-11 Top	70	155	5.5959	867.3645
17	Section-11 bottom	70	155	5.6667	878.3385
18	Section-11 left	70	179.9	7.1603	1288.13797
19	Section-11 right	70	179.9	12.943	2328.4457
20	Section-12 Top	70	155	4.8303	748.6965
21	Section-12 bottom	70	155	4.8753	755.6715
22	Section-12 left	60	154.2	6.5872	1015.74624
23	Section-12 right	60	154.2	11.352	1750.4784
24	Section-13 Top	70	155	4.1826	648.303
25	Section-13 bottom	70	155	4.21	652.55
26	Section-13 left	60	154.2	5.8077	895.54734
27	Section-13 right	60	154.2	10.065	1552.023
28	Section-14 Top	70	155	3.6034	558.527
29	Section-14 bottom	70	155	3.6155	560.4025
30	Section-14 left	60	154.2	4.8682	750.67644
31	Section-14 right	60	154.2	8.4882	1308.88044
32	Section-15 Top	65	154.6	3.0741	475.25586
33	Section-15 bottom	65	154.6	3.0781	475.87426
34	Section-15 left	60	154.2	3.953	609.5526
35	Section-15 right	50	128.5	6.8124	875.3934
36	Section-16 Top	50	128.5	2.6909	345.78065
37	Section-16 bottom	50	128.5	2.6924	345.9734
38	Section-16 left	50	128.5	2.8351	364.31035
39	Section-16 right	70	179.9	5.1284	922.59916
40	Section-17 Top	40	102.8	1.9229	197.67412
41	Section-17 bottom	40	102.8	1.9221	197.59188
42	Section-17 left	30	77.1	2.0922	161.30862
43	Section-17 right	30	77.1	3.8504	296.86584
44	Section-17 face	10	25.7	0.054017	1.3882369
45	Beam 1-right	130	309.2	29.85953	9232.566676
46	Beam m2-left	105	257.4	32.66255	8407.34037

Micromechanical Modelling of Material for Wind Turbine Blade

Table 6.6 Elements of the blade and its mass using hybrid glass-carbon/epoxy

No	Elements of the blade	Hybrid glass-carbon /epoxy			
		Thickness (mm)	Weight /area(kg/m ²)	Surface area of each element (m ²)	Mass of each element (Kg)
1	Section-2	100	216.5	7.6314	1652.1981
2	Section-3	100	216.5	7.6319	1652.30635
3	Section-4	100	216.5	7.631	1652.1115
4	Section-5	100	216.5	7.6346	1652.8909
5	Section-6	100	216.5	7.606	1646.699
6	Section-7	100	216.5	7.5563	1635.93895
7	Section-8	100	216.5	37.626	8146.029
8	Section-9 Top	90	174.0	6.7952	1182.3648
9	Section-9 bottom	90	174.0	7.0207	1221.6018
10	Section-9 left	70	138.7	8.9645	1243.37615
11	Section-9 right	70	138.7	16.18	2244.166
12	Section-10 Top	90	174.0	6.161	1072.014
13	Section-10 bottom	90	174.0	6.2545	1088.283
14	Section-10 left	70	138.7	8.1633	1132.24971
15	Section-10 right	70	138.7	13.889	1926.4043
16	Section-11 Top	70	130.7	5.5959	731.38413
17	Section-11 bottom	70	130.7	5.6667	740.63769
18	Section-11 left	70	138.7	7.1603	993.13361
19	Section-11 right	70	138.7	12.943	1795.1941
20	Section-12 Top	70	130.7	4.8303	631.32021
21	Section-12 bottom	70	130.70	4.8753	637.20171
22	Section-12 left	60	129.9	6.5872	855.67728
23	Section-12 right	60	129.9	11.352	1474.6248
24	Section-13 Top	70	130.70	4.1826	546.66582
25	Section-13 bottom	70	130.70	4.21	550.247
26	Section-13 left	60	129.9	5.8077	754.42023
27	Section-13 right	60	129.9	10.065	1307.4435
28	Section-14 Top	70	130.70	3.6034	470.96438
29	Section-14 bottom	70	130.70	3.6155	472.54585
30	Section-14 left	60	129.9	4.8682	632.37918
31	Section-14 right	60	129.9	8.4882	1102.61718
32	Section-15 Top	65	130.30	3.0741	400.55523
33	Section-15 bottom	65	130.30	3.0781	401.07643
34	Section-15 left	60	129.9	3.953	513.4947
35	Section-15 right	50	95.4	6.8124	649.90296
36	Section-16 Top	50	97.42	2.6909	262.147478
37	Section-16 bottom	50	97.42	2.6924	262.293608
38	Section-16 left	50	98.71	2.8351	279.852721
39	Section-16 right	70	138.7	5.1284	711.30908
40	Section-17 Top	40	86.6	1.9229	166.52314
41	Section-17 bottom	40	86.6	1.9221	166.45386
42	Section-17 left	30	64.95	2.0922	135.88839
43	Section-17 right	30	64.95	3.8504	250.08348
44	Section-17 face	10	21.65	0.054017	1.16946805
45	Beam 1-right	130	268.12	29.85953	8005.937184
46	Beam m2-left	105	216.9	32.66255	7084.507095

Flap-wise loading was used to characterize the composite materials at wind speeds 3m/s, 6m/s and 9m/s and at temperatures 25°C, 40°C, 55°C and 70°C. The orientation on each

Micromechanical Modelling of Material for Wind Turbine Blade

section was based on the fibre strength in the load direction. Figure 6.2 shows thickness distribution for the wind turbine blades.

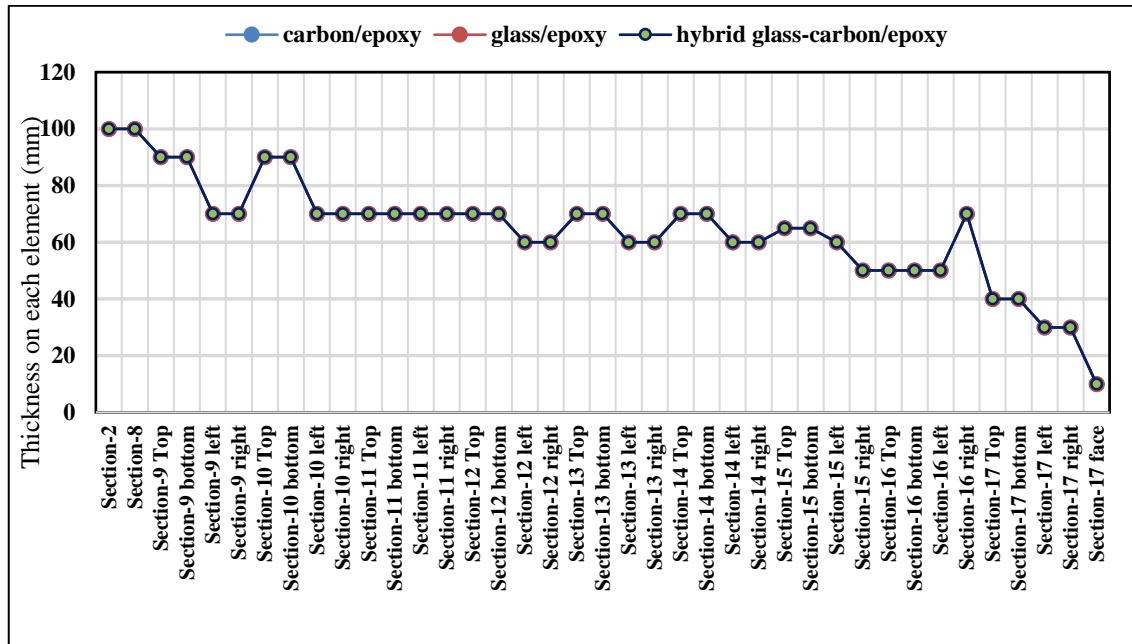


Figure 6.2 Thickness distribution on shell and spar-caps along the length of the blades

The weight of a blade has its own impact in increasing the gravitational load. Currently, most manufacturing industries design the wind blades using light materials to reduce the weight. Carbon fibre has been the choice of the industries because of its light weight and high strength but the cost of carbon fibre is ten times more than that of glass fibre.

Figure 6.3 compares the three blades based on the ratio of weight distribution on the shell and spar-caps along the lengths of the blades. Comparisons are shown in Figure 6.4 for the box shear webs along the length of the blades. Figure 6.5 shows the mass distribution plotted against the ratio of the total length of the blades. Figure 6.6 shows the total mass of the blade for different types of blades. Total mass of the glass/epoxy blade is 31.48% more than the carbon/epoxy blade and 16.92% more than the glass/carbon blade. The mass of each section of the blade is optimized based on the flap-wise loading. The mass of the blade is higher at the root section and lower at the tip section due to more material used near the root section to minimize the deflection of the blade. The gravitational loading on the glass/epoxy blade is high and fatigue loading may lower the life time of the blade.

Micromechanical Modelling of Material for Wind Turbine Blade

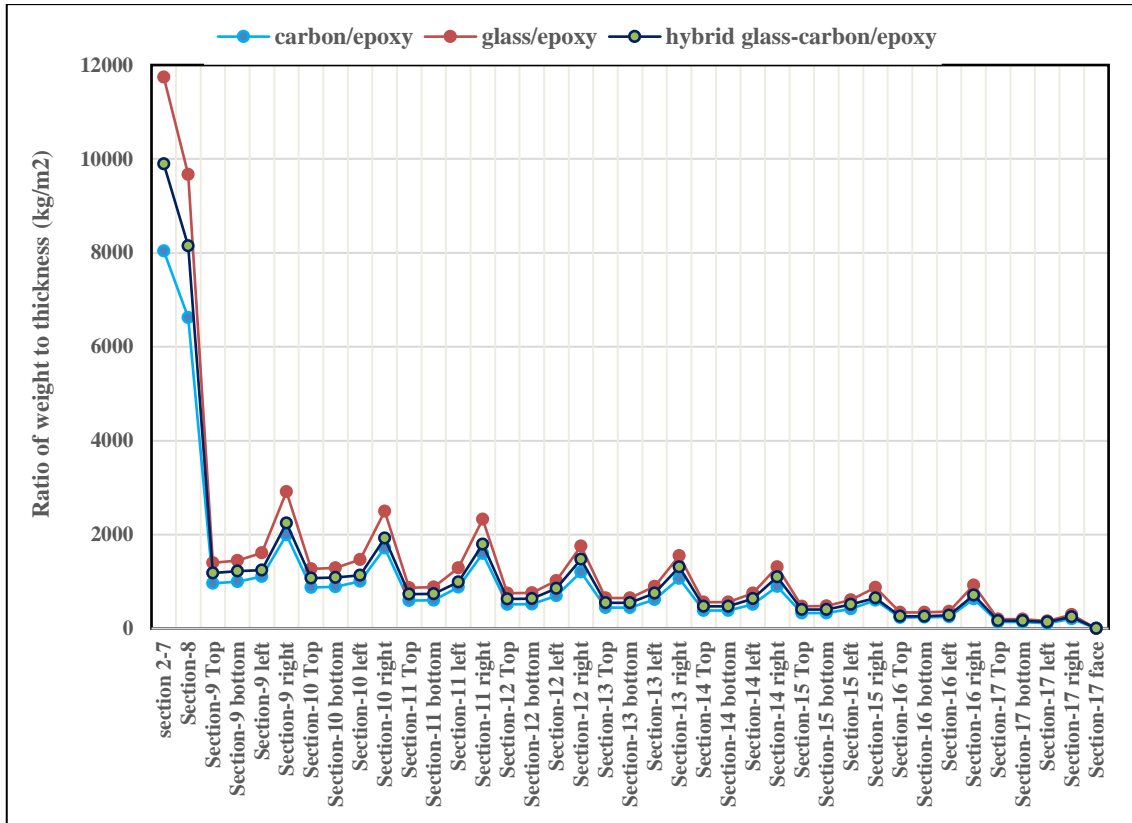


Figure 6.3 Ratio of weight to thickness on shell and spar-caps along the length of the blades

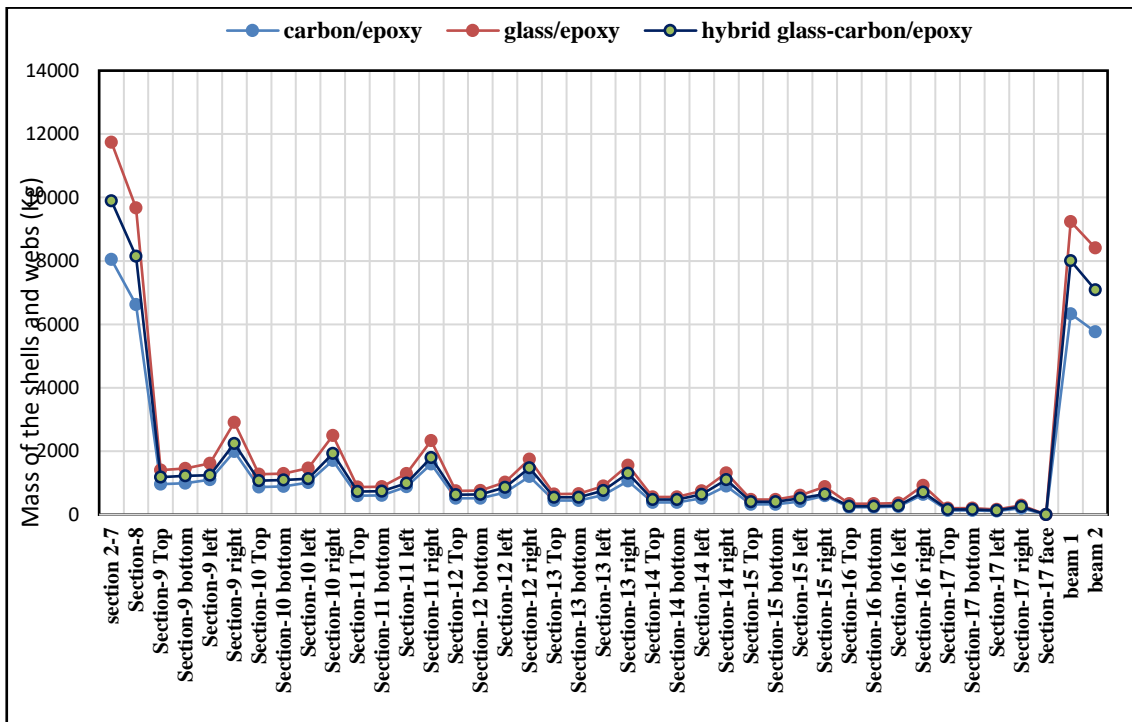


Figure 6.4 Ratio of weight to thickness of shell, spar-caps and shear web along the length of the blades

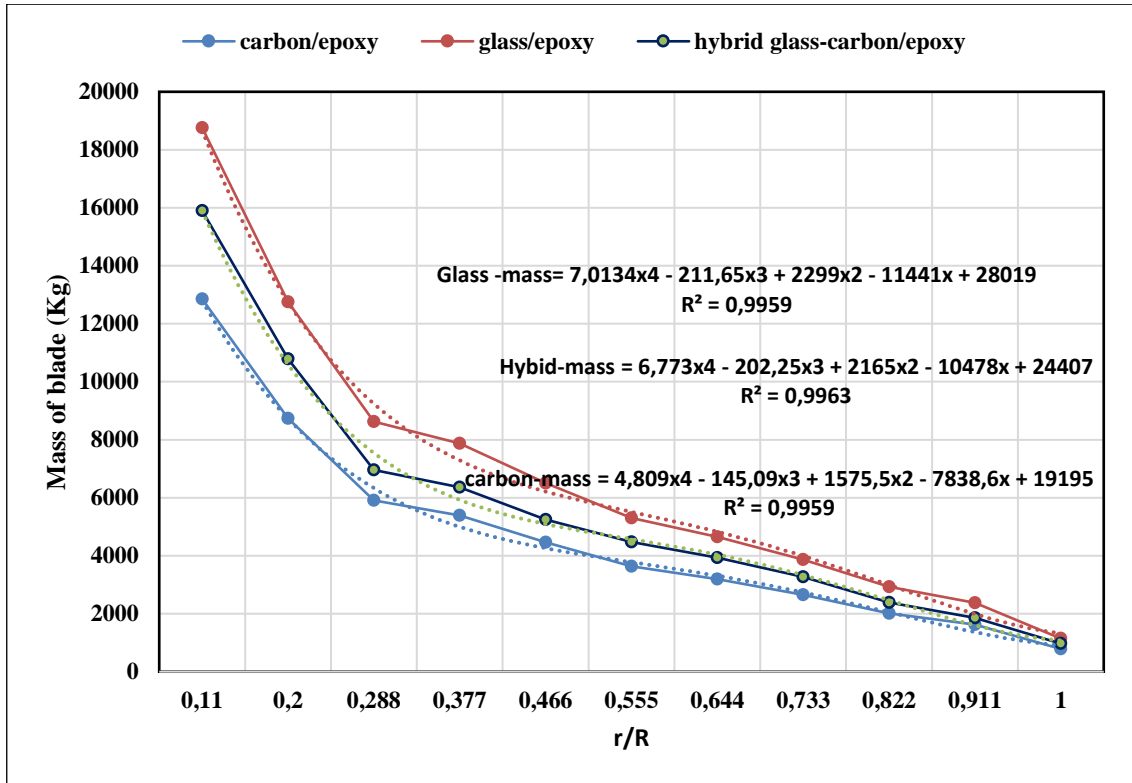


Figure 6.5 Mass distribution vs ratio of total length

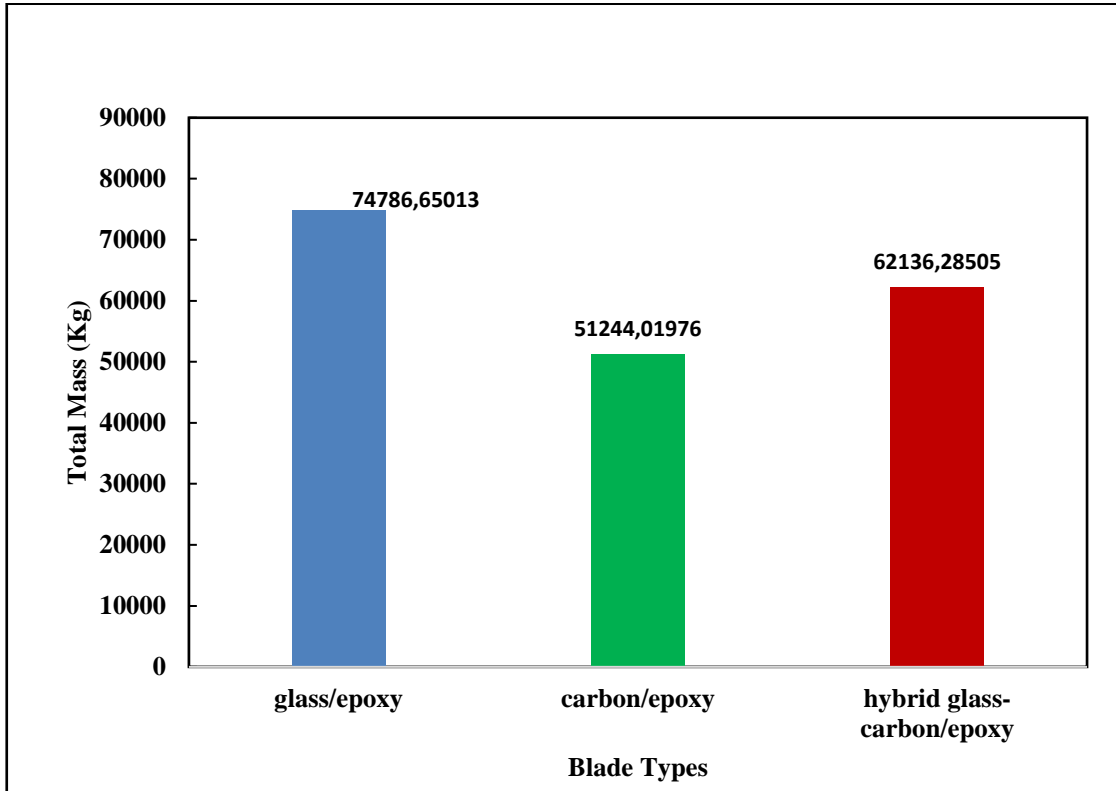


Figure 6.6 Total mass of the blade vs. blade types

6.3 Numerical Modelling of Turbine Blade under Variable Temperature

6.3.1 Geometrical Modeling

The finite element method (FEM) is employed to compute the eigen-frequencies, buckling load, tip deflection, stress-strain behaviour and the failure index of the blades using ANSYS software [103, 104]. The geometrical modelling of the blades is done using SolidWork software. The total lengths of the blades are specified as 54m. Maximum chord length is specified as 4.05m, minimum chord length as 0.81m and the largest twisting angle as 18° . The turbine blades are the critical structural members of wind turbines and rectangular hollow cross-sections are used along the length of the blades to support the structures and to reduce flap-wise bending. The airfoils selected using QBlade and ANSYS-fluent software have good aerodynamic properties under working conditions taking the Reynolds number as ($Re = 6 \times 10^6$). Figures 6.7 and 6.8 show airfoil configurations and the twist angle distributions from the tip to the largest chord section for the horizontal axis wind turbine blades. The shell thickness of the blade includes the internal shear web and the outer surfaces of the airfoil created by using a boundary surface, and then transferred to ANSYS-ACP (Pre)-Designmodeler.

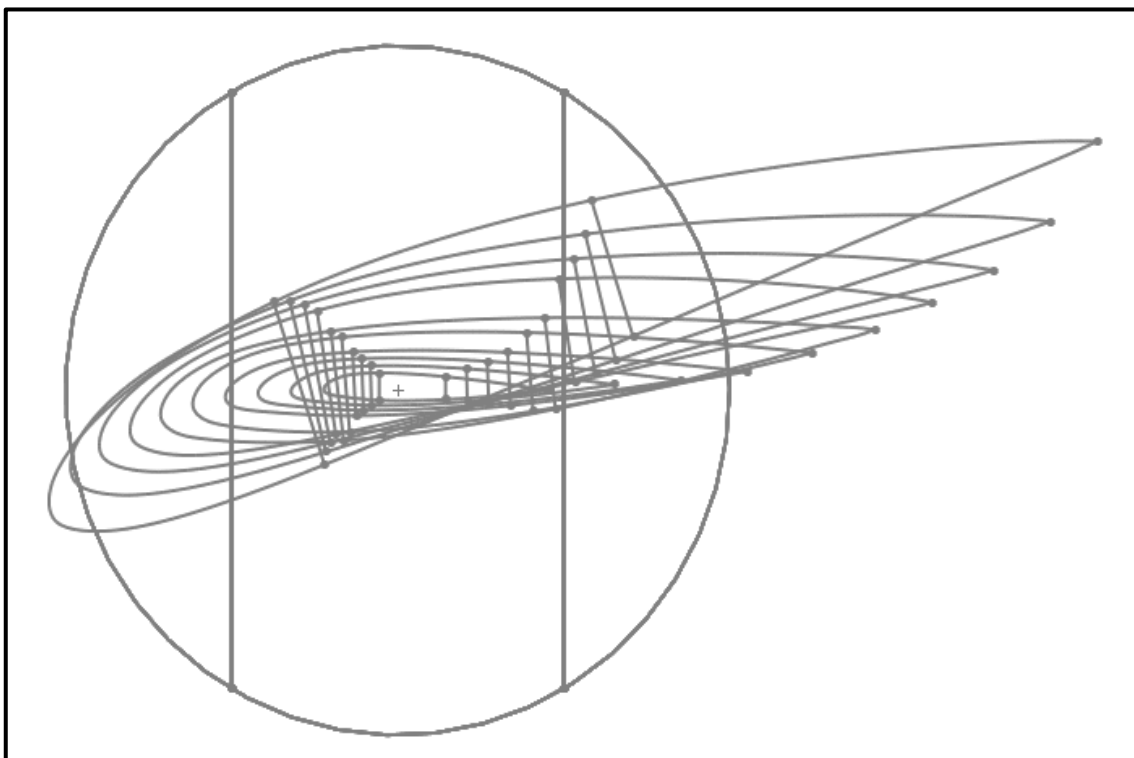


Figure 6.7 NACA aerofoil twisting angles

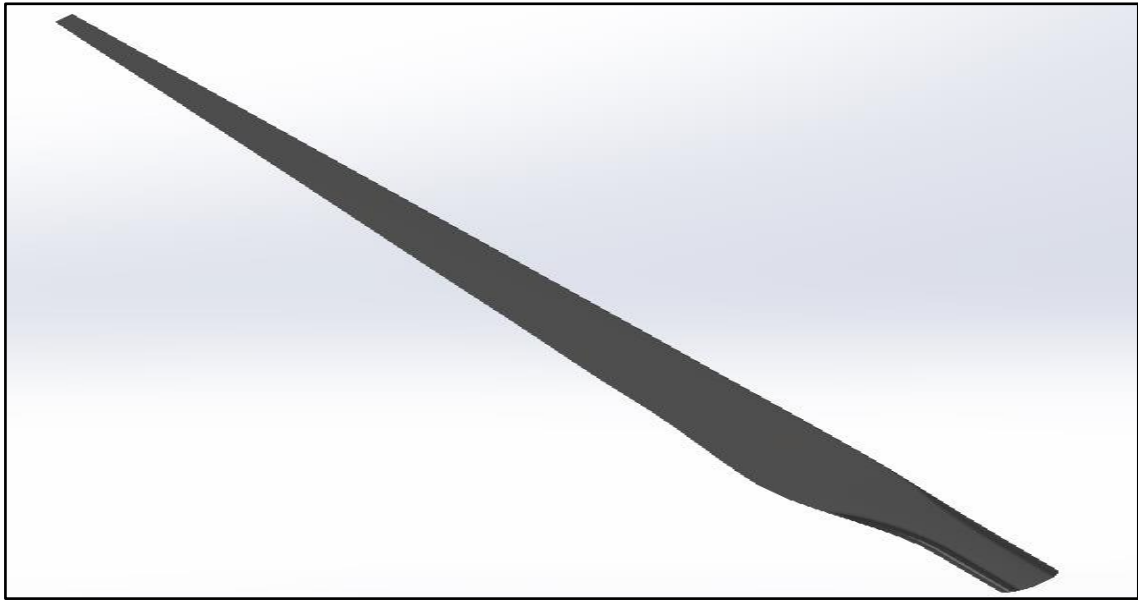


Figure 6.8 Wind turbine blade model using SolidWork software

Figure 6.9 shows sectional elemental blades used to model the composite materials with different thicknesses and material types to resist the wind loads and the bending moment.

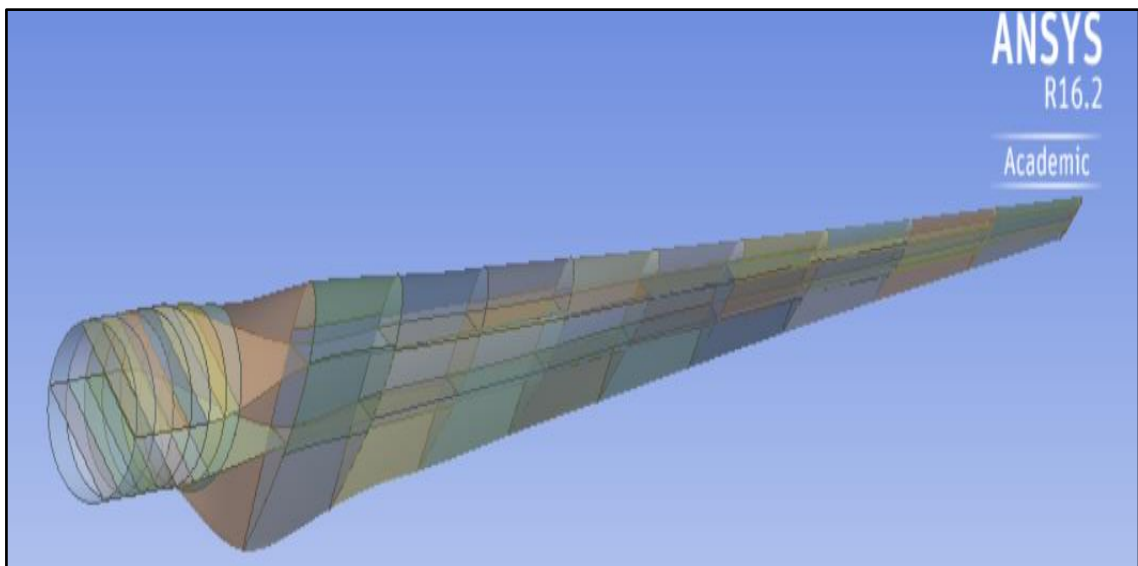


Figure 6.9 Sectional elements of the blades

Different sectional parts of shell thickness of the blade were transferred to ANSYS Static Structure software. The thicknesses of the turbine blades were specified and the mapping mesh was imposed on each section. The turbine blade contains 344051 elements, 165428 nodes and 36322 areas meshed. The meshed sections of the blades were connected to

Numerical Modelling of Turbine Blade under Variable Temperature

each other with mesh edit (mesh connecting groups) at a tolerance value of $9 \times 10^{-3} m$. Figure 6.10 shows the meshed surface of the blade model ready for further analysis. The challenge in the modelling of the blades is the meshing and mesh editing. It needs higher capacity computers for making meshing fine.

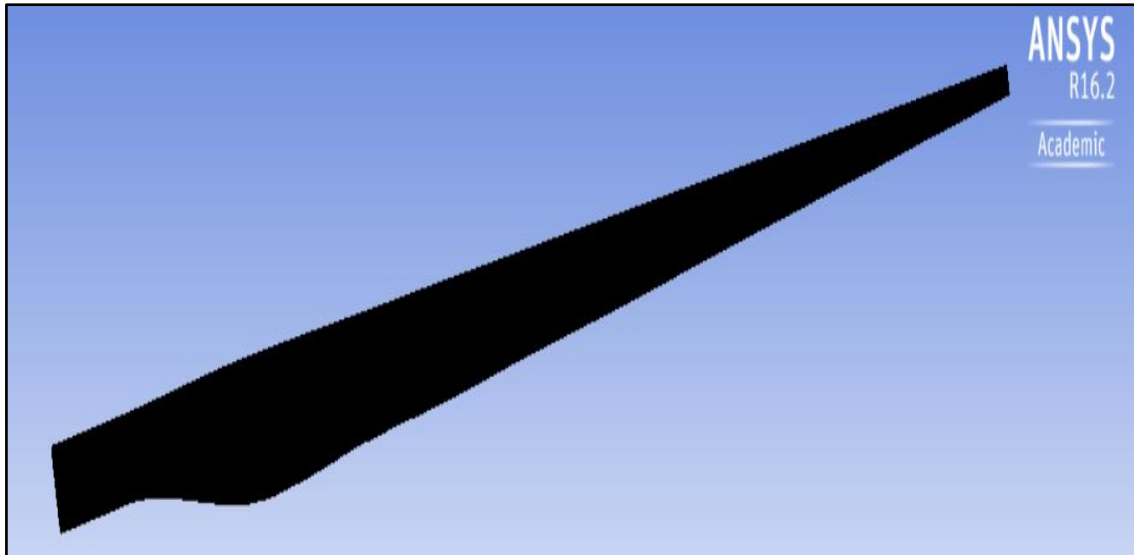
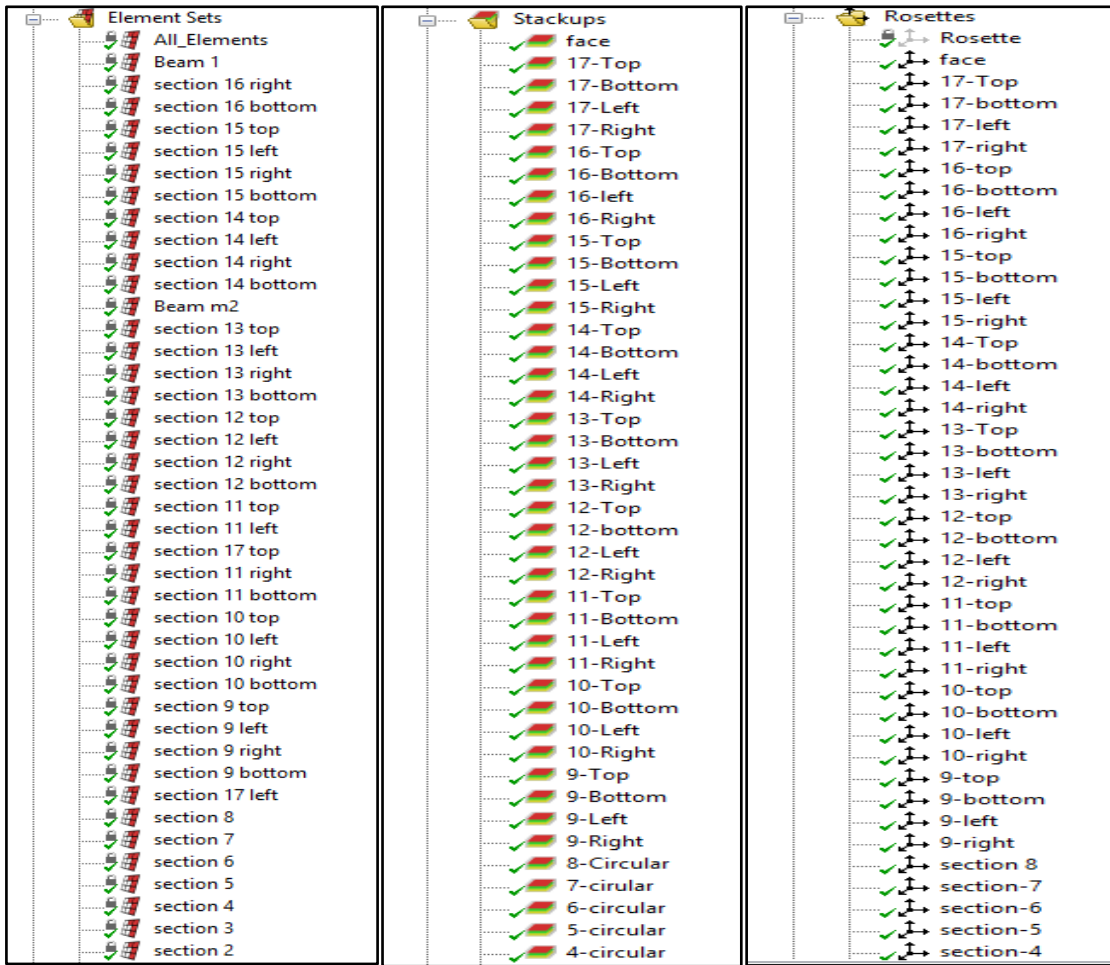


Figure 6.10 Wind turbine blade meshed surface using ANSYS software

A name was assigned for each section of the FEM blade model and then the model was transferred to ANSYS composite Prep-Post. Similarly, materials applicable for modelling the structure were also transferred from engineering database to ACP-Pre. The FEM model of the blades resulted from using five different composite materials to find the effect of temperature variation on the tip deflection and the failure index for each element. To do that, unidirectional CFRP, GFRP, hybrid GFRP-CFRP, and hybrid CFRP-GFRP composites and PVC foam were used to model the blades. The thicknesses, stack-ups and fibre orientation of the materials were set-up on ACP-Pre for each wind turbine blade. Figure 6.11 shows the stack-ups, fibre orientations and thickness distribution of the blade structures. The profile of a composite blade is shown in Figure 6.12. There are 46 elements of the blades and each of them has a different name and thicknesses. Taking into account that the flap-wise bending moment occurs at different wind speeds, the lengthwise thickness of the blade was approximated and the solid models of the blades were developed on ANSYS composites Prep-Post as shown in Figure 6.13.

Numerical Modelling of Turbine Blade under Variable Temperature



(a) Elements of blade (b) Different stack-ups (c) Fibre directions

Figure 6.11 FEM blade thickness distributions

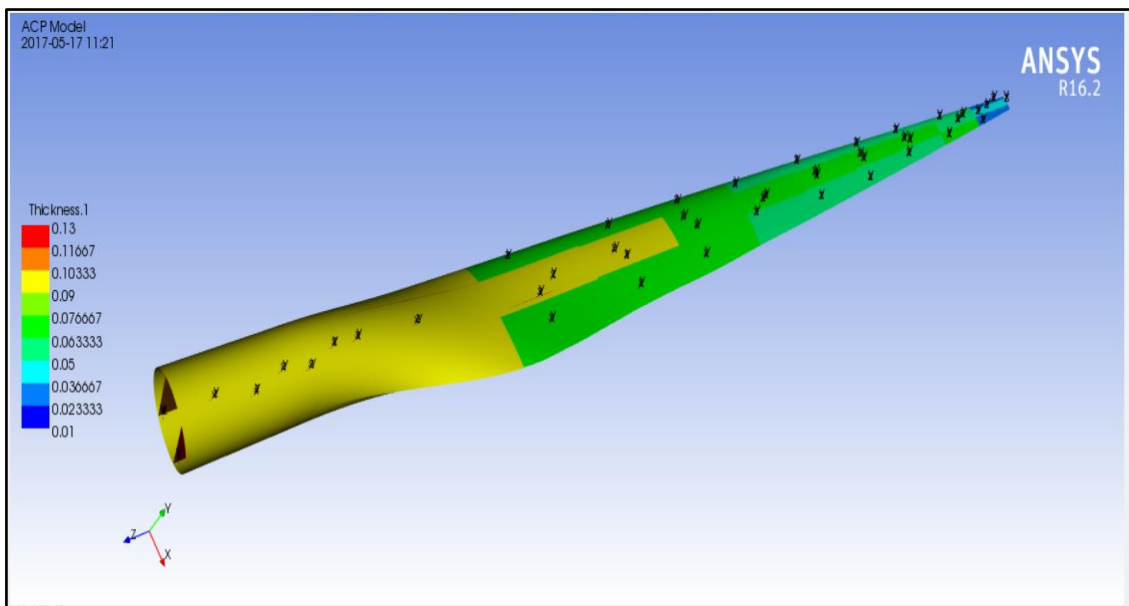


Figure 6.12 Composite blade profile in ANSYS ACP (pre)

Numerical Modelling of Turbine Blade under Variable Temperature

After putting the necessary parameters and updating on ACP-Pre, the blade model was transferred to ANSYS static structure for analysis. Four wind turbine blade models were prepared for CFRP, GFRP, hybrid GFRP-CFRP and hybrid CFRP-GFRP composite materials for characterization purposes.

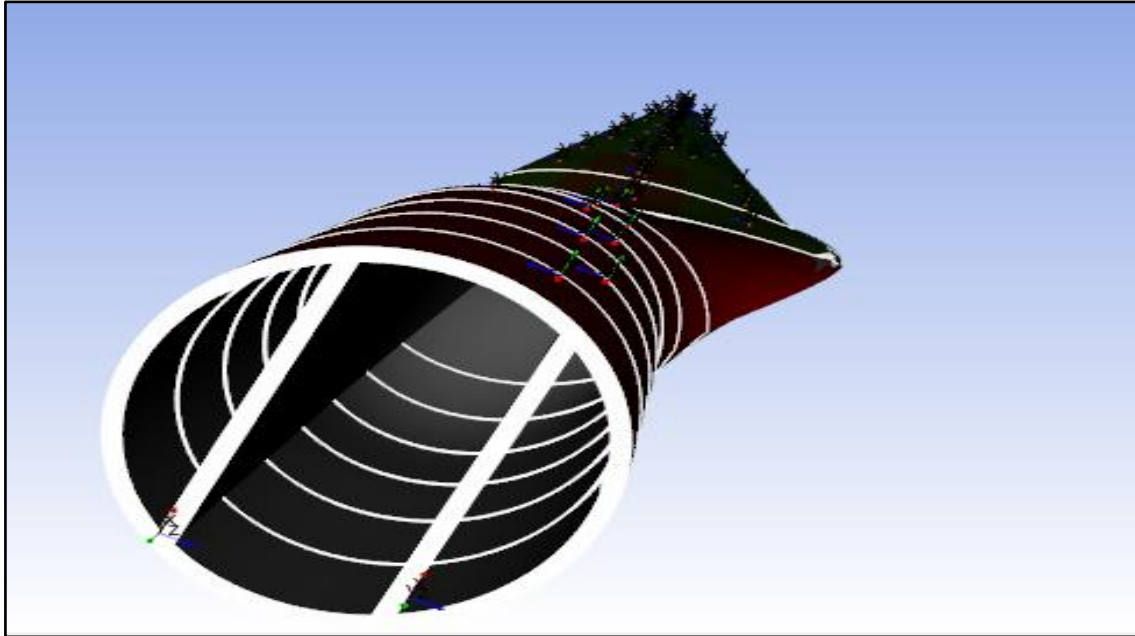


Figure 6.13 FE model of the blades after placing the composite material on each element

6.3.2 Boundary and Loading Conditions under Variable Temperatures

Before the simulations using ANSYS static structure software, the blade was attached to the root section with a fixed support and was restrained in its movement with respect to a different axis. Four different thermal loadings were applied to four different blades to assess the impact of temperature variations on their mechanical behaviour. This included total deformation, tip deflection and the failure limit. Flap-wise loading at wind speeds of 3m/s, 6m/s and 9m/s in the flap-wise directions was simulated. Fixed support and restraining of the composite blades on different axes and the loadings are shown in Figure 6.14. On ANSYS static simulations, the solutions for total deformation under different thermal and flap-wise loadings were obtained for four different blade types. To view and compare the simulation results under flap-wise and thermal loading conditions, the solutions of ANSYS static structural simulations were transferred to ANSYS ACP (post).

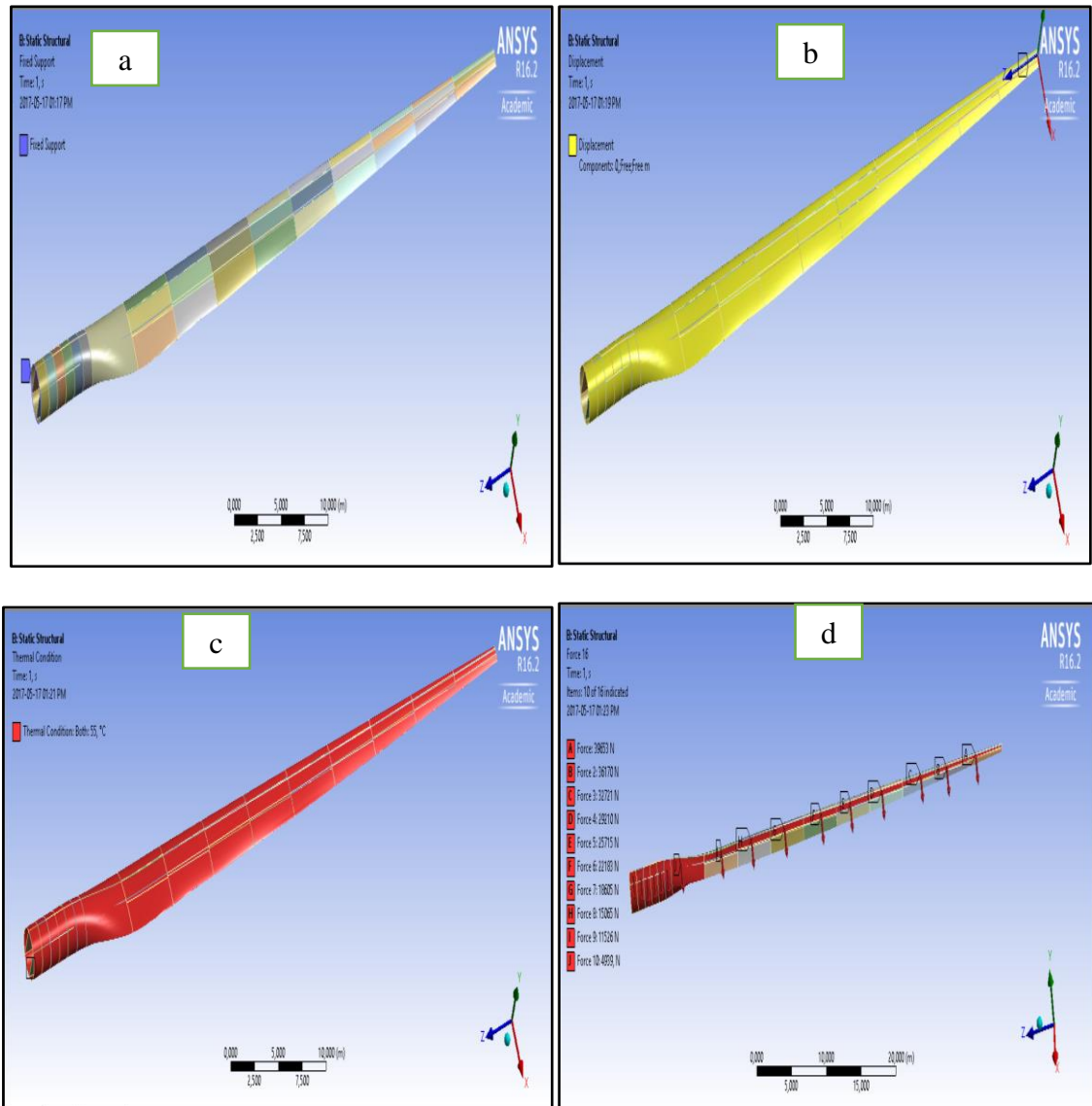


Figure 6.14 FEM model simulation on ANSYS static structure

6.4 Finite Element Analysis and Results

In this section, simulations using ANSYS software are performed for wind turbine blades built from CFRP, GFRP, hybrid GFRP-CFRP and hybrid CFRP-GFRP composites. Simulation results are given for total deformation, tip deflection and the failure of the blades. The simulation results for total deformation under different wind loads and thermal conditions are given in Table 6.7. Comparisons of total deformations of the blades are shown in Figure 6.15. The results for the glass/epoxy blade show that the total deformation of the blade increased by about 65.56 % as compared to the carbon/epoxy blade. Comparing it with the glass/carbon hybrid and carbon-glass hybrid blades, the total deformation of the glass/epoxy blade increased by 47.77 % and 50.10%. The total

deformation of the glass/carbon hybrid blade increased approximately by 4.14%. The total deformation of the blades under different thermal loadings were less than 0.2%. The static structural simulation analysis results for four FRP composite materials are shown in Figure 6.16.

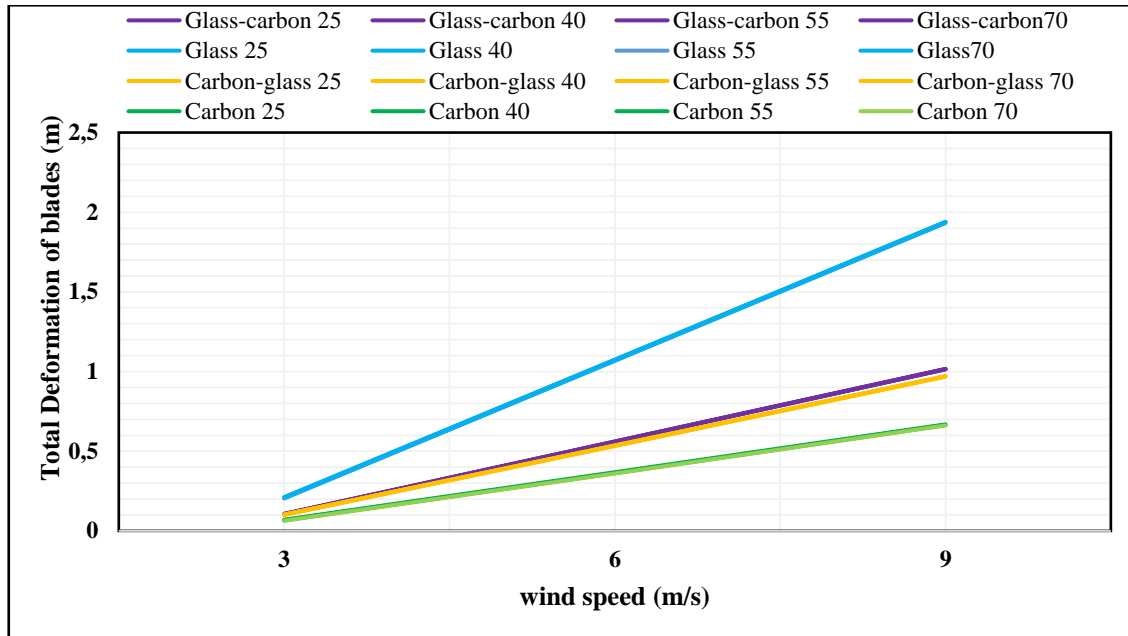
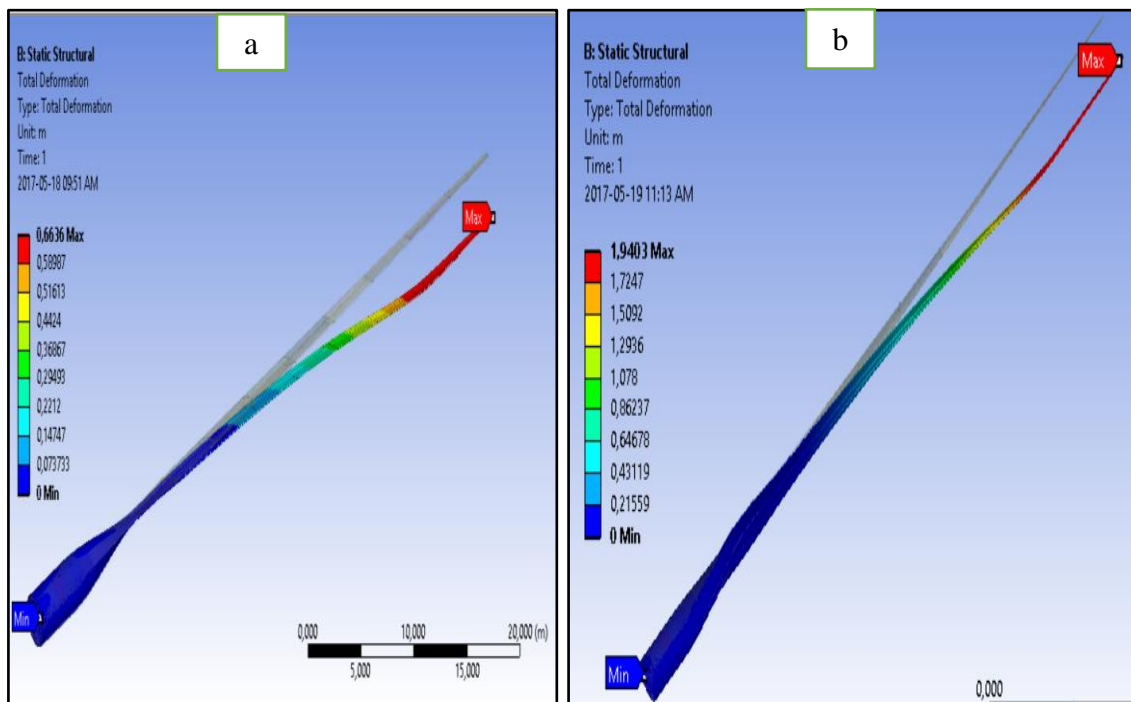


Figure 6. 15 Total deformation of blades under various flap-wise loadings and thermal conditions



(a) Carbon/epoxy blade

(b) Glass/epoxy blade

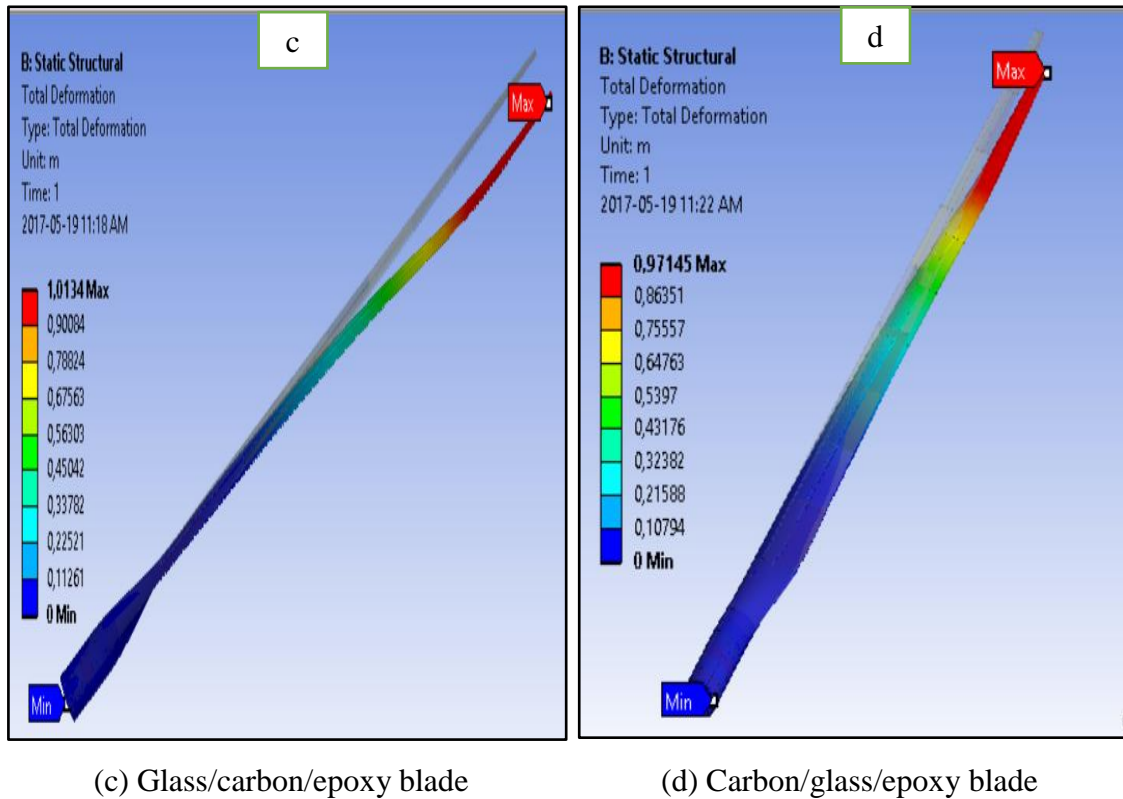


Figure 6.16 Total deformations of blades

Table 6.7 Total deformation of blades under different wind speeds and thermal conditions

No	Composite Materials used for modelling the wind turbine blade structures	Thermal conditions (°C)	Deformation of the blade at [3m/s] wind speed	Deformation of the blade at [6m/s] wind speed	Deformation of the blade at [9 m/s] wind speed
1	Carbon/epoxy	25	0,06991	0,36738	0,66818
2	Carbon/epoxy	40	0,067459	0,36491	0,66566
3	Carbon/epoxy	55	0,065423	0,36287	0,6636
4	Carbon/epoxy	70	0,063388	0,36083	0,66154
5	Glass /epoxy	25	0,20298	1,0670	1,9320
6	Glass /epoxy	40	0,20618	1,0702	1,9351
7	Glass /epoxy	55	0,20899	1,0728	1,9377
8	Glass /epoxy	70	0,2119	1,0755	1,9403
9	Hybrid glass-carbon/epoxy	25	0,10687	0,56153	1,0166
10	Hybrid glass-carbon/epoxy	40	0,10569	0,56032	1,0154
11	Hybrid glass-carbon/epoxy	55	0,10472	0,55934	1,0144
12	Hybrid glass-carbon/epoxy	70	0,10377	0,55836	1,0134
13	Hybrid carbon-glass/epoxy	25	0,10213	0,53675	0,97145
14	Hybrid carbon-glass/epoxy	40	0,10213	0,53549	0,97018
15	Hybrid carbon-glass/epoxy	55	0,10111	0,53448	0,96916
16	Hybrid carbon-glass/epoxy	70	0,10011	0,53346	0,96814

Next, simulations were applied to find the tip deflection (along Y-axis) and the results are shown in Table 6.8. The tip deflection of the blades is one of the parameters to consider in the selection of the specific composite material for the blades. The clearance between the blade and the tower at different wind speeds must be large enough to avoid collision. Figure 6.17 shows the comparison of tip deflection for blades at different flap-wise loadings and under different wind speeds and thermal conditions. The results for glass/epoxy blades show that the largest tip deflection along the Y-axis due to flap-wise and thermal loading is about 65.80% higher as compared to a carbon/epoxy blade model. The tip deflections of the two hybrids blades are between those of the carbon/epoxy blade and glass/epoxy blade. Glass/carbon and carbon/glass hybrid blades have tip deflections which are 34.52% and 31.69% higher as compared to that of a carbon/epoxy blade. Hybrid blades cost less compared to carbon/epoxy blades. The differences in tip deflections at ambient and higher temperatures were about 0.2%. This value was too small to assess the effect of temperature on the mechanical behaviour of the wind turbine blades. The largest and smallest tip deflections for CFRP, GFRP, GFRP-CFRP and CFRP-GFRP materials are shown in Figure 6.18 with respect to different flap-wise loadings.

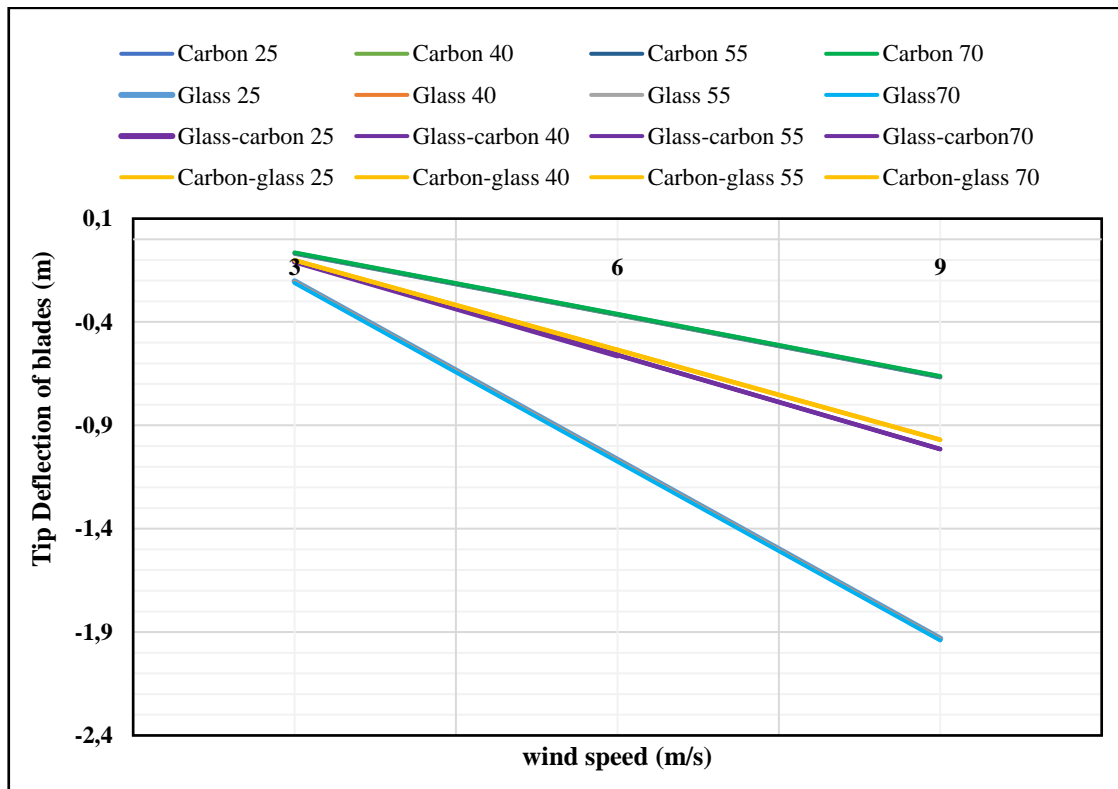
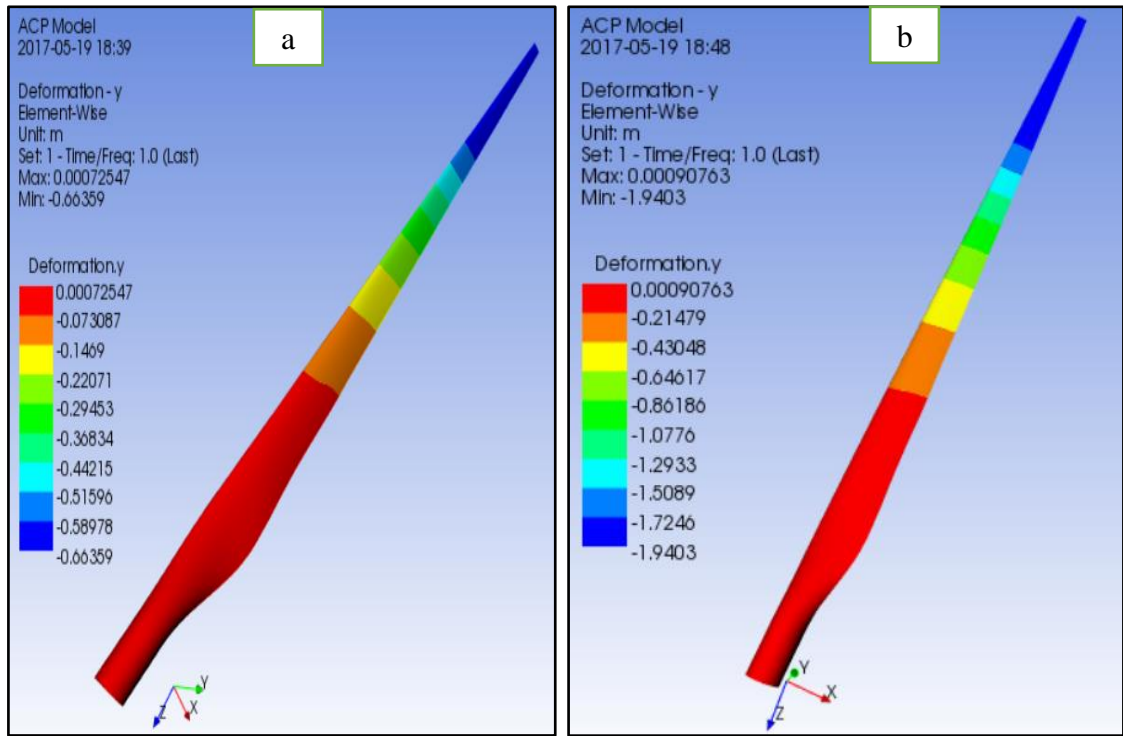
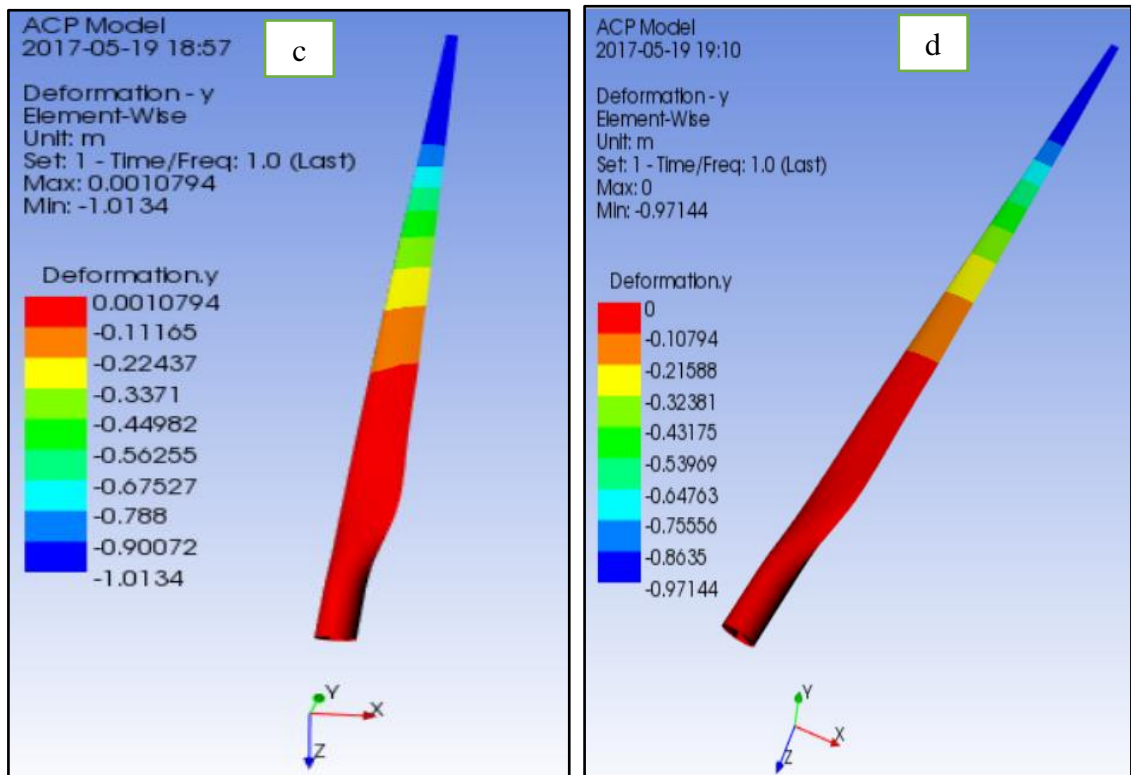


Figure 6.17 Tip deflection of blades under various flap-wise wind loads and thermal conditions



(a) Carbon/epoxy blade

(b) Glass/epoxy blade model



(c) Glass-carbon blade

(d) Carbon-glass blade

Figure 6.18 Tip deflections of blades

Table 6.8 Tip defections of blades under different wind loads and thermal conditions

No	Composite Materials used for model the wind turbine blades	Thermal condition (°C)	Tip deflection of the blade at [3m/s] wind speed	Tip deflection of the blade at [6m/s] wind speed	Tip deflection of the blade at [9m/s] wind speed
1	Carbon/epoxy	25	-0,069909	-0,36738	-0,66817
2	Carbon/epoxy	40	-0,067457	-0,3649	-0,66565
3	Carbon/epoxy	55	-0,065421	-0,36286	-0,66359
4	Carbon/epoxy	70	-0,063384	-0,36082	-0,66153
5	Glass /epoxy	25	-0,20297	-1,0670	-1,9320
6	Glass /epoxy	40	-0,20613	-1,0702	-1,9351
7	Glass /epoxy	55	-0,20876	-1,0728	-1,9377
8	Glass /epoxy	70	-0,21139	-1,0754	-1,9403
9	Hybrid glass-carbon/epoxy	25	-0,10686	-0,56153	-1,0166
10	Hybrid glass-carbon/epoxy	40	-0,10569	-0,56032	-1,0154
11	Hybrid glass-carbon/epoxy	55	-0,10471	-0,55934	-1,0144
12	Hybrid glass-carbon/epoxy	70	-0,10373	-0,55836	-1,0134
13	Hybrid carbon-glass/epoxy	25	-0,10213	-0,53674	-0,97144
14	Hybrid carbon-glass/epoxy	40	-0,10213	-0,53549	-0,97018
15	Hybrid carbon-glass/epoxy	55	-0,10111	-0,53448	-0,96915
16	Hybrid carbon-glass/epoxy	70	-0,10009	-0,53346	-0,96814

6.5 FEM Blade Structural Failure Analysis

There are different failure modes to determine the service life of rotating blade structures and it is important to determine the failure index under different loading conditions. Failure of the blades occurs due to increasing flap-wise loading and increasing wind loading. Harsh environmental conditions have also an impact on the failure of the blade operating in cold or warm climates. Tsai-Wu, Puck and LaRC failure criteria are implemented to investigate the failure index for four different blade models. The simulation results for the three failure criteria were very close and the Tsai-Wu failure criterion was used to assess the influence of temperature and wind load on the failure of the blades. The model implemented in the present study has the advantage of optimizing each section of the blade against failure due to increasing wind load. Based on these modelling techniques, simulations for the four blade models were implemented with flap-wise loading at a wind speed of 3m/s and at temperatures 25°C, 40°C, 55°C and 70°C.

Failure Index (FI) for each element was computed using ANSYS composite Prep Post. Figure 6.19 shows the failure index for carbon/epoxy composite blades. Results indicate that failure occurs due to increasing temperature. At temperatures above 40°C, the failure limit is exceeded in the main structural components of the blade. Figure 6.20 shows the failure index for a glass/epoxy blade. Failure occurs due to increasing temperature and the failure limit is exceeded in the main spar caps section of the blade above 40°C. Figure 6.21 shows the simulation results for the hybrid composite blade with carbon fibre at the top and bottom sections of the blade. Figure 6.22 shows the results of hybrid composite blade with the glass fibre at the top and bottom sections of the blade. The materials in both cases fail as the temperature increases above 40°C, and the spar-cap sections which have more PVC foam, fail. No failure occurs at the ambient temperature.

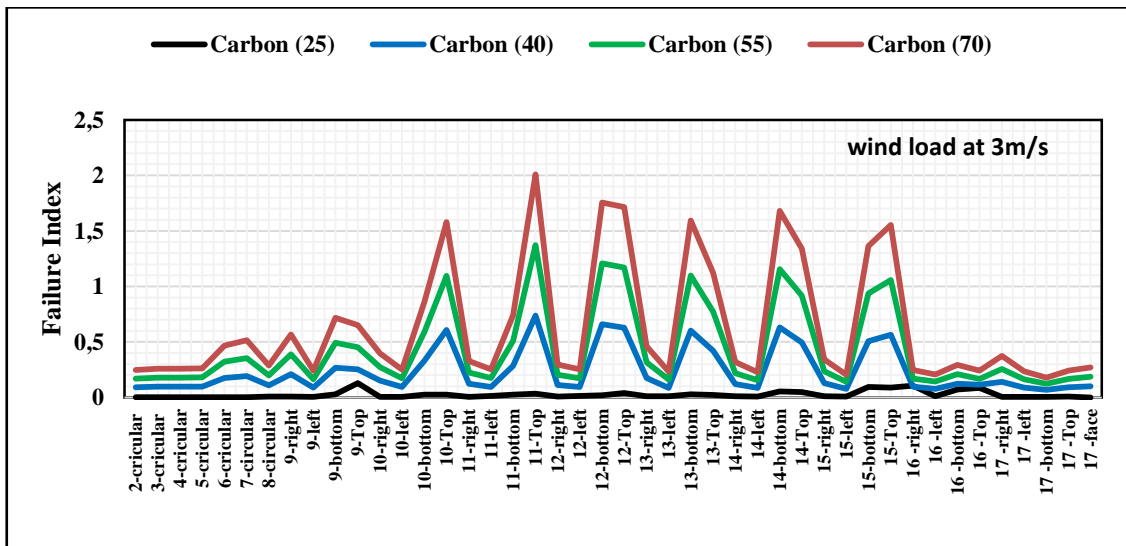


Figure 6. 19 Failure index vs. flap-wise and thermal loading for carbon fibre blade

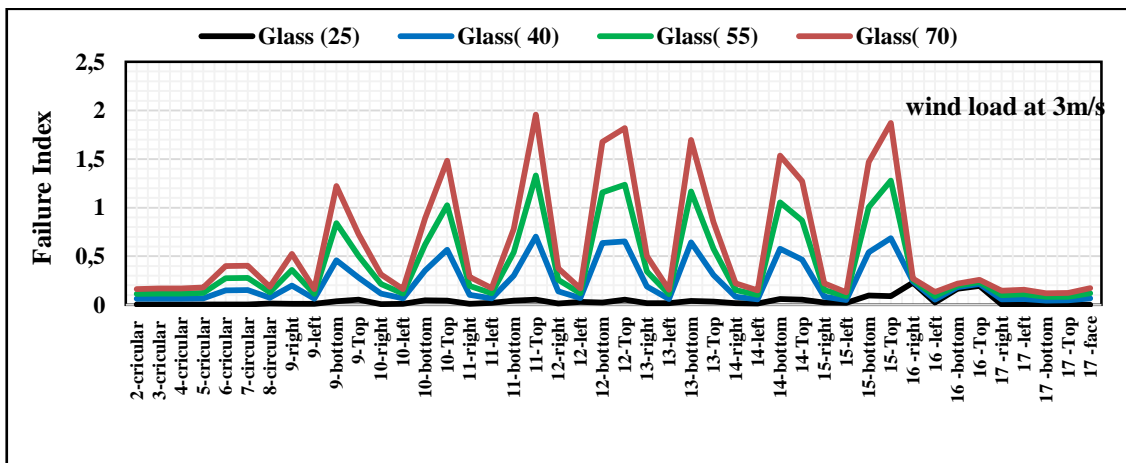


Figure 6. 20 Failure index vs. flap-wise and thermal loading for glass fibre blade

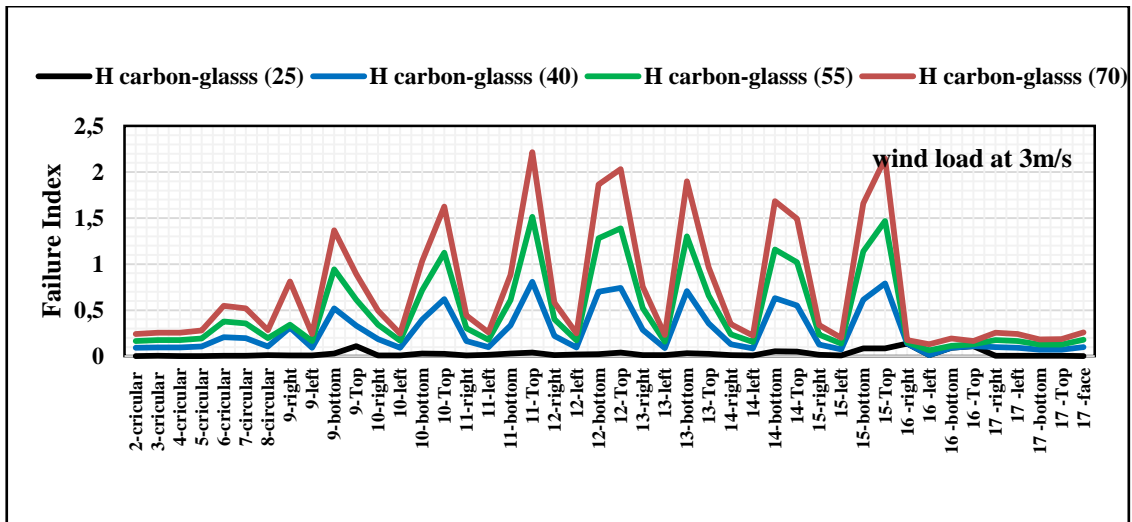


Figure 6. 21 Failure index vs. flap-wise and thermal loading on carbon-glass fibre blade

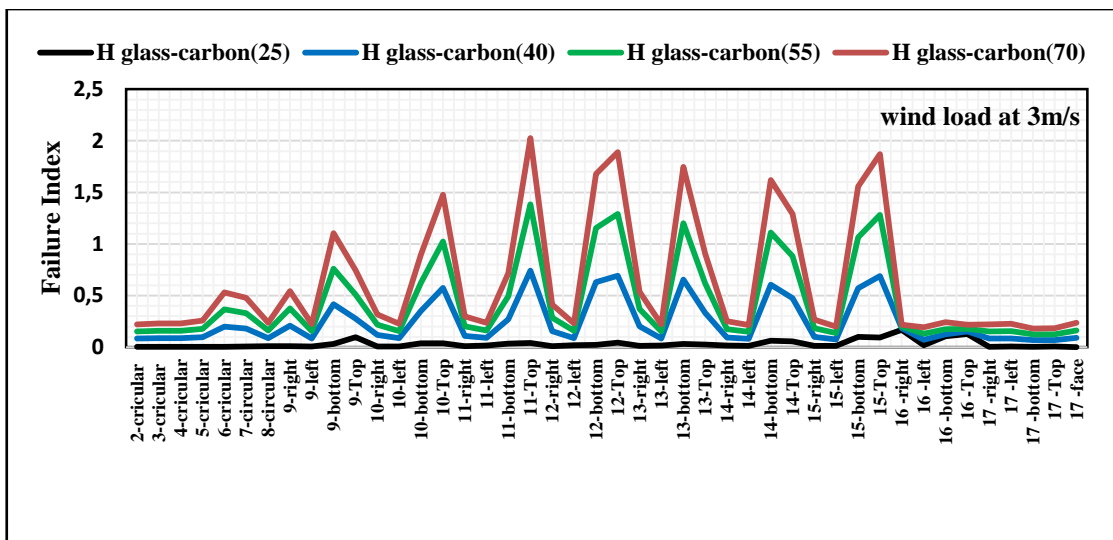


Figure 6. 22 Failure index vs. flap-wise and thermal loading on a glass-carbon fibre blade

Simulations were conducted on the blades by changing the flap-wise loading at a wind speed of 6m/s and at temperatures 25°C, 40°C, 55°C and 70°C. The thickness, fibre orientation and fibre direction of each section were taken the same. Figure 6.23 shows the simulation results for the carbon/epoxy blade subject to flap-wise loading at a wind speed of 6m/s. Results indicate that failure occurs at temperatures above 40°C. As the temperature goes above 40°C, the blade fails as shown in Figure 6.19. Simulations for glass/epoxy blade are shown in Figure 6.24 taking into account flap-wise loading at a wind speed of 6m/s and at temperatures 25°C, 40°C, 55°C and 70°C. The results indicate that failure occurs at temperatures above 40°C. The strength of glass fibre is lower than that of carbon fibre as shown in Figure 6.24. Simulations for carbon-glass and glass-

carbon composites are shown in Figures 6.25 and 6.26. Results show that the failure index exceeds the failure limit when the temperature goes above 40°C. This result is in agreement with the experiment results. Blade material satisfies the IEC 61400-1 standard and failure does not occur below 40°C. This indicates that the volume fraction of fibres and the resin used are correct in order to improve the mechanical properties and glass transition temperatures of the blades.

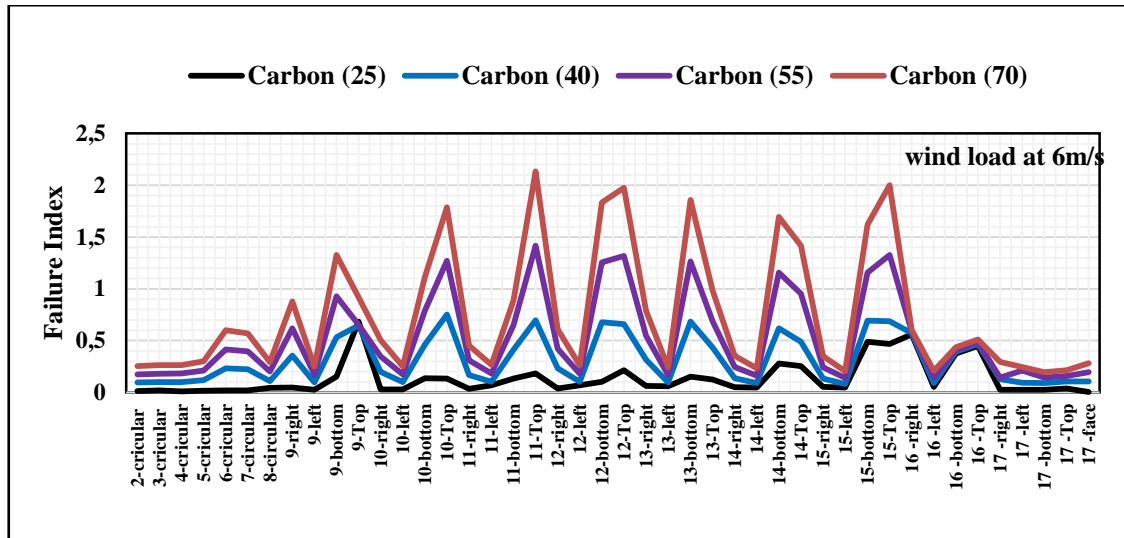


Figure 6.23 Failure index vs. flap-wise and thermal loading for carbon/epoxy blade

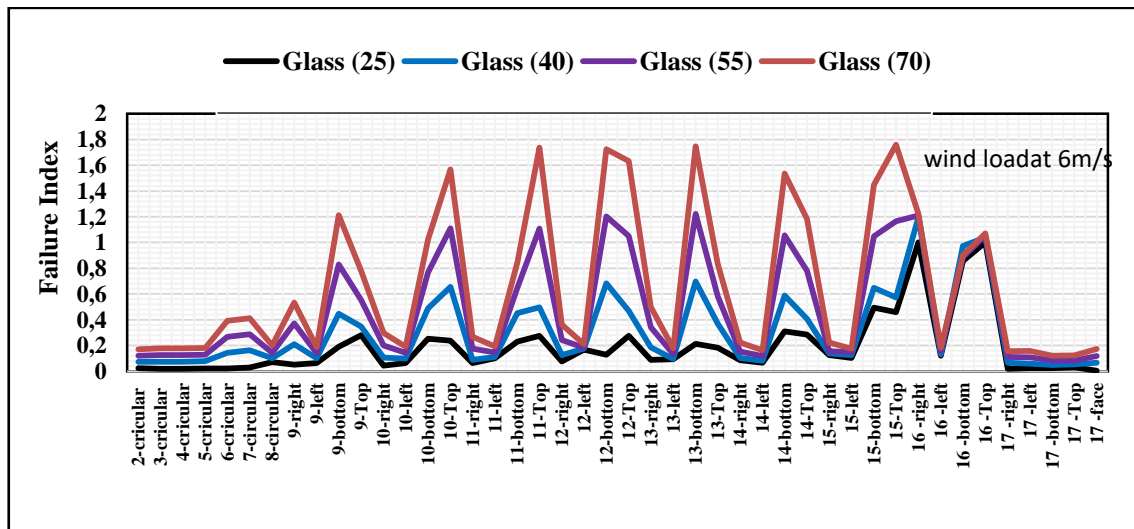


Figure 6.24 Failure index vs. flap-wise and thermal loading on glass fibre blade

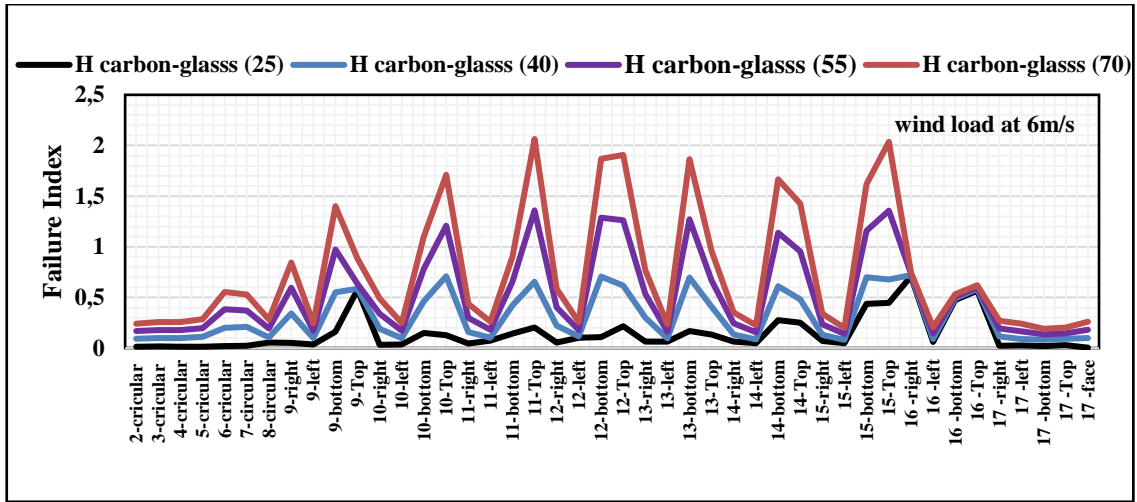


Figure 6.25 Failure index vs. flap-wise and thermal loading for carbon-glass blade

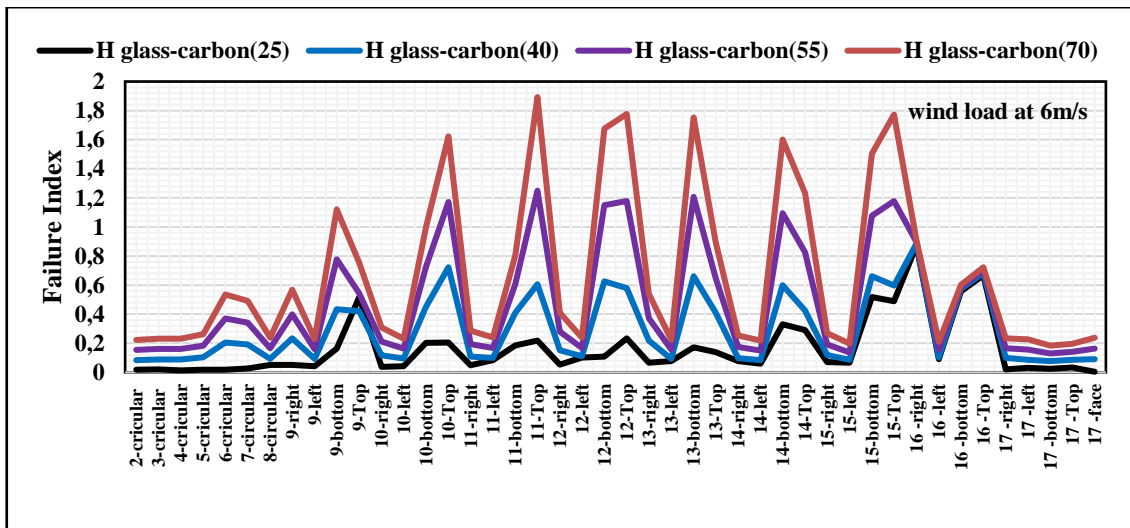


Figure 6.26 Failure index vs. flap-wise and thermal loading on glass-carbon blade

Failure of wind blades occurs under various loading conditions involving the flap-wise and thermal loadings. Before the computer simulations were conducted, experimental analysis of composite materials was conducted to compare and identify the right materials with good static and dynamic properties under high temperatures. The test results indicated that unidirectional hybrid composites are strong, have high T_g values, are cost effective and good damping and noise properties. The strength of composite blades decreased as the temperature increased and reached beyond 40°C . This happens due to low glass transition temperatures of epoxy resins used in the blades. The glass transition temperatures of the composites used in the tests and simulations fulfil the IEC standards. In addition to experimental work, FEM simulations are employed to identify the right blade model with respect to failure taking flap-wise wind load and thermal conditions

into account. Four blade models were studied for comparison with identical thicknesses along their elements. CFRP, GFRP, CFRP-GFRP and GFRP-CFRP blades were compared at a wind speed of 9m/s and at temperatures 25°C, 40°C, 55°C and 70°C. Figure 6.27 shows the simulation results for carbon/epoxy blades at a wind speed of 9m/s and at temperatures 25°C, 40°C, 55°C and 70°C. The simulation results show that the failure index approaches failure limit at ambient temperature. This is due to higher wind loads on the structures. The simulation results for glass/epoxy blades are shown in Figure 6.28 subject to the same wind load and thermal conditions. The results show that the failure index exceeds the failure limit due to flap-wise loading at ambient temperature. Material modelling using ANSYS composite Prep Post is employed to compare the failure indexes. Figures 6.29 and 6.30 show the simulation results for two hybrid composites with carbon fibre on the outside and on the inside of the laminations. The results shown in Figure 6.29 indicate that carbon-glass hybrid blades approach the failure limit in one of their sections at ambient temperature. The results in Figure 6.30 show that glass-carbon hybrid blade exceeds the failure limit at one of the sections of the blades at ambient temperature. As we observed from the previous simulations, the failure of the blades occurs at temperatures above 40°C. The comparison of the blades using FEM simulations shows that carbon/epoxy and carbon-glass/epoxy hybrids are the right choices considering the wind loads at ambient temperature. In any design, strength and cost considerations are of utmost importance. Based on this principle, hybrid carbon-glass/epoxy is the right composite material for modelling blades in warm areas considering the wind loads and ambient conditions.

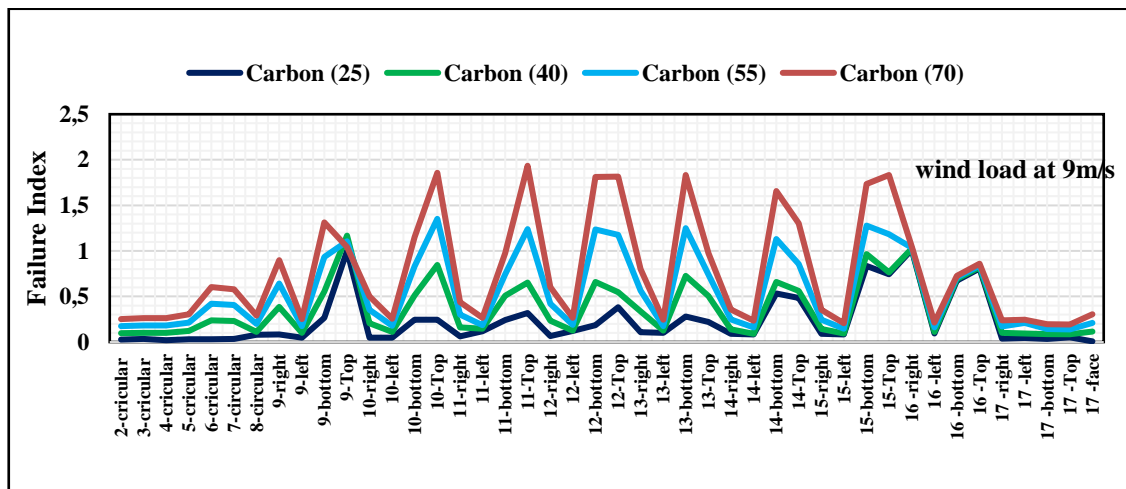


Figure 6. 27 Failure index vs. flap-wise and thermal loading for carbon/epoxy blade

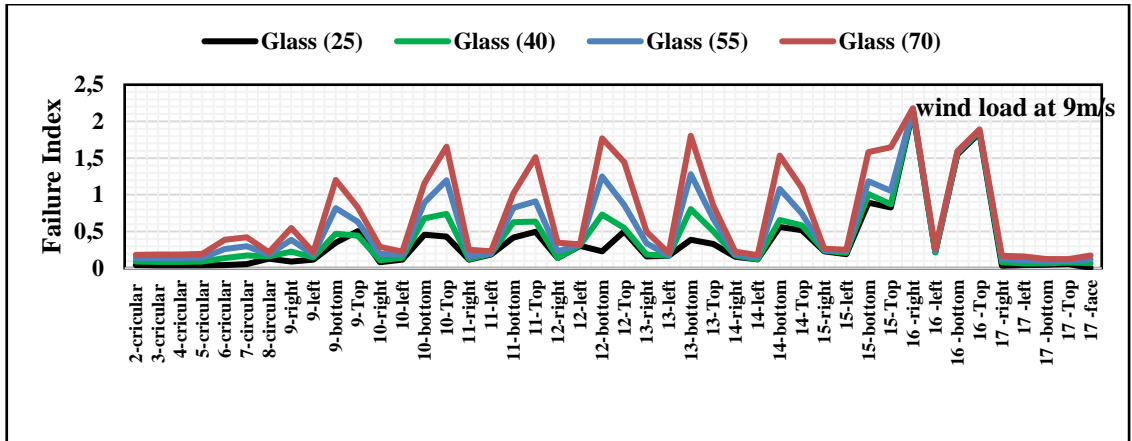


Figure 6.28 Failure index vs. flap-wise and thermal loading on glass/epoxy blade

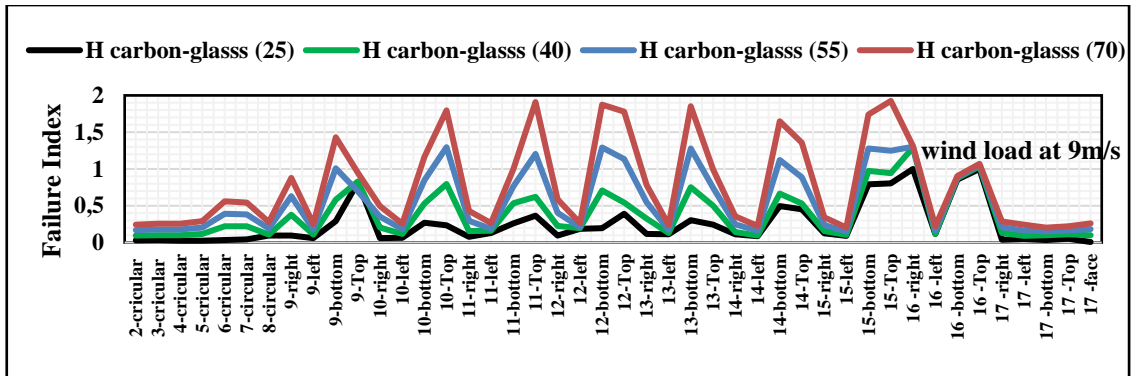


Figure 6.29 Failure index vs. flap-wise and thermal loading for carbon-glass blade

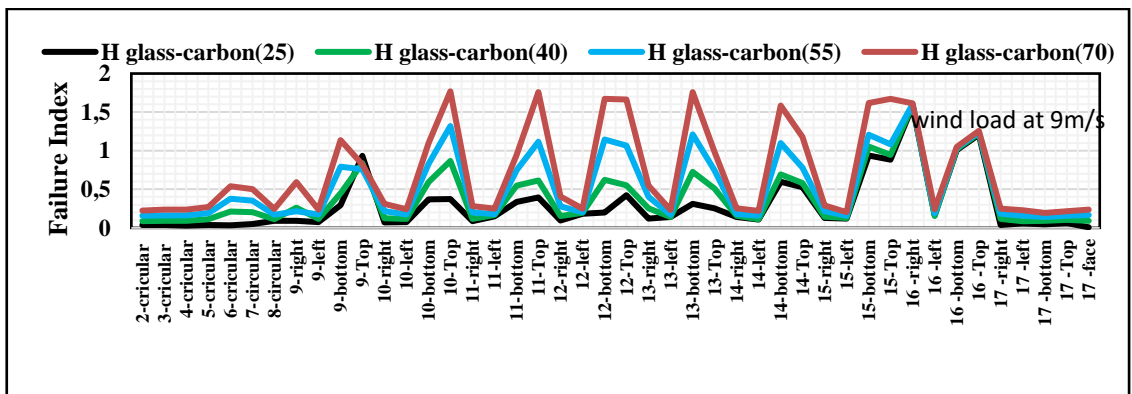
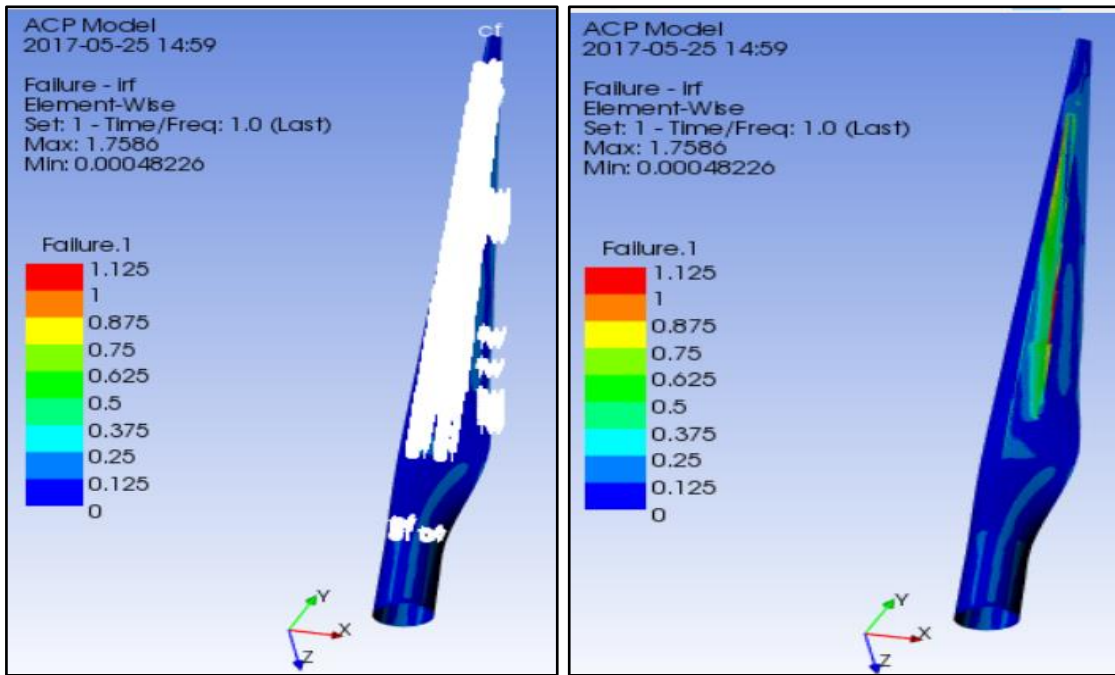
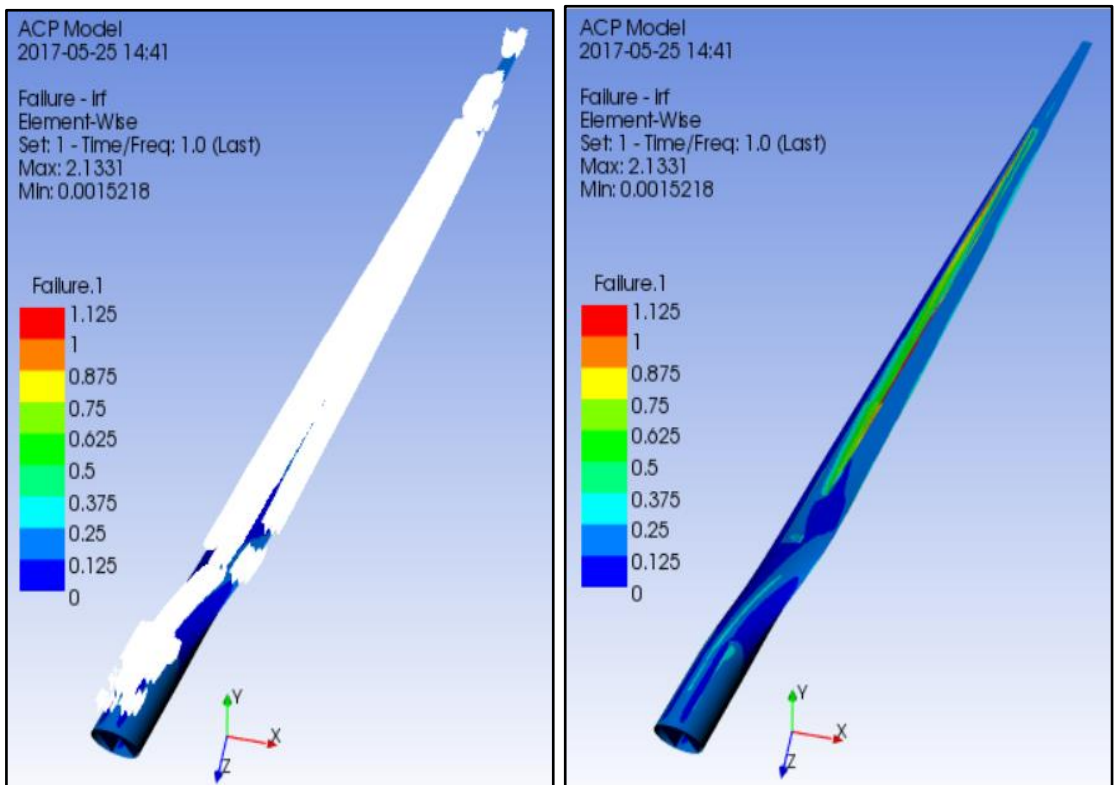


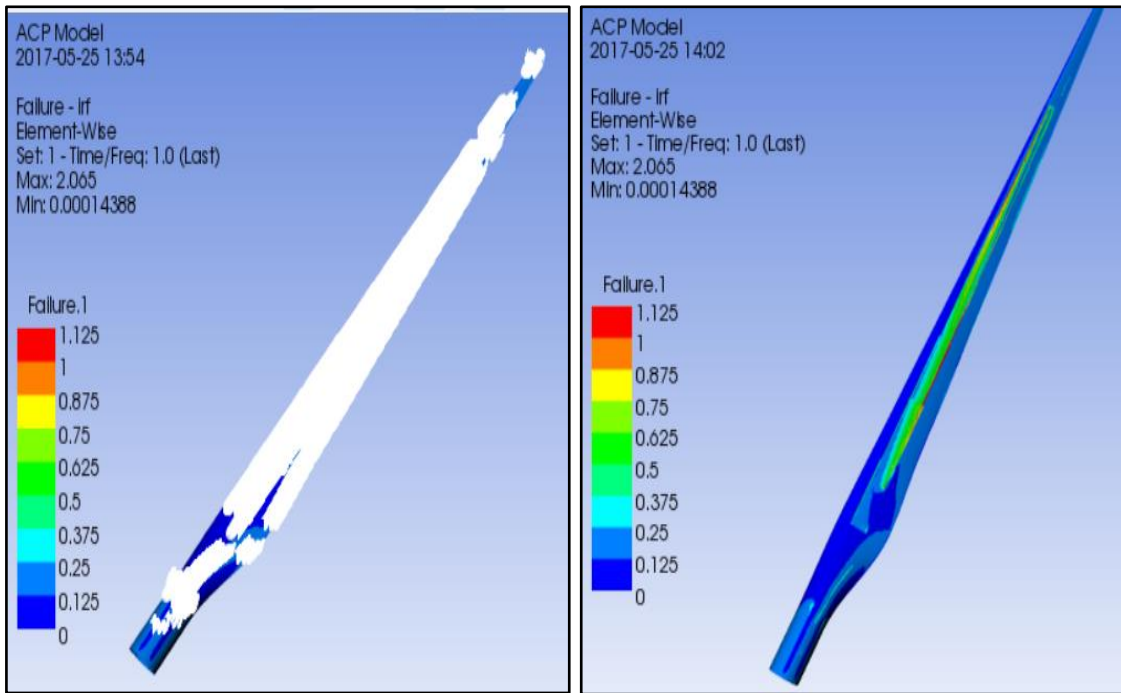
Figure 6.30 Failure index vs. flap-wise and thermal loading on glass- carbon fibre blade



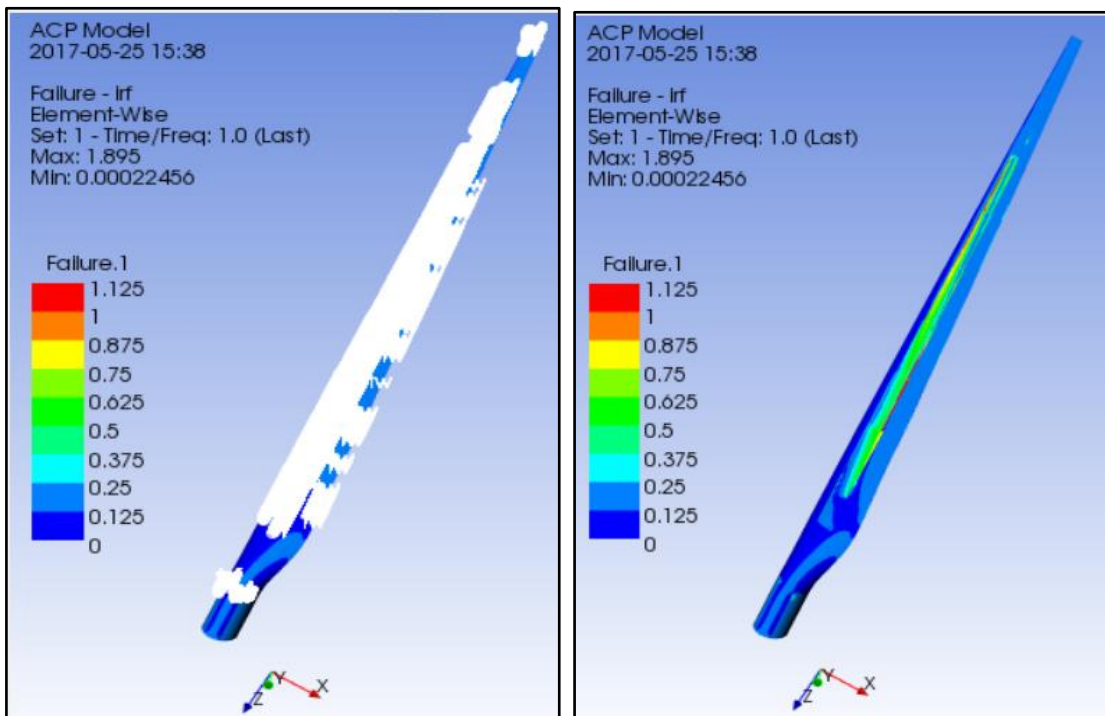
(a) Failure index of glass fibre at temperature 70°C and wind load at 6m/s



(b) Failure index of carbon fibre at temperature 70°C and wind load at 6m/s



(c) Failure index of hybrid carbon-glass fibre at temperature 70°C and wind load at 6m/s



(d) Failure index of hybrid glass-carbon fibre at temperature 70°C and wind load at 6m/s

Figure 6. 31 Failure on FEM structural models of composite blades under variable loading

6.6 Summary of Chapter

In the structural modelling phase of this composite blade study, the shear webs of the blade were designed using rectangular and hollow sections positioned on 25% and 55% of each chord length of NACA airfoils. The rectangular hollow section was used to reduce the bending of the spar caps of blades under flap-wise loading. In this study, a minimum chord length of 0.81m and a maximum chord length of 4.05m were taken into account when modelling the shape of wind turbine blades. The largest twist angle of the blade at the largest chord length considered 18° and 0° at the tip. The wind turbine blades consist of 46 sections for material modelling and optimization.

Micromechanical modelling of composite materials used the Rule of Mixture (ROM) as shown in Appendix B. The profile of blade was developed on SolidWork and transferred to ANSYS software for composite modelling and analysis. Meshing, naming and material modelling on each section of the blade was performed. Materials considered in the FEA and experimental testing were identical.

The present wind turbine blade was developed using four different composite materials taking into account the same thickness on each section of the blade. Flap-wise (bending) loading occurred at wind speeds of 3m/s, 6m/s and 9m/s. The first simulations were done using minimum flap-wise loading under increasing temperatures. Failure on blade sections occurred when thermal loading exceeded 40°C . Second simulations were done using the average flap-wise loading under increasing temperatures. No failure was registered at ambient temperatures but failure occurred when the thermal loading was beyond 40°C . This indicates that the mechanical properties of the blades decrease when the temperature rises. Third simulations were done using the maximum flap-wise loading under increasing temperatures. Failure occurred on glass and glass-carbon hybrid composite blades at ambient temperature. No failure was observed for carbon and carbon-glass hybrid composite blades at ambient temperature. Failure occurred when the temperature beyond was 40°C . This shows the simulation and experimental testing results are identical and it is more economical to use the hybrid composite structures in hotter areas.

The tip deflection, total deformation and failure behaviour optimization discussed in this chapter was to find the right composite wind turbine blade structures in increasing temperatures using simulations results.

Chapter 7

Discussion of Results

7.1 Introduction

The main structural components of wind turbines are the blade sections. Glass fibre reinforced polymer composites are used to construct the wind turbine blades. For very large blades, carbon fibre reinforced polymer composite is the choice of most industries. Composite materials have high stiffness, strength and facilitate the forming of the aerofoil profiles to maximize the power output. Even though the composite materials have these advantages, the mechanical properties of the materials depend on temperature. IEC 61400-1 stipulates the essential design requirements to model wind turbine blades within temperatures between -20°C to 50°C . Currently, the daily working temperatures of tropical regions are close to the design temperatures. It is important to investigate the effect of temperature variation on the mechanical properties of current materials available for construction of wind turbine blades and to identify the right material to be used in tropical wind farms. In this chapter, effects of temperature variation on static and dynamic mechanical behaviour of unidirectional carbon fibre/epoxy, glass fibre/epoxy and hybrids of these two materials are critically discussed based on the experimental and numerical findings presented in the previous chapters.

7.2 Static Mechanical Behaviour

The main aim of the experimental study was to find the effect of temperature variations on the mechanical behaviour of carbon/epoxy, glass/epoxy, hybrid carbon-glass/epoxy and hybrid glass-carbon/epoxy composite specimens. It is important to investigate one of the static mechanical properties of composite materials which is the interlaminar shear strength. The interlaminar shear strength behaviour of composite materials can be studied using short beam shear test methods [105, 106, 107]. The experimental findings for the composite specimens under various test temperatures are shown in Table 4.1. The results show that average interlaminar shear failure stress of the composite specimens was lowered as the test temperature increased [108, 109]. As shown in Figure 4.1, there is a difference in the interlaminar shear failure stress values at different test temperatures. This may be related to fibre/matrix interfacial bond strength and the effects of voids in the composite specimens [110, 111, 112]. Longitudinal micro-cracks in the middle

sections of carbon/epoxy, glass/epoxy and hybrid glass-carbon/epoxy composite specimens were verified using a scanning electron microscopic (SEM) using a magnification factor of 2000X. The micrographs of composite specimens indicated that interfacial or delamination failure modes occurred in unidirectional specimens. The microstructural analysis of specimens shows micro-cracks of epoxy resin occurred. However, the micro-cracks between specimens vary. This may occur due to difference in infusion behaviour of epoxy resin with carbon and glass fibres. From this experimental observations, the peak load that was a cause for interfacial failure lowered as the testing temperature rised. When we compared the interlaminar shear strength of the specimens, the average interlaminar shear failure stress values obtained from carbon/epoxy and hybrid of carbon-glass epoxy were close for each test temperature.

Tensile testing is one of the methods used to find the static mechanical behaviour of fibre reinforced polymer composites in the longitudinal directions. The analytical analysis on composite materials indicates that longitudinal fibre arrangement can support the centrifugal force created during the rotation of the horizontal axis wind turbines. Mainly, tensile testing is preferred to evaluate and predict the tensile strength and stiffness behaviour of fibre-reinforced composites at elevated temperatures [113, 114, 115, 116]. Experimental findings of this study on the static mechanical behaviour of unidirectional carbon/epoxy, glass/epoxy and hybrid glass-carbon/epoxy composite specimens under various test temperatures are shown in Table 4.6. The results of the average stress-strain behaviour of the composite specimens were lower during increasing test temperatures. This degradation may happen due to the lowering of the bond strength of the fibre/matrix interface when temperature increases. The epoxy resin softens when the test temperatures approaches the glass transition temperature and due to this, the capacity of the matrix to transfer the load to the neighbouring fibres is reduced. There was a difference in the average stress-strain values of carbon/epoxy and glass/epoxy composite specimens. Mainly, carbon/epoxy has a higher average strength and lower failure strain compared to the glass/epoxy composite specimens. Hybridization of the two materials increased the average strain failure values above those of carbon/epoxy composite and the average strength values above those of glass/epoxy composite under test temperatures [117, 118]. It is necessary to find the failure modes of unidirectional carbon, glass and hybrid of the composite materials before developing the wind turbine blades under elevated temperatures [119]. Figure 4.15 shows the failure modes of composite specimens at a

temperature of 55°C. The experimental findings on carbon/epoxy specimens show sudden catastrophic failure with extensive splitting of fibres when bonding of the polymeric matrix did not occur. Bonding of fibre/matrix was observed for the glass/epoxy specimens. Hybridization of carbon and glass fibre composite specimens changed the failure behaviour which occurred after extensive splitting of fibres, and when fibres were still bound together by the polymeric matrix.

Tensile behaviour of composite materials under various loads, including thermal and tensile loading was analysed using different failure criteria using numerical simulations [120, 121]. The experimental results were compared with the numerical simulations for the tensile behaviour of composite specimens for various test temperatures as shown in Table 4.7. The stress, strain and failure values for each ply and the thickness of the composite specimens cannot be analysed experimentally. The stress, strain and failure values were taken into account to compare with the experimental findings. The differences in the average stress values were within acceptable ranges. It was challenging to control the amount of heat when putting an extensometer in the oven during experimental work. A numerical simulation was another alternative to validate the tensile testing at different test temperatures.

The finding of this static study illustrates that the increasing temperature lowers the mechanical properties of the composite specimens. Hybrid composite specimens are the right choice to use for the development of wind turbine blades taking into account the interlaminar shear failure strength and failure behaviours of the specimens.

7.3 Dynamic Mechanical Behaviour

The main objective of this experimental study was to find the effect of temperature change on the dynamic mechanical properties of unidirectional carbon/epoxy, glass/epoxy, hybrid carbon-glass and hybrid glass-carbon/epoxy composite specimens. A dynamic mechanical analyser (DMA) was used to analyse storage modulus, loss modulus, loss factor and glass transition temperature of composite materials under increasing temperatures [122, 123, 124, 125]. The findings for the storage modulus under increasing temperatures are shown in Figure 4.7. The storage modulus of the composite specimens is lowered as the test temperature increases. As shown, load-bearing capacity of carbon/epoxy composites decreased linearly up to 40°C. After that, the load bearing capacity fluctuates and increases up to its glass transition temperature. These types of

behaviour are not recommended to design structures in hot areas. Linear material behaviour is important for structural design. On the other hand, the load bearing capacity of glass/epoxy decreased linearly up to the glass transitions temperatures and this material has the lowest load bearing capacity when compared to other specimens. Hybridization of carbon and glass fibre composite improved the mechanical behaviour and linearly decreased the load bearing capacity as the temperature increased. Mainly, the load bearing capacity of the hybrid composite was higher when carbon fibre was on the surfaces of the composite specimens.

It is necessary to find the fatigue and damping behaviours of unidirectional fibre reinforced polymer composites applicable for the design of wind turbine blades. The behaviour of the loss factor of composite material, which is the ratio of loss modulus to storage modulus, were used to analyse the damping properties. Damping behaviours of carbon/epoxy, glass/epoxy, hybrid carbon-glass and hybrid glass-carbon/epoxy composite specimens under increasing temperatures are shown in Figure 4.9. The experimental findings illustrate that glass/epoxy composite specimen has the smallest loss factor which has a maximum of 0.3701. For the hybrid carbon-glass/epoxy and hybrid glass-carbon/epoxy composite specimens, the loss factors reached 0.5667 and 0.5669 under increasing temperatures. The graph is used to compare the damping behaviours of composite specimens. This experimental finding indicated that hybrid/epoxy specimens behave well during vibration and suitable for noise reduction. The loss factors of the two hybrid specimens are close but the glass transition temperatures of the two specimens varies.

The dynamic mechanical analysis findings illustrate that hybrids of carbon and glass fibre composite materials have better load bearing and damping behaviour before the glass transition temperature of the polymeric resin is reached. The overall experimental findings of the static and dynamic study illustrate that hybrid carbon-glass/epoxy composite material is the right choice to develop the structure of horizontal axis wind turbine blades taking into account ILSS, failure and damping behaviours under increasing temperatures. Additionally, the good fatigue strength behaviour of carbon fibres can improve the fatigue strength of the hybrid/epoxy specimens with the carbon fibres placed on the top layers of the composite specimens.

7.4 Airfoil Profile and Structural Development of HAWT

With proper airfoil profile design, composite wind turbine blades are expected to give service from 20 to 30 years. Desirable properties of the airfoils families require the improvement of aerodynamic and structural interactions. It is important to select the appropriate airfoils to improve the aerodynamic performance of rotating blades. In the development of modern wind turbine blades, maximizing the aerodynamic performance is the priority. In this study, we initially used the Blade Element Momentum (BEM) theory to develop the shape of 54m horizontal axis wind turbine blades, and then designed a HAWT for a 2MW power from wind which is effective in tropical wind farms [126]. Three NACA airfoil families were studied to maximize the extraction of energy from wind. QBlade/XFoil and CFD software's were applied to analyse the lift and drag coefficients at different Reynolds numbers and angles of attacks. The simulation findings of lift coefficient of NACA 4415, NACA 23012 and NACA 23015 airfoils are shown in Figures 5.14, 5.15 and 5.16 at an angle of attack 8.5° and wind tip speed ratio 9. These airfoils were analysed to study the chord and twist distributions along the length of blades using BEM theory [127, 128, 129]. After extensive iterations, the maximum chord length was calculated to be 4.05m which was nearly 20% of the blade length from the root of the blade. The chord length at the tip of the wind turbine blade was 0.81m and the remaining sections of the blades were reduced linearly from maximum chord length towards the tip of the blade which is shown in Figure 5.49. The twist angle distortion was close to 0° at the tip of the blade and 18° at 20% of the blade length from the root. As shown in Appendix A, the angle of attack α is constant on each airfoil section. The angle of relative wind varies from 21° at the maximum chord position to 3.6° at the tip of the blade.

The position of the airfoils was determined using the simulation results of aerodynamic efficiency (L/D) of the airfoils. NACA 4415, NACA 23015 and NACA 23012 airfoils begin from 20%, 55% and 75% of the full lengths of the blades from the root. Betz's and Glaunt modelling techniques were applied for the iteration of axial and angular induction factors on each airfoil along the length of the blade. The iteration results are given in Appendix A, and revealed that the maximum accessible power coefficient found in this design was $C_{p,Max} = 0.592$. This indicated that this wind turbine blade has a capacity of 2MW power at a wind speed of 9m/s and higher if the mechanical efficiency

of the components is more than 85%. The airfoils and circular profile distribution used to develop the optimum shape of blades are shown in Figure 7.1.

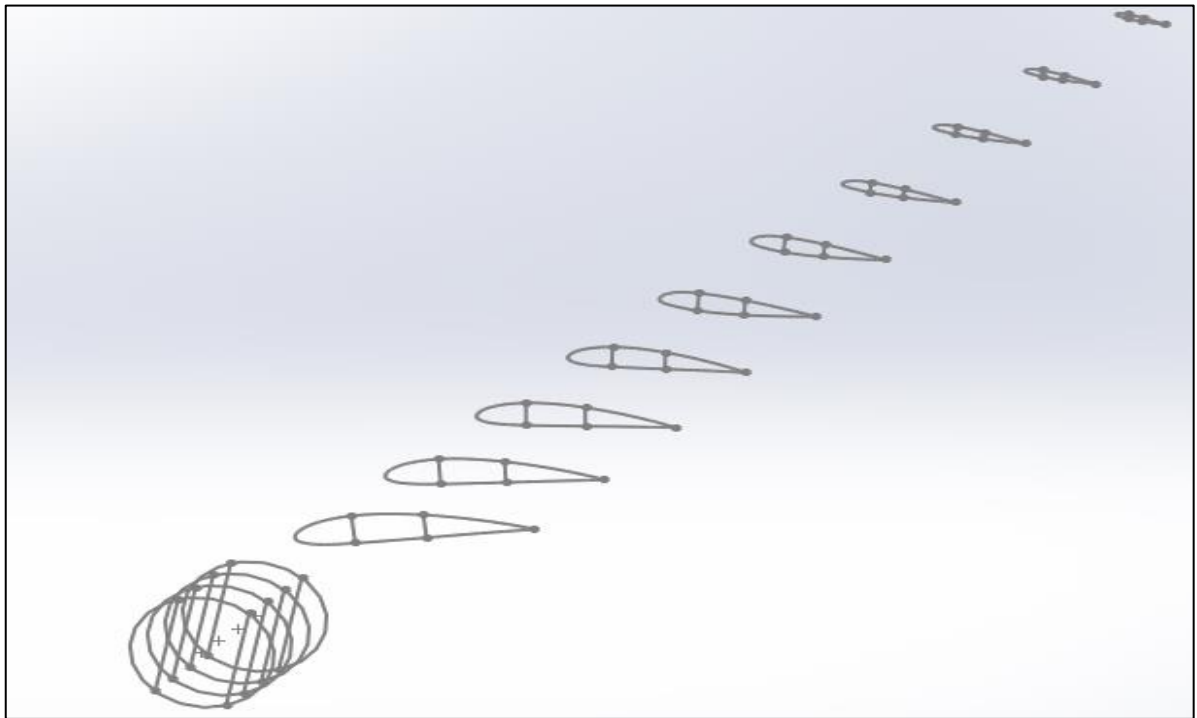


Figure 7.1 Airfoil distribution of three NACA airfoils along the length of the blade

We determined the proper composite material and developed optimized blade shapes which can generate 2MW power. It is not enough to only investigate extraction of energy from the wind. It is essential to analyse different loadings and design blades which withstands these loads. Figures 5.50 and 5.51 show the results of shear force and the bending moment when it occurred at variable wind speeds along the length of the blade. We considered the wind turbine blade as a cantilever beam to analyse the values of shear force and bending moment. The results show that the shear force and bending moment distribution increased from tip towards root of the blade. The critical loading occurred on the flap-wise direction of the blades. The magnitude of flap-wise shear force distribution on blade was dependent on the wind speed values and higher shear force on the blade occurred at cut-out wind speed. Due to the variation of flap-wise shear force along the length of the blades, the material distribution varies to withstand this loading. Mostly, wind turbine blade designers assume the flap-wise loading to estimate and then iterate to find thickness on each element of the blade. Flap-wise loading is not enough to consider for tropical wind farms and thermal loadings need to be included in the design and analysis. Most wind turbine blade designers only assume the flap-wise loading and thickness on each element of the blade. This is not enough when taking into account the

tropical wind farms and especially with flap-wise loading, thermal loadings have to be also included.

In the present study, flap-wise and thermal loadings were considered to find the response of materials used to model the wind turbine blades. We took into account the materials used in the construction of blades and conducted experimental studies. PVC foam was used on the spar cap and shear web sections to develop four different wind turbine blade structures. To minimize the bending of large wind turbine blades, the internal section needs support. Figure 6.1 and Table 6.3 show the rectangular hollow section and its position used in this study to find the deflection and total deformation of the blade. The static mechanical behaviour of the composite blade structures were analysed making allowance for flap-wise loading at wind speeds of 3m/s, 6m/s and 9m/s and thermal loadings at 25°C, 40°C, 55°C and 70°C. Figure 6.15 and Figure 6.17 show the responses of each composite blade structures for total deformation and tip deflection. The numerical simulation results indicated that the total deformation and tip deflection of glass/epoxy blades are the highest, whereas carbon/epoxy blades have the lowest values. Tip deflection is one of the challenges of the wind turbine blades which may collide with the tower during rotation. Numerical simulation results show different response values for the tip deflection and deformation using composite materials. The response of materials under thermal loading has a minimum impact and cannot be detected for the tip deflection and deformation values. It is important to study the response of blade materials under variable thermal loadings to validate the experimental findings.

The effect of thermal loading, optimization of mass and thickness distribution for wind turbine blade structures were studied with ANSYS ACP Prep and ANSYS ACP Post code using Tsai-Wu, Puck and LaRC failure criteria. The simulation results of three failure criteria were close and only Tsai-Wu failure criterion was considered for this study. Primarily, the full length of the blade (54m) was divided into 46 elements and a specific name was given for each blade elements as shown in Figure 6.11. The failure index of each elements of the four wind turbine blades were simulated using the Tsai-Wu allowing for flap-wise and thermal loadings. Figures 6.19, 6.20, 6.21 and 6.22 show the failure index vs. flap-wise and thermal loading at a wind speed of 3m/s and temperatures 25°C, 40°C, 55°C and 70°C. The simulation results of four wind turbine blades indicated that failure on elements occurred when the thermal loading exceeded 40°C irrespective of flap-wise loading. When the flap-wise loading changed to 9m/s with the same thermal loading, as shown in Figures 6.27, 6.28, 6.29 and 6.30, glass/epoxy and hybrid glass-

carbon composite blades failed irrespective of the thermal loading. The remaining carbon/epoxy and hybrid carbon-glass blade structures gave service at ambient thermal loading. The simulation results indicated that there was failure of some elements of the wind turbine blades when the thermal loading exceeded 40°C. This indicated that the experimental and simulation findings are valid. In the simulations, the responses of two of the composite blade materials were close for flap-wise and thermal loadings. Allowing for cost and strength, hybrid carbon-glass blades are the choice for tropical wind farms. Figure 6.13 shows the composite wind turbine blade developed by FEM using hybrid carbon-glass composite material.

Using these modelling methods, optimization of thickness and mass can be done and different fibre arrangements can be analysed to delay the failure based on Tsai-Wu failure criterion. The major achievements in this study were the development of hybrid composite materials, optimised blade shape, maximized power coefficient with the wind turbine generating 2MW power, modelling of new methods to optimize mass, thickness and fibre arrangements to delay the failure of the composite blades installed in tropical wind farms. Generally, this study needs a knowledge of composite mechanics, aerodynamic and structural engineering. It will help if postgraduate students know the production process of different fibre and matrix composites, testing methods, design of composite materials and development of optimized shape of blades applicable for different sizes of wind turbine blades, civil and automobile structures. Additionally, these research findings will support the government and stakeholders working on importing blades from different countries to have the opportunity to understand the behaviour of wind turbine blade structures in their own countries' environmental conditions. Particularity, all African countries which imported wind turbine blade from different countries. I hope that this research idea will motivate young African researchers to take up this field, to research, design and manufacture wind turbine blades by Africans. It will give job opportunities and improve power production from renewable energy sources to their country.

Airfoil Profile and Structural Development of HAWT

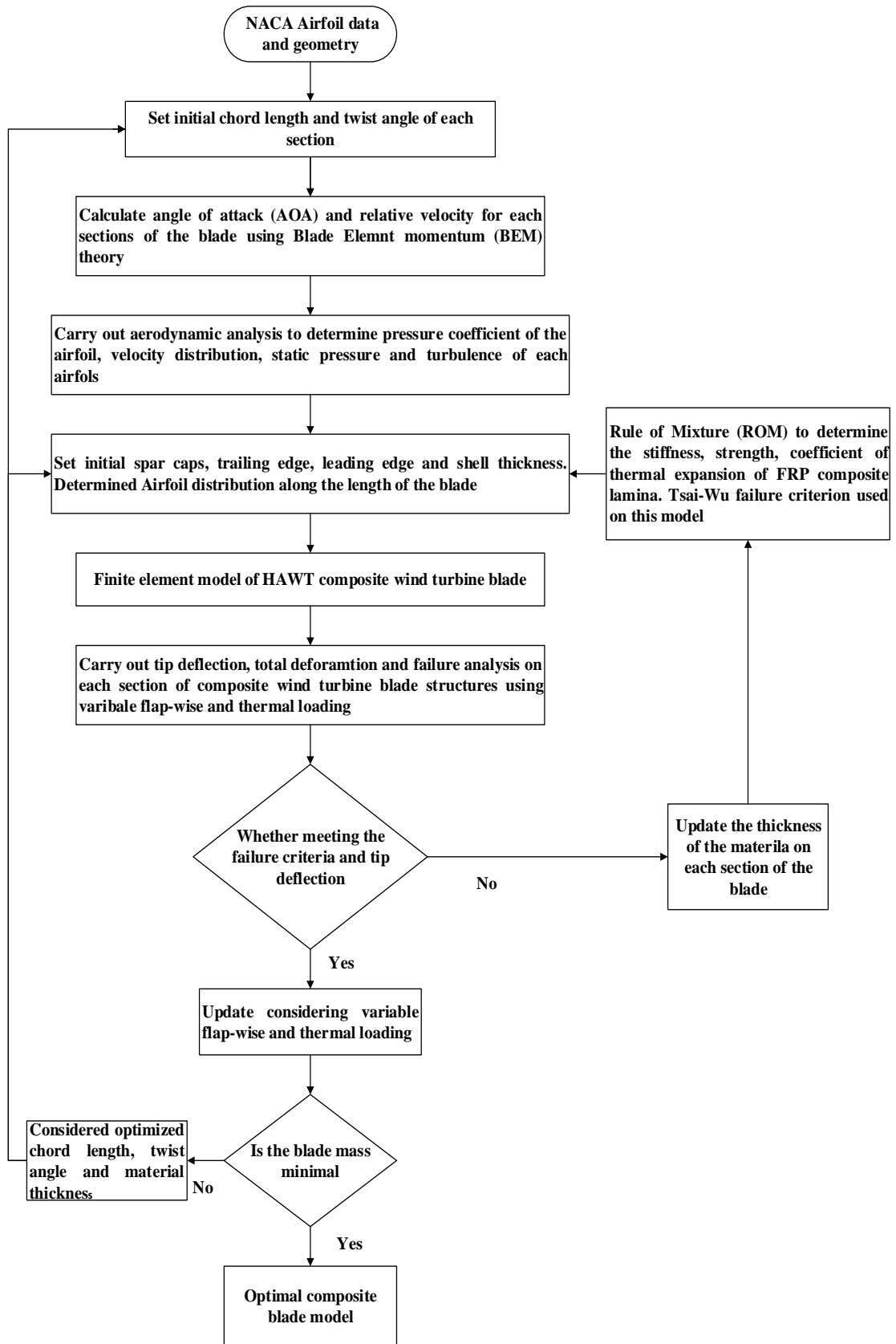


Figure 7.2 Flow chart to model the optimized shape of wind turbine blades

7.5 Summary of Discussion

The effect of temperature on the static and dynamic mechanical behaviour of composite materials was investigated. These materials are used extensively for the design of large horizontal axis wind turbine blades. The static mechanical behaviour of composite materials was studied and characterized using short beam shear tests and tensile tests. It was observed that their strength and stiffness decreased when the test temperature was increased. The dynamic mechanical behaviour of specimens was studied and characterized using Dynamic Mechanical Analyser. The stiffness of the specimens decreased as the test temperature increased. Based on the static and dynamic test and simulation results, carbon-glass/epoxy composite specimens were the better candidates for wind turbine blades.

It was found that the optimized horizontal axis wind turbine blade shape could generate 2MW power using NACA airfoils at the maximum power coefficient $C_{P,Max} = 0.592$. Different flap-wise and thermal loadings were applied to study the response of the composite materials. Simulation findings indicated that the tip deflection and total deformation of glass/epoxy blades were the highest and those of the carbon/epoxy blades were the lowest. Optimization of blade thickness and its response to thermal loading were analysed using failure analysis. Failure occurred on elements of the blades as the thermal loading went beyond 40°C. Based on this, the simulation results were close to the experimental ones and the results are considered to be valid. Figure 7.2 shows Airfoil profile and structural optimization of wind turbine blade.

Chapter 8

Conclusions and Recommendations

8.1. Conclusions

The main aim of the current study was to create a better understanding of how temperature may affect the mechanical behaviour of unidirectional carbon fibre/epoxy, unidirectional glass fibre/epoxy and the hybrid of the two composite materials and find composite material applicable for modelling wind turbine blades structures for tropical regions. This encompassed generating experimental proof taking into account composite specimens and a numerical model to simulate the coupling phenomena between changes of temperature and mechanical behaviour of composite turbine blades.

Experimentally, composite specimens were prepared from a carbon composite laminate, a glass composite laminate, a carbon-glass hybrid composite laminate and a glass-carbon hybrid composite laminate using hand lay-up and a vacuum infusion manufacturing process. Short Beam Shear (SBS), Dynamic Mechanical Analysis (DMA) and tensile testing occurred on composite laminates under increasing temperature. The conclusion obtained from the experimental findings on the effect of temperature variation on composite mechanical behaviour of the study includes:

1. When the inter-laminar shear failure strengths (ILSS) of UD-glass composite specimens, UD-carbon composite specimens, UD-glass-carbon hybrid composite specimens and UD-carbon-glass composite specimens were tested, the results showed that the applied loading causing delamination decreases as the test temperature rises. The inter-laminar shear failure strength of UD-glass composite laminates and UD-carbon composite specimens decreased by 38.70% and 36.30% as the test temperature changed from ambient to 55°C. Similarly, ILSS of hybrid carbon-glass composite laminates decreased by 35.96% and ILSS of hybrid glass-carbon composite laminates decreased by 38.12% due to increasing temperature. This result suggests that the composite specimens fail at low loading rates when the temperature increases.

The viscoelastic behaviours of the UD-glass composite specimens, UD-carbon composite specimens, UD-glass-carbon hybrid composite specimens and UD-carbon-glass hybrid composite specimens were tested using the Dynamic Mechanical Analysis (DMA), and the indications were that the storage stiffness

of composite specimens decreased as the test temperature increased. In the case of carbon composite, the storage stiffness decreased linearly up to 40°C, while the storage stiffness values for other specimens were practically constant up to 59°C before T_g of the specimens was reached. After the temperature exceeded T_g values of the specimens, the storage stiffness values dropped quickly.

2. The tensile strength of UD-glass composite specimens was measured using tensile tests under increasing temperatures. The strength decreased by 4% when the test temperature changed from ambient to 55°C. The tensile strength of carbon composite specimen lost its value by 2.08% and glass-carbon hybrid composite specimens by more than 15% as the test temperature reached 55°C. Catastrophic failure with the splitting of fibres occurred for carbon/epoxy specimens. Hybridization of carbon and glass fibres changed the failure behaviour. Failure occurred after extensive splitting and fibres were still bound together by the polymeric matrix.

The following conclusions are drawn from the analytical and numerical studies:

1. Micromechanics of composite materials were applied using Rule of Mixture (ROM) to find the weight, stiffness, strength and coefficient of thermal expansion for unidirectional composite laminates under ambient temperature.
2. To investigate the effect of temperature variation on composite material at the structural level, optimized airfoil profiles of horizontal-axis wind turbine blades were developed using a combination of Betz's Elementary Momentum Theory and the Glauert Model at the maximum power coefficient. Several iterations were done using QBlade and ANSYS fluent software to identify the right NACA airfoil and the location along the lengths of the blades which have a high lift to drag ratio in order to maximize power output. The amount of wind load distribution along the length of the blades was determined using the Blade Element Momentum (BEM) theory to study the response of materials under flap-wise and thermal loadings.
3. The effect of temperature variation on the mechanical behaviour of composite blades was analysed using ANSYS software. The simulation results of composite blades were evaluated using Tsai-Wu failure criterion under flap-wise and thermal loadings. The failure index of composite materials was used to predict the coupling phenomenon. Numerical simulation results show that failure on

elements of blades occur when the thermal loading exceeds 40°C. Moreover, simulations were done to determine the smallest value of the total deformation and the tip deflection of the blades under flap-wise and thermal loadings.

The material behaviour studied by experimental tests and numerical simulations are identical and the results are valid. Because of this, composite wind turbine blades were developed using carbon-glass hybrid composite materials which are economical and give longer service in tropical wind farms.

8.2. Recommendations for Future Research

Since wind farms were built in tropical areas, the composite blades have been affected by high temperatures in these areas. Further experimental studies are needed to find the effect of temperature on fatigue, bucking, flexural strength and impact behaviour of composite materials applicable to modern composite wind turbine blades. The fatigue properties of FRP composite materials are the main parameters for the delay of failure on composite wind turbine blades and it needs extensive experimental and simulation work using ANSYS n-code software to study the fatigue failures.

Simulations of large wind turbine blades need higher capacity computers which are necessary for static, dynamic and CFD analysis of wind turbine blades, especially for blade thickness optimization where a high capacity computer is very useful.

The distribution of force along the length of the blade was analysed taking into account the Blade Element Momentum theory. It is important in the analysis to use CFD methods for comparison with the Blade Element Momentum theory. Maximum energy extraction from the wind can be achieved by selecting proper airfoil families and further research and iteration are required to study other airfoil families.

References

- [1] A. Chehouri, R. Youunes, A. Ilinca, J. Perron, “Review of performance optimization techniques applied to wind turbines”, *Applied Energy*, Vol. 142, pp. 361–388, 2015.
- [2] O.T. Thomsen, “Sandwich materials for wind turbine blades-present and future”, *Journal of Sandwich Structures and Materials*, Vol. 11, pp. 7–20, 2009.
- [3] C. Kong, J. Bang, Y. Sugiyama, “Structural investigation of composite wind turbine blade considering various load cases and fatigue life”, *Energy*, Vol. 30, pp. 2101–2114, 2005.
- [4] M.E. Bechly, P.D. Clausen, “Structural design of a composite wind turbine blade using finite element analysis”, *Computers & Structures*, Vol. 63, pp. 639–646, 1997.
- [5] J. Zhu, X. Cai, P. Pan, R. Gu, “Optimisation design of spar cap layout for wind turbine blade”, *Frontiers of Structural and Civil Engineering*, Vol. 6, pp. 53–56, 2012.
- [6] International Standard IEC 61400–1, “Wind turbines-1: Design requirements”, International Electrotechnical Commission, Geneva 20, Switzerland, 2005–2008.
- [7] T.J. Price, J.C. Blyth, “Britain’s first modern wind power pioneer”, *Wind Engineering*, Vol. 29, pp. 191–200, 2005.
- [8] R. Thresher, M. Robinson, P. Veers, “Wind energy technology: Current status and R&D future”, In *Physics of Sustainable Energy Conference*, University of California at Berkeley, 1-2 March, 2008.
- [9] Y.C. Dennis, Y.Y. Leung, “Composite materials for wind power turbine blades”, *Annual Rev. Mater. Res*, Vol. 35, pp. 505–538, 2005.
- [10] Y.C. Dennis, Y.Y. Leung, “Wind energy development and its environmental impact: A review”, *Renewable and Sustainable Energy Reviews*, Vol. 16, pp. 1031–1039, 2012.
- [11] Friend Lauha, “Global wind statistics”, Brussels, Belgium, 2017.
- [12] A.F. Agbetuyi, I.A. Odigwe, A.A. Awelewa, C.O.A. Awosope, “Wind power potential and integration in Africa”, *International Journal of Development and Sustainability*, Vol. 2, pp. 232–239, 2013.
- [13] S. Adeleke, “Development of wind energy in Africa”, Tunisia, 2013.

- [14] R.-M. Wang, S.-R. Zheng, Y.-P. Zheng, “Polymer matrix composites and technology”, Woodhead Publishing Limited and Sciences Press Limited, Beijing, China, 2011.
- [15] D. Gay, S.V. Hoa, S.W. Tsai, “Composite Materials: Design and Applications”, CRC Press, Boca Raton, London, New York, Washington, 2003.
- [16] S.K. Mazumdar, “Composite Manufacturing: Materials, Product, and Process Engineering”, CRC Press, Boca Raton, London, New York, Washington, 2002.
- [17] B. Eker, A. Akdogan, A. Vardar, “Using of composite material in wind turbine blades”, *Journal of Applied Sciences*, Vol. 6, pp. 2917-2921, 2006.
- [18] L. Mishanevsky Jr, “Composite materials in wind energy technology”, Technical University of Denmark, Roskilde, Denmark.
- [19] C. Berggreen, K. Branner, J.F. Jensen, J.P. Schultz, “Application and analysis of sandwich elements in the primary structure of large wind turbine blades”, *Journal of Sandwich Structures and Materials*, Vol. 9, pp. 525-552, 2007.
- [20] S. Wang, H. Xie, C. Zhang, “Static structural analysis of parked composite wind turbine blades”, In: 8th International Conference on Structural Dynamics Eurodyn, Leuven Belgium, 4-6 July 2011.
- [21] E.E Supeni, J.A. Epaarachchi, M.M. Islam, K.T. Lau, “Design of smart structures for wind turbine blades”, In: 2nd Malaysian Postgraduate Conference, Bond University, Australia, 7-9 July 2012.
- [22] J. Zhou, J.P. Lucas, “Hygrothermal effect of epoxy resin. Part I: The nature of water in epoxy”, *Polymer*, Vol. 40, pp. 5505-5512, 1999.
- [23] G. Alawsi, S. Aldajah, S. Abdulrahmaan, “Impact of humidity on the durability of E-glass/polymer composites”, *Materials and Design*, Vol. 30, pp. 2506-2512, 2009.
- [24] J. Mercier, A. Bunsell, P. Castaing, J. Renard, “Characterization and modeling of aging of composites”, *Composites: Part A*, Vol. 39, pp. 424-438, 2008.
- [25] M.H. Zamri, H.M. Akil, A. Abubakar, Z.A.M. Ishak, L.W. Cheng, “Effect of water absorption on pultruded jute/glass fibre-reinforced unsaturated polyester hybrid composites”, *Journal of Composite Materials*, Vol. 46, pp. 51-56, 2011.
- [26] A. Smaili, M.A. Mahdi, L.M. Ouahchi, “Numerical investigation of free-convection within wind turbine nacelle operating in hot climate”, Algiers, Algeria, ISBN: 978-1-61804-358-0.

- [27] B. Yu, V. Till, K. Thomas, "Modeling of thermos-physical properties for FRP composites under elevated and high temperature", *Composite Science and Technology*, Vol. 67, pp. 3089-3109, 2007.
- [28] C.-H. Shen, G.S. Springer, "Effects of moisture and temperature on the tensile strength of composite materials", *J. Composite Materials*, Vol. 11, pp. 1-15, 1977.
- [29] G.S. Springer, "Model for predicting the mechanical properties of composites at elevated temperatures", *Journal of Reinforced Plastic and Composites*, Vol. 3, pp. 85-95, 1984.
- [30] Y. Ou, D. Zhu, H. Zhang, L. Huang, Y. Yao, G. Li, B. Mobasher, "Mechanical characterization of the tensile properties of glass fibre and its reinforced polymer (GFRP) composite under varying strain rates and temperatures", *Polymers*, Vol. 8, pp. 2-16, 2016.
- [31] J.L. Thomason, L. Yang, "Temperature dependence of the interfacial shear strength in glass-fibre polypropylene composites", *Composites Science and Technology*, Vol. 71, pp. 1600-1605, 2011.
- [32] J.L. Thomason, L. Yang, "Temperature dependence of the interfacial shear strength in glass-fibre epoxy composites", *Composite Science and Technology*, Vol. 96, pp. 7-12, 2014.
- [33] M.A. Torabizadeh, "Tensile, compressive and shear properties of unidirectional glass/epoxy composite subjected to mechanical loading and low temperature services", *Indian J. of Eng & Material Sciences*, Vol. 20, pp. 299-309, 2013.
- [34] Y. Ou, D. Zhu, "Tensile behavior of glass fibre reinforced composite at different strain rates and temperatures", *Constructions and Building Materials*, Vol. 96, pp. 648-656, 2015.
- [35] S. Cao, Z. Wu, X. Wang, "Tensile properties of CFRP and hybrid FRP composite at elevated temperatures", *Composite Materials*, Vol. 43, pp. 315-330, 2009.
- [36] J.K. Chen, C.T. Sun, C.I. Chang, "Failure analysis of a graphite/epoxy laminate subjected to combined thermal and mechanical loading", *Composite Materials*, Vol. 19, pp. 408-423, 1985.
- [37] M. Detassis, A. Pegoretti, C. Migliaresi, "Effect of temperature and strain rate on interfacial shear stress transfer in carbon/epoxy model composites", *Composite Science and Technology*, Vol. 53, pp. 39-46, 1995.

- [38] Y. Bai, T. Keller, T. Vallee, "Modeling of stiffness of FRP composites under elevated and high temperatures", *Composite Science and Technology*, Vol. 68, pp. 3099-3106, 2008.
- [39] C.A. Mahieux, K.L. Reifsnider, "Property modeling across transition temperatures in polymers: application to the thermoplastic systems", *Material Science*, Vol. 37, pp. 911-920, 2002.
- [40] Z.-S. Guo, J. Feng, H. Wang, H. Hu, J. Zhang, "A new temperature-dependent modulus model of glass/epoxy composite at elevated temperatures", *Composite Materials*, Vol. 47, pp. 3303-3310, 2012.
- [41] L. Di Landro, M. Pegoraro, "Evaluation of residual stresses and adhesion in polymer composites", *Composites: Part A*, Vol. 27(9), pp. 847-853, 1996.
- [42] K.-H. Im, C.-S. Cha, S.-K. Kim, I.-Y. Yang, "Effects of temperature on impact damages in CFRP composites laminates", *Composites: Part B*, Vol. 32, pp. 669-682, 2001.
- [43] J. Lopez-Puente, R. Zaera, C. Navarro, "The effect of low temperatures on the intermediate and high velocity impact response of CFRPs", *Composites: Part B*, Vol. 33, pp. 559-566, 2002.
- [44] S. Benli, O. Saymen, "The effect of temperature and thermal stresses on impact damage in laminated composites", *Mathematical and Computational Applications*, Vol. 16, No. 2, pp. 392-403, 2011.
- [45] A.A.M. Badawy, "Impact behavior of glass fibres reinforced composite laminates at different temperatures", *Ain Shams Engineering Journal*, Vol. 3, pp. 105-111, 2012.
- [46] M. Sayer, N.B. Bektas, E. Demir, H. Callioglu, "The effect of temperature on hybrid composite laminates under impact loading", *Composites: Part B*, Vol. 43, pp. 2152-2160, 2012.
- [47] A. Salehi-Khojin, R. Bashirzadeh, M. Mahinfalah, R. Nakhaei-Jazar, "The role of temperature on impact properties of Kevlar/fiberglass composite laminates", *Composites: Part B*, Vol. 37, pp. 593-602, 2006.
- [48] A. Salehi-Khojin, M. Mahinfalah, R. Bashirzadeh, B. Freeman, "Temperature effect on Kevlar/hybrid and carbon fibre composite sandwiches under impact loading", *Composite Structures*, Vol. 78, pp. 197-206, 2007.

- [49] A. Halvorsen, A. Salehi-Khojn, M. Mahinfalah, R. Nakhaei-Jazar, "Temperature effects on the impact behavior of fiber glass and fibre glass/Kevlar sandwich composites", *Applied Composite Materials*, Vol. 13, pp. 369-383, 2006.
- [50] M.D. Erickson, A.R. Kallmeyer, K.G. Kellogg, "Effect of temperature on the low-velocity impact behavior of composite sandwich panels", *Journal of Sandwich Structures and Materials*, Vol. 7, pp. 245-265, 2005.
- [51] Y. Miyano, M. Nakada, "Time and temperature dependent fatigue strengths for three directions of unidirectional CFRP", *Experimental Mechanics*, Vol. 46, pp. 155-162, 2006.
- [52] N. Ramanujam, P. Vaddadi, T. Nakamura, R.P. Singh, "Interlaminar fatigue crack growth of cross-ply composites under thermal cycles", *Composite Structures*, Vol. 85, pp. 175-187, 2008.
- [53] H. Mivehchi, A. Varvani-Farahani, "The effect of temperature of fatigue strength and cumulative fatigue damage of FRP composites", *Procedia Engineering*, Vol. 2, pp. 2011-2020, 2010.
- [54] A. Varvani-Farahani, H. Mivehchi, "Temperature dependence of stress-fatigue life data of FRP composites", *Mechanics of Composite Materials*, Vol. 47, pp. 185-192, 2011.
- [55] P. Coronado, A. Arguelles, J. Vina, V. Mollon, I. Vina, "Influence of temperature on a carbon-fibre epoxy composite subjected to static and fatigue loading under Mode-I delamination", *International J. of Solids and Structures*, Vol. 49, pp. 2934-2940, 2012.
- [56] M.-H.R. Jen, Y.-C. Tseng, H.-K. Kung, J.C. Huang, "Fatigue response of APC-2 composite laminates at elevated temperatures", *Composites Part B*, Vol. 39, pp. 1142-1146, 2008.
- [57] L.E. Asp, A. Sjogren, "Effects of temperature on delamination growth in a carbon/epoxy composite under fatigue loading", *International Journal of Fatigue*, Vol. 24, pp. 179-184, 2002.
- [58] J.A.M. Ferreira, J.D.M Costa, P.N.B Reis, M.O.W. Richardson, "Analysis of fatigue and damaging in glass-fibre-reinforced polypropylene composite materials", *Composite Science and Technology*, Vol. 59, pp. 1461-1467, 1999.
- [59] B. Abdel-Magid, S. Ziaee, K. Gass, M. Schneider, "The combined effects of load, moisture and temperature on the properties of E-glass/epoxy composites", *Composite Structures*, Vol. 71, pp. 320-326, 2005.

- [60] P.C. Upadhyay, D.W. Lyons, W.S. Wayne, "Hygrothermal effect on the compressive strength of uniaxial fibre-reinforced polymer matrix composites", *Journal of Reinforced Plastics and Composites*, Vol. 28, pp. 2655-2664, 2009.
- [61] C. Xiaoquan, Y. Baig, Z., "Effects of hygrothermal environmental conditions on compressive strength of CFRP stitched laminates", *Journal of Reinforced Plastics and Composites*, Vol. 30, pp. 110-122, 2011.
- [62] B.D. Davidson, M.A. Soffa, M. Kumar, "Temperature and moisture effects in a particulate interlayered composite: Mode I data reduction and toughness", *Journal of Reinforced Plastics and Composites*, Vol. 28, pp. 2049-2068, 2009.
- [63] S.S. Shivarudraiah, "Effect of temperature on the hygrothermal and mechanical behavior of glass-epoxy laminates", *Advanced Engineering Technology*, Vol. 10, pp. 225-231, 2010.
- [64] F. Ellyin, C. Rohrbacher, "The influence of aqueous environmental temperature and cyclic loading on glass-fibre/epoxy composite laminates", *Journal of Reinforced Plastics and Composites*, Vol. 22, pp. 615-622, 2003.
- [65] G. Mishra, S.R. Mohapatra, P.R. Behera, B. Dash, U.K. Mohanty, B.C. Ray, "Environmental stability of GFRP laminated composites: An emphasis on mechanical behavior", *Aircraft Engineering and Aerospace Technology*, Vol. 82, pp. 258-266, 2010.
- [66] Z. Boualem, N. Sereir, "Reduction of hygrothermal transverse stresses in unidirectional hybrid composites under cyclic environmental conditions", *Mechanics of Time-Dependent Materials*, Vol. 15, pp. 51-71, 2011.
- [67] B. Qi, I. Herszberg, "An engineering approach for predicting residual strength of carbon/epoxy laminates after impact and hygrothermal cycling", *Composite Structures*, Vol. 47, pp. 483-490, 1999.
- [68] A.K. Upadhyay, R. Pandey, K.K Shukla, "Nonlinear flexural response of laminated composite plates under hygro-thermo-mechanical loading", *Commun. Nonlinear Sci Numer Simulat*, Vol. 15, pp. 2634-2650, 2010.
- [69] ASTM International, "ASTM standard D 3171 test method for matrix digestion for composites", U.S.A, 1999.
- [70] J.A. Quinn, "Design Manual", Liverpool, England, 2002.
- [71] ASTM International, "ASTM standard D 3039/D3039M test method for tensile properties of polymer matrix composite materials", U.S.A, December 2002.

- [72] I.S. Radebe, S. Adali, "Minimum cost design of hybrid cross-ply cylinders with uncertain material properties subjected to external pressure", *Ocean Engineering*, Vol. 38, pp. 310-317, 2014.
- [73] D. Rathore, B.C. Ray, "Durability and integrity studies of environmentally conditioned interfaces in fibrous polymeric composites: Critical concepts and comments", *Advances in Colloid and Interface Science*, Vol. 209, pp. 68-83, 2014.
- [74] B.C. Ray, "Thermal shock on interfacial adhesion of thermally conditioned glass fibre/epoxy composites", *Material Letters*, Vol. 58, pp. 2175-2177, 2004.
- [75] D.K. Rathore, B.C. Ray, S. Sethi, "Effect of temperature and loading speed on interface-dominated strength in fibre/polymer composites: an evaluation for in-situ", *Materials and Design*, Vol. 65, pp. 617-626, 2015.
- [76] B.C. Ray, S. Sethi, "An assessment of mechanical behavior and fractography study of glass/epoxy composites at different temperatures and loading speeds", *Materials and Design*, Vol. 64, pp. 160-165, 2014.
- [77] ASTM International, "ASTM standard D2344/D2344M test method for short-beam strength of polymer matrix composite materials", U.S.A, 2000.
- [78] A. Makeev, Y. He, "Nonlinear shear behavior and interlaminar shear strength of unidirectional polymer matrix composites: a numerical study", *International Journal of Solids and Structures*, Vol. 51, pp. 1263-1273, 2014.
- [79] R. Matsuyama, M. Sakaib, M. Lia, "Interlaminar shear strength of C/C-composites: The dependence on test methods", *Carbon*, Vol. 37, pp. 1749-1757, 1999.
- [80] M.L. Costa, S.F.M. de Almeida, M.C. Rezende, "The influence of porosity on the interlaminar shear strength of carbon/epoxy and carbon/bismaleimide fabric laminates", *Composite Science and Technology*, Vol. 61, pp. 2101-2108, 2001.
- [81] S.L. Donaldson, R.Y. Kim, "Experimental and analytical studies on the damage initiation in composite laminates at cryogenic temperatures", *Composite Structures*, Vol. 76, pp. 62-66, 2006.
- [82] M. Hojo, S. Ochiaia, K. Schulte, M. Ando, B. Fiedler, "Failure behavior of an epoxy matrix under different kinds of static loading", *Composite Science and Technology*, Vol. 61, pp. 1615-1624, 2001.
- [83] C.M. Landis, R.M. McMeeking, "Stress concentrations in composites with interface sliding matrix stiffness and uneven fibre spacing using shear lag theory", *International Journal of Solids and Structures*, Vol. 36, pp. 4333-4361, 1999.

- [84] Y. Swolfs, R.M. McMeeking, V.P. Rajan, F.W. Zok, I. Verpoest, “Global load-sharing model for unidirectional hybrid fibre-reinforced composites”, *Mechanics and Physics of Solids*, Vol. 84, pp. 380-394, 2015.
- [85] Y. Swolfs, I. Verpoest, L. Gorbatiikh, “Issues in strength models for unidirectional fibre-reinforced composites related to Weibull distributions, fibre packings and boundary effects”, *Composites Science and Technology*, Vol. 114, pp. 42-49, 2015.
- [86] S. Blassiau, A. Thionnet, A.R. Bunsell, “Micromechanism of load transfer in a unidirectional carbon fibre-reinforced epoxy composite due to fibre failures. Part 2: influence of viscoelastic and plastic matrices on the mechanisms of load transfer”, *Composite Structures*, Vol. 74, pp. 319-331, 2006.
- [87] P.J. Hine, M. Bonner, I.M. Ward, Y. Swolfs, I. Verpoest, A. Mierzwa, “Hybrid carbon fibre/nylon 12 single polymer composites”, *Composites Part A*, Vol. 65, pp. 19-26, 2014.
- [88] Y. Swolfs, R.M. McMeeking, I. Verpoest, L. Gorbatiikh, “Matrix cracks around fibre breaks and their effect on stress redistribution and failure development in unidirectional composites”, *Composites Science and Technology*, Vol. 108, pp. 16-22, 2015.
- [89] Y. Swolfs, L. Crauwels, E. Van Breda, L. Gorbatiikh, P. Hine, I. Ward, “Tensile behavior of interlayer hybrid composites of carbon fibre and self-reinforced polypropylene”, *Composites Part A*, Vol. 59, pp. 78-84, 2014.
- [90] Y. Swolfs, R.M. McMeeking, I. Verpoest, L. Gorbatiikh, “The effect of fibre dispersion on initial failure strain and cluster development in unidirectional carbon/glass hybrid composites”, *Composites Part A*, Vol. 69, pp. 279-287, 2015.
- [91] S. Behzadi, F.R. Jones, “The effect of temperature on stress transfer between a broken fibre and the adjacent fibres in unidirectional fibre composites”, *Composite Science and Technology*, Vol. 68, pp. 2690-2696, 2008.
- [92] A.B. de Morais, “Stress distribution along broken fibres in polymer-matrix composites”, *Composite Science and Technology*, Vol. 61, 1571-1580, 2001.
- [93] A.T. Jones, K.D. Dibenedetto, “The role of interphase debonding on cumulative fibre fractures in a continuous fibre-reinforced composite”, *Composites Part A*, Vol. 27, pp. 869-879, 1996.
- [94] J.F. McGown, J.G. Manwell, “Wind energy explained: Theory, design and application”, Washington, U.S.A, 2009.

- [95] E. Hau, "Wind turbines: Fundamentals, Technologies, Application, Economics", Springer, Berlin, 2006.
- [96] R.E. Wilson, "Wind-turbine aerodynamics", *Industrial Aerodynamics*, Vol. 5, pp. 357-372, 1980.
- [97] A. Memon, S.R. Samo, M. Asad, F.H. Mangi, "Modeling of aerodynamic forces on the wind turbine blades", *Clean Energy Technology*, Vol. 3, pp. 406-410, 2015.
- [98] T.D. Ashwill, "Materials and innovations for large blade structures: research opportunities in wind energy technology", In *50th AIAA Structures, Structural Dynamics & Materials Conference*, Sandia National Laboratories, Albuquerque, New Mexico, 2009.
- [99] M. Grujicic, G. Arakere, B. Pandurangan, V. Sellappan, A. Vallejo, M. Ozen, "Multidisciplinary design optimization for glass-fibre epoxy matrix-composite 5MW horizontal-axis wind turbine blades", *Materials Engineering and Performance*, Vol. 19, pp. 1116-1127, 2010.
- [100] D.A. Griffin, "Blade system design studies volume II: Preliminary blade designs and recommended test matrix", Sandia National Laboratories, New Mexico, 2004.
- [101] J. Chen, Q. Wang, W.Z. Shen, X. Pang, S. Li, X. Gue, "Structural optimization study of composite wind turbine blade", *Materials and Design*, Vol. 46, pp. 247-255, 2013.
- [102] K.-N. Chen, P.-Y. Chen, "Structural optimization of 3 MW wind turbine blades using a two-step procedure", *Int. J. Simulation and Multidisciplinary Design Optimization*, Vol. 4, pp. 159-165, 2010.
- [103] J. Zhu, X. Cai, P. Pan, R. Gu, "Multi-objective structural optimization design of horizontal-axis wind turbine blades using the non-dominated sorting genetic algorithm II and finite element method", *Energies*, Vol. 7, pp. 988-1002, 2014.
- [104] T.S. Thakur, B. Patel, "Structural analysis of a composite wind turbine blade to optimize its constructional parameters using a FEA software", *Scientific Research & Development*, Vol. 3, pp. 572-578, 2016.
- [105] K.J. Bowles, S. Frimpong, "Void effects on the interlaminar shear strength of unidirectional graphite fiber reinforced composites", *Journal of Composite Materials*, Vol. 26, pp. 1487-1510, 1992.
- [106] F. Rosselli, M.H. Santare, "Comparison of the short beam shear (SBS) and interlaminar shear device (ISD) tests", *Composites Part A*, Vol. 28, pp. 587-594, 1997.

- [107] Z. Fan, M.H. Santare, S.G. Advani, "Interlaminar shear strength of glass fiber reinforced epoxy composites enhanced with multi-walled carbon nanotubes", *Composites Part A*, Vol. 39, pp. 540-554, 2008.
- [108] E.C. Botelho, L.C. Pardini, M.C. Rezende, "Hygrothermal effects on the shear properties of carbon fiber/epoxy composites", *J. Material Science*. Vol. 41, pp. 7111-7118, 2006.
- [109] B.C. Ray, "Temperature effect during humid ageing on interfaces of glass and carbon fibers reinforced epoxy composites", *Journal of Colloid and Interface Science*, Vol. 298, pp. 111-117, 2006.
- [110] P.J. Herrera-Franco, L.T. Drzal, "Comparison of methods for the measurement of fibre/matrix adhesion in composites", *Composites*, Vol. 23, pp. 2-27, 1992.
- [111] M.S. Madhukar, L.T. Drzal, "Fiber-matrix adhesion and its effect on composite mechanical properties: I. In-plane and interlaminar shear behavior of graphite/epoxy composites", *J. of Composite Materials*, Vol. 25, pp. 932-958, 1991.
- [112] M.L. Costa, S.F. M. de Almeida, M.C. Rezende, "The influence of porosity on the interlaminar shear strength of carbon/epoxy and carbon/bismaleimide fabric laminates", *Composite Science and Technology*, Vol. 61, pp. 2101-2108, 2001.
- [113] R.A. Hawileh, A. Adi-Obeidah, Jamal A. Abdalla, Adil Al-Tamimi, "Temperature effect on the mechanical properties of carbon, glass and carbon-glass FRP laminates", *Construction and Building Materials*, Vol. 75, pp. 342-348, 2015.
- [114] Z. Lu, G. Xian, H. Li, "Effect of elevated temperatures on the mechanical properties of basalt fibers and BFRP plates", *Construction and Building Materials*, Vol. 127, pp. 1029-1036, 2016.
- [115] S. Cao, X. Wang, Z. Wu, "Evaluation and prediction of temperature-dependent tensile strength of unidirectional carbon fiber-reinforced polymer composites", *Journal of Reinforced plastics and Composites*, Vol. 30(9), pp. 799-807, 2011.
- [116] S.K. Ha, G.S. Springer, "Nonlinear mechanical properties of a thermoset matrix composite at elevated temperatures", *Journal of Composite Materials*, Vol. 23, pp. 1130-1159, 1989.
- [117] A. R. Bunsell, B. Harris, "Hybrid carbon and glass fibre composites", *Composites*, Vol. 1, pp. 157-164, 1974.
- [118] M.N. Gururaja, A.N. Harirao, "Hybrid effects on tensile properties of carbon/glass angle ply composites", *Advances in Materials*, Vol. 2, pp. 36-41, 2013.

- [119] A.B. de Morais, "Stress distribution along broken fibers in polymer-matrix composites", *Composite Science and Technology*, Vol. 61, pp. 1571-1580, 2001.
- [120] J. Xue, W.-X. Wang, J.-Z. Zhang, S.-J. Wu, H. Li, "Experimental and numerical study on the tensile behavior of UACS/Al fibre metal laminate", *Applied Composite Materials*, Vol. 22, pp. 489-505, 2015.
- [121] S. Fischer, "A material model for FE-simulation of UD composites", *Applied Composite Materials*, Vol. 23, pp. 197-217, 2016.
- [122] M. Jawaid, H.P.S. Abdul Khalil, O.S. Alattas, "Woven hybrid biocomposites: Dynamic mechanical and thermal properties", *Composites Part A*, Vol. 43, pp. 288-293, 2012.
- [123] N. Saba, M. Jawaid, O.Y. Alothman, M.T. Paridah, "A review on dynamic mechanical properties of natural fibre reinforced polymer composites", *Construction and Building Materials*, Vol. 106, pp. 149-159, 2016.
- [124] S.N. Goyanes, P.G. Konig, J.D. Marconi, "Dynamic mechanical analysis of particulate-filled epoxy resin", *Journal of Applied Polymer Science*, Vol. 88, pp. 883-892, 2003.
- [125] E.J. Bosze, A. Alawar, O. Bertschger, Y.-I. Tsai, S.R. Nutt, "High-temperature strength and storage modulus in unidirectional hybrid composites", *Composite Science and Technology*, Vol. 66, pp. 1963-1969, 2006.
- [126] M.M. Afess, A. Assefa, "Prediction of performance parameters and determination of aerodynamic characteristics of wind turbine airfoil using CFD modeling: A case study of Adama I- Wind turbine blade airfoil section", *International Journal of Engineering and Technical Research*, Vol. 3, pp. 241-250, 2015.
- [127] A. Sedaghat, M. Mirhosseini, "Aerodynamic design of a 300kW horizontal axis wind turbine for province of Semnan", *Energy Conversion and Management*, Vol. 63, pp. 87-94, 2012.
- [128] J.R.P. Vaz, J.T. Pinho, A.L.A. Mesqita, "An extension of BEM method applied to horizontal-axis wind turbine design", *Renewable Energy*, Vol. 36, pp. 1734-1740, 2011.
- [129] K. Kishinami, H. Taniguchi, J. Suzuki, H. Ibano, T. Kazunou, M. Turuhami, "Theoretical and experimental study on the aerodynamic characteristics of a horizontal axis wind turbine", *Energy*, Vol. 30, pp. 2089-2100, 2005.
- [130] K. Kaw, "Mechanics of Composite Materials", CRC Press, Boca Raton, London, New York, 2006.

- [131] S.P. Davison, "Enviro-mechanical durability of graphite/epoxy composite materials", Dissertation, 2003.
- [132] O. Al-Qabandi, A. De Silva, S. Al-Enezi, M. Bassyouni, "Synthesis, fabrication and mechanical characterization of reinforced epoxy and polypropylene composites for wind turbine blades", *Journal of Reinforced Plastics and Composites*, Vol. 33, pp. 2287-2299, 2014.
- [133] R.D. Singh, M.M. Adams, "The dynamic properties of fibre-reinforced polymers exposed to hot, wet conditions", *Composite Science and Technology*, Vol. 56, pp. 977-997, 1996.
- [134] B. Ray, "Temperature effect during humid ageing on interfaces of glass and carbon fibres reinforced epoxy composites", *Advances in Colloid and Interface Science*, Vol. 298, pp. 111-117, 2006.
- [135] R. Murugan, R. Ramesh, K. Padmanabhan, "Investigation on static and dynamic mechanical properties of epoxy based woven fabric glass/carbon hybrid composite laminates", *Procedia Engineering*, Vol. 97, pp. 459-468, 2014.
- [136] B.C. Ray, D. Rathore, "Durability and integrity studies of environmentally interfaces in fibrous polymeric composites: critical concepts and comments", *Advances in Colloid and Interface Science*, Vol. 209, pp. 68-83, 2014.
- [137] J.D.D. Melo, D.W. Radford, "Time and temperature dependence of the viscoelastic properties of CFRP by dynamic mechanical analysis", *Composite Structures*, Vol. 70, pp. 240-253, 2005.
- [138] W. Hufenbach, M. Gude, R. Bohm, M. Zschehyge, "The effect of temperature on mechanical properties and failure behavior of hybrid yarn textile- reinforced thermoplastics", *Materials and Design*, Vol. 32, pp. 4278-4288, 2011.
- [139] A.G. Gibson, M.E. Otheguy Torres, T.N.A. Browne, S. Feih, A.P. Mouritz, "High temperature and fire behavior of continuous glass fibre/polypropylene laminates", *Composites Part A*, Vol. 41, pp. 1219-1230, 2010.
- [140] S.K. Ha, G.S. Springer, "Nonlinear mechanical properties of a thermoset matrix composite at elevated temperatures", *Composite Materials*, Vol. 23, pp. 1130-1158, 1989.
- [141] C.A. Mahieux, K.L. Reifsnider, S.W. Case, "Property modeling across transition temperature in PMC's: Part I. tensile properties", *Applied Composite Materials*, Vol. 8, pp. 217-234, 2001.

- [142] G. Odegard, M. Kumosa, “Elastic-plastic and failure properties of a unidirectional carbon/PMR-15 composite at room and elevated temperatures”, *Composites Science and Technology*, Vol. 60, pp. 2979-2988, 2000.
- [143] D.J. Lekou, T.P. Philippidis, “Mechanical property variability in FRP laminates and its effect on failure predication”, *Composites Part B*, Vol. 39, pp. 1247-1256, 2008.
- [144] R.E. Walpole, R.H. Myers, S.L. Myers, K. Ye “Probability and Statistics for Engineers and Scientists”, Pearson Education, 2016.
- [145] K.P. Menard, “Dynamic Mechanical Analysis-A Practical Introduction”, Florida, U.S.A, 1999.
- [146] F.M. Jensen, B.G. Falzon, J. Ankerson, H. Stang, “Structural testing and numerical simulation of a 34m composite wind turbine blade”, *Composite Structures*, Vol. 76, pp. 52-61, 2006.
- [147] L.C.T. Overgaard, E. Lund, “Structural collapse of a wind turbine blade Part B: Progressive interlaminar failure models”, *Composites Part A*, Vol. 41, pp. 271-283, 2010.
- [148] F.-B. Hsiao, C.-J. Bai, W.-T. Chong, “The performance test of three different horizontal-axis wind turbine blade shapes using experimental and numerical methods”, *Energies*, Vol. 6, pp. 2784-2803, 2013.
- [149] P.J. Schubel, R.J. Crossley, “Wind turbine blade design”, *Energies*, Vol. 5, pp. 3425-3449, 2012.
- [150] Z. Lanting, “Research on structural lay-up optimum design of composite wind turbine blade”, *Energy Procedia*, Vol. 14, pp. 637-642, 2012.

Appendix: A

Parameters to select airfoils and BEM theory to find flap-wise loading under different wind speeds

Location	Blade families	Chord length (m)	Center of section	Twist angle	Relative wind	Section pitch	Angle of attack	Lift coefficient $Re6*10^6$	Drag coefficient $Re6*10^6$	Tip speed ratio	L/D Ration
0.00	Circular	2.430	-	0							
1.00	Circular	2.430	-	0							
2.00	Circular	2.430	-	0							
3.00	Circular	2.430	-	0							
4.00	Circular	2.430	-	0							
5.00	Circular	2.430	-	0							
6.00	Circular	2.430	-	0							
10.80	N4415	4.05	1.35	17.05	20.08	11.58	8.5	1.42	0.010	9.0	143.82
15.60	N4415	3.69	1.23	15.20	18.23	9.73	8.5	1.42	0.010	9.0	143.82
20.40	N4415	3.33	1.11	13.37	16.40	7.9	8.5	1.42	0.010	9.0	143.82
25.20	N4415	2.97	0.99	11.55	14.58	6.08	8.5	1.42	0.010	9.0	145.04
30.00	N23015	2.61	0.87	6.70	9.74	1.24	8.5	1.086	0.007	9.0	145.04
34.80	N23015	2.25	0.75	5.17	8.20	-0.3	8.5	1.086	0.007	9.0	145.04
39.60	N23012	1.89	0.63	4.06	7.09	-1.41	8.5	1.094	0.007	9.0	146.31
44.40	N23012	1.53	0.51	2.70	5.74	-2.76	8.5	1.094	0.007	9.0	146.31
49.20	N23012	1.17	0.39	1.35	4.38	-4.12	8.5	1.094	0.007	9.0	146.31
54.00	N23012	0.81	0.27	0	3.033	-5.467	8.5	1.094	0.007	9.0	146.31

Sections and NACA airfoils with different parameters used to model the blade

Location	Blade families	Local solidity	Linear induction factor(a)	angular induction factor(a')	Relative wind. angle	Modified R.W.angle	Modified (a)	Modified (a')	Twist angel (mod)
0.00	Circular								
1.00	Circular								
2.00	Circular								
3.00	Circular								
4.00	Circular								
5.00	Circular								
6.00	Circular								
10.80	N4415	0.1791	0.3363	0.0726	20.08	20.21	0.3333	0.0727	18.00
15.60	N4415	0.113	0.2802	0.0441	18.23	16.12	0.3333	0.0436	12.62
20.40	N4415	0.078	0.2499	0.0297	16.40	13.42	0.3333	0.0293	9.92
25.20	N4415	0.0563	0.2339	0.0211	14.58	11.42	0.3332	0.0208	7.92
30.00	N23015	0.0415	0.2795	0.0116	9.74	8.59	0.3331	0.0115	5.09
34.80	N23015	0.0309	0.2899	0.0085	8.20	7.42	0.3328	0.0085	3.92
39.60	N23012	0.0228	0.2889	0.0063	7.09	6.40	0.3328	0.0063	3.00
44.40	N23012	0.0165	0.3098	0.0046	5.74	5.44	0.3333	0.0046	1.94
49.20	N23012	0.0114	0.3555	0.0031	4.38	4.53	0.3326	0.0031	1.03
54.00	N23012	0.0072	0.4126	0.0020	3.033	3.60	0.3327	0.0020	0

Local solidity, modified linear, angular induction factor and twist angle considered

Appendix: A

location	Blade families	Modified (a)	Modified (a')	Modified R.W.angle	Relative Velocity (3m/s)	Relative Velocity (9.56m/s)	Relative Velocity (12m/s)	Relative Velocity (25m/s)	Twist angel (mod)
0.00	Circular								
1.00	Circular								
2.00	Circular								
3.00	Circular								
4.00	Circular								
5.00	Circular								
6.00	Circular								
10.80	N4415	0.3333	0.0727	21.00	5.58	17.78	22.32	46.50	18.00
15.60	N4415	0.3330	0.0436	16.13	7.20	22.95	28.81	60.02	12.63
20.40	N4415	0.3333	0.0293	13.42	8.62	27.46	34.47	71.82	9.92
25.20	N4415	0.3332	0.0208	11.42	10.10	32.20	40.41	84.19	7.92
30.00	N23015	0.3331	0.0115	8.59	13.39	42.69	53.58	111.62	5.09
34.80	N23015	0.3333	0.0085	7.41	15.508	49.42	62.033	129.23	3.91
39.60	N23012	0.3328	0.0063	6.40	17.96	57.22	71.83	149.64	3.00
44.40	N23012	0.3333	0.0046	5.44	21.09	67.23	84.39	175.81	1.94
49.20	N23012	0.3326	0.0031	4.53	25.35	80.78	101.40	211.25	1.03
54.00	N23012	0.3327	0.0020	3.60	31.88	101.60	127.53	265.68	0

Relative velocity, twist angle and wind speeds on each sections along the length of the blades.

Location	Blade families	Chord length (m)	Lift coefficient Re $6 \cdot 10^6$	Density of air (kg/m ³)	Relative Velocity (3m/s)	Relative Velocity (9.56m/s)	Lift force (3m/s)	Lift force (9.56m/s)
0.00	Circular			1.225				
1.00	Circular			1.225				
2.00	Circular			1.225				
3.00	Circular			1.225				
4.00	Circular			1.225				
5.00	Circular			1.225				
6.00	Circular			1.225				
10.80	N4415	4.05	1.42	1.225	5.58	17.78	526.4524	5.3451e+03
15.60	N4415	3.69	1.42	1.225	7.20	22.95	733.43	8.1139e+03
20.40	N4415	3.33	1.42	1.225	8.62	27.46	883.07	1.0483e+04
25.20	N4415	2.97	1.42	1.225	10.10	32.20	1.0336e+03	1.2856e+04
30.00	N23015	2.61	1.086	1.225	13.39	42.69	1.3611e+03	1.5187e+04
34.80	N23015	2.25	1.086	1.225	15.508	49.42	1.7277e+03	1.7545e+04
39.60	N23012	1.89	1.094	1.225	17.96	57.22	1.8152e+03	1.9903e+04
44.40	N23012	1.53	1.094	1.225	21.09	67.23	2.1888e+03	2.2242e+04
49.20	N23012	1.17	1.094	1.225	25.35	80.78	2.4183e+03	2.4556e+04
54.00	N23012	0.81	1.094	1.225	31.88	101.60	2.6478e+03	2.6893e+04

Chord length and lift force distribution at different wind speeds along the span of the blade

Location	Blade families	Chord length (m)	Lift coefficient Re $6 \cdot 10^6$	Density of air (kg/m ³)	Relative Velocity (12m/s)	Relative Velocity (25m/s)	Lift force (12m/s)	Lift force (25m/s)
0.00	Circular			1.225				
1.00	Circular			1.225				
2.00	Circular			1.225				
3.00	Circular			1.225				
4.00	Circular			1.225				
5.00	Circular			1.225				
6.00	Circular			1.225				
10.80	N4415	4.05	1.42	1.225	22.32	46.50	8.4232e+03	3.6559e+04
15.60	N4415	3.69	1.42	1.225	28.81	60.02	1.2786e+04	5.5495e+04
20.40	N4415	3.33	1.42	1.225	34.47	71.82	1.6518e+04	7.1709e+04
25.20	N4415	2.97	1.42	1.225	40.41	84.19	2.0247e+04	8.7885e+04
30.00	N23015	2.61	1.086	1.225	53.58	111.62	2.3923e+04	1.0382e+05
34.80	N23015	2.25	1.086	1.225	62.033	129.23	2.7644e+04	1.1997e+05
39.60	N23012	1.89	1.094	1.225	71.83	149.64	3.1364e+04	1.3612e+05
44.40	N23012	1.53	1.094	1.225	84.39	175.81	3.5046e+04	1.5210e+05
49.20	N23012	1.17	1.094	1.225	101.40	211.25	3.8692e+04	1.6794e+05
54.00	N23012	0.81	1.094	1.225	127.53	265.68	4.2372e+04	1.8389e+05

Chord length and lift force distribution at different wind speeds along the span of the blade

Appendix: A

Location	Blade families	Chord length (m)	Drag coefficient $Re6^{10}$	Density of air (kg/m ³)	Relative Velocity (3m/s)	Relative Velocity (9.56m/s)	Drag force (3m/s)	Drag force (9.56m/s)
0.00	Circular			1.225				
1.00	Circular			1.225				
2.00	Circular			1.225				
3.00	Circular			1.225				
4.00	Circular			1.225				
5.00	Circular			1.225				
6.00	Circular			1.225				
10.80	N4415	4.05	0.010	1.225	5.58	17.78	3.7074	37.6414
15.60	N4415	3.69	0.010	1.225	7.20	22.95	5.6239	57.1398
20.40	N4415	3.33	0.010	1.225	8.62	27.46	7.2745	73.8232
25.20	N4415	2.97	0.010	1.225	10.10	32.20	8.9073	90.5348
30.00	N23015	2.61	0.007	1.225	13.39	42.69	9.6305	97.8900
34.80	N23015	2.25	0.007	1.225	15.508	49.42	11.1363	113.0924
39.60	N23012	1.89	0.007	1.225	17.96	57.22	12.5464	127.3512
44.40	N23012	1.53	0.007	1.225	21.09	67.23	14.0052	142.3190
49.20	N23012	1.17	0.007	1.225	25.35	80.78	15.4735	157.1227
54.00	N23012	0.81	0.007	1.225	31.88	101.60	16.9421	172.0750

Chord length and drag force distribution at different wind speeds along the span of the blade

Location	Blade families	Chord length (m)	Drag coefficient $Re6^{10}$	Density of air (kg/m ³)	Relative Velocity (12m/s)	Relative Velocity (25m/s)	Drag force (12m/s)	Drag force (25m/s)
0.00	Circular			1.225				
1.00	Circular			1.225				
2.00	Circular			1.225				
3.00	Circular			1.225				
4.00	Circular			1.225				
5.00	Circular			1.225				
6.00	Circular			1.225				
10.80	N4415	4.05	0.010	1.225	22.32	46.50	59.3186	257.4591
15.60	N4415	3.69	0.010	1.225	28.81	60.02	90.0451	390.8100
20.40	N4415	3.33	0.010	1.225	34.47	71.82	116.3253	504.9895
25.20	N4415	2.97	0.010	1.225	40.41	84.19	142.5875	618.9062
30.00	N23015	2.61	0.007	1.225	53.58	111.62	154.2025	669.2215
34.80	N23015	2.25	0.007	1.225	62.033	129.23	178.1860	773.3117
39.60	N23012	1.89	0.007	1.225	71.83	149.64	200.6868	870.9688
44.40	N23012	1.53	0.007	1.225	84.39	175.81	224.2429	973.2490
49.20	N23012	1.17	0.007	1.225	101.40	211.25	247.5752	1.0745e+03
54.00	N23012	0.81	0.007	1.225	127.53	265.68	271.1160	1.1767e+03

Chord length and drag force distribution at different wind speeds along the span of the blade

Location	Blade families	Relative wind. angle	Lift force (3m/s)	Lift force (9.56m/s)	Lift force (3m/s)*cos φ	Lift force (9.56m/s)* cos φ
0.00	Circular					
1.00	Circular					
2.00	Circular					
3.00	Circular					
4.00	Circular					
5.00	Circular					
6.00	Circular					
10.80	N4415	21.00	526.4524	5.3451e+03	491.4857	4.9901e+03
15.60	N4415	16.13	733.43	8.1139e+03	704.5577	7.7945e+03
20.40	N4415	13.42	883.07	1.0483e+04	858.9577	1.0197e+04
25.20	N4415	11.42	1.0336e+03	1.2856e+04	1.0131e+03	1.2601e+04
30.00	N23015	8.59	1.3611e+03	1.5187e+04	1.3458e+03	1.5017e+04
34.80	N23015	7.41	1.7277e+03	1.7545e+04	1.7133e+03	1.7398e+04
39.60	N23012	6.40	1.8152e+03	1.9903e+04	1.8039e+03	1.9779e+04
44.40	N23012	5.44	2.1888e+03	2.2242e+04	2.1789e+03	2.2142e+04
49.20	N23012	4.53	2.4183e+03	2.4556e+04	2.4107e+03	2.4479e+04
54.00	N23012	3.60	2.6478e+03	2.6893e+04	2.6426e+03	2.6840e+04

Lift force under variable angle of relative wind and different wind speeds

Appendix: A

Location	Blade families	Relative wind. angle	Lift force (12m/s)	Lift force (25m/s)	Lift force (12.m/s) *cos φ	Lift force (25m/s) *cos φ
0.00	Circular					
1.00	Circular					
2.00	Circular					
3.00	Circular					
4.00	Circular					
5.00	Circular					
6.00	Circular					
10.80	N4415	21.00	8.4232e+03	3.6559e+04	7.8637e+03	3.4131e+04
15.60	N4415	16.13	1.2786e+04	5.5495e+04	1.2283e+04	5.3310e+04
20.40	N4415	13.42	1.6518e+04	7.1709e+04	1.6067e+04	6.9751e+04
25.20	N4415	11.42	2.0247e+04	8.7885e+04	1.9846e+04	8.6145e+04
30.00	N23015	8.59	2.3923e+04	1.0382e+05	2.3655e+04	1.0266e+05
34.80	N23015	7.41	2.7644e+04	1.1997e+05	2.7413e+04	1.1897e+05
39.60	N23012	6.40	3.1364e+04	1.3612e+05	3.1169e+04	1.3527e+05
44.40	N23012	5.44	3.5046e+04	1.5210e+05	3.4888e+04	1.5141e+05
49.20	N23012	4.53	3.8692e+04	1.6794e+05	3.8571e+04	1.6742e+05
54.00	N23012	3.60	4.2372e+04	1.8389e+05	4.2288e+04	1.8353e+05

Lift force under variable angle of relative wind and different wind speeds

Location	Blade families	Relative wind. angle	Drag force (3m/s)	Drag force (9.56m/s)	Drag force (3m/s)*sin φ	Drag force (9.56m/s) *sin φ
0.00	Circular					
1.00	Circular					
2.00	Circular					
3.00	Circular					
4.00	Circular					
5.00	Circular					
6.00	Circular					
10.80	N4415	21.00	3.7074	37.6414	1.3286	13.4895
15.60	N4415	16.13	5.6239	57.1398	1.5624	15.8744
20.40	N4415	13.42	7.2745	73.8232	1.6883	17.1334
25.20	N4415	11.42	8.9073	90.5348	1.7636	17.9258
30.00	N23015	8.59	9.6305	97.8900	1.4384	14.6211
34.80	N23015	7.41	11.1363	113.0924	1.4362	14.5854
39.60	N23012	6.40	12.5464	127.3512	1.3985	14.1957
44.40	N23012	5.44	14.0052	142.3190	1.3277	13.4923
49.20	N23012	4.53	15.4735	157.1227	1.2221	12.4097
54.00	N23012	3.60	16.9421	172.0750	1.0638	10.8047

Drag force under variable angle of relative wind and different wind speeds

Location	Blade families	Relative wind. angle	Drag force (12m/s)	Drag force (25m/s)	Drag force (12.m/s) *sin φ	Drag force (25m/s) *sin φ
0.00	Circular					
1.00	Circular					
2.00	Circular					
3.00	Circular					
4.00	Circular					
5.00	Circular					
6.00	Circular					
10.80	N4415	21.00	59.3186	257.4591	21.2579	92.2651
15.60	N4415	16.13	90.0451	390.8100	25.0161	108.5739
20.40	N4415	13.42	116.3253	504.9895	26.9976	117.2017
25.20	N4415	11.42	142.5875	618.9062	28.2323	122.5431
30.00	N23015	8.59	154.2025	669.2215	23.0321	99.9568
34.80	N23015	7.41	178.1860	773.3117	22.9804	99.7330
39.60	N23012	6.40	200.6868	870.9688	22.3703	97.0860
44.40	N23012	5.44	224.2429	973.2490	21.2590	92.2672
49.20	N23012	4.53	247.5752	1.0745e+03	19.5538	84.8652
54.00	N23012	3.60	271.1160	1.1767e+03	17.0235	73.8856

Drag force under variable angle of relative wind and different wind speeds

Appendix: A

Location	Lift force (3m/s)*cos φ	Lift force (9.56m/s) *cos φ	Lift force (12.m/s) *cos φ	Lift force (25m/s) *cos φ	Drag force (3m/s)*sin φ	Drag force (9.56m/s) *sin φ	Drag force (12.m/s) *sin φ	Drag force (25m/s) *sin φ
0.00								
1.00								
2.00								
3.00								
4.00								
5.00								
6.00								
10.80	491.4857	4.9901e+03	7.8637e+03	3.4131e+04	1.3286	13.4895	21.2579	92.2651
15.60	704.5577	7.7945e+03	1.2283e+04	5.3310e+04	1.5624	15.8744	25.0161	108.5739
20.40	858.9577	1.0197e+04	1.6067e+04	6.9751e+04	1.6883	17.1334	26.9976	117.2017
25.20	1.0131e+03	1.2601e+04	1.9846e+04	8.6145e+04	1.7636	17.9258	28.2323	122.5431
30.00	1.3458e+03	1.5017e+04	2.3655e+04	1.0266e+05	1.4384	14.6211	23.0321	99.9568
34.80	1.7133e+03	1.7398e+04	2.7413e+04	1.1897e+05	1.4362	14.5854	22.9804	99.7330
39.60	1.8039e+03	1.9779e+04	3.1169e+04	1.3527e+05	1.3985	14.1957	22.3703	97.0860
44.40	2.1789e+03	2.2142e+04	3.4888e+04	1.5141e+05	1.3277	13.4923	21.2590	92.2672
49.20	2.4107e+03	2.4479e+04	3.8571e+04	1.6742e+05	1.2221	12.4097	19.5538	84.8652
54.00	2.6426e+03	2.6840e+04	4.2288e+04	1.8353e+05	1.0638	10.8047	17.0235	73.8856

Summary of modified lift force and drag force for the analysis of normal force

section	Location	Blade families	Normal force at wind speed (3m/s)	Normal force at wind speed (9.56m/s)	Normal force at wind speed (12m/s)	Normal force at wind speed (25m/s)
1	0.00	Circular				
2	1.00	Circular				
3	2.00	Circular				
4	3.00	Circular				
5	4.00	Circular				
6	5.00	Circular				
7	6.00	Circular				
8	10.80	N4415	492.8143	5.0036e+03	7.8850e+03	3.4223e+04
9	15.60	N4415	706.1201	7.8104e+03	1.2308e+04	5.3419e+04
10	20.40	N4415	860.6460	1.0214e+04	1.6094e+04	6.9868e+04
11	25.20	N4415	1.0149e+03	1.2619e+04	1.9874e+04	8.6268e+04
12	30.00	N23015	1.3472e+03	1.5032e+04	2.3678e+04	1.0276e+05
13	34.80	N23015	1.7147e+03	1.7413e+04	2.7436e+04	1.1907e+05
14	39.60	N23012	1.8053e+03	1.9793e+04	3.1191e+04	1.3537e+05
15	44.40	N23012	2.1802e+03	2.2155e+04	3.4909e+04	1.5150e+05
16	49.20	N23012	2.4119e+03	2.4491e+04	3.8591e+04	1.6750e+05
17	54.00	N23012	2.6437e+03	2.6851e+04	4.2305e+04	1.8360e+05

Normal force values along the length of the blade under variable wind speeds

Location	Blade families	Relative wind. angle	Lift force (3m/s)	Lift force (9.56m/s)	Lift force (3m/s)*sin φ	Lift force (9.56m/s) *sin φ
0.00	Circular					
1.00	Circular					
2.00	Circular					
3.00	Circular					
4.00	Circular					
5.00	Circular					
6.00	Circular					
10.80	N4415	21.00	526.4524	5.3451e+03	188.6637	1.9155e+03
15.60	N4415	16.13	733.43	8.1139e+03	203.7598	2.2542e+03
20.40	N4415	13.42	883.07	1.0483e+04	204.9495	2.4330e+03
25.20	N4415	11.42	1.0336e+03	1.2856e+04	204.6523	2.5455e+03
30.00	N23015	8.59	1.3611e+03	1.5187e+04	203.2977	2.2684e+03
34.80	N23015	7.41	1.7277e+03	1.7545e+04	222.8192	2.2628e+03
39.60	N23012	6.40	1.8152e+03	1.9903e+04	202.3384	2.2186e+03
44.40	N23012	5.44	2.1888e+03	2.2242e+04	207.5055	2.1086e+03
49.20	N23012	4.53	2.4183e+03	2.4556e+04	190.9999	1.9395e+03
54.00	N23012	3.60	2.6478e+03	2.6893e+04	166.2567	1.6886e+03

Lift force under variable angle of relative wind

Appendix: A

Location	Blade families	Relative wind. angle	Lift force (12m/s)	Lift force (25/s)	Lift force (12m/s)*sin φ	Lift force (25m/s) *sin φ
0.00	Circular					
1.00	Circular					
2.00	Circular					
3.00	Circular					
4.00	Circular					
5.00	Circular					
6.00	Circular					
10.80	N4415	21.00	8.4232e+03	3.6559e+04	3.0186e+03	1.3102e+04
15.60	N4415	16.13	1.2786e+04	5.5495e+04	3.5522e+03	1.5417e+04
20.40	N4415	13.42	1.6518e+04	7.1709e+04	3.8336e+03	1.6643e+04
25.20	N4415	11.42	2.0247e+04	8.7885e+04	4.0089e+03	1.7401e+04
30.00	N23015	8.59	2.3923e+04	1.0382e+05	3.5732e+03	1.5507e+04
34.80	N23015	7.41	2.7644e+04	1.1997e+05	3.5652e+03	1.5472e+04
39.60	N23012	6.40	3.1364e+04	1.3612e+05	3.4961e+03	1.5173e+04
44.40	N23012	5.44	3.5046e+04	1.5210e+05	3.3225e+03	1.4420e+04
49.20	N23012	4.53	3.8692e+04	1.6794e+05	3.0559e+03	1.3264e+04
54.00	N23012	3.60	4.2372e+04	1.8389e+05	2.6606e+03	1.1547e+04

Lift force under variable angle of relative wind under variable wind speeds

blade families	Relative wind. angle	Drag force (3m/s)	Drag force (9.56m/s)	Drag force (12m/s)	Drag force (25m/s)	Drag force (3m/s)*cos φ	Drag force (9.56m/s)*cos φ	Drag force (12.m/s) *cos φ	Drag force (25m/s) *cos φ
Circular									
Circular									
Circular									
Circular									
Circular									
Circular									
N4415	21.00	3.7074	37.6414	59.3186	257.4591	3.4612	35.1413	55.3787	240.3588
N4415	16.13	5.6239	57.1398	90.0451	390.8100	5.4025	54.8904	86.5004	375.4253
N4415	13.42	7.2745	73.8232	116.3253	504.9895	7.0759	71.8075	113.1490	491.2007
N4415	11.42	8.9073	90.5348	142.5875	618.9062	8.7310	88.7424	139.7646	606.6532
N23015	8.59	9.6305	97.8900	154.2025	669.2215	9.5225	96.7919	152.4727	661.7145
N23015	7.41	11.1363	113.0924	178.1860	773.3117	11.0433	112.1479	176.6979	766.8535
N23012	6.40	12.5464	127.3512	200.6868	870.9688	12.4682	126.5575	199.4361	865.5409
N23012	5.44	14.0052	142.3190	224.2429	973.2490	13.9421	141.6780	223.2329	968.8655
N23012	4.38	15.4735	157.1227	247.5752	1.0745e+03	15.4283	156.6638	246.8521	1.0714e+03
N23012	3.033	16.9421	172.0750	271.1160	1.1767e+03	16.9184	171.8340	270.7362	1.1751e+03

Summary of drag force under variable wind speed for the analysis of tangential force.

blade families	Lift force (3m/s)*cos φ	Lift force (9.56m/s)*sin φ	Lift force (12.m/s)*sin φ	Lift force (25m/s)*sin φ	Drag force (3m/s)*cos φ	Drag force (9.56m/s)*cos φ	Drag force (12.m/s)*cos φ	Drag force (25m/s)*cos φ
Circular								
Circular								
Circular								
Circular								
Circular								
Circular								
N4415	188.6637	1.9155e+03	3.0186e+03	1.3102e+04	3.4612	35.1413	55.3787	240.3588
N4415	203.7598	2.2542e+03	3.5522e+03	1.5417e+04	5.4025	54.8904	86.5004	375.4253
N4415	204.9495	2.4330e+03	3.8336e+03	1.6643e+04	7.0759	71.8075	113.1490	491.2007
N4415	204.6523	2.5455e+03	4.0089e+03	1.7401e+04	8.7310	88.7424	139.7646	606.6532
N23015	203.2977	2.2684e+03	3.5732e+03	1.5507e+04	9.5225	96.7919	152.4727	661.7145
N23015	222.8192	2.2628e+03	3.5652e+03	1.5472e+04	11.0433	112.1479	176.6979	766.8535
N23012	202.3384	2.2186e+03	3.4961e+03	1.5173e+04	12.4682	126.5575	199.4361	865.5409
N23012	207.5055	2.1086e+03	3.3225e+03	1.4420e+04	13.9421	141.6780	223.2329	968.8655
N23012	190.9999	1.9395e+03	3.0559e+03	1.3264e+04	15.4283	156.6638	246.8521	1.0714e+03
N23012	166.2567	1.6886e+03	2.6606e+03	1.1547e+04	16.9184	171.8340	270.7362	1.1751e+03

Summary of modified lift force and drag force for the analysis of tangential force

Section	Location	Blade families	Tangential force at wind speed (3m/s)	Tangential force at wind speed (9.56m/s)	Tangential force at wind speed (12m/s)	Tangential force at wind speed (25m/s)
1	0.00	Circular				
2	1.00	Circular				
3	2.00	Circular				
4	3.00	Circular				
5	4.00	Circular				
6	5.00	Circular				
7	6.00	Circular				
8	10.80	N4415	185.2025	1.8804e+03	2.9632e+03	1.2862e+04
9	15.60	N4415	198.3573	2.1993e+03	3.4657e+03	1.5042e+04
10	20.40	N4415	197.8736	2.3612e+03	3.7205e+03	1.6152e+04
11	25.20	N4415	195.9213	2.4568e+03	3.8691e+03	1.6794e+04
12	30.00	N23015	193.7752	2.1716e+03	3.4207e+03	1.4845e+04
13	34.80	N23015	211.7759	2.1507e+03	3.3885e+03	1.4705e+04
14	39.60	N23012	189.8702	2.0920e+03	3.2967e+03	1.4307e+04
15	44.40	N23012	193.5634	1.9669e+03	3.0993e+03	1.3451e+04
16	49.20	N23012	175.5716	1.7828e+03	2.8090e+03	1.2193e+04
17	54.00	N23012	149.3383	1.5168e+03	2.3899e+03	1.0372e+04

Tangential force values along the length of the blade under variable wind speeds

Location	Normal force at wind velocity (3m/s)	Bending moment at wind velocity (3m/s) N/m	Normal force at wind velocity (9.56m/s)	Bending moment at wind velocity (9.56m/s)	Normal force at wind speed (12m/s)	Bending moment at wind velocity (12m/s)	Normal force at wind speed (25m/s)	Bending moment at wind velocity (25m/s)
0.00		2.6536e+06		2.7812e+07		4.3821e+07		1.9549e+08
1.00		2.6536e+06		2.7812e+07		4.3821e+07		1.9019e+08
2.00		2.5807e+06		2.7038e+07		4.2601e+07		1.8489e+08
3.00		2.5079e+06		2.6263e+07		4.1380e+07		1.7959e+08
4.00		2.4350e+06		2.5488e+07		40159800		1.7430e+08
5.00		2.3622e+06		2.4714e+07		3.8939e+07		1.6900e+08
6.00		2.2893e+06		2.3939e+07		3.7719e+07		1.6370e+08
10.80	492.8143	2.2166e+06	5.0036e+03	2.3165e+07	7.8850e+03	3.6498e+07	3.4223e+04	1.5841e+08
15.60	706.1201	1.8725e+06	7.8104e+03	1.9504e+07	1.2308e+04	3.0731e+07	5.3419e+04	1.3337e+08
20.40	860.6460	1.5423e+06	1.0214e+04	1.5991e+07	1.6094e+04	2.5196e+07	6.9868e+04	1.0935e+08
25.20	1.0149e+03	1.2302e+06	1.2619e+04	1.2686e+07	1.9874e+04	1.9988e+07	8.6268e+04	8.6749e+07
30.00	1.3472e+03	9.3965e+05	1.5032e+04	9.6434e+06	2.3678e+04	1.5195e+07	1.0276e+05	6.5945e+07
34.80	1.7147e+03	6.7632e+05	1.7413e+04	6.9196e+06	2.7436e+04	1.0903e+07	1.1907e+05	4.7319e+07
39.60	1.8053e+03	4.4826e+05	1.9793e+04	4.5696e+06	3.1191e+04	7.2001e+06	1.3537e+05	3.1249e+07
44.40	2.1802e+03	2.6075e+05	2.2155e+04	2.6483e+06	3.4909e+04	4.1726e+06	1.5150e+05	18109440
49.20	2.4119e+03	1.1915e+05	2.4491e+04	1.2101e+06	3.8591e+04	1.9066e+06	1.6750e+05	8274816
54.00	2.6437e+03	3.0455e+04	2.6851e+04	3.0932e+05	4.2305e+04	4.8735e+05	1.8360e+05	2115072

Bending moment along the length of the blades on flap-wise-direction

Location	Normal force at wind velocity (3m/s)	shear force as the wind velocity (3m/s)	Normal force at wind velocity (9.56m/s)	shear force as the wind velocity (9.56m/s)	Normal force at wind speed (12m/s)	shear force as the wind velocity (12m/s)	Normal force at wind speed (25m/s)	shear force as the wind velocity (25m/s)
0.00		7.2852e+04		7.7463e+05		1.2205e+06		5.2972e+06
1.00		7.2852e+04		7.7463e+05		1.2205e+06		5.2972e+06
2.00		7.2852e+04		7.7463e+05		1.2205e+06		5.2972e+06
3.00		7.2852e+04		7.7463e+05		1.2205e+06		5.2972e+06
4.00		7.2852e+04		7.7463e+05		1.2205e+06		5.2972e+06
5.00		7.2852e+04		7.7463e+05		1.2205e+06		5.2972e+06
6.00		7.2852e+04		7.7463e+05		1.2205e+06		5.2972e+06
10.80	492.8143	7.2852e+04	5.0036e+03	7.7463e+05	7.8850e+03	1.2205e+06	3.4223e+04	5.2972e+06
15.60	706.1201	7.0486e+04	7.8104e+03	7.5062e+05	1.2308e+04	1.1827e+06	5.3419e+04	5132904
20.40	860.6460	6.7097e+04	1.0214e+04	7.1313e+05	1.6094e+04	1.1236e+06	6.9868e+04	4.8765e+06
25.20	1.0149e+03	6.2966e+04	1.2619e+04	6.6410e+05	1.9874e+04	1.0463e+06	8.6268e+04	4.5411e+06
30.00	1.3472e+03	5.8094e+04	1.5032e+04	603528	2.3678e+04	950928	1.0276e+05	4127040
34.80	1.7147e+03	5.1628e+04	1.7413e+04	5.3137e+05	2.7436e+04	8.3727e+05	1.1907e+05	3633792
39.60	1.8053e+03	4.3397e+04	1.9793e+04	447792	3.1191e+04	7.0558e+05	1.3537e+05	3062256
44.40	2.1802e+03	3.4732e+04	2.2155e+04	3.5279e+05	3.4909e+04	555864	1.5150e+05	2412480
49.20	2.4119e+03	2.4267e+04	2.4491e+04	2.4644e+05	3.8591e+04	3.8830e+05	1.6750e+05	1685280
54.00	2.6437e+03	1.2690e+04	2.6851e+04	1.2888e+05	4.2305e+04	203064	1.8360e+05	881280

Shear force along the length of the blades on flap-wise-direction

Appendix: A

Location	Tangential force at wind velocity (3m/s)	moment along tangential force as the wind velocity (3m/s)	Tangential force at wind velocity (9.56m/s)	moment along tangential force as the wind velocity (9.56m/s)	Tangential force at wind velocity (12m/s)	moment along tangential force as the wind velocity (12m/s)	Tangential force at wind velocity (25m/s)	moment along tangential force as the wind velocity (25m/s)
0.00		2.6653e+05		2.8565e+06		4.9037e+06		1.9533e+07
1.00		2.6653e+05		2.8565e+06		4.9037e+06		1.9533e+07
2.00		2.5746e+05		2.7577e+06		4.7385e+06		1.8858e+07
3.00		2.4838e+05		2.6589e+06		4.5733e+06		1.8182e+07
4.00		2.3930e+05		2.5601e+06		4.4080e+06		1.7507e+07
5.00		2.3022e+05		2.4614e+06		4.2428e+06		1.6831e+07
6.00		2.2114e+05		2.3626e+06		4.0776e+06		1.6156e+07
10.80	185.2025	2.1207e+05	1.8804e+03	2.2638e+06	2.9632e+03	3.8335e+06	1.2862e+04	1.5480e+07
15.60	198.3573	1.7063e+05	2.1993e+03	1.8113e+06	3.4657e+03	3.1534e+06	1.5042e+04	1.2386e+07
20.40	197.8736	1.3360e+05	2.3612e+03	1.4059e+06	3.7205e+03	2.4685e+06	1.6152e+04	9.6135e+06
25.20	195.9213	1.0115e+05	2.4568e+03	1.0529e+06	3.8691e+03	1.8664e+06	1.6794e+04	7.2002e+06
30.00	193.7752	7.3224e+04	2.1716e+03	7.5550e+05	3.4207e+03	1.3517e+06	1.4845e+04	5.1665e+06
34.80	211.7759	4.9792e+04	2.1507e+03	5.1140e+05	3.3885e+03	9.2099e+05	1.4705e+04	3.4972e+06
39.60	189.8702	3.1032e+04	2.0920e+03	3.1708e+05	3.2967e+03	4.9961e+05	1.4307e+04	2.1684e+06
44.40	193.5634	1.6899e+04	1.9669e+03	1.7164e+05	3.0993e+03	2.7044e+05	1.3451e+04	1.1738e+06
49.20	175.5716	7.1837e+03	1.7828e+03	7.2958e+04	2.8090e+03	1.1495e+05	1.2193e+04	4.9892e+05
54.00	149.3383	1.7204e+03	1.5168e+03	1.7474e+04	2.3899e+03	2.7532e+04	1.0372e+04	1.1949e+05

Bending moment along the length of the blades on edgewise-direction

Location	Tangential force at wind velocity (3m/s)	Shear force as the wind velocity (3m/s)	Tangential force at wind velocity (9.56m/s)	Shear force as the wind velocity (9.56m/s)	Tangential force at wind velocity (12m/s)	Shear force as the wind velocity (12m/s)	Tangential force at wind velocity (25m/s)	Shear force as the wind velocity (25m/s)
0.00		9.0780e+03		9.8772e+04		1.5563e+05		6.7547e+05
1.00		9.0780e+03		9.8772e+04		1.5563e+05		6.7547e+05
2.00		9.0780e+03		9.8772e+04		1.5563e+05		6.7547e+05
3.00		9.0780e+03		9.8772e+04		1.5563e+05		6.7547e+05
4.00		9.0780e+03		9.8772e+04		1.5563e+05		6.7547e+05
5.00		9.0780e+03		9.8772e+04		1.5563e+05		6.7547e+05
6.00		9.0780e+03		9.8772e+04		1.5563e+05		6.7547e+05
10.80	185.2025	9.0780e+03	1.8804e+03	9.8772e+04	2.9632e+03	1.5563e+05	1.2862e+04	6.7547e+05
15.60	198.3573	8.1890e+03	2.1993e+03	8.9747e+04	3.4657e+03	1.4141e+05	1.5042e+04	6.1373e+05
20.40	197.8736	7.2369e+03	2.3612e+03	7.9190e+04	3.7205e+03	1.2477e+05	1.6152e+04	5.4153e+05
25.20	195.9213	6.2871e+03	2.4568e+03	6.7856e+04	3.8691e+03	1.0691e+05	1.6794e+04	4.6400e+05
30.00	193.7752	5.3467e+03	2.1716e+03	5.6064e+04	3.4207e+03	8.8340e+04	1.4845e+04	3.8339e+05
34.80	211.7759	4.4166e+03	2.1507e+03	4.5640e+04	3.3885e+03	7.1920e+04	1.4705e+04	3.1213e+05
39.60	189.8702	3.4000e+03	2.0920e+03	3.5316e+04	3.2967e+03	5.5656e+04	1.4307e+04	2.4155e+05
44.40	193.5634	2.4887e+03	1.9669e+03	2.5275e+04	3.0993e+03	3.9831e+04	1.3451e+04	1.7288e+05
49.20	175.5716	1.5596e+03	1.7828e+03	1.5838e+04	2.8090e+03	2.4955e+04	1.2193e+04	108312
54.00	149.3383	716.8238	1.5168e+03	7.2806e+03	2.3899e+03	1.1472e+04	1.0372e+04	4.9786e+04

Shear force along the length of the blades on edgewise-direction

Appendix: B

Micromechanical modelling of the lamina [122]

The density and the elastic moduli determined by rule of mixtures (ROM) as given by the following relations:

$$\rho_c = \rho_f V_f + \rho_m V_m \quad E_{11} = E_f V_f + E_m V_m \quad \frac{1}{E_{22}} = \frac{V_f}{E_f} + \frac{V_m}{E_m} \quad \frac{1}{G_{12}} = \frac{V_f}{G_f} + \frac{V_m}{G_m}$$

where ρ_c , ρ_f and ρ_m are the densities of glass and carbon fibre and epoxy resin, E_{11} and E_{22} are longitudinal and transvers elastic moduli, G_{12} is in-plane shear modulus, E_f and E_m are the elastic moduli, G_f and G_m are shear modulus of the glass and carbon fibre and the epoxy resin. V_f and V_m are the volume fraction of glass and carbon fibre and the epoxy resin, respectively. The major Poisson's ratio ν_{12} is given by

$$\nu_{12} = \nu_f V_f + \nu_m V_m$$

Where ν_f and ν_m are Poisson's ratios of the glass and carbon fibre and the epoxy resin.

The generalized Hooke's law:

$$\{\sigma\} = [\bar{Q}]\{\varepsilon\} \quad \text{or it can be represented} \quad \{\varepsilon\} = [\bar{S}]\{\sigma\}$$

Where $\{\sigma\}$ and $\{\varepsilon\}$ are, the stress and strain of the material, $[\bar{S}]$ and $[\bar{Q}]$ are compliance and reduce stiffness of the material. The stiffness matrix obtained inverting the compliance matrix $[\bar{Q}] = [\bar{S}]^{-1}$. The strain and stress in the local coordinate system can be analysed.

$$\begin{Bmatrix} \varepsilon_1 \\ \varepsilon_2 \\ \gamma_{12} \end{Bmatrix} = \begin{bmatrix} 1/E_1 & -\nu_{21}/E_2 & 0 \\ -\nu_{12}/E_1 & 1/E_2 & 0 \\ 0 & 0 & 1/G_{12} \end{bmatrix} \begin{Bmatrix} \sigma_1 \\ \sigma_2 \\ \sigma_{12} \end{Bmatrix}$$

The elements of the compliance stiffness matrix are given by:

$$S_{11} = \frac{1}{E_1}, S_{22} = \frac{1}{E_2}, S_{12} = -\frac{\nu_{21}}{E_2}, S_{21} = -\frac{\nu_{12}}{E_1}, \text{ and } S_{66} = \frac{1}{G_{12}}$$

Inverting the above compliance matrix to get the stiffness matrix $[Q]$ of the material and represented by:

$$\begin{Bmatrix} \sigma_1 \\ \sigma_2 \\ \tau_{12} \end{Bmatrix} = \begin{bmatrix} Q_{11} & Q_{12} & 0 \\ Q_{21} & Q_{22} & 0 \\ 0 & 0 & Q_{66} \end{bmatrix} \begin{Bmatrix} \varepsilon_1 \\ \varepsilon_2 \\ \gamma_{12} \end{Bmatrix}$$

Where σ_1 and σ_2 , in-plane normal stresses, τ_{12} , in-plane shear stress: ε_1 and ε_2 are in-plane normal strains, and γ_{12} is in-plane shear strain. The elements of the stiffness matrix of single lamina using the classical laminate theory denoted:

$$Q_{11} = \frac{E_1}{1 - \nu_{12}\nu_{21}}, Q_{22} = \frac{E_2}{1 - \nu_{12}\nu_{21}}, Q_{12} = \frac{\nu_{21}E_2}{1 - \nu_{12}\nu_{21}} \text{ and } Q_{66} = G_{12}$$

A lamina can have several ply orientations, it can be written in the global frame (x,y,z) by using the transformation:

$$\{\sigma\}_{1,2} = [T]\{\sigma\}_{x,y}, \{\varepsilon\}_{1,2} = [T]^{-t}\{\varepsilon\}_{x,y} \text{ and } [S]_{x,y} = [T]^t[S]_{1,2}[T],$$

$[Q]_{x,y} = [T]^{-t}[Q]_{1,2}[T]^{-1}$, the transfer matrix $[T]$ on θ_k ply angle of the k^{th} layer is given by:

$$[T]_k = \begin{bmatrix} \cos^2 \theta_k & \sin^2 \theta_k & -2 \sin \theta_k \cos \theta_k \\ \sin^2 \theta_k & \cos^2 \theta_k & 2 \sin \theta_k \cos \theta_k \\ \sin \theta_k \cos \theta_k & -\sin \theta_k \cos \theta_k & \cos^2 \theta_k - \sin^2 \theta_k \end{bmatrix}$$

$\sigma = \{\sigma_x \ \sigma_y \ \sigma_{xy}\}^t$, indicates the total transformed stress tensor. $\varepsilon = (\varepsilon_x \ \varepsilon_y \ \gamma_{xy})^t$, denote the strain Tensor. Each ply in a laminate stressed due to deformation differences of adjacent lamina contributes for the formation of residual stress among the laminates are given by.

$$\begin{Bmatrix} \sigma_x \\ \sigma_y \\ \tau_{xy} \end{Bmatrix} = \begin{bmatrix} \bar{Q}_{11} & \bar{Q}_{12} & \bar{Q}_{16} \\ \bar{Q}_{21} & \bar{Q}_{22} & \bar{Q}_{26} \\ \bar{Q}_{16} & \bar{Q}_{26} & \bar{Q}_{66} \end{bmatrix} \begin{Bmatrix} \varepsilon_x \\ \varepsilon_y \\ \gamma_{xy} \end{Bmatrix}$$

where \bar{Q} is the transformed reduced stiffness matrix of single layer with the following elements

$$\begin{aligned} \bar{Q}_{11k} &= Q_{11k} \cos^4 \theta_k + 2(Q_{12k} + 2Q_{66k}) \sin^2 \theta_k \cos^2 \theta_k + Q_{22k} \sin^4 \theta_k \\ \bar{Q}_{12k} &= (Q_{11k} + Q_{22k} - 4Q_{66k}) \sin^2 \theta_k \cos^2 \theta_k + Q_{12k} (\sin^4 \theta_k + \cos^4 \theta_k) \\ \bar{Q}_{22k} &= Q_{11k} \sin^4 \theta_k + 2(Q_{12k} + 2Q_{66k}) \sin^2 \theta_k \cos^2 \theta_k + Q_{22k} \cos^4 \theta_k \\ \bar{Q}_{16k} &= (Q_{11k} - Q_{12k} - 2Q_{66k}) \sin \theta_k \cos^3 \theta_k + (Q_{12k} - Q_{22k} + 2Q_{66k}) \sin^3 \theta_k \cos \theta_k \\ \bar{Q}_{26k} &= (Q_{11k} - Q_{12k} - 2Q_{66k}) \sin^3 \theta_k \cos \theta_k + (Q_{12k} - Q_{22k} + 2Q_{66k}) \sin \theta_k \cos^3 \theta_k \\ \bar{Q}_{66k} &= (Q_{11k} + Q_{22k} - 2Q_{12k} - 2Q_{66k}) \sin^2 \theta_k \cos^2 \theta_k + Q_{66k} (\sin^4 \theta_k + \cos^4 \theta_k) \end{aligned}$$

Based on the Kirchhoff assumptions, the strain displacement relation is given by:

$$\varepsilon = \varepsilon^0 + z k$$

where $\varepsilon = (\varepsilon_x, \varepsilon_y, \gamma_{xy})$, $\varepsilon_x, \varepsilon_y$ and γ_{xy} the displacement of the lamina in the x and y direction, furthermore, γ_{xy} denote the displacement along the x-y plane.

$k_x = -\frac{\partial^2 w}{\partial x^2}$; $k_y = \frac{-\partial^2 w}{\partial y^2}$, are bending deflection ratios of the mid-plane and

$k_{xy} = -2\frac{\partial^2 w}{\partial x \partial y}$ represents twisting deflection ratio of the mid-plane. w is the displacement

component in z- direction on the mid-plane. The extensional stiffness matrix with the element is denoted by:

$$A_{ij} = \sum_{k=1}^n [\bar{Q}_{ij}]_k (z_k - z_{k-1}) \quad (i, j = 1, 2, 6).$$

The matrix B is zero due to symmetrical fibre arrangement and the matrix D represents bending stiffness is represented by:

$$D_{ij} = \frac{1}{3} \sum_{k=1}^n [\bar{Q}_{ij}]_k (z_k^3 - z_{k-1}^3) \quad (i, j = 1, 2, 6).$$

The properties of wind turbine blade modelled using pure and hybrid composite structures were analysed using classical laminated plate theory (CLPT) based on behaviour of each layer.

$$\begin{Bmatrix} N_x \\ N_y \\ N_{xy} \\ M_x \\ M_y \\ M_{xy} \end{Bmatrix} = \begin{bmatrix} A_{11} & A_{12} & A_{16} \\ A_{12} & A_{22} & A_{26} \\ A_{16} & A_{26} & A_{66} \\ D_{11} & D_{12} & D_{16} \\ D_{12} & D_{22} & D_{26} \\ D_{16} & D_{26} & D_{66} \end{bmatrix} \begin{Bmatrix} \varepsilon_x^0 \\ \varepsilon_y^0 \\ \gamma_{xy}^0 \\ k_x \\ k_y \\ k_{xy} \end{Bmatrix}$$

Where N_x, N_y, N_{xy} , in-plane forces per unit length, M_x, M_y, M_{xy} , moments per unit length, $\varepsilon_x^0, \varepsilon_y^0, \varepsilon_{xy}^0$, the strains in the mid-plane and k_x, k_y, k_{xy} are the plane curvatures.

[A] is the extensional stiffness matrix and [D] is bending stiffness matrix.

Thermal strain vector is given by

$$\varepsilon_k^T = \alpha_{xyk}^t \Delta T$$

where $\alpha_{xyk}^t = (\alpha_{xk} \quad \alpha_{yk} \quad \alpha_{xyk})^t$, α_x and α_y are coefficients of thermal expansion in the x and y directions and α_{xyk} is the thermal expansion coefficient in the x-y plane.

The relation between thermal expansion coefficients in the material and off-axis directions is given by

$$\alpha_{xyk} = T_k^t \alpha_{12k}$$

where $\alpha_{12k} = (\alpha_{1k} \ \alpha_{2k} \ 0)^t$, α_{1k} and α_{2k} are thermal expansion coefficients in the material directions.

The thermal expansion coefficients can be computed by the rule of mixtures as

$$\alpha_{1k} = \frac{(\alpha_{fk} E_{fk} V_{fk} + \alpha_{mk} E_{mk} V_{mk})}{E_{1k}}$$

$$\alpha_{2k} = (1 + \nu_{fk}) \alpha_{fk} V_f + (1 + \nu_{mk}) \alpha_{mk} V_{mk} - \alpha_{1k} \nu_{12k}$$

where α_{fk} and α_{mk} are the thermal expansion coefficients of the fiber and the matrix.

The axial force acting on the laminate can be evaluated by substituting the stress-strain relation $\sigma_k = \overline{Q}_k [\varepsilon_k - \alpha_{xyk}^t \Delta T]$ into the expression for $N = (N_x, N_y, N_{xy})^t$ given by

$$N = \int_{-h/2}^{h/2} \sigma_k dz = \sum_{k=1}^3 \int_{z_{k-1}}^{z_k} \overline{Q}_k (\varepsilon_k - \alpha_{xyk}^t \Delta T) dz$$

where N_x and N_y are axial forces in the x and y directions and N_{xy} is the shear

force in $x - y$ plane. Strain at distance z from the mid-plane is given by $\varepsilon = \varepsilon^0 + zk$

where $\varepsilon = (\varepsilon_x, \varepsilon_y, \gamma_{xy})$, ε_x , ε_y and γ_{xy} are the strains in the $x - y$ plane and

$k = (k_x, k_y, k_{xy})^t$ is the curvature vector. Noting that stretching-bending coupling matrix

$B = 0$, substituting $\varepsilon = \varepsilon^0 + zk$

$$N = A\varepsilon - N^T$$

where A is the extensional stiffness matrix elements of which are given by

$$A_{ij} = \sum_{k=1}^3 [\overline{Q}_{ij}]_k (z_k - z_{k-1}) \text{ for } (i, j = 1, 2, 6)$$

and $N^T = (N_x^T \ N_y^T \ N_{xy}^T)^t$ is the axial force due to ΔT given by

$$N^T = \int_{-h/2}^{h/2} \overline{Q}_k \alpha_{xyk}^t \Delta T dz = \Delta T \sum_{k=1}^3 \overline{Q}_k \alpha_{xyk}^t (z_k - z_{k-1})$$

Expression for the bending moment is given by

$$M = Dk - M^T$$

where matrix D is the bending stiffness given by

$$D_{ij} = \frac{1}{3} \sum_{k=1}^3 [\bar{Q}_{ij}]_k (z_k^3 - z_{k-1}^3) \quad (i, j = 1, 2, 6)$$

and $M^T = (M_x^T \ M_y^T \ M_{xy}^T)^t$ is the bending moment due to ΔT given by

$$M^T = \int_{-h/2}^{h/2} \bar{Q}_k \alpha_{xyk}^t \Delta T z dz = \frac{1}{2} \Delta T \sum_{k=1}^3 \bar{Q}_k \alpha_{xyk}^t (z_k^2 - z_{k-1}^2)$$

6.2 Mechanical properties of unidirectional layers

The strength properties of unidirectional layers in the wind turbine blade was analysed based on rule of mixture (ROM) for prediction in longitudinal, transverse and in-plane shear.

The failure strain for the matrix is higher than for the fibre in the case for polymeric matrix composite in unidirectional arrangement. The ultimate failure strain of the fibre and matrix can be represented by:

$$(\varepsilon_f)_{ult} = \frac{(\sigma_f)_{ult}}{E_f}$$

where $(\sigma_f)_{ult}$ is the ultimate tensile strength of fibre and (E_f) is the young's modulus of the fibre. The ultimate failure strain of the matrix is given by:

$$(\varepsilon_m)_{ult} = \frac{(\sigma_m)_{ult}}{E_m}$$

where $(\sigma_m)_{ult}$ is the ultimate tensile strength of the matrix and (E_m) is the young's modules of the matrix. The longitudinal tensile strength is given by:

$$(X_1^T)_{ult} = (\sigma_f)_{ult} (V_f) + (\varepsilon_f)_{ult} E_m (1 - V_f)$$

where $(X_1^T)_{ult}$ is the ultimate longitudinal tensile strength of the composite (lamina)

Using the maximum strain theory, if the transvers strain of the composite exceeds the ultimate transverse tensile strain of the composite, the lamina is considered as failed in the transverse directions [123]. The ultimate transverse tensile strain can be denoted

$$(\varepsilon_2^T)_{ult} = (\varepsilon_m^T)_{ult} (1 - V_f)^{1/3}$$

where $(\varepsilon_2^T)_{ult}$ is ultimate transverse tensile strain. The ultimate longitudinal compressive strength can be analysed.

$$(X_1^c)_{ult} = \frac{E_1(\varepsilon_2^T)_{ult}}{\nu_{12}}$$

where $(X_1^c)_{ult}$ is the ultimate longitudinal compressive strength

Assumed that the transverse failure of the lamina is because of the failure of the matrix, and then the ultimate transverse strain is analysed

$$(\varepsilon_2^T)_{ult} = \left[\frac{d}{s} \frac{E_m}{E_f} + \left(1 - \frac{d}{s}\right) \right] (\varepsilon_m^T)_{ult}, \quad \frac{d}{s} = \left[\frac{4(V_f)}{\Pi} \right]^{1/2}$$

where $(\varepsilon_2^T)_{ult}$, ultimate tensile transverse strain of the matrix, d, diameter of the fibre and s, distance between centres of the fibres. The ultimate transverse tensile strength can be analysed

$$(X_2^T)_{ult} = E_2(\varepsilon_2^T)_{ult},$$

where $(X_2^T)_{ult}$, ultimate transvers tensile strength

The actual compressive strength lower due to interfacial bonds and longitudinal fibre splitting is given by:

$$(\varepsilon_2^c)_{ult} = \left[\frac{d}{s} \frac{E_m}{E_f} + \left(1 - \frac{d}{s}\right) \right] (\varepsilon_m^c)_{ult}$$

where $(\varepsilon_2^c)_{ult}$ ultimate transvers compressive strain

$$(X_2^c)_{ult} = E_2(\varepsilon_2^c)_{ult}$$

where $(X_2^c)_{ult}$ is the ultimate transvers compressive strength

The shearing is represented by the sum of the deformation in the fibre and matrix

$$(\gamma_{12})_{ult} = \left[\frac{d}{s} \frac{E_m}{E_f} + \left(1 - \frac{d}{s}\right) \right] (\gamma_{12})_{mult}$$

where $(\gamma_{12})_{ult}$ is the ultimate shear strain

$$(S_{12})_{ult} = G_{12}(\gamma_{12})_{ult}$$

where $(S_{12})_{ult}$ is the ultimate shear strength

For the calculation of strength properties of the beam, the Tsai-Wu failure criteria is implemented to predicate the failure of the rotating composite beam under variable angular speeds as failure index (\hat{f}_i) in a laminate reaches less than or equal to one as follows:

$$\hat{f}_i = F_1\sigma_1 + F_2\sigma_2 + F_6\tau_{12} + F_{11}\sigma_1^2 + F_{22}\sigma_2^2 + F_{66}\tau_{12}^2 + 2F_{12}\sigma_1\sigma_2 \leq 1$$

where σ_1 , longitudinal stress, σ_2 , transverse stress and τ_{12} , in-plane shear strength. The components $F_1, F_2, F_6, F_{11}, F_{22}, F_{66}$ and F_{12} of the failure theory can be found using strength parameter of unidirectional lamina.

$$F_1 = \frac{1}{X_1^T} + \frac{1}{X_1^C}, F_2 = \frac{1}{X_2^T} + \frac{1}{X_2^C}, F_{11} = -\frac{1}{X_1^T X_1^C}, F_{22} = -\frac{1}{X_2^T X_2^C}, F_{66} = \frac{1}{S_{12}^2}, F_{12} = -\frac{1}{2} \sqrt{F_{11} F_{22}}$$